ABSTRACT

Title of Document: DEVELOPMENT AND TEST OF A SUPERCONDUCTING HELICON PLASMA THRUSTER

John Joseph Vitucci
Doctor of Philosophy, 2019

Directed By: Professor Raymond J. Sedwick
Department of Aerospace Engineering

Helicon thrusters have emerged as a viable technology for station-keeping and deep-space exploration applications due to their high-efficiency plasma generation and amenability to propellants such as water vapor. A proposed design and performance analysis for the superconducting helicon thruster is presented. First, a zero-dimensional power flow analysis is performed, demonstrating an increase in the power efficiency for the superconducting helicon thruster versus the baseline helicon plasma thruster. This superconducting helicon thruster is composed of two subsystems: the superconducting magnet subsystem and the thermal management subsystem. The superconducting magnet subsystem shows that by using the combination of a solenoid and permanent magnet, a

desirable magnetic field geometry for a helicon plasma can be supported. By adding a high-temperature (type-II) superconductor, the induced current in the superconductor that results from quenching the solenoid can sustain the same magnetic field geometry without the need to continuously power the electromagnet. The thermal management subsystem then maintains cryogenic temperatures in a closed-loop design for continuous operation of the thruster.

A triple Langmuir probe was used to experimentally characterize the bulk plasma, and the downstream ion energies were measured with a retarding potential analyzer (RPA). Using the measured electron temperature and ion energies, it was shown that the baseline helicon thruster demonstrates slightly better performance metrics, however this comes at the cost of lower propulsive efficiencies. In instances where maximum thrust and maximum specific impulses are desired, the baseline helicon thruster would be more advantageous. If RF input power mitigation is of larger concern, the superconducting helicon thruster outperforms the baseline helicon thruster. Additionally, substantially larger ion beam energies were measured using the RPA compared to other independent studies. This anomalous acceleration mechanism has the potential to provide vast improvement to the performance of the helicon thruster.

DEVELOPMENT AND TEST OF A SUPERCONDUCTING HELICON PLASMA THRUSTER

by

John Joseph Vitucci

Dissertation submitted to the Faculty of the Graduate School of the
University of Maryland, College Park, in partial fulfillment
of the requirements for the degree of
Doctor of Philosophy
2019

Advisory Committee:
Professor Raymond Sedwick, Chair
Professor Christine Hartzell
Professor James Baeder
Professor Peter Sunderland
Professor Adil Hassam

Dedication

This work has truly been a labor of love. The most important lesson I've learned throughout my research is that no matter how difficult something may get, at the end of the day it still builds character. This has been the motto of the Space, Power, and Propulsion Laboratory from day one, and is very true to the graduate research experience. Much like anything in life, there were ups and downs; days where a solution seemed so far out of reach, and days where anything seemed possible. In the end, all the trials and tribulations resulted in one of the most rewarding of experiences in my life. One that will be very difficult to best. This all would never have been possible without a multitude of people in my life. Most important to me was the support I had of my family. My mom, dad, brother, and grandparents may never quite understand the lengthy process of graduate work, but no matter what, I always knew I had their never-ending support. To my advisor, Dr. Sedwick, I could never fully express my gratitude for providing the means to undertake this journey. I'll be forever grateful for the opportunity. My colleagues and fellow graduate students have been the best people to go through this experience with. No matter what the occasion, they were the most supportive, gave the best advice, and always provided an ear when I just wanted to rant or explain some major breakthrough, even if they truly didn't care. All of my close friends and loved ones from outside of the lab were also instrumental in making this happen. Without them, life would truly have just revolved around work. I always had people to count on when I just needed to decompress and enjoy life. While I want to name everyone who made this possible,

there just simply wouldn't be enough pages, nor do I wish to leave anyone out. If you're reading this, then you absolutely know who you are. So with that I say, thank you.

Acknowledgements

In order to make this research possible, it truly took a large number of people throughout the years. Primarily, I must thank the NASA Office of the Chief Technologist for the NASA Space Technology Research Fellowship. This funded me for a large portion of my graduate studies, and without this support I would never have been able to travel to the various conferences around the world to connect with other individuals in the field or experience the space propulsion work at NASA's Glenn Research Center. Once again, I must also thank my advisor, Dr. Sedwick, for the opportunity to work under him at the University of Maryland Space, Power, and Propulsion laboratory. The experiences have been life-changing, and something I would gladly do over again in a heartbeat. I also extend the sincerest appreciation to my committee members for all of their time and input along the way. The feedback and time they contributed to the comprehensive examination and pre-defense were invaluable. I would also like to acknowledge the staff of the Department of Aerospace Engineering who were also available to help with all of the administrative challenges that came up. Without all of these individuals involved, none of this would have been possible. Thank you for allowing me the means to pursue what can only be described as a dream.

Table of Contents

List of Figures

Nomenclature

A	=	Cross-Sectional Area of the Thruster (m^2)
A_p	=	Triple Langmuir Probe Tip Area (m^2)
A_{RPA}	=	RPA Cross-Sectional Area (m^2)
a	=	Thruster or Plasma Source Radius (m)
ANU	=	Australia National University
B	=	External Magnetic Field Strength (G)
$\boldsymbol{B}$	=	Perturbed Electric Field (T)
$\boldsymbol{B_0}$	=	Equilibrium Magnetic Field (T)
BSCCO	=	Bismuth Strontium Calcium Copper Oxide
C_f	=	Antenna Feed Line Capacitance (F)
c	=	Speed of Light in Vacuum (m/s^2)
c_p	=	Specific Heat at Constant Pressure (J/kg K)
CFDL	=	Current-Free Double-Layer
D	=	Dispersion Relation
d	=	Distance from Heat Element (m)
d_{pp}	=	Distance between Parallel-Plate Capacitor (m)
$\boldsymbol{E}$	=	Perturbed Electric Field (V/m)
E'_{ion}	=	Total Ionization Cost per Ion-Electron Pair (eV)
E_{ion}	=	First Ionization Energy of Propellant (eV)
E_r	=	Resonant Ionization Energy (eV)
e	=	Elementary Particle Charge (C)
F	=	Thrust (N)
F/A	=	Thrust Per Area Ratio (N/m^2)
f	=	Operating Frequency (1/s)
FEM	=	Finite Element Method
G	=	Antenna Gain
g	=	Acceleration Due to Gravity (m/s^2)
h_{we}	=	Latent Heat of Vaporization for Water (J/kg)
h_{wm}	=	Latent Heat of Melting for Water (J/kg)
HDLT	=	Helicon Double-Layer Thruster
I	=	Solenoid Current (A)
I_+	=	Current into Positive Probe (A)
I_-	=	Current into Negative Probe (A)
I_{fl}	=	Current into Floating Probe (A)
I_G	=	Cost of Neutral Particle Ionization (J)
I_{RPA}	=	Ion Current Measured by RPA (A)
I_{sp}	=	Specific Impulse (s)
i	=	Complex Imaginary Component
ICH	=	Ion Cyclotron Heating
IEDF	=	Ion Energy Distribution Function
J_1	=	Bessel's Function of the First Kind
$\boldsymbol{j}$	=	Perturbed Current
k	=	Parallel Wavenumber (1/m)

k_B	=	Boltzmann's Constant (J/K)
k_T	=	Thermal Conductivity (W/m K)
L	=	Antenna Length (m)
L_f	=	Antenna Feed Line Inductance (H)
L_p	=	Total Power Loss within Plasma (W/m^3)
L_{pp}	=	Parallel-Plate Capacitor Length (m)
L_s	=	Solenoid Length (m)
L_z	=	Plasma Source Length (m)
M	=	Propellant Molecular Mass (kg)
m	=	Bessel Function Mode
m_e	=	Electron Mass (kg)
m_i	=	Ion Mass (kg)
$\dot{m}$	=	Mass Flow Rate (kg/s)
MPD	=	Magnetoplasma Dynamic Rocket
n_e	=	Plasma Density (1/m^3)
n_n	=	Neutral Density (1/m^3)
n_{RPA}	=	Downstream Density from RPA Measurements (1/m^3)
n_s	=	Number of Solenoid Turns
n_0	=	Equilibrium Density (1/m^3)
NEXT	=	NASA's Evolutionary Xenon Thruster
OML	=	Orbital Motion Limited Theory
P_{base}	=	Vacuum Chamber Base Pressure (torr)
P_f	=	Power Imparted to the Plasma Flow (W/m^3)
P_J	=	Jet Power (W/m^3)
P_m	=	Electromagnet Power Consumption (W)
$\dot{P_{rad}}$	=	Radiated Power (W/m^3)
P_{RF}	=	RF Input Power (W)
P_{tube}	=	Pressure in the Plasma Confining Tube (torr)
P_{vap}	=	Power Required to Vaporize Water (W)
P_0	=	Total Input Power (W/m^3)
p	=	First Zero of the Bessel Function J_1
PPT	=	Pulsed Plasma Thruster
Q	=	Throughput (torr L/s)
q	=	Heat Flux Density (W/m^2)
$\dot{q_r}$	=	Conducted Power (W/m^2)
R_{ion}	=	Ionization Rate (m^3/s)
r	=	Radial Position (m)
R	=	Resistance (Ohm)
RF	=	Radio Frequency
RPA	=	Retarding Potential Analyzer
SCM	=	Superconducting Magnets
S_p	=	Pumping Speed of Turbo Pump (L/s)
T	=	Temperature (K)
T_{boil}	=	Boiling Temperature of Water (K)
T_e	=	Electron Temperature (eV)
T_k	=	Transverse Wavenumber (1/m)

T_{melt}	=	Melting Temperature of Ice (K)
T_1	=	Characteristic Temperature of Propellant (eV)
t	=	Time (s)
TG	=	Trivelpiece-Gould
TRL	=	Technology Readiness Level
$U_{\|\|}$	=	Average Axial Velocity of the Plume (m/s)
u_e	=	Exit Velocity (m/s)
UMD SPPL	=	University of Maryland Space Power and Propulsion Laboratory
V_+	=	Positive Probe Bias with Respect to Ground (V)
V_-	=	Negative Probe Bias with Respect to Ground (V)
V_{beam}	=	Beam Potential (V)
V_{bias}	=	Bias Voltage Between Positive and Negative Probes (V)
V_f	=	Floating Probe Bias with Respect to Ground (V)
V_s	=	Plasma Potential with Respect to Ground (V)
VASIMR	=	Variable Specific Impulse Magnetoplasma Rocket
v_p	=	Phase Velocity (m/s)
v_{th}	=	Thermal Velocity
W_{pp}	=	Parallel-Plate Capacitor Width (m)
Z_m	=	Root of the Bessel Function J_m
z	=	Axial Position (m)
α	=	Beam Divergence Angle
Γ_{max}	=	Maximum Plasma Flux at the Pre-sheath $\left(\frac{particles}{m^3 s}\right)$
ε	=	Parallel-Plate Dielectric Permittivity (s^4A^2/m^3kg)
ϵ_c	=	Cost of Ionization per Ion-Electron Pair (eV)
ϵ_i	=	Ionization Energy (eV)
ϵ_{sh}	=	Total Energy Lost to Plasma Sheath (eV)
ϵ_{swall}	=	Total Energy Lost to Plasma Sheath at Upstream Wall (eV)
ϵ_0	=	Permittivity of Free Space
ϵ_1	=	Characteristic Energy of Propellant (eV)
η	=	Propulsive Efficiency
η_{RF}	=	Power Delivery Efficiency
η_{tr}	=	RPA Grid Transparency
λ	=	Plasma Skin Depth (m)
λ_{CX}	=	Wavelength (m)
λ_w	=	Wavelength (m)
μ	=	Propellant Flow Rate (kg/s)
μ_0	=	Permeability of Free Space (N/A^2)
θ	=	Angular Position
σ_{CX}	=	Charge Exchange Collision Cross-Section (m^2)
ν	=	Electron Collision Frequency (1/s)
ν_{eff}	=	Effective Collision Frequency (1/s)
ν_{LD}	=	Landau Collision Frequency (1/s)
ω	=	Angular Frequency (1/s)
ω_c	=	Plasma Frequency (1/s)
ω_p	=	Electron Cyclotron Frequency (1/s)

1. Chapter 1: Introduction

1.1 Electric Propulsion

1.1.1 Convectional Electric Propulsion Devices

The concept of electric propulsion has existed since as early as 1903 with the introduction and derivation of the Tsiolkovsky rocket equation. Tsiolkovsky then published the first notional idea of electric propulsion eight years later by stating the possibility of using electricity to accelerate particles from a "rocket device" [1]. Since then the technology has progressed in leaps and bounds. Typical applications of electric propulsion devices include station keeping by overcoming translational and rotational perturbations in a satellite's orbit, orbit raising, and interplanetary travel[2]. To date, over 200 spacecraft utilize electric propulsion for these purposes[3].

Each propulsion system requires an energy source, propellant, and a power conversion system. The most common metrics for evaluating the performance of any propulsive device are thrust (F) or thrust density (F/A), specific impulse (I_{sp}), total input power (P_0), and propulsive efficiency (η_p). Thrust is the amount of force imparted to a spacecraft and is given by the following equation:

$$F = \dot{m}u_e \tag{1.1}$$

where $\dot{m}$ is the mass flow rate and u_e is the exit velocity. Specific impulse provides a good indication of the thruster's efficiency. Larger specific impulses mean that a thruster

can produce a set amount of thrust for less propellant. The specific impulse can be derived from the thrust equation and is given by:

$$I_{sp} = \frac{u_e}{g} \tag{1.2}$$

where g is the acceleration due to gravity. While input power can directly increase thrust, this is not ideal as space applications are limited by the available power; thus it is advantageous to have a system that produces maximum thrust and specific impulse at minimum input powers. The propulsive efficiency is used to determine the percentage of input power that directly contributes to the jet power, P_J. The jet power is the quantity that directly contributes to directed thrust. For space propulsion applications, the propulsive efficiency is given as:

$$\eta = \frac{P_J}{P_0} \tag{1.3}$$

Compared to chemical rockets, electric propulsion devices will exhibit specific impulses that are orders of magnitude larger. Conversely, chemical rockets achieve thrust values that are orders of magnitude larger than those exhibited by electric propulsion devices.

Electric propulsion devices can be categorized as electrothermal, electrostatic, or electromagnetic. Electrothermal devices electrically heat the propellant, which is then thermodynamically expanded with the use of a nozzle. The most common electrothermal devices are the resistojet and the arcjet. The resistojet uses resistive elements to heat the propellant, however, it is limited by the effectiveness of the resistive material to uniformly heat the propellant. The material limitations also play an important role in the operational capabilities as the surrounding walls of the main chamber are in direct contact with the increasingly hot propellant. Limiting the temperature of the propellant then

restricts the achievable specific impulse, since the specific impulse is directly proportional to the stagnation temperature of the propellant at the nozzle throat. To improve the propellant heating, the arcjet was developed, consisting of a constricted arc in parallel flow. The improved design ensured that a greater volume of the propellant came in contact with the heating element than seen in the resistojet. Ultimately, this design is subject to the same material limitations as the resistojet. Typical specific impulses achieved by the resistojet are 200-300 s, where as the arcjet can achieve up to 1000 s^2.

Electrostatic devices, which include but are not limited to the ion engine and Hall thruster, rely on electric fields to electrostatically accelerate propellant particles. The ionization stage of an ion engine consists of a cathode, called the emitter, which provides the system with free electrons. The electrons are then accelerated towards the walls of the ionization chamber, which contain the anode. Magnetic fields are then used to confine the electrons and prevent them from easily reaching the walls. Once the propellant enters the ionization region, the free electrons collide with the neutral gas particles to generate plasma. The ions are then accelerated through a potential difference between a series of grids that lead to the exit of the device. An external neutralizing cathode ensures that the emerging beam is quasi-neutral to prevent spacecraft charging. Typical ion engines have a thrust ranging between 0.01 and 200 mN with specific impulses between 1500 and 5000 s and can be throttled with the use of a decelerator grid[2]. The primary limitation of this design is the maximum achievable thrust density, which is space charge limited in the volume between the grids. This space charge limitation is given by the Child-Langmuir Law. In addition, the thruster suffers from

lifetime issues. While most of the ions are accelerated through the grids, there is still a percentage that impacts the grids causing erosion. Newer designs, as seen in NASA's Evolutionary Xenon Thruster (NEXT), for example, are showing the capabilities of extending the lifetime of ion engines through longer grid and cathode lifetimes[4].

The Hall thruster, on the other hand, does not suffer from the space charge limitation or grid erosion because it does not use grids to accelerate the ions. Instead, the Hall thruster is composed of an annular, cylindrical ionization region with an axial electric field and radial magnetic field. The crossed electric and magnetic field causes the free electrons to undergo an azimuthal drift called the Hall current. This causes the injected propellant to ionize due to collisions with the drifting electrons. These collisions are the only mechanism through which the electrons can reach the anode at the upstream wall. The combination of the external neutralizing cathode and anode at the upstream wall creates the axial electric field, which accelerates the ions out of the thruster. The Hall thruster is capable of thrust values up to 2 N and can operate at up to 2000 s of specific impulse[2]. Unlike the ion engine, the Hall thruster is more readily scaled to higher powers, however it similarly suffers from erosion and sputtering of the dielectric chamber walls.

Electromagnetic devices accelerate propellant particles through both electric and magnetic fields. Of this type are the pulsed plasma thruster (PPT) and magnetoplasma dynamic rocket (MPD). The MPD thruster utilizes radial electric fields to ionize the propellant and an azimuthal magnetic field that results in a Lorentz force on the ions in the direction of the thruster exit. While the design is simplistic and can yield high thrust densities and high specific impulses, the impracticality lies in the large power

requirements and large hardware requirements, such as the size and weight of the power supply. With specific impulses between 2000 and 5000 s, and the capability to achieve up to 2 N of thrust, MPD thrusters have been considered for several space applications[2]. The PPT generates thrust equal to the Lorentz force as well, however, the design is more simplistic than the MPD. The most prevalent propellant for a PPT is Teflon. Using two slab electrodes, short pulses, on the order of milliseconds, are used to sublimate and ionize the Teflon. The time varying electric field in turn generates a magnetic field, causing a force on the ions in the direction of the thruster exit. While this design requires low input powers, it suffers in its ability to only generate a maximum of about 10 mN with specific impulses comparable to the range of Hall thrusters[2].

1.1.2 Helicon Thruster

Helicon plasma thrusters have emerged as a potentially viable propulsion mechanism for space applications due to their high efficiency plasma generation[5]. In its simplest form, the helicon thruster consists of a helical antenna, plasma confining quartz tube, an RF power system with impedance matching network, and externally applied magnetic field. The RF current is passed through the helical, typically copper, antenna that induces a time varying magnetic field. By Maxwell's equations, this results in a curling electric field that accelerates free electrons until the ionization energy is achieved. Once the electron density reaches a critical point, the plasma ignites due to the electron avalanche effect[6]. The resulting plasma is characterized by the right-handed circularly polarized wave that propagates along the source length, and is confined by the quartz tube.

The externally applied magnetic field acts to support the propagation of this helicon wave, while also supporting the formation of a natural acceleration mechanism at the thruster exit[7,8,9]. The strength of the magnetic field directly determines the plasma density that can be supported, which saturates for magnetic fields in excess of 1000 G[9]. Helicon plasma generation has been observed to yield high plasma densities at relatively low power inputs[5], making the technology attractive for space propulsion applications. A schematic of an existing helicon thruster setup and image of the thruster in operation at the University of Maryland Space Power and Propulsion Laboratory (UMD SPPL) can be seen in Figure 1.1 and Figure 1.2, respectively.

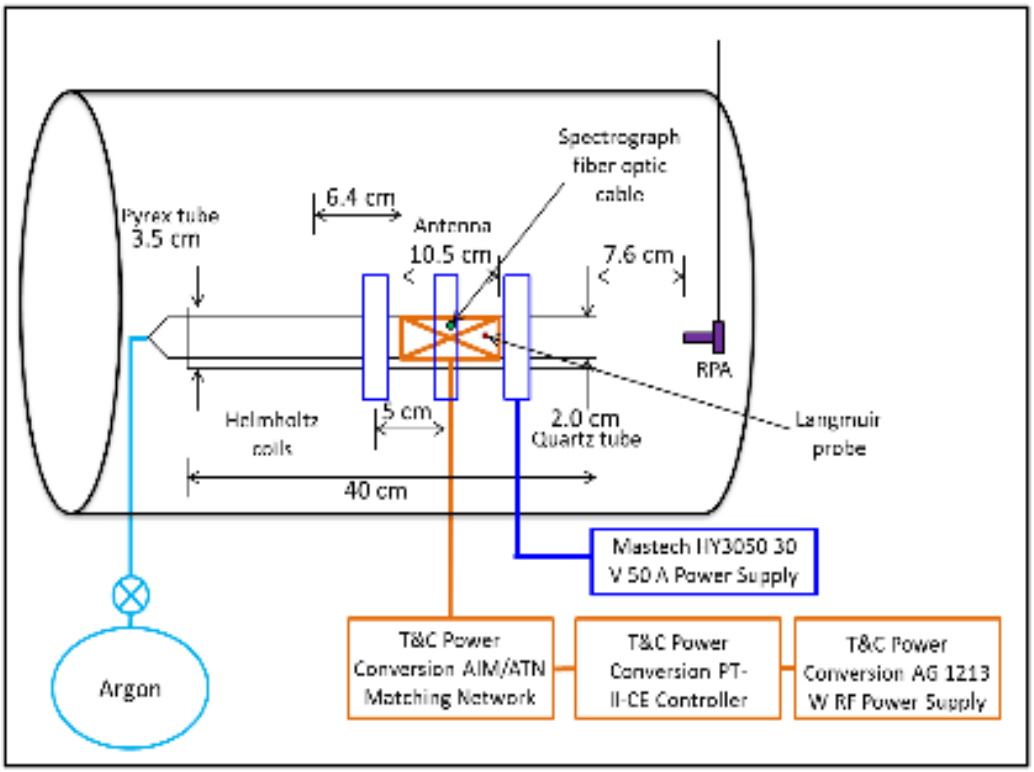

Figure 1.1: Schematic of helicon thruster setup.[10]

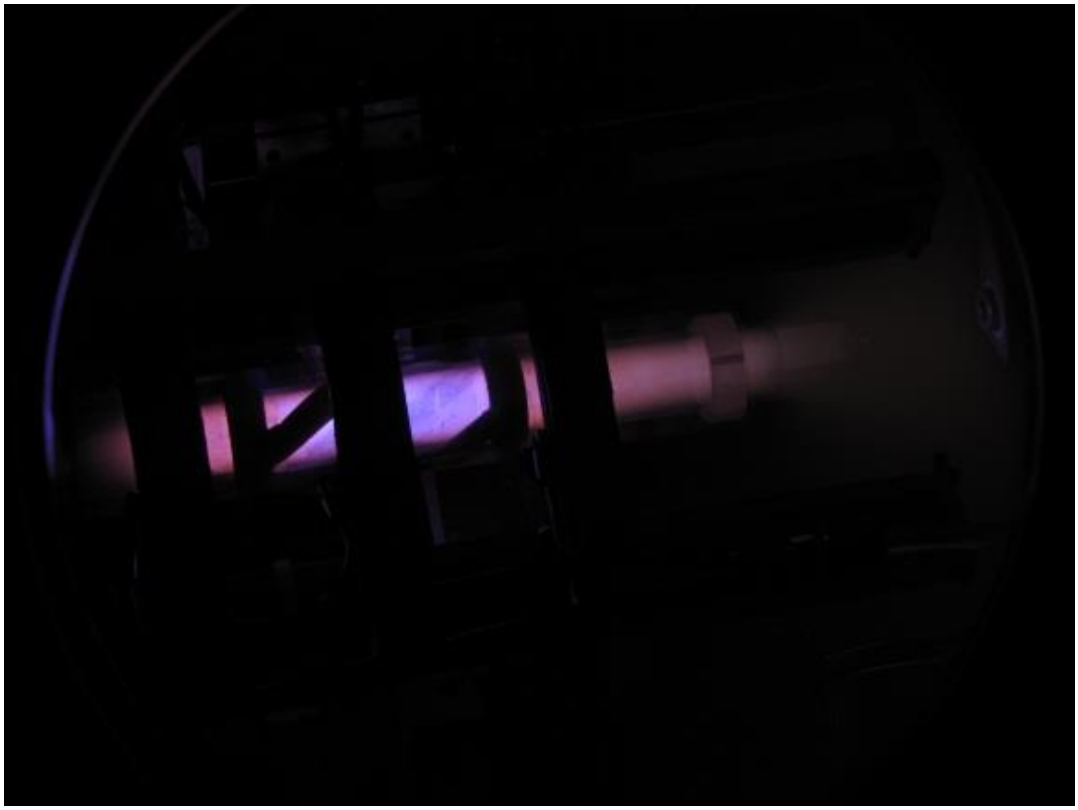

Figure 1.2: Helicon thruster in operation.[10]

The primary advantage of the helicon plasma source as a thruster is that the RF antenna is not in direct contact with the plasma. This allows for a variety of propellant selections, most notably, water vapor. By using water vapor propellant, in-situ resource utilization may be realized. With ice found throughout the solar system, replenishing diminished propellant can be achieved mid-mission. Unlike other traditional electric propulsion systems, the exhaust is quasi-neutral, eliminating the need for an external neutralizing cathode. Additionally, the helicon thruster does not require any external acceleration mechanism due to a naturally occurring plasma sheath at the exit boundary, which provides a potential difference through which the ions are accelerated. This will be discussed in more detail in Chapter 2.

Performance evaluations of standalone helicon plasma thrusters have yielded approximately 1-6 mN of thrust for RF power inputs ranging from 215 W to 840 W, where maximum specific impulses are around 377 s[11,12,13]. Of more importance is the power efficiency, which these studies report as between 8% and 30%. This indicates that a significant amount of the RF input power is consumed in the generation of the ion-electron pairs, rather than into directed kinetic energy. Ziemba and Winglee[14] have managed to produce specific impulses of 2000 s and a thrust near 1 N in a high power helicon thruster capable of operating at powers between 5-50 kW with argon propellant. A smaller Argon helicon thruster (mass of 1.5 kg and a volume of 1 cm^3) has been produced by Manente et al[15] for station keeping purposes, which operates at 50 W and is expected to generate 1 mN of thrust at a specific impulse of 1350 s.

Compared to the conventional electric propulsion devices discussed above, these performances are distinctly inferior. Williams [11] suggests that improvements beyond beam collimation and higher propellant utilization, such as increasing input power or implementing an ion acceleration stage, would be needed to increase efficiency beyond 30%. Possible augmentations include the combination of a helicon plasma source with a gridded ion acceleration stage[16], and also the combination of a helicon ionization stage with a Hall thruster acceleration chamber[17]. The most notable is the Variable Specific Impulse Magnetoplasma Rocket (VASIMR)[18], which makes use of a resonant ion cyclotron heating (ICH) stage to further heat the plasma before it is ejected from the rocket via a magnetic nozzle[19]. This allows the VASIMR® to yield thrust values on the order of 1 N and specific impulses on the order of a few thousand seconds[20]. Even though the subpar performance values detract from the applicability for certain mission

applications, the advantages of the helicon thruster warrant further investigation into improving the performance of the thruster.

1.2 Project Overview

1.2.1 Motivation

Since thrust directly scales with the input power, the more important metric to focus on is the power efficiency. This gives a better evaluation of how much of the input power actually contributes to thrust. Figure 1.3 shows a survey of power efficiencies for conventional electric propulsion devices. With efficiencies no greater than 10% for input powers less than 500 W[7, 9,11-14], the helicon thruster must be improved upon in order to be competitive with other systems. One method of determining potential improvements to the power efficiency of the helicon thruster is to perform a power flow analysis for the purpose of inspecting where the largest quantities of power are lost in the system. That is, determine the power that does not directly contribute to the jet power.

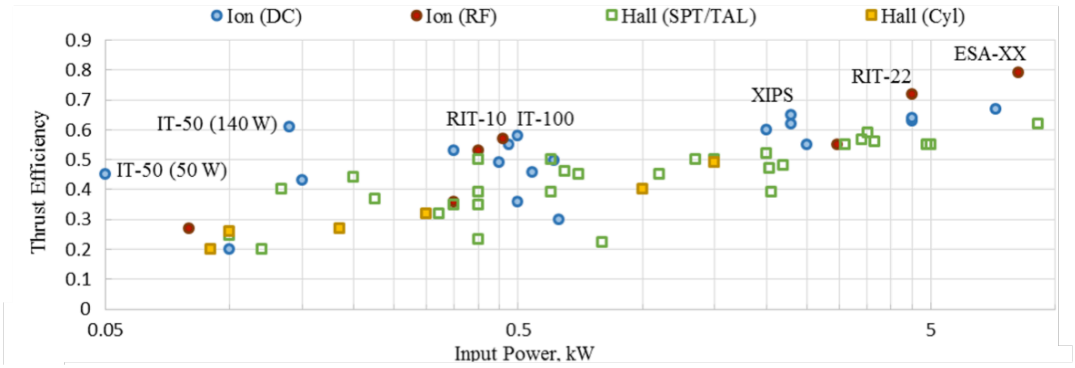

Figure 1.3: Survey of power efficiency for conventional electric propulsion devices[21].

The largest power sink in the helicon thruster is due to particles leaving the plasma through the plasma sheath at the boundaries[22]. As discussed above, the external

magnetic field from the electromagnets provide means of ion confinement, and can be used to generate a magnetic mirror for upstream confinement. Since this is a necessary power draw integral to the operation of the device, it should be considered in the total power efficiency; however, it is never included. Past studies[6,23,24] have proposed the use of permanent magnets to eliminate this power requirement. While Chen[23] demonstrated increased plasma densities, the research performed by Shamrai[24] indicates that the helicon wave does not propagate when in the presence of a null point in the magnetic field of a permanent magnet. By placing the antenna, such that the null was on one side, the plasma only formed on the opposite side. Furthermore, a null on either side of the antenna restricted wave propagation and plasma ejection such that no accelerated ions were observed. Upon removal of the null points, increased plasma densities and accelerated ions were observed. Utilizing a helicon plasma source for space propulsion applications requires the ejection of ions in order to impart a force on the system, eliminating the possibility of maintaining a null point near the thruster's exit plane.

1.2.2 Objectives and Methodology

As mentioned in the previous section, the largest power loss mechanism is associated with the plasma sheath that forms at the plasma boundaries. Additionally, the power required by the electromagnets will reduce the power efficiency. A novel approach to mitigating both is with the application of superconductors. It is well understood that below a superconductor's critical temperature, the material acts to expel magnetic fields via the Meissner effect[25] and provide a resistance-free path for current flow. Combining permanent magnets with superconducting material to yield a magnetic field topology

suitable for helicon plasma thruster applications can provide means of improved plasma confinement. This reduces undesired power loss to the plasma boundary upstream and along the lateral walls while simultaneously removing the power draw from an electromagnet without the unintended consequences that permanent magnets would introduce.

This complete system can be divided into two distinct subsystems. The first is the superconducting magnets, and focuses on generating the desired magnetic field topology for optimal plasma confinement. The second is the thermal management subsystem, and is required to maintain cryogenic temperatures to ensure the temperature of the superconductors always remains below the critical temperature. The first objective of this research is the analytical design of a complete superconducting helicon thruster with practical flight applications. In support of this objective, and integral to the design of the superconducting magnet subsystem, a power flow analysis is used to determine the impact of power loss mitigations implemented by the superconducting helicon thruster. This power efficiency analysis will also be used to compare with the experimentally determined efficiencies. The second objective is the construction and test of a laboratory helicon thruster and superconducting helicon thruster for direct comparison of performance metrics. Determination of the experimental power efficiency of each device will allow for validation of the analytical power efficiency model. Additionally, the ion current and electron temperature of each device will be measured to ensure comparable plasma characteristics.

1.2.3 Previous Work[*]

Wilson [26] has experimentally and computationally quantified the impact of superconductors, specifically a high temperature type II superconducting tube, on the magnetic field of a permanent magnet at the UMD SPPL. His research is summarized here to show proof of principle work supporting the magnetic field topology changes made possible through the use of high temperature type II superconductors. Conceptualizing the geometry of the magnetic field was made possible through computational means, utilizing COMSOL Multiphysics. Figure 1.4 demonstrates the shape of the magnetic field generated by a permanent magnet that caps the end of a superconducting flux tube above its critical temperature. Once the superconducting material reaches its critical temperature, a uniform field is observed along the axis of the tube, as seen in Figure 1.5.

It is important to note that type II superconductors, unlike type I, lock-in magnetic field lines that penetrate the material prior to reaching the critical temperature, and the Meissner effect is considered incomplete[27]. Thus, a mechanism to keep the magnetic field lines out from the confines of the material prior to cooling is required to obtain a similar effect in comparison to what would be expected of a type I superconductor. This computational model does not take into account any such mechanism, as its purpose is

---

[*] Parts of this chapter have been published in: Vitucci, J. J. and Sedwick, R. J., "Development of a Superconducting Helicon Thruster," Paper AIAA 2012-3866, 48th AIAA/ASME/SAE/ASEE Joint Propulsion Conference and Exhibit, Atlanta, GA, July-August 2012.

solely to gather qualitative data regarding the field geometry. From this model, modifications were made to mimic the experimental method as closely as possible.

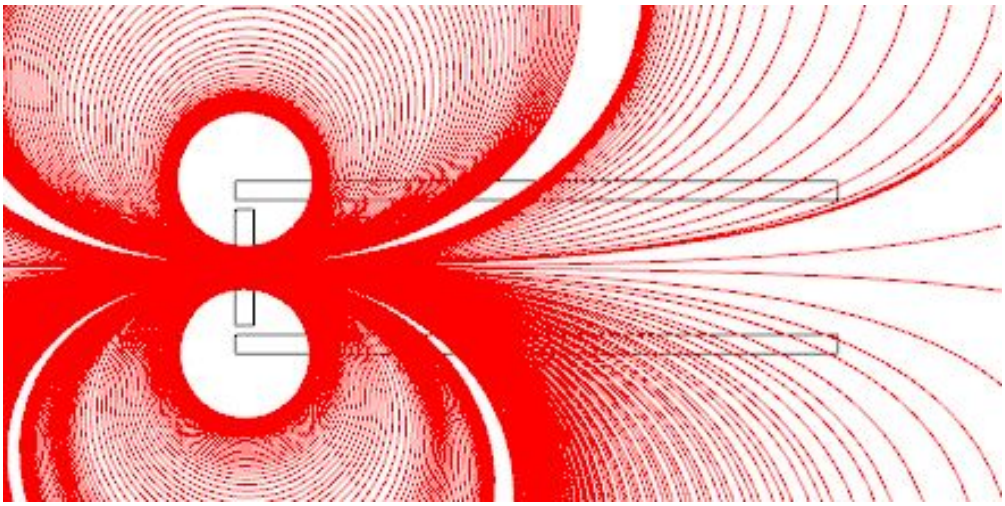

Figure 1.4: COMSOL simulation of magnetic field lines from a permanent disc magnet placed inside the end of the HTS tube at room temperature.[26]

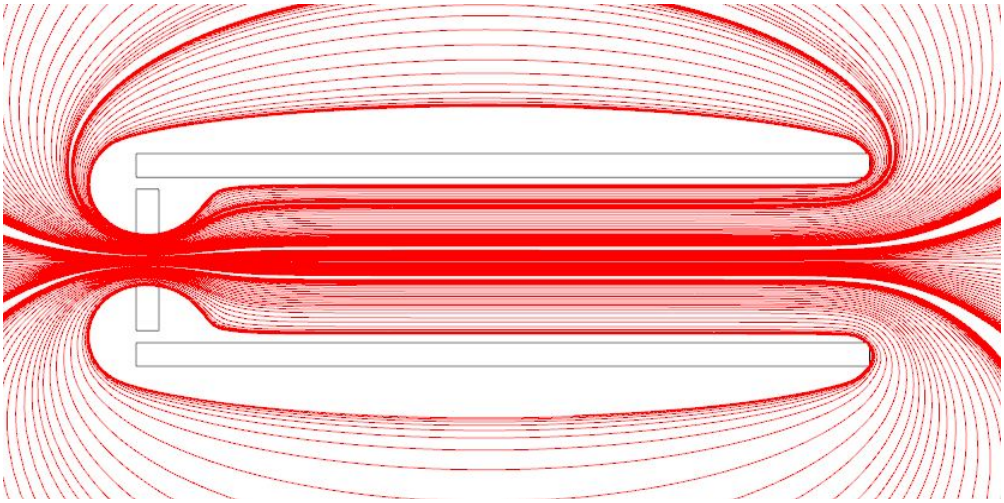

Figure 1.5: COMSOL simulation of magnetic field lines from a permanent disc magnet placed inside the end of the HTS tube while superconducting.[26]

The experiment was performed within the confines of a vacuum chamber. The necessity to cool the system yields condensation of oxygen on the interior walls of the flux tube. Performing measurements within a vacuum chamber helps thermally control the system, eliminates the possibility of condensation, and more accurately provides

conditions under which the thruster's mechanisms will be operating. The superconductor used was a 21.4 mm inner diameter, 26.2 mm outer diameter, and 12.3 cm long Bi-223 flux tube, which is part of the bismuth strontium calcium copper oxide (BSCCO) family. To avoid the problem of confining the magnetic field lines prior to cooling the Bi-2223 flux tube, a ferromagnetic sleeve, in combination with a ferromagnetic rod, was used to keep the flux lines out of the superconducting tube until the system was cooled below the critical temperature, 107 K. The entire apparatus was then encapsulated in a sealable, vacuum rated, annular vessel. This vessel was constructed from concentric brass cylinders, capped at one end, with a removable cap on the opposite end. This provided a sealable container through, which liquid nitrogen can flow. After the critical temperature was achieved, the ferromagnetic rod was removed from the center of the tube. From an engineering standpoint, this solution will not suffice for the superconducting helicon thruster, but was intended only to demonstrate a proof of principle. A Gauss probe was then used to perform magnetic field strength measurements along the axis of the flux tube.

As mentioned previously, the computational model was modified to mimic the experiment as closely as possible. The primary difference between the experimental apparatus and the computational model is that the computational model treats the flux tube as though it were a low temperature type I superconductor. The results of the experimental measurements and computational model can be seen in Figure 1.6. The primary region of interest ranges from 0 m to approximately 0.1 m, which corresponds to the extent of the superconducting material tube. From this model, a uniform magnetic field can be observed spanning approximately the entire length of the centerline. The

computational model is nearly identical to the experimental measurements from 0.03 m to 0.1 m. The reason for the rapid reduction in field strength just off the face of the magnet and the baseline value seen down the length of the tube is a result of the gap between the magnet and the tube, which in this design is approximately 0.03 - 0.04 m. This small gap allows some of the magnetic field lines to immediately curve back around to the opposite face of the magnet without interacting with the flux tube at all. A tight fit would ensure the capture of nearly all of the field lines, thereby increasing the overall field strength confined axially within the tube, but reducing or eliminating the magnetic bottle, or mirror, effect[28]. At the flux tube exit, a rapidly diverging magnetic field can be seen, as anticipated.

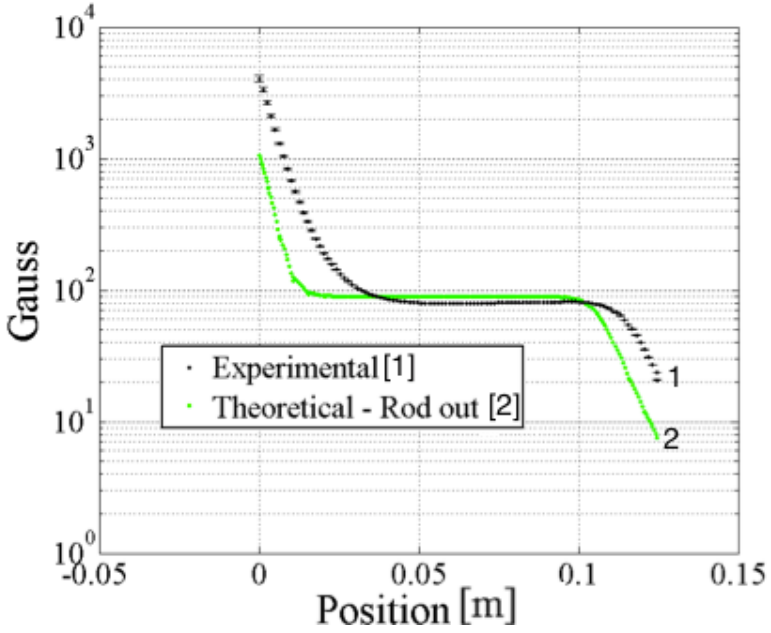

Figure 1.6: Axial Gauss probe experimental data (Superconducting) vs. theoretical data (COMSOL) as a function of distance from the face of the permanent magnet. The first curve corresponds to the experimental data and the second curve corresponds to the simulated theoretical data.[26]

The results of this study, as evidenced by Figure 1.6, confirm the ability to utilize high temperature type II superconductors in place of a low temperature type I superconductor to confine the magnetic field lines of a permanent magnet.

1.2.4 Outline and Contribution Overview

This research employs methods that are analytical, computational, and experimental in nature. First and foremost is a complete literature survey, presented in Chapter 2, which serves to fully detail the nature of a helicon plasma source, its dispersion relation, the applicability to space propulsion, and the role of an externally applied magnetic field. Secondly, an analytical power flow analysis is performed to determine the largest power sinks occurring within a typical helicon plasma system. This also serves to quantify the impact an electromagnet generated external magnetic field has on the overall power efficiency. This study will be detailed in Chapter 3. Next, the superconducting magnet subsystem design is presented in Chapter 4. This includes the design aspects, parameters, and simulations as well as an experimental mapping of the magnetic field topology to match the simulations. The thermal management subsystem considerations and cryo-cooler system requirements are detailed in Chapter 5. Chapter 6 will focus on the helicon plasma source operating with the standard electromagnet system and with the finalized superconducting magnet design, including a direct comparison explaining the benefits and disadvantages of such a system. Finally, the complete superconducting magnet system is summarized and presented in Chapter 7, including future work to further progress the research.

The first major contribution to the state-of-the-art is a power efficiency analysis that details power loss mitigation through the use of a superconducting magnet system, which takes into account the power consumption of the electromagnets. The second major contribution is the complete design and analysis of a superconducting helicon thruster composed of a superconducting magnet subsystem, and a thermal management subsystem. With the superconducting magnet subsystem, a COMSOL Multiphysics model is presented that accurately predicts the magnetic field topology of a tube shaped superconductor at steady state. The thermal management subsystem presents a design to maintain cryogenic temperatures in a closed-loop control system through the use of a cold-tip cryocooler and radiator. This is a novel approach to power loss mitigation for helicon thrusters that also has potential scientific ramifications in that magnetic fields can be achieved at no Ohmic power dissipation, where the topology of the field is only limited to the manufacturing limitations of solid superconducting material. Third, this is the first study to detail and characterize the plasma parameters of such a thruster and how they impact the baseline design of conventional helicon thrusters. The fourth, and most intriguing contribution, is the discovery of an anomalous acceleration mechanism yielding beam energies in excess of the measurements from comparable systems in the literature. Lastly, this research provides a test-bed for future in-situ resource utilization applications, particularly, for water vapor propellant usage.

2. Chapter 2: Helicon Plasma Source

2.1 Early Development

Helicon waves belong to a category of right-handed circularly polarized waves known as whistler waves. Whistler waves were first observed in the latter half of World War I and were named according to the sound soldiers heard while using cables in an attempt to eavesdrop on the opposing forces' telegraphic communications[29]. While initially attributed as having extraterrestrial origins, it was later discovered that plasma in the Earth's magnetosphere, in response to lightning strikes, caused the phenomenon[29]. It was several years later, at a semiconductor conference in Prague, that Aigrain coined the term 'helicon'[30], which he used to describe electromagnet waves with frequencies between the ion and electron cyclotron frequencies observed in low temperature solid metals[29]. While helicons are classified as whistlers based on their polarization, they are distinguishable from classical whistler waves in that: "(a) they are of such low frequency that the electrons' gyrations may be disregarded and only their guiding center motions kept, and (b) they are modes of bounded systems, in which their purely electromagnetic character cannot be maintained."[31]

The progression of the helicon research to date was made possible through research conducted by Lahane and Thonemann[32], who first demonstrated the propagation of helicon waves in gaseous plasmas[33]. This discovery spurred a series of studies throughout the 1960's intent on expanding the theoretical understanding of helicon waves in plasmas. Of particular interest were the studies by Klozenberg, McNamara, and Thonemann[34], who first formulated the dispersion relation for helicon waves in uniform

plasmas. The dispersion relation provides the relationship between wavelength, wavenumber, frequency, and energy. From there Blevin and Christiansen[35], determine the dispersion relation for helicon waves in a non-uniform plasma. This led to further modifications to incorporate other instances of helicon waves in plasmas. The technology had not progressed to the point of applications outside of scientific experimentation until Boswell's[36] discovery that increases in power and applied axial magnetic field yielded three distinct step-wise increases in plasma density. In the final mode change, the argon neutral gas is observed to be completely ionized in the core of the plasma as indicated by the presence of Ar II emission spectra, in the range of 480-520 nm[10], and observable as a bright blue color. This is in contrast to a purple glow, in the range of 510-520 nm,[10] indicating the presence of Ar I. In the same study, Boswell noted that the power was nearly 100% efficiently coupled to the plasma, where 50% of the power was lost to the plasma boundary and the remaining 50% was attributed to ionization. The helicon model only accounts for this phenomenon when the collision frequency is set to 1000 times that of the standard Coulomb collision frequency. To date, the true mechanism behind this efficient plasma generation is still debated, however, this inherent nature of the helicon plasma source has made it attractive for the plasma processing industry for deposition and plasma etching[37,38].

2.2 Helicon Plasma Dispersion Relation

The dispersion relation for a plasma is used to determine how the energy, wavenumber, wavelength, and frequency are connected. In experimental work, the dispersion relation can be used to determine whether a plasma falls into a certain regime

based on whether the parameters follow the dispersion relation. In an RF generated plasma, if the parameters obey the dispersion relation then it can be classified as a helicon plasma, otherwise the RF power could be coupled inductively or capacitively to the plasma. This will be further elaborated on in the following section. To derive the helicon dispersion relation, the work performed by Chen[8] is widely accepted for the simplest form of helicon waves sans damping and will be used for this research. Perturbation theory is applied to the derivation and it is assumed that the guiding center of the $\boldsymbol{E}$ x $\boldsymbol{B}$ drift for electrons carries the entire plasma current, such that the electron cyclotron motion is too fast to contribute, ion motion can be neglected, and $E_z = 0$ (meaning the resistivity is zero). In addition, the displacement current in Ampere's Law will be neglected as small compared to the electron current. Thus, the derivation begins with the following linearized equations:

$$\nabla \times \boldsymbol{E} = -\frac{\partial \boldsymbol{B}}{\partial t} \tag{2.1}$$

$$\nabla \times \boldsymbol{B} = \mu_0 \boldsymbol{j} \tag{2.2}$$

$$\boldsymbol{E} = -(\boldsymbol{j} \times \boldsymbol{B_0})/en_0 \tag{2.3}$$

$$\nabla \cdot \boldsymbol{B} = 0 \tag{2.4}$$

$$\nabla \cdot \boldsymbol{j} = 0 \tag{2.5}$$

Here $\boldsymbol{B}$, $\boldsymbol{E}$, and $\boldsymbol{j}$, represent the perturbed magnetic and electric fields, current, and density, respectively, while $\boldsymbol{B_0} = B_0\hat{z}$ and n_0 are the equilibrium magnetic field and density. Resulting from (2.1) – (2.3) are the following:

$$\boldsymbol{j}_\perp = en_0\boldsymbol{E} \times \boldsymbol{B_0}/{B_0}^2 \tag{2.6}$$

As is typical in perturbation theory, all perturbations are assumed to take the form $exp[i(m\theta + kz - \omega t)]$. Applying this form, and combining (2.1) and (2.3), yields an expression for the perturbed magnetic field as a function of the wavenumber, frequency, equilibrium magnetic field and density, and the perturbed current.

$$i\omega \boldsymbol{B} = i\frac{kB_0}{en_0}\boldsymbol{j} \tag{2.7}$$

Applying (2.2) to (2.7), $\boldsymbol{j}$ can be eliminated, leaving an equation for the perturbed magnetic field.

$$\alpha \boldsymbol{B} = \nabla \times \boldsymbol{B} \tag{2.8}$$

Here α is defined as follows:

$$\alpha = \frac{\omega}{k}\frac{\mu_0 e n_0}{B_0} = \frac{\omega}{k}\frac{{\omega_p}^2}{\omega_c c^2} \tag{2.9}$$

where ω_p and ω_c are the plasma and cyclotron frequencies, respectively. Applying the definition of the transverse wave number, ${T_k}^2 \equiv \alpha^2 - k^2$, given by Chen[8], the final dispersion relation to lowest order can be written.

$$\frac{B_0}{n_0} = \frac{\omega \mu_0 e}{k\sqrt{{T_k}^2 + k^2}} \tag{2.10}$$

Rewriting (2.10) in the more standard notation for the dispersion relation using $D(\omega,k)$, where D is the dispersion relation:

$$D(\omega, k) = \frac{\omega \mu_0 e n_0}{B_0 k\sqrt{{T_k}^2 + k^2}} - 1 = 0 \tag{2.10}$$

2.3 RF Power Coupling

2.3.1 RF Antennae

The most important aspect in helicon plasma generation is the RF antenna, as this device couples the power to the plasma. Traditionally, three specific types of antennae have been used in helicon research. These are the Nagoya type III, Boswell type, and the helical type. Representations of these antennae with current directions can be seen in Figure 2.1. For the setup at the UMD SPPL, the half-wavelength helical type antenna was chosen since it was found to be more efficient at coupling power to the plasma than the other two types[39]. Moreover, helical antennae that launch right-handed polarized waves, known by the mode m = +1, have been found to be more efficient than those that launch a wave of the opposite polarization, or the m = -1 mode[40]. The Nagoya type III antenna has been shown to launch waves with both helicities, corresponding to the m = ±1 mode, and yet the dominance of the helical type antenna still trumps this type[40]. Counter-intuitively, the half-wavelength antennae have been demonstrated to couple power more efficiently than full-wavelength antennae of the same type[41].

As mentioned in section 2.1, early studies by Boswell[36] had shown a step-wise increase in plasma density with increases in power and axial magnetic field strength. This was one of the first findings to demonstrate the three distinct coupling modes of the antenna to the plasma. The RF field can couple power to the plasma capacitively, inductively, or through the helicon wave propagating through the discharge. It is in the highest mode, where the power is coupled through the helicon wave that the high power efficiencies are observed. This was verified by first determining the phase difference

between the antenna power and the time-varying magnetic field, using a B-dot probe. The phase difference is then matched to the helicon dispersion relation to prove that the measured plasma waves indeed follow that of a helicon wave[42]. The next sections will detail the three different operational regimes and the transitions between them.

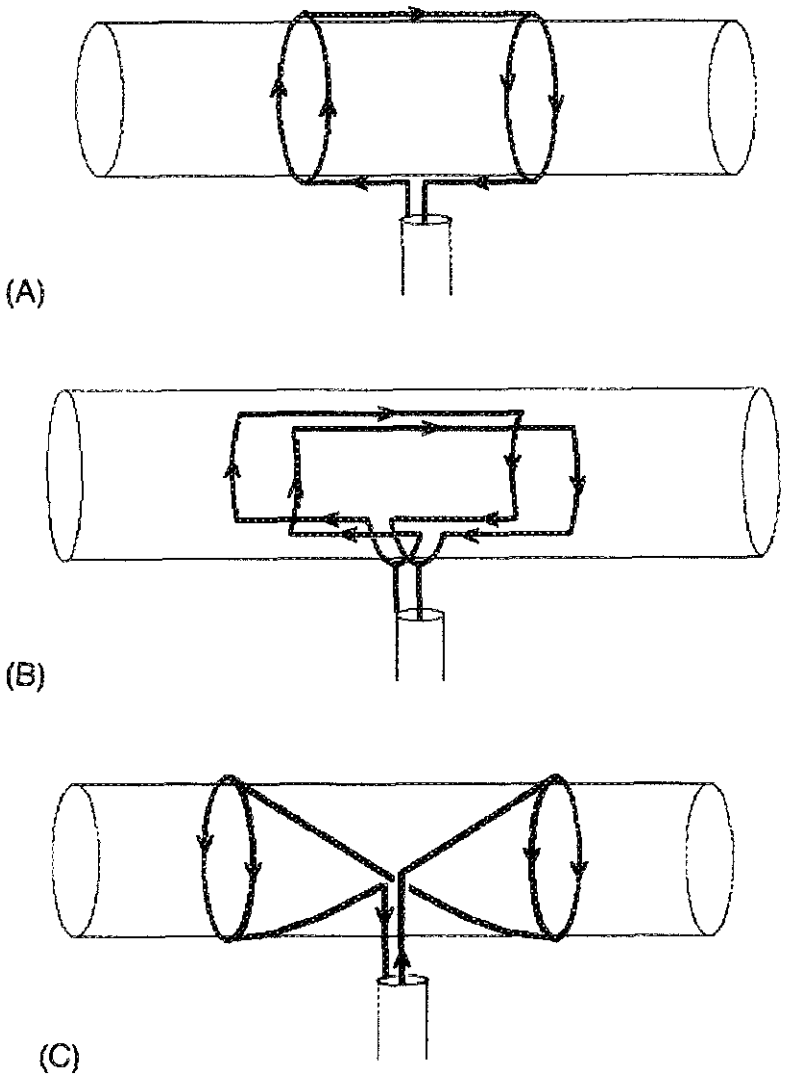

Figure 2.1: Half-wavelength antennae: (a) Nagoya type III, (b) Boswell type, and (c) Helical (or Shoji) type[39].

The antenna length is designed around the excitation of specific resonant energies given by the following equation:

$$E_r = \frac{1}{2} m_e {v_p}^2 \tag{2.11}$$

Solving for the phase velocity allows for the calculation of the corresponding wavelength using $\lambda_w = v_p/f$, where f is the operating frequency. Determining the ratio of the wavelength to the source tube radius, a, determines the antenna gain[8]:

$$G = 0.61 \frac{\lambda_w}{a} \tag{2.12}$$

The inverse of the antenna gain gives the ratio of the transverse wavenumber, T_k, to the parallel wavenumber, k. The final equation for the antenna length, specifically for a half-wavelength antenna, is then given as[8]:

$$L = \frac{\pi a}{3.83} G \tag{2.13}$$

2.3.2 Capacitive Coupling

The capacitive mode, otherwise known as the E-mode, is the weakest form of power coupling from the antenna to the plasma. Since the power is not coupled to the helicon wave, the plasma can be sustained without the need for an external magnetic field[43]. The E-mode of a helicon plasma source can be achieved at low power inputs, where the upper limit, before the transition to the inductively coupled or H-mode, is set based on the background pressure, the RF power input, and the axial magnetic field strength. These three parameters all directly influence the plasma density, which is the primary indicator of mode transitions. The E-mode typically exhibits low plasma

densities on the order of 10^9 cm^{-3} and in this regime, the upper limit is more strongly tied to the background pressure[43]. The highly inefficient nature of power deposition is due to the role of the electric fields on the plasma electrons in the oscillating sheaths in the near field of the RF antenna. The antenna acts as a biased electrode and the sheath leading to the plasma boundary acts as a grounded electrode[43]. The inefficiency and low densities of the E-mode make it less than a desirable operating mode.

As the RF power is increased, or the background pressure decreased, the plasma density steadily increases until a large spike, usually an order of magnitude difference, occurs marking the transition to the H-mode. The process by which this happens is directly related to the skin depth of the plasma. The skin depth of a plasma is given by the following equation:

$$\lambda = \frac{c}{\omega_p} = \frac{c}{\sqrt{n_e e^2/(\epsilon_0 m_e)}} \tag{2.14}$$

Since it is well observed that the density increases with increasing RF input power and with decreasing background pressure, one can see that as the density increases, the skin depth decreases. Once the skin depth decreases below the scale of the device, that is the diameter of the source tube, the electrons will absorb power in the skin depth layer via the induced currents[44], and the E-mode will transition into the H-mode[43].

2.3.3 Inductive Coupling

The H-mode, or inductively coupled mode, has been more widely studied for the interest in the transition between the lower efficiency power coupling modes to the high efficiency helicon wave coupling. With an order of magnitude increase in the density,

now around 10^{10} cm^{-3}, a decrease in the plasma potential, which is attributed to a greater prower loss in response to the increasing density[43], is also observed through the use of RF compensated Langmuir probes. One of the more unexpected results in the H-mode is the existence of an m = 0 wave, as determined based on the existence of in-phase azimuthal magnetic field components, even for antennae intended to excite only the m = 1 or m = -1 modes[45]. This is consistent with studies showing the presence of a non-rotating azimuthal electric field in the core of the plasma. In the presence of an external magnetic field, the azimuthal electric field component can penetrate the boundaries of the plasma, and can couple with the helicon wave to induce the H-W mode transition causing the rotation of that component[46]. This can be directly seen by the electric field structure for the m = 1 mode given by Chen[8]. In addition, the axial component of the magnetic field is also non-existent in the H-mode, but becomes the dominant component as the mode switches to the W-mode, or helicon-wave mode[44].

2.3.4 Helicon-Wave Coupling

Once the plasma transitions to the W-mode, the largest plasma densities are observed and are typically in the range of 10^{11} and 10^{12} cm^{-3}. In this regime, the power is strongly coupled to the helicon wave resulting in more complete ionizations occurring in the core of the discharge. This is immediately noticeable in an argon plasma, where the core emits a blue color associated with singly ionized argon and the outer shell of the plasma emits a purple color, indicative of excited neutral argon[47,48]. This regime is also beneficial in that once a stable discharge is achieved, the RF input power can be reduced while still maintaining the stability of the discharge[49]. Keiter et al[49] have determined that

once the threshold input RF power is satisfied, the transition into the W-mode is largely governed by the boundary conditions set by the source tube and antenna design, in addition to the externally applied magnetic field. This threshold power level varies depending on the axial magnetic field, and decreases as the magnetic field strength increases[50].

The most important aspect governing the verification of the W-mode regime, as mentioned previously, is the matching of the measured waves to the helicon dispersion relation. As mentioned in the previous section, the wave coupling occurs due to the penetration of the axial magnetic field component. Once this dominates the radial and azimuthal components, an appreciable axial current can be supported and driven by the axial electric field, resulting in resonant wave-particle heating[44]. Since the plasma is now supported by the wave, a phase delay is introduced to the system in the form of the rotating azimuthal electric field component, again mentioned in the previous section. To provide a complete image of the mode transitions, an experimental relationship between the RF input power and the resulting plasma density for various background pressures can be seen in Figure 2.2[43].

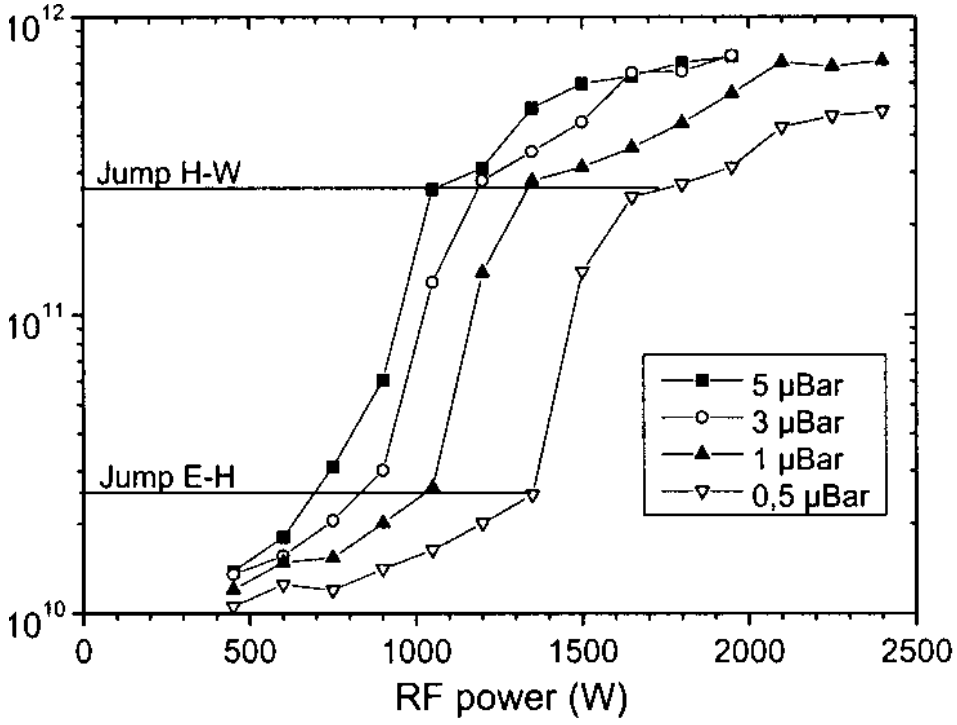

Figure 2.2. Mode transitions in an argon helicon plasma demonstrated by density increases as a result of an increasing input power[43].

2.4 Efficient Plasma Generation

2.4.1 Landau Damping

While it has been shown[5] that the W-mode efficiently couples power from the RF antenna to the plasma, the true mechanism by which this occurs is not fully understood. In the initial formulation of the dispersion relation by Chen[8], he proposed that Landau damping serves as the driving mechanism behind the efficient power deposition. Landau damping in a helicon wave, similarly with Alfvén waves, is the process by which drag is caused by collisions on electrons moving in the direction of the perturbed magnetic field[8]. To account for this process, equation (2.3) is modified as follows:

$$\boldsymbol{E} = \frac{\boldsymbol{j} \times \boldsymbol{B_0}}{en_0} - \frac{im_e}{n_0 e^2}(\omega + i\nu_{eff})\boldsymbol{j} \tag{2.15}$$

Here the second term represents the inclusion of collisions, assuming $\nu_{eff} \ll \omega \ll \omega_c$ and that kinetic effects in the perpendicular direction, with respect to the *z*-direction, are negligible due to a finite electron Larmor radius[8]. This latter assumption breaks down for magnetic fields below 100 G[51]. The effective collision frequency, ν_{eff}, is the sum of the plasma collision frequency in addition to the Landau collision frequency, $\nu_{eff} = \nu + \nu_{LD}$. The Landau term is derived from the Boltzmann-Vlasov equation and is given by Chen[8] as:

$$\nu_{LD} = 2\sqrt{\pi}\zeta^3 e^{-\zeta^2} \tag{2.16}$$

Where ζ collects the plasma frequency, collision rate, wavenumber, and thermal velocity in the following manner:

$$\zeta = \frac{\omega + i\nu}{k v_{th}} \tag{2.17}$$

In this Landau damping regime, the energy deposition is directly linked with the *z*-component of the electric field[8].

It was later determined by Shamrai[52], that in most helicon plasmas, the Landau damping regime does not hold and that another mechanism must be responsible for the efficient power coupling in the W-mode. The Landau damping theory breaks down for longitudinal wavelengths that are on the order of the scale of the device and for densities greater than are capable in helicon sources[52]. In the same study by Shamrai[52], it was proposed that a second wave, called the Trivelpiece-Gould (TG) wave, would combine with the helicon wave. This can only occur in the presence of non-conducting boundary

conditions such that the radial RF current is eliminated at a surface since the radial RF current cannot close[52].

2.4.2 Trivelpiece-Gould Modes

The concept of the existence of TG-modes outside of the typical helicon modes is the currently accepted explanation for the efficient nature of helicon plasma sources. The TG-mode can be considered a separate mode, because once the TG-wave amplitude dominates that of the helicon wave, the helicon modes essentially vanish[52]. The boundary between the two modes is the skin depth given by (2.14). Longer waves, such that $kc \ll \omega_p$, exist in the helicon regime and follow the dispersion relation given by (2.9) or (2.10)[52]. These waves exhibit weak damping and exist in a low collision rate regime, whereas the shorter TG-waves ($kc \gg \omega_p$) are strongly absorbed as they propagate radially inward[53]. The two waves exist simultaneously when the wavelength is on the order of the skin depth, that is $kc \approx \omega_p$. The dispersion relation is then as follows[52]:

$$\omega = \omega_c \frac{k}{\sqrt{k^2 + {T_k}^2}} - i\nu \tag{2.18}$$

Independently, Borg and Boswell[54] and Arnush[55] computationally verified the experimental results of Miljak and Chen[40] that in the TG-mode, improved antenna coupling is not as a direct result of resonance phenomena, but rather that the high amplitude electric field in the TG-mode enhances wave damping and absorption[54]. Up until that point, the direct measurement of TG-waves had been difficult to detect because they tend to remain localized in an unresolved layer near the plasma boundary.

Blackwell et al[53] has suggested that the TG-modes could extend farther into the interior of the discharge for magnetic fields below 50 G, such that spatial resolution is no longer an issue. In the same study, a J-probe, or miniature RF Rogowski coil, was used to measure the axial current, j_z. This data was then compared to the theoretical current profile for TG waves in helicon plasma and shows good agreement in the behavior along a radial slice[53].

2.5 Helicon Thruster Acceleration Mechanisms

As mentioned in Chapter 1, the helicon plasma source lends itself well to electric propulsion applications for its efficient high-density plasma generation, which can be especially attractive for compact applications[56]. In addition, the primary electrode is not in direct contact with the plasma allowing for corrosive propellants such as water vapor. The mechanism by which the ions are accelerated by the helicon source is inherent to the nature of the plasma. According to researchers at the Australia National University (ANU), the process by which the ions are accelerated out of the system is the current-free double-layer (CFDL), which is capable of producing supersonic ion beams[57]. A double-layer is the boundary that forms between two different plasmas. Like the plasma sheath forming at a boundary, a potential difference between the two plasmas forms. A schematic of the potential profile for a typical plasma sheath at a boundary is shown in Figure 2.3. Comparatively, the potential profile for a double-layer can be seen in Figure 2.4. In the region between the two plasmas, the merging of two sheaths can be seen. In this region, quasi-neutrality is not necessarily upheld[58]. Populations of electrons and ions

can traverse the double-layer, and when the net current flow over the boundary is zero, the double-layer is considered a CFDL[58].

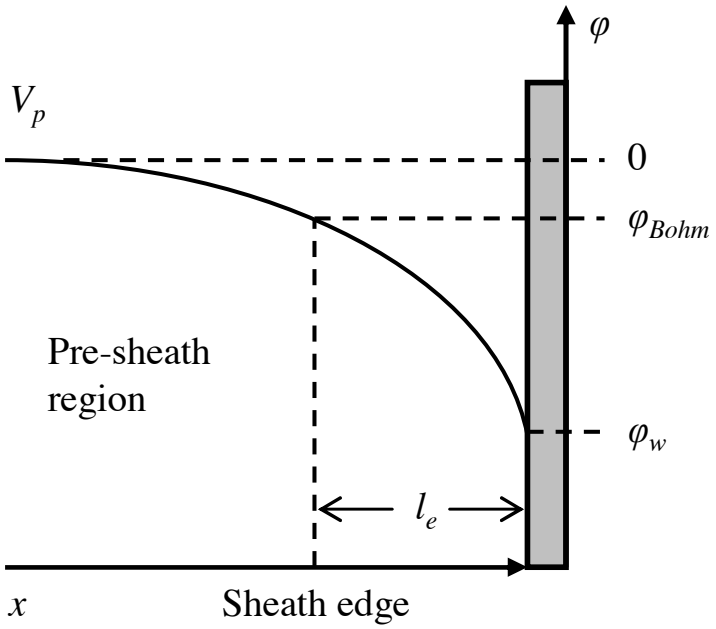

Figure 2.3. Schematic of the potential profile for a typical plasma sheath[59].

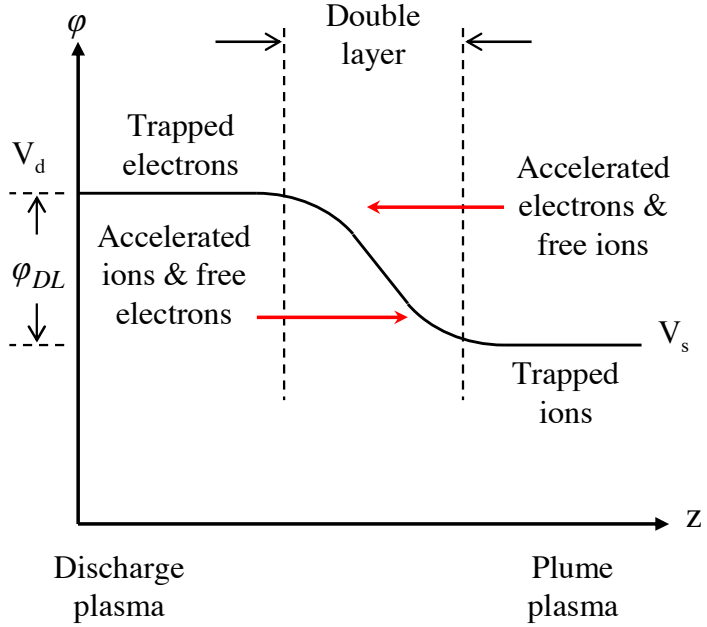

Figure 2.4. Schematic of the potential profile of a double-layer[14].

The CFDL has been observed in helicon plasmas in the vicinity of a diverging magnetic field[57,60,61], which is typical near the exit plane of the a helicon source as the result of the magnetic field geometry produced by either electromagnets or permanent magnets. Acceleration of ions to supersonic velocities is aided by the potential difference across the CFDL, where the structure of the divergence directly determines the axial location of the CFDL[62]. The threshold for CFDL formation was determined to be approximately 45 G, above which, the potential difference across the CFDL exhibits weak dependence on the magnitude of the magnetic field[63] with little to no change in the parallel ion flow speed[61]. Below the threshold, specifically in the range of 10 G to 35 G, an ion beam has still been observed coupled with increases in plasma density, and is attributed to a low-magnetic field, high-density mode in the helicon plasma[64,65].

The thruster in development at ANU, known as the Helicon Double-Layer Thruster (HDLT), generates thrust by the electric field within the double-layer and the detachment of the emergent beam from the external magnetic field[66]. This electric field is aligned with the magnetic field, yielding low pitch angles for the expelled ions[66]. These pitch angles have shown to yield a beam divergence below 5 degrees in the argon propellant case[67], and matches the computational model for the beam detachment[68]. While Lieberman, Charles, and Boswell[69] support the double-layer theory, Chen has proposed another mechanism in which the double-layer sheath is rather a single-layer that can be explained through classical sheath theory[70]. This formulation was shown to match the same results as formulated using the CFDL argument.

A third proposition to detail the particle acceleration is that of a magnetic nozzle. The contribution to directed kinetic energy is two-fold. The first is through thermal

expansion of the plasma, similar to a de Laval nozzle. Since the electrons are magnetized and follow the diverging magnetic field lines, electromagnetic forces acting on the plasma form a boundary that acts as a magnetic wall for the expanding plasma[72]. Additionally, there is a diamagnetic contribution that occurs from an azimuthal current that forms as a result of the charge separation at the exit plane of the thruster. As seen in Figure 2.5, the electrons leave the exit faster than the ions due to their smaller mass, causing the ions to be accelerated through the potential difference created by the charge separation in order to maintain quasi-neutrality. It is hypothesized that this behaviour can closely mimic the appearance of a freestanding or current-free double-layer sheath[71]. The azimuthal current then results from the $\boldsymbol{E}$ x $\boldsymbol{B}$ drift of the electrons and the absence of an equal and opposite drift from the unmagnetized ions[72]. This electron current produces a diamagnetic field that acts to further accelerate the plasma.

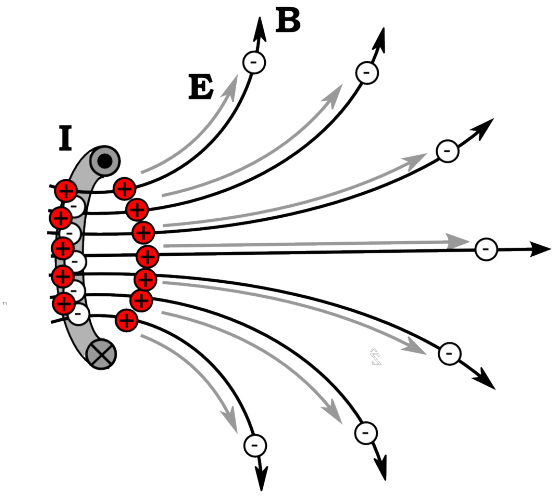

Figure 2.5: Ion acceleration driven by fast-moving electrons leaving the system[72].

Currently, the mode of plasma detachment from the magnetic is the topic of investigation. Full or partial detachment may occur, which introduces a multi-faceted

problem in simulations making determination of the detachment point difficult. If the plasma detaches quite rapidly, the emergent ion beam will be more collimated, yielding larger thrust densities than cases where the plasma follows the diverging magnetic field over a longer span. The greater the plasma divergence, the less energy transfer that is occurring in the axial direction and contributing to thrust.

The mechanism and formulation behind the supersonic ion beam is still debated, specifically over whether a double-layer indeed exists, whether the boundary is simply a classical plasma sheath, or whether a magnetic nozzle is the predominant acceleration mechanism. Whatever the true formulation may be, the result remains the same that an emergent ion beam does exist and is capable of producing thrust. Moreover, the beam is produced through naturally occurring ambipolar effects without the need for an external acceleration mechanism.

3. Chapter 3: Power Flow Analysis†

3.1 Plasma Boundary Losses and Jet Power

In the simplest case, as discussed by Fruchtman[22,73], the helicon plasma source can be used as a stand-alone thruster. In his study, any natural acceleration mechanisms, such as the CFDL[66], are neglected in favor of momentum delivered by the plasma as a result of the maximal electron pressure to the upstream wall. In this analysis, the power contributing to thrust is instead attributed to the ion acceleration through a single sheath. We maintain the assumption of a completely collimated beam, which is possible due to the potentially rapid detachment of the plasma from the magnetic field[74]. To properly model the propulsive efficiency, one must define all power sources and sinks occurring within the system. As has been done in other studies, we deem the cross-field particle flux as negligible compared to the particle flux at the ends of the plasma column[75]. It is observed[73] that the primary loss mechanisms arise from the cost of ionization per ion-electron pair and the power sink at the plasma sheath. These terms can be collected and defined as

$$L_p(T_e) = \Gamma_{max}(T_e)[\varepsilon_c(T_e) + \varepsilon_{sh}(T_e)]. \tag{3.1}$$

---

† Parts of this chapter have been published in: Vitucci, J. J. and Sedwick, R. J., "Development of a Superconducting Helicon Thruster," Paper AIAA 2012-3866, 48th AIAA/ASME/SAE/ASEE Joint Propulsion Conference and Exhibit, Atlanta, GA, July-August 2012.

An approximation for ε_c can be expressed[73] as

$$\varepsilon_c(T_e) = \varepsilon_i + \varepsilon_1 \, Exp[\tfrac{-6(T_e - T_1)}{\varepsilon_i}], \tag{3.2}$$

where ε_i is the ionization energy, and ε_1 and T_1 are the characteristic energy and temperature, respectively, of the 1s-shell ionization threshold for the propellant. The power draw occurs at three locations; the plasma boundary at the front wall, the plasma boundary at the open exit of the thruster, and the lateral boundary walls of the source tube. Since the axial magnetic field aides in plasma confinement and restricts conductive losses to the lateral walls to ambipolar, cross-field diffusion, the power loss at the lateral walls is assumed to be negligible. Furthermore, the radiative losses are considered negligible in comparison to the conductive losses to the boundaries. This will be further explored and verified in Section 5.1. In the presence of a sufficiently strong, diverging magnetic field, the open downstream plasma boundary and the upstream plasma boundary both behave as if a wall were present. The energy sink at the plasma sheath at the front wall is given by the potential difference across the boundary.

$$\varepsilon_{swall}(T_e) = \tfrac{T_e}{2}\left(1 + ln\left[\tfrac{m_i}{2\pi \, m_e}\right]\right), \tag{3.3}$$

Here, m_i is the mass of the ions and m_e is the mass of an electron. Since this power sink occurs at the front wall and at the thruster exit, the total energy draw to the sheath, ε_{sh} can be expressed as

$$\varepsilon_{sh}(T_e) = 2\varepsilon_{swall}(T_e). \tag{3.4}$$

A secondary power draw mechanism is the power imparted to the flow. The study in Ref. 73 provides a detailed analysis of this power draw for collisionless plasmas and for a high collision case. The power imparted to the plasma flow is represented as

$$P_f(T_e) = \Gamma_{max}(T_e)\{\, T_e[2RG + 3]\}, \tag{3.5}$$

where R and G are dimensionless and functions of the collision ratio, β_c/β. Assuming collisionless plasma, R=2 and G=0.2854 (Ref. 73). An expression for Γ_{max} can be obtained from the plasma flux at the pre-sheath and is given by the Bohm flux:

$$\Gamma_{max}(T_e) = 0.6 n_p \left(\frac{e\, T_e}{m_i}\right)^{1/2}, \tag{3.6}$$

where e is the elementary electron charge and n_p is the maximum plasma density. A relationship for n_p in terms of the applied magnetic field, B, is given[8] as

$$n_p = \frac{B}{\frac{e\, \mu_0\, a}{Z_m}\left(\frac{\omega}{k} + \frac{\omega\, a}{m\, Z_m{}^2}\right)}, \tag{3.7}$$

where μ_0 is the permeability of free-space, a is the radius of the thruster tube, Z_m is the root of the Bessel function J_m, m is the mode of the Bessel function, ω is the angular frequency, and k is the wavenumber. In the case where the first mode is excited, m=1, Z_m=3.83. By combining the above equations, the total power draw per area to the naturally occurring mechanisms within the thruster as a function of electron temperature, T_e, can be expressed as

$$P_0(T_e) = P_f(T_e) + L(T_e). \tag{3.8}$$

The final term required to properly evaluate the efficiency is the power contributing to the thrust. The energy contributing to the thrust must first be determined,

and is assumed to the energy acquired by the ions after being accelerated through a single free-standing sheath at the thruster exit plane[22].

$$E(T) = \frac{eT_e}{2}\left(1 + ln\left[\frac{m_i}{2\pi\, m_e}\right]\right) \tag{3.9}$$

Assuming argon propellant, equation (3.9) is further simplified by inserting the mass of an argon ion.

$$E(T) = 5.2T_e \tag{3.10}$$

The power contributing to thrust, or the jet power, is then written as

$$P_J(T_e) = 5.2T_e\, \Gamma_{max}(T_e). \tag{3.11}$$

3.2 Power Lost to Electromagnets

We define P_m as the power consumed by the electromagnets for use in the power efficiency analysis. It is typical for studies to neglect the electromagnet power, which would solely represent the RF power conversion efficiency of the device. Here we maintain this term in order to closely model the system as it would be represented in a flight-ready device. This further highlights the benefit of a system where this power draw is not required. Selecting a representative electromagnet power is inherently dependent on the magnetic field and size of the thruster. Since magnetic field strength is proportional to the current through the electromagnet, larger magnetic field requirements demand a larger current, and thereby a larger power draw. Conversely, one can increase the number of turns in a solenoid to decrease the necessary current per turn at the cost of increasing the resistance of the device. This effectively increases the size of the electromagnet and causes the resistance to increase, which also requires larger power

levels. Since the power is equal to the product of resistance and the square of the current, the power is more sensitive to changes in current versus resistance, so the primary limitation to increasing the turn density of the electromagnet is the physical size and weight that comes with the increase in turns.

For the purpose of this analysis, we select a power draw that can be readily achievable with a laboratory power supply. For the remainder of the power efficiency analysis, we will select the power draw by the electromagnets to be 120 W. This is representative of 18.5 A per turn and a 6.5 V drop over the solenoid, which is identical to the solenoid used in the experimental study of this research, and yields a magnetic field of approximately 200 G. The solenoid details will be elaborated on in the following chapter.

3.3 Power Efficiency Analysis

The total system power efficiency is defined as the quotient of the power contributing to thrust, or the jet power, and the total input power. Using the jet power from equation (3.11), the total input power from equation (3.8), P_m of the electromagnetic, and the thruster cross-sectional area, A, we define the power efficiency as follows.

$$\eta = \frac{AP_J(T_e)}{AP_0(T_e)+P_m}. \tag{3.12}$$

Assuming a collisionless plasma, a=0.0164 m, P_m=120 W, and a corresponding magnetic field of B=0.02 T, a plot of the efficiency versus electron temperature can be seen in Figure 3.1.

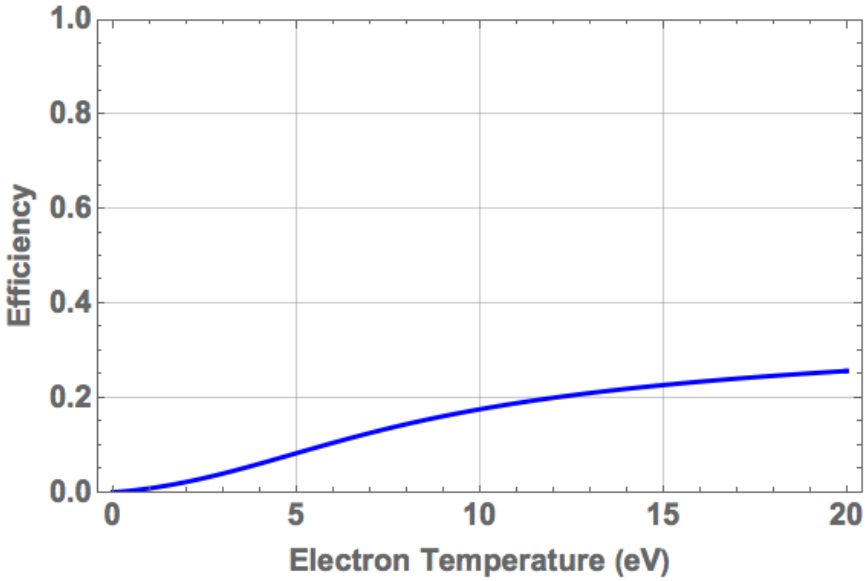

Figure 3.1: Power efficiency versus electron temperature with argon propellant, magnet power consumption of 120W, magnetic field of 0.02T, and thruster radius of 0.0164m

The first primary modification that can be made to the helicon thruster by means of the superconducting approach is to remove the power draw to the electromagnets. By utilizing permanent magnets and the high-temperature type-II superconductor, as opposed to electromagnets, no continuous power is required to supply the magnetic field. A further modification that can be achieved through the use of magnetic field modification is to construct a magnetic mirror[76] at the front wall of the thruster. Achievement of such a field would ideally eliminate the losses from the plasma sheath at the upstream plasma boundary. Practically, this loss area would be reduced to the hybrid loss area of a magnetic mirror. This reduces one of the largest power sinks occurring inherently within the system. Assuming a collisionless plasma, a plot can be generated of the best-case scenario for the superconducting helicon thruster. This case assumes that the only loss mechanisms are the power sink to the plasma sheath at the thruster exit, the cost of ionization, and the power lost through the upstream mirror. The efficiency for this

scenario can be seen in Figure 3.2. A significant increase in the propulsive efficiency is demonstrated.

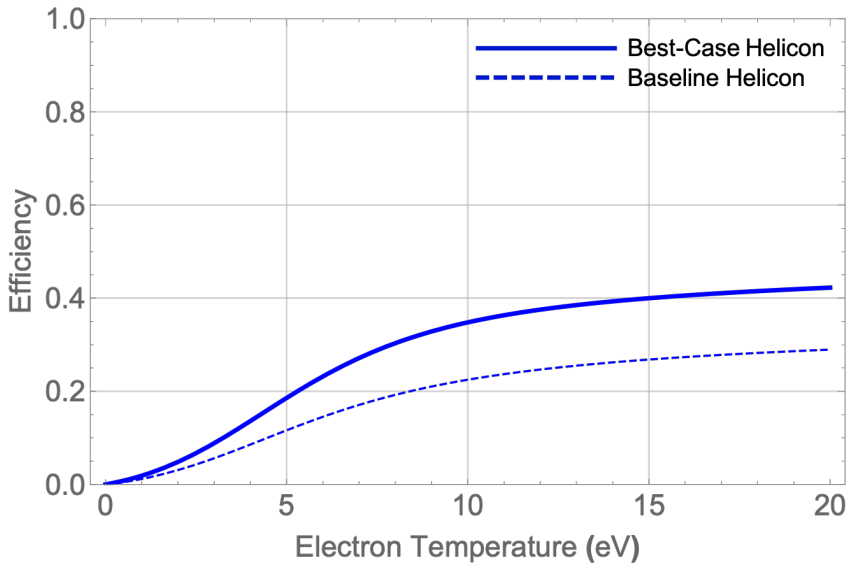

Figure 3.2: Best case power efficiency versus electron temperature with baseline helicon efficiency.

3.4 Summary and Discussion

This analysis indicates that the primary driving term in the efficiency determination is the power draw to the sheath as indicated by Fruchtman[22]. At an electron temperature of 10 eV, the power draw to the electromagnet only accounts for 3% of the total power. For the same electron temperature in the best-case scenario, removal of the power loss to the lateral walls and to the upstream plasma boundary allows for a more substantial, 12%, increase in efficiency. In each case, the effective loss area and the neutral density will govern the electron temperature. Due to neutral pumping[77], low neutral densities will be observed in order to drive the electron temperature higher.

The efficiency analysis presented above also indicates that the efficiency improves with increasing electron temperatures because of the assumption that the

acceleration mechanism is that of a single freestanding plasma sheath as a result of ambipolar flow. The primary consequence of this assumption is that as the helicon thruster transitions between the three different power coupling modes (E-mode to H-mode and H-mode to W-mode), the electron temperature will decrease in favor of increasing plasma densities. This effect is due to an increase in power deposition towards neutral ionization rather than electron heating. To avoid the necessity of capturing this effect, the plasma density in equation (3.7) is a formulation of the maximum density that can be supported by a helicon thruster for a given magnetic field. In actuality, this plasma density will vary inversely with changes in electron temperature, which further supports the assumption that Figure 3.2 represents the best-case scenario for the superconducting helicon thruster.

The significance of this efficiency analysis is two-fold. First, it provides an analytical model that can be experimentally verified. Experimental measurements of the electron temperature and plasma density are necessary to evaluate the power efficiency for comparison with this model. Chapter 6 will discuss the diagnostic equipment used for these measurements as well as a comparison of the expected efficiency for the helicon and superconducting helicon thrusters using the analysis discussed above. Second, this model provides the necessary information to identify what the superconducting magnet subsystem must achieve as far as power loss mitigation. Because it is also the first consider the electromagnet losses in the total power efficiency, the model serves as the first major contribution to the state-of-the-art.

4. Chapter 4: Superconducting Magnet Subsystem

4.1 Superconductor Integrated Magnet Design

4.1.1 Subsystem Requirements

According to the literature survey and power flow analysis previously discussed, we impose two requirements on the design of the superconducting magnetic subsystem:

1. Axial uniformity downstream of the helical antenna to ensure the propagation of the helicon wave throughout the ionization and accelerations regions within the helicon plasma.
2. Upstream magnetic mirror to confine the plasma, increase ion residence times, and also to reduce power losses to the upstream plasma sheath.

The principle idea is that of an ideal superconducting tube capped at one end by a permanent disk magnet. Once the superconductor reaches its critical temperature, the magnetic flux will be expelled from the material, via the Meissner effect[25], and wrap sharply around the open end of the tube to reconnect with the opposite pole of the magnet. A qualitative model of this can be seen in Figure 4.1. The sharp divergence at the exit plane is also hypothesized to provide a more collimated beam due to a more rapid detachment of the plasma.

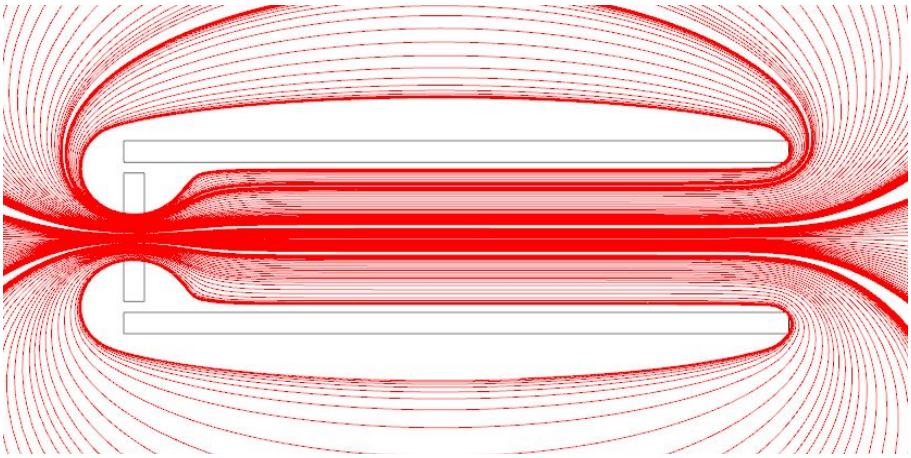

Figure 4.1: COMSOL simulation of magnetic field lines from a permanent disc magnet placed inside the end of the HTS tube while superconducting[26].

Experimental implementation would require the use of a low-temperature (type-I) superconductor since they exhibit perfect diamagnetism and will completely expel magnetic flux within the material[26]. The difficulty lies in developing a cooling system capable of reaching temperatures in the range of 1 – 20 Kelvin, which is typical of the critical temperatures of these materials. To avoid this design constrain, high-temperature type-II superconductors may be used instead. Specifically, we chose a superconducting tube from CAN Superconductors used for current limiters made of Bismuth Strontium Calcium Copper Oxide (BSSCO) in the 2223 phase. It has an inner diameter of 59 mm, length of 100 mm, and wall thickness of approximately 2.5 mm. The critical temperature is 110 K, which makes cooling the system far more achievable in a laboratory environment since liquid nitrogen at 77 K can be used. Using a solid material also allows for higher current densities provided the tangential critical current of 2000 A is not surpassed.

Using a high-temperature type-II superconductor in lieu of a low-temperature type-I superconductor does not come without consequence. High-temperature type-II

superconductors do not exhibit perfect diamagnetism, and thus will not completely expel the magnetic flux from the material. They instead exhibit a mixed, or vortex, state[78], which allows for partial penetration of magnetic flux when the external magnetic field dominates the Meissner current on the materials surface[79]. This results in a phenomenon known as flux pinning, where magnetic flux becomes trapped within supercurrent vortices, preventing the flux from moving within the material, and shielding the other regions of the superconductor from the trapped magnetic flux[80]. This effect occurs when magnetic flux is present within the material prior to achieving the critical temperature, and poses a design challenge in that the flux would need to be removed before reaching the critical temperature. Alternatively, a flux conservation approach can be used and will be discussed in more detail in the following section.

Additionally, the conceptual design in Figure 4.1 does not allow for a propellant inlet. Because of this, a solid permanent disc magnet cannot be used and must be replaced by a ring magnet. While the magnetic field topology in the near field of the ring magnet is dissimilar to that of a disc magnet, the only requirement off the face of the magnet is to provide the upstream magnetic mirror, which can be achievable with either magnet type. In the far field, the magnetic flux lines diverge similarly, and would be less of a concern.

4.1.2 Principles of Operation

Using the aforementioned flux conservation approach, a combination of electromagnets, permanent magnets, and high-temperature type-II superconductors can be used to achieve the two subsystem design constraints, while also minimizing the total

power into the system by eliminating the need to continuously power the electromagnet. A solenoid is used to satisfy the first criterion of the axially uniform magnetic field, with a high-temperature type-II superconducting tube located coaxially within the solenoid as seen in Figure 4.2. The solenoid initially generates the magnetic field, at which point the superconductor is cooled to below its critical temperature by feeding liquid nitrogen into an aluminum vessel containing the superconductor. The axial magnetic field strength inside the solenoid is found by using Ampère's Law, $B = \frac{\mu_0 n_s I}{L_s}$. Here, n_s is the number of turns, I is the current in the solenoid, and L_s is the solenoid's length. Once the critical temperature has been reached, the solenoid can be powered off. A current will be induced in the superconductor according to Lenz's Law that is not subject to Ohmic resistance due to the superconducting state of the material. The magnitude of this current is equal to the product of the number of turns in the solenoid and the current in the solenoid windings. If the superconductor is treated as though it were a solenoid itself, then the axial magnetic field strength will be identical to what was produced with the solenoid (provided the superconductor and solenoid have the same length), without the need to continuously power the solenoid. To generate the upstream convergence, a permanent ring magnet is placed outside of the upstream end of the superconductor housing, and coaxial with the superconductor. The magnetic moments of the solenoid and the ring magnet must be aligned such that the magnetic field from the solenoid will strengthen as it passes through the core of the permanent ring magnet.

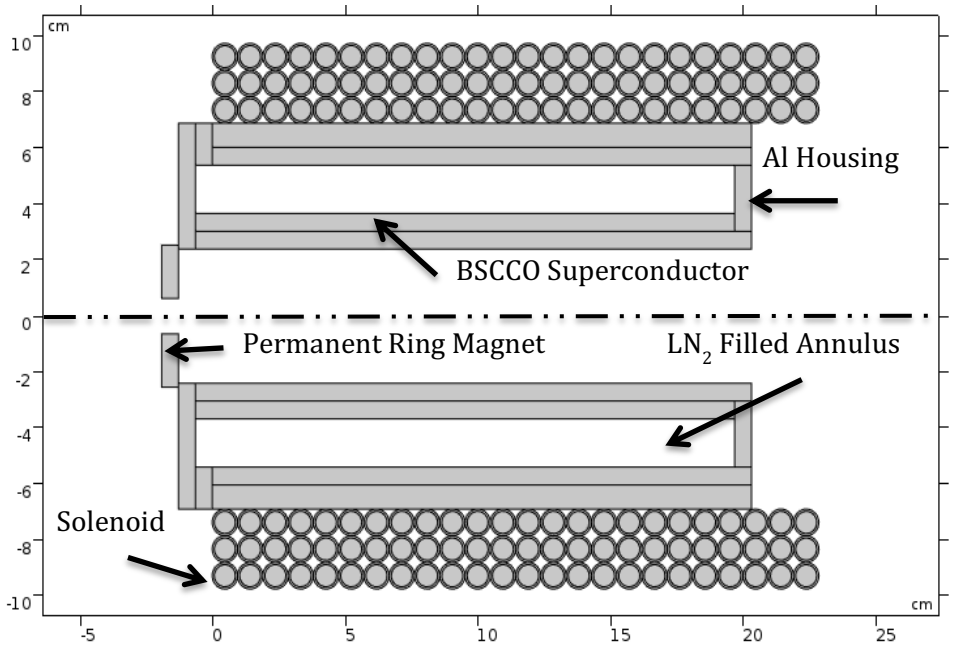

Figure 4.2: Superconducting magnet schematic in COMSOL Multiphysics.

4.1.3 Construction and Laboratory Implementation

The design of the superconducting magnet system was limited to the manufacturing capabilities of the superconducting tubes. The size of a single superconductor was provided at the beginning of this chapter. To increase the length of the thruster, two superconductors are placed end-to-end, bringing the total length to 200 mm. To cool the superconductors, they are placed in an aluminum enclosure into which liquid nitrogen can be fed. Aluminum was selected because the enclosure cannot be ferromagnetic and is more cost effective than brass. The aluminum enclosure is composed of two coaxial tubes capped by a welded ring on one end. This creates an annular cavity, where the superconductors rest coaxially around the inner cylinder and the liquid nitrogen fills in the remainder of the cavity. To close off and seal the opposite end, an aluminum ring is screwed onto a base plate with O-rings to ensure a leak-free

seal. On the opposite, welded side, two Swagelok® ports are connected 180° away from each other. With the superconducting magnet subsystem lying on its side, coaxial with the plasma source, liquid nitrogen can be fed into the bottom port, filling the cavity, and extending into an outlet pipe at the top. This ensures that the entire cavity can be filled with liquid nitrogen. An image of the aluminum enclosure can be seen in Figure 4.3 and is of the same dimensions as the schematic in Figure 4.2.

Figure 4.3: Aluminum enclosure for superconductors.

Because the superconductors are the primary design constraint, the maximum allowable outer diameter for the plasma source and antenna is 48 mm. This accounts for an aluminum wall thickness of about 5.5 mm. Since the antenna is placed within the inner diameter of the enclosure, the antenna leads must enter axially and presents another design challenge that will be addressed in Chapter 6. The liquid nitrogen ports on the end of the enclosure can be connected directly to a large dewar, or even a liquid nitrogen

reservoir that can be replenished as needed. The outer diameter of the aluminum enclosure sets the inner diameter of the surrounding solenoid at about 11 cm.

The solenoid must be capable of providing a magnetic field no greater than 200 G. This limitation is set by the tangential critical current of the superconducting material. By treating the superconductors as a single-turn solenoid, the critical magnetic field can be calculated using the critical current. Initially, the solenoid was constructed out of 3/8" copper tubing with 3 layers of 26 turns. The purpose of the tubing is so that the solenoid could be readily water-cooled through its core while simultaneously carrying current. Additionally, the thickness of the tubing allows for higher current densities should larger magnetic fields be required. It is powered by 20 Nickel-Cadmium D-cell batteries, wired with two series of 10 in parallel, providing 64 A and 2.4 V to the solenoid. This solenoid was used throughout the modeling and validation of the superconducting magnet subsystem discussed within this chapter. For the experimental integration of the superconducting magnets, a smaller, more compact solenoid is used. This one is constructed out of 10 AWG wire wound around a G10 spool with 4 layers of 52 turns, and is powered by a Mastech 3050E DC Power Supply. In either case, the solenoid provides a maximum on-axis magnetic field strength of 180 G. To ensure excess heat would not be conducted into the liquid nitrogen filled cavity of the aluminum enclosure, a foam insulating layer is placed between the solenoid and the aluminum enclosure.

To provide the upstream convergence, a permanent ring magnet with 1.27 cm inner diameter, 5.08 cm outer diameter, and 1.27 cm thickness is mounted coaxially to the removable cap of the aluminum enclosure. The inner diameter is just large enough to allow clearance of a propellant feed stem that opens up to a larger diameter just past the

magnet and within the aluminum enclosure. To ensure that the magnet does not shift as a result of the magnetic interaction with the solenoid or superconductors, it is securely mounted to the aluminum baseplate with a cap that screws into an outer centering ring as seen in Figure 4.4. The magnet is placed within the centering ring and oriented such that the magnetic moment is aligned with that of the solenoid before the securing cap is connected to the baseplate.

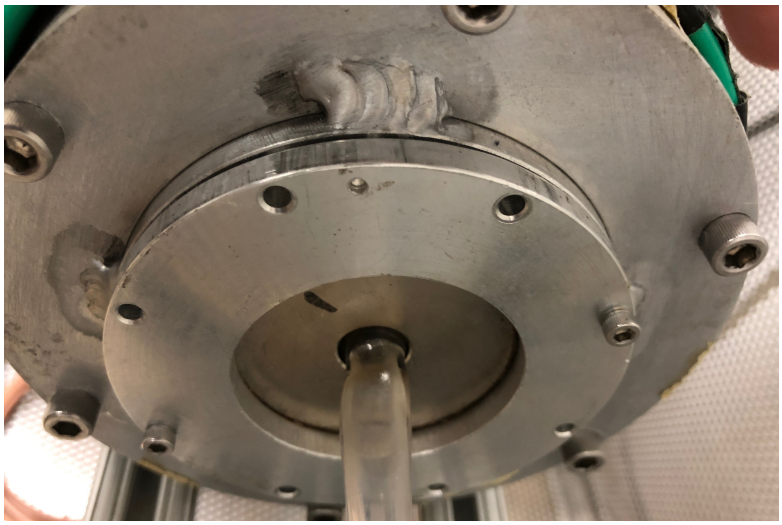

Figure 4.4: Permanent ring magnet mounted to superconductor housing.

4.2 Computational Modeling Using COMSOL Multiphysics

In order to visualize and predict the strength and shape of the magnetic field, a model using COMSOL Multiphysics was developed. The model was used to predict the magnetic field using the combination of the solenoid and the permanent magnet, and then modified to predict the magnetic field of the superconducting magnet subsystem. This model was then verified experimentally by mapping the magnetic field topology of both magnet subsystems. The COMSOL model was designed to match the experimental system to allow for direct comparison with the measured field.

COMSOL Multiphysics is a modeling program that uses the finite element method (FEM) to subdivide the governing equations into a system of solvable algebraic (steady state problems) or ordinary differential equations (transient problems). The program then recombines the elements to fully solve the original governing equations. To reduce computation time and to simplify the system of equations, COMSOL has a built-in set of algorithms to precondition elements. When creating a COMSOL model, the user selects one of two studies, either steady state or transient, then selects what physics modules to include. These modules contain the particular set of governing equations for the parameters of interest.

In this study, we use an axisymmetric steady-state solver with the AC/DC module. To define the material properties, we use the built-in definitions for copper and aluminum. For the BSCCO superconductor, the relative permeability is changed from unity to $1(10^{-6})$, depending on if it is not or is respectively, in the superconducting state. Because COMSOL cannot model the superconducting transition across the critical temperature, and the subsequent depowering of the solenoid, we treat the solenoid case and superconductor case as two separate steady state solutions. This is one aspect of the model that requires experimental validation and is addressed in the following section. The geometry of the two-dimensional model in Figure 4.2 is maintained, but converted to an axisymmetric geometry to simplify the COMSOL solver by invoking symmetry.

At each boundary with the open environment, we apply a magnetic insulation boundary condition and ensure that a zero magnetic vector potential is given as the initial condition. The treatment of the permanent magnet is handled by applying an Ampère's Law condition on the permanent magnet domain with a magnetization of $9.75(10^5)$ A/m

in the axial direction pointing towards the center of the device. The solenoid is given an external current density of $2.3(10^6)$ A/m^2 in the azimuthal direction. In the superconductor case, similar treatment is implemented, where the same current density is applied to the entirety of the superconductor domain. This represents the current that would be induced in the superconductor to maintain the same magnetic flux once the solenoid is depowered. In switching between the solenoid case and the superconductor case, the only required changes to the model are to change the magnetic permeability of the superconducting material to reflect its critical temperature transition, and to change the domain over which the external current density is applied, from the solenoid turns to the superconductor.

Once the material and physical properties of the model are established, a COMSOL generated physics-controlled mesh is used for the FEM solver. From there, the stationary solver calculates the remaining parameters contained within the governing equations of the AC/DC module. The normal magnetic flux density is of primary interest, as well as its radial and axial components. This lets us generate a color plot for the magnetic flux density with a magnetic field streamline overlay. The results for both the solenoid and superconducting cases can be seen in Figure 4.5. A cutline was added along the axis of the model to plot the axial magnetic field strength versus the axial position to compare with the experimental magnetic field measurements. This is used in the following section and will be discussed in more detail there. Qualitatively, this model is used to verify the existence of the two criteria required of the superconducting magnet subsystem; axial uniformity along the length of the device with an upstream magnetic mirror.

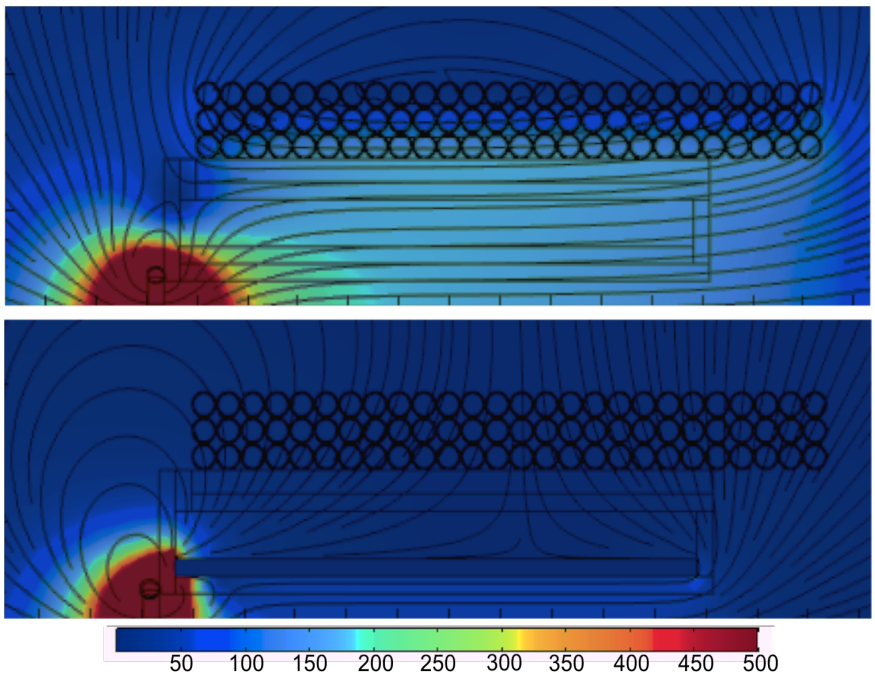

Figure 4.5: COMSOL magnetic field model of solenoid and permanent ring magnet (top), and superconducting magnet subsystem (bottom). Units in Gauss.

Analyzing the central region just off the axis of symmetry, which is to contain the plasma, the magnetic field in both cases satisfies the axial uniformity condition based on the magnetic field streamline overlay. The magnetic field does increase in strength upstream, just off the face of the permanent magnet as necessary for upstream plasma confinement. Another qualitative observation is the sharp divergence of the magnetic field at the exit plane of the superconductors. This is hypothesized to help lead to more rapid plasma detachment, thus resulting in a more collimated beam for increased jet power. Also of note is the point at which the magnetic field begins to diverge. In order to provide a strong enough magnetic field at a smaller current density, the solenoid was required to be of a greater length than the superconductors. While this is of little consequence to the magnetic field within the core of the device, it does affect the axial location of the divergence, which impacts the position of the theorized double-layer

according to Charles and Boswell[57]. Additionally, this leads to the more rapid falloff of the magnetic field at the aluminum enclosure exit plane.

4.3 Magnetic Field Topology Mapping

To verify that the model accurately predicts the magnetic field geometry for the solenoid and superconductor cases, the magnetic field was measured experimentally. A magnetic field mapping apparatus was constructed using aluminum 80/20 beams, as seen in Figure 4.6. A pair of Velmex bi-slides was used to translate the magnetic field probe within the open volume inside of the aluminum enclosure. As discussed earlier in the chapter, power to the solenoid was provided by a set of Nickel-Cadmium D-cell batteries at about 64 A of current and a potential drop over the solenoid of about 2.4 V. The current into the solenoid was monitored using a Rogowski coil, in order to verify a steady current was maintained throughout the magnetic field sweep. In the superconducting magnet case, the aluminum enclosure ports were connected to a liquid nitrogen reservoir. The superconductors were pre-cooled to avoid battery lifetime issues, so with the batteries running, the critical temperature could be more rapidly achieved. To monitor the temperature of the liquid nitrogen filled annulus, a thermocouple was placed down the overflow tubing at the upper, exit port of the enclosure. Once this temperature settled at the temperature of the liquid nitrogen, it was assumed that the rest of the cavity also reached that temperature at steady-state. Once below the critical temperature, the batteries were disconnected from the solenoid circuit, and the liquid nitrogen reservoir was refilled as needed throughout the course of the measurement sweeps.

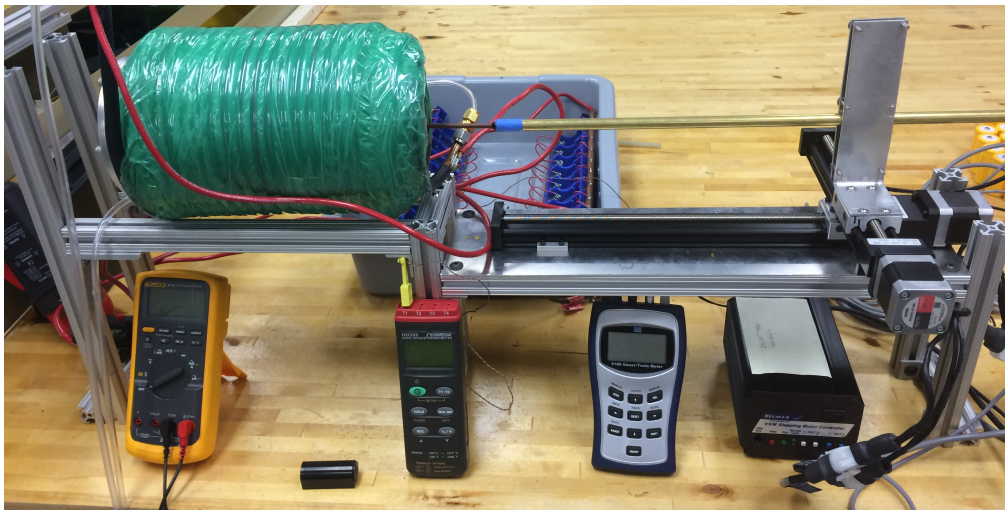

Figure 4.6: Solenoid and magnetic field mapping apparatus.

A LabVIEW VI was written to measure the magnetic flux density in the axial direction and log its two-dimensional position over the course of sweep. The on-axis magnetic flux density was then plotted using MATLAB, where the results are shown in Figure 4.7 along with the results from the COMSOL model. Included with the experimental data are one standard deviation error bars calculated as the standard deviation of the data over a total of ten magnetic field sweeps. There are two notable comparisons to be made in Figure 4.7. The first is comparing the experimental results for the solenoid and superconductor case with the COMSOL Multiphysics model. In this comparison, very good agreement is observed, verifying the accuracy of the model. The importance of this is that in modeling the transition of the superconductors in their superconducting state, the two different states may be each individually treated as separate steady-states. This was assumed in the development of the COMSOL model, but as discussed previously, required experimental validation. The data also verifies the correctness of the treatment of the superconducting material in the COMSOL model. Simply changing its relative magnetic permeability will accurately account for the change

in its material properties when determining the magnetic field topology of the superconducting magnet subsystem.

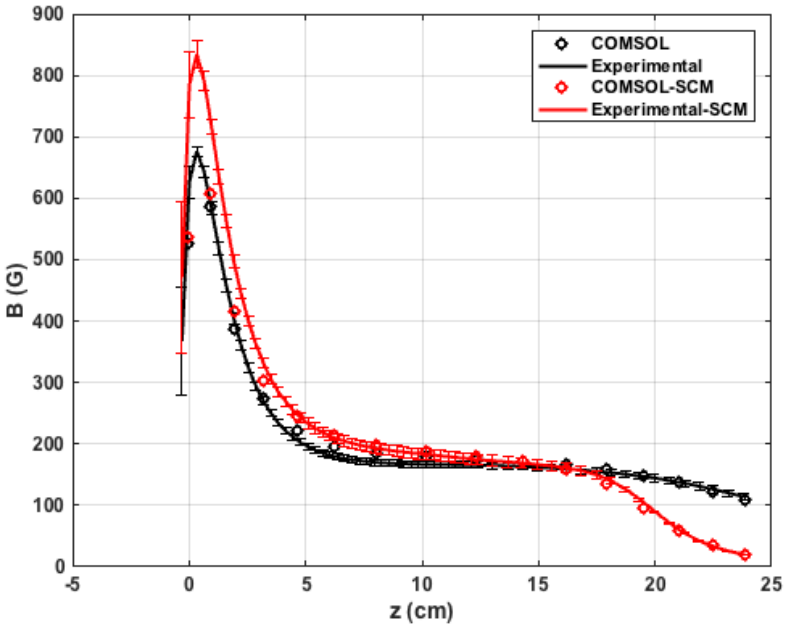

Figure 4.7: On-Axis magnetic flux density for the solenoid and superconducting magnet subsystem.

A secondary comparison to be made is of the magnetic field between the solenoid and the superconducting magnet cases. In the superconducting magnet case, the magnetic field at the permanent ring magnet center is higher than that of the solenoid case. This is likely due to a smaller superconductor diameter in comparison to the solenoid. While the magnetic field from each is assumed to be the same, in treating the superconductors as a single-turn solenoid, the magnetic flux density interacts with that from the other source over a smaller volume, and thus cannot expand as in the solenoid case. This can be observed by looking at the color map between the two cases in Figure 4.5. Because of this, along the length of the device, the magnetic field is less axially uniform than the solenoid case. This is not expected to be impactful, as the gradient in

the magnetic field is small over the length of the plasma source. Another feature of note is the more rapid drop-off of the magnetic field in the superconducting magnet case. This was discussed previously in the chapter but warrants another mention. Since the length of the superconducting material does not extend as far as the solenoid, the magnetic field is expected to diverge farther upstream than in the solenoid case. This, in addition to the qualitative analysis of Figure 4.5, does demonstrate a more rapidly diverging magnetic field at the exit plane, which could support more efficient plasma detachment from the magnetic field. One final note worth mentioning is that the magnetic field strength along the axis is low enough to avoid exceeding the critical current limitation of the superconductor. This avoids issues where the superconductors would transition out of their superconducting state in mid-operation because of large tangential current densities.

5. Chapter 5: Thermal Control Subsystem

5.1 Thermal Control Parameters

In order to maintain the critical temperature of the superconductor, a thermal management subsystem must also be incorporated. In order to operate as an in-space platform, we impose two requirements on this subsystem:

1. Maintain cryogenic temperatures below the critical temperature of the superconductor.
2. Insulate the cryogenic region from heat generated by the plasma, and radiate excess thermal power.

This can be achieved through a series of conductive and insulating layers that intercept heat from the plasma, and conduct it to a radiator, which ultimately prevents the heat from reaching the cryogenic region. To maintain temperatures below the superconductor critical temperature, a cold-tip cryocooler would be used. The helical antenna introduces an additional challenge. Since the plasma source will be within the confines of the superconducting magnet subsystem, the power leads must be oriented in the axial direction. This requires electrically insulating layers, in addition to the thermally insulating layers, in order to prevent the RF power from conducting to other regions of the thermal management subsystem.

In a practical application of the superconducting helicon thruster, the cryogenic temperatures must be maintained in a closed-loop system. For laboratory testing, the solution is simpler in that an open-loop liquid nitrogen cooling system can be applied. This study assumes that the primary contribution of thermal energy to the system comes

from the plasma column, and that the heat initially generated by the solenoid is removed prior to its depowering once the critical temperature of the superconductor has been reached. The primary contributions from the plasma column are the conducted and radiated powers that result from maintaining the plasma. The total conducted and radiated powers are calculated and the insulated layers separating the plasma column and the cryogenic region are determined based on the power to be removed by a cryocooler. A radiator must then remove any excess heat, where its area is uniquely determined based on the power to be radiated and its temperature.

The equations for the radiated power per volume and conducted power per area are as follows[81]:

Radiated Power: $$\dot{P}_{rad} = e(E'_{ion} - E_{ion})n_e n_n R_{ion} \qquad \left[\frac{W}{m^3}\right] \tag{5.1}$$

Conducted Power: $$q_r = \left(2 + \frac{1}{2} ln\left(\frac{m_i}{2\pi m_e}\right)\right) eT_e \Gamma_{max} \qquad \left[\frac{W}{m^2}\right] \tag{5.2}$$

Here, E'_{ion} and E_{ion}, represent the total cost of ionization per ion-electron pair and the first ionization energy of the propellant, respectively. To calculate the ionization cost, a curve-fit[75] is used assuming an electron temperature of 10 eV, which yields a cost per ion-electron pair of 30 eV. The ionization rate is represented as R_{ion}, which at 10 eV is 10^{-14} m^3/s. We also assume an argon plasma with a $5(10^{17})$ m^{-3} plasma density, 40 cm plasma source length, and 1.64 cm source radius for the calculation of the particle flux. The neutral density is calculated using information about the vacuum chamber in the experimental setup. First the pressure in the source tube, P_{tube}, must be known, and is given as:

$$P_{tube} = P_{base} + \frac{Q}{S_p} \tag{5.3}$$

The turbo pump is capable of achieving a base pressure, P_{base}, of $5.5(10^{-5})$ torr at a pumping speed, S_p, of 2100 L/s. The throughput, Q, is calculated using a volumetric mass flow rate of 3.1 sccm, which is set by a 10 micron orifice. This yields a tube pressure of $7.4(10^{-5})$ torr, which by the ideal gas law gives a neutral density of $2.4(10^{18})$ m^{-3}.

First, we will focus on the radiative heat flux distribution to the upstream and lateral walls. At the upstream wall, the source is discretized into a series of differential disks, where the wall is also assumed to be a disk of fixed radius. The view factor is then that of parallel circular discs with centers along the same normal. The distribution across the radial direction of the upstream wall, seen in Figure 5.1, is achieved by summing the contribution of each differential disk element along the total length of the plasma. The open downstream boundary is not accounted for as any losses here are not contributing to heating the device. The lateral wall is treated as a sum of differential ring elements, where the plasma source is divided into a line of differential elementals. The view factor then reduces to $\frac{r}{2\pi d}$, where r is the radius of the lateral wall, and d is the distance from the heat element. The distribution along the lateral wall, seen in Figure 5.2, is determined by summing the contributions from each element along the line source to each differential ring. By integrating Figure 5.1 and Figure 5.2 over the area of the upstream and lateral walls, respectively, we find that the power radiated to the lateral wall significantly dominates the power radiated to the back wall. This leaves a total radiated power of about 17 W.

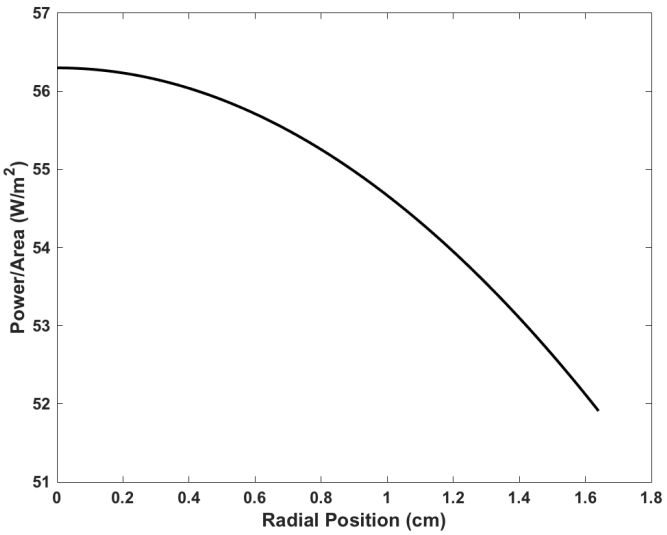

Figure 5.1: Radiative heat flux distribution to the upstream wall.

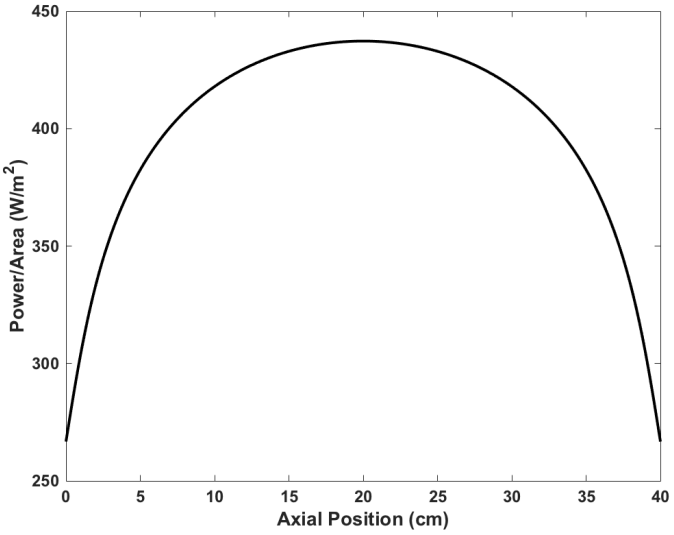

Figure 5.2: Radiative heat flux distribution to the lateral wall.

The conducted power is only assumed to be through the lateral wall since the upstream convergence yields a negligible contribution of conducted power. As was done with the radiated power distribution, the conducted power density to the lateral wall can be integrated over the total area, yielding a total conducted power of 650 W. This,

however, does not account for the presence of the magnetic field, which helps confine the ion flux to the wall and thus reduces the conducted power to the lateral wall. Assuming that the particle flux to the lateral wall is equal to that due to ambipolar, cross-field diffusion[82], the particle flux in equation (5.2) can be substituted with the following:

$$\Gamma_s = \frac{T_e \nu}{m_e \omega_p^2} \frac{p}{a} n_e J_1 \left(\frac{pr}{a}\right) \cos\left(\frac{\pi z}{L_z}\right) \tag{5.4}$$

The only required condition is that the electrons are magnetized, which can readily be seen using an on-axis magnetic field strength of 200 G. This magnetic field strength is also used to calculate the electron cyclotron frequency, ω_p. The electron temperature is once again assumed to be 10 eV with a plasma density of $5(10^{17})$ m^{-3}. Here, the collision frequency, ν, is the product of the density and R_{ion}. Taking the radial position to be at the boundary, $r = a$, and integrating over the axial direction yields a conducted power of 12 mW. Comparatively, this is negligible when considering the sum of the conducted and radiated power, therefore, the 17 W of radiated power must be removed from the system to maintain cryogenic temperatures.

5.2 Subsystem Design

The thermal management subsystem is composed of four distinct insulating layers, a copper radiator, and a cryocooler. The insulating layers serve the purpose of thermally isolating the cryogenic region and also electrically isolating the helical antenna leads. Since the plasma source tube, simply made of quartz, is confined within the superconductor housing, the antenna leads must be fed into the system along the axis and cannot come into electrical contact with any other conducting layers. This is especially

important since the first layer outside of the source tube is a 0.16 cm conformal copper layer that intercepts the radiated heat and readily conducts it to the radiator. The next layer is a 0.08 cm Kapton layer, which electrically insulates and separates the 0.16 cm thick antenna leads from the conformal copper layer and helical antenna. Another 0.08 cm Kapton layer is wrapped around the antenna leads to ensure they are electrically isolated from the conformal copper layer and the copper antenna. This now leaves a 0.08 cm vacuum gap separating the final Kapton layer and the aluminum housing wall. The conformal copper layer is connected to a conical radiator at the thruster exit. In order to radiate the remnant power to be removed by the cryocooler, the final Kapton layer is aluminized (emissivity 0.03) on the side facing the inner wall of the aluminum housing. A schematic of the various insulating layers can be seen in Figure 5.3.

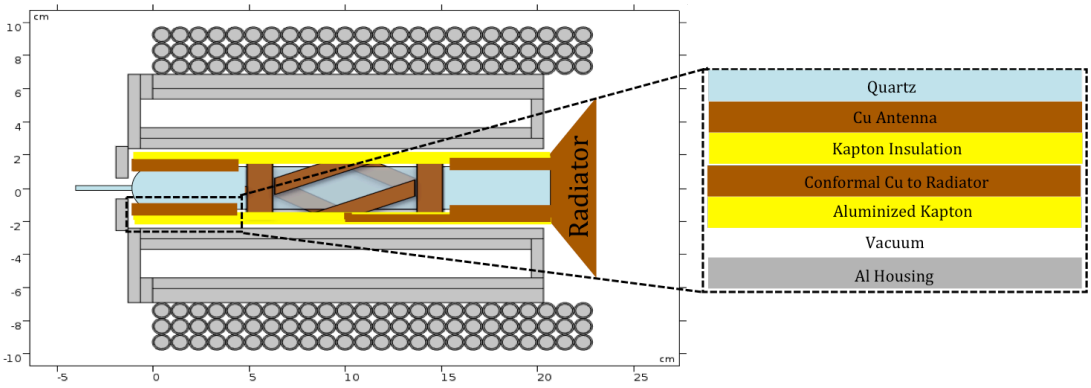

Figure 5.3: Schematic of thermal management design for the superconducting helicon thruster.

The area of the radiator can be found since the temperature of the conformal copper layer can be calculated and the required radiated power is known. By setting a maximum allowable power of 5 W to be removed by the cryocooler, 12 W must now be removed by the radiator. Given that the aluminized Kapton layer must radiate 5 W of power, its temperature can be uniquely determined since its area is known. This results

in a temperature of 474 K. The emissivity of the radiator is chosen to be 0.9, corresponding to a rough, black matte paint coating on the copper. To calculate the temperature of the conformal copper layer, the one-dimensional heat transfer equation must be solved for each layer:

$$T_1 = \frac{q_1 r_1}{k_{T1}} ln\left(\frac{r_2}{r_1}\right) + T_2 \tag{5.5}$$

Doing so results in the temperature profile seen in Figure 5.4, and yields a temperature of 475.5 K for the copper radiator. Now that the radiated power and temperature are known, the Stefan-Boltzmann law can uniquely determine the size of the radiator. To radiate the remaining 12 W at 475.5 K, the radiator area must be 46 cm^2. To further reduce the size of the radiator, excess power can be used to preheat the propellant. This is especially attractive for water vapor propellant applications, to which this system lends itself well.

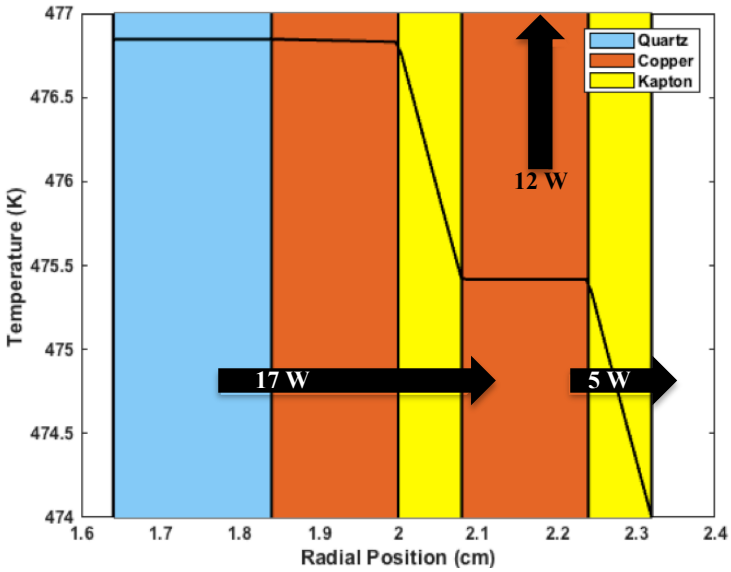

Figure 5.4: Temperature profile for thermal management subsystem insulating layers.

Knowing that the cryocooler must remove 5 W and have a cold tip of 77 K, we can use a survey of known cryocooler models performed by Porter[83] to determine the

minimum power requirement based on the current state-of-the-art. Using a Stirling type CryoTel MT by Sunpower, the required input power would be 80 W. While the need to continuously power the cryocooler will not drastically detract from the maximum possible power efficiency discussed in Section III. B., it does prove to be a slight improvement over the need to continuously power an electromagnet. This then demonstrates the ability to reduce the overall power draw from components necessary for prolonged thruster operation.

5.3 Environmental Loading and In-Situ Resource Utilization

Having a copper radiator exposed to the space environment means that it is also subject to solar loading. As determined in the previous section, a radiator of size 46 cm^2 is required to radiate the excess 12 W from the plasma. When in solar view, a radiator of this size collects 2 W of heat, assuming a copper radiator. In this case, the radiator area must be increased to account for the solar loading. If not, then the radiator temperature will increase, thereby increasing the temperature of the aluminized kapton layer that radiates power to the cryogenic region. If this increases beyond the 5 W removed by the cryocooler, then the cryogenic region temperature will eventually increase to beyond the critical temperature of the superconductors, leading to a device failure. Incorporating the 2 W of solar loading increases the radiator area to 54 cm^2. When not in solar view, the radiator temperature lowers to about 457 K, which would effectively lower the temperature of the device, while simultaneously reducing the power removed by the cryocooler.

An alternative approach to managing the 12 W of excess power is to preheat and evaporate liquid water for use as the propellant. To determine the power requirement to evaporate water, the required mass flow rate must be known. Maintaining the prior assumption of a 10 eV plasma, and continuing to assume that the acceleration mechanism is that of a single freestanding plasma sheath from ambipolar flow, then the ion exit velocity can be calculated using the following equation:

$$\frac{1}{2} m_i u_e^2 = \frac{eT_e}{2}\left(1 + ln\left[\frac{m_i}{2\pi\, m_e}\right]\right) \tag{5.6}$$

Integrating this with respect to time, we arrive at a relationship between the exit velocity, mass flow rate, and jet power.

$$\frac{1}{2} \dot{m}_\iota u_e^2 = P_J \tag{5.7}$$

The jet power is then calculated using equation (1.3), where the total power is the sum of the excess plasma power, 12 W, and the jet power. From the efficiency analysis in Chapter 3, the expected power efficiency for the superconducting helicon thruster is 35% at 10 eV. For these parameters, the supported mass flow rate is 0.023 mg/s.

If the vaporization rate is assumed to be identical to this mass flow rate, then the required power is calculated using the equation for the thermodynamic phase change.

$$P_{vap} = \dot{m}_\iota \left((T - T_{boil}) c_{p,H2O} + h_{we}\right) \tag{5.8}$$

Assuming the liquid water is stored at 300 K, the power required to support the above mass flow rate is only 55 mW. If the power acquired via solar loading is combined with the 12 W excess plasma power, then a mass flow rate of up to 5.9 mg/s can be supported. In the case of in-situ resource utilization, the propellant would be harvested as solid ice.

This would require melting the ice before the liquid water could be vaporized for use as a propellant. According to data from the Cassini-Huygens mission, Saturn's outer rings are at a temperature of 90 K[84]. Assuming this would be the temperature of the ice collected, the required power to vaporize at the supported flow rate is calculated using the equation for thermodynamic phase change in equation (5.8), but incorporating the power required to raise the temperature of the ice to melting and the power required to melt the ice.

$$P_{vap} = \dot{m}_{\iota}\left((T - T_{melt})c_{p,ice} + h_{wm} + (T_{melt} - T_{boil})c_{p,H2O} + h_{we}\right) \tag{5.9}$$

Here, the power required to support the above mass flow rate is 79 mW. If the power acquired via solar loading is combined with the 12 W excess plasma power, then a mass flow rate of up to 4.1 mg/s can be supported.

5.4 Laboratory Implementation

Developing a thermal management subsystem for laboratory testing is far simpler because it does need to operate in a closed-loop environment. This means that an open-loop liquid nitrogen cooling system can be used, where depleted liquid nitrogen coolant can simply be replaced. In this case, we attach a liquid nitrogen reservoir to the aluminum enclosure and maintain the supply by refilling from a larger dewar. To intercept the plasma heat, the conformal copper layer discussed previously is used, and conducted via a copper strap to a simple heat sink. The primary disadvantage to such a system is that for laboratory models where the thruster components are external to the vacuum chamber, condensation can rapidly accumulate and introduce electrical shorts if not electrically insulated. For vacuum applications or space platforms, this does not present an issue.

6. Chapter 6: Helicon Plasma Thruster with Integrated Superconducting Magnets

6.1 Diagnostic Equipment

6.1.1 Triple Langmuir Probe

One of the most common plasma diagnostic tools is the Langmuir probe. Developed in the 1920's by Mott-Smith and Langmuir[85], this device measures the current response of a biased spherical or cylindrical conductor immersed in a plasma environment where the Debye length is significantly smaller than the radius of the conductor. Assuming a Maxwellian distribution of electrons, Mott-Smith and Langmuir demonstrated how the floating potential, plasma potential, electron temperature, and density of the plasma relates to the ion current collected by the conductor as a function of the probe bias voltage. An example I-V trace from a Langmuir probe can be seen in Figure 6.1. Here, V_f is the floating potential, which is determined by the bias voltage at which the ion and electron currents are equal. The plasma potential, V_s, is the potential at which the electron current saturates occurring at the "knee" of the I-V trace. In low-density plasmas ($n_e < 10^{17}$ m^{-3}), they determined that the ion current collected by the conductor is not affected by the shape of the plasma potential, but rather is limited by the angular momentum of the orbiting ions in what became known as orbital motion limited (OML) theory. Since its inception, the Langmuir probe has grown to become the most common diagnostic tool for determining the electron temperature of a plasma.

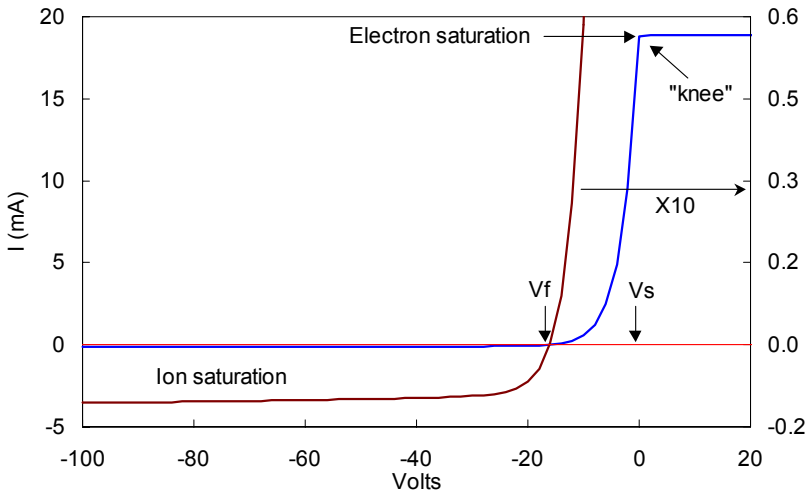

Figure 6.1: Idealized I-V trace from Langmuir probe. Ion saturation curve expanded 10x to show detail[86].

In RF plasmas, such as a helicon plasma, Langmuir probe measurements are not as straightforward as stationary plasmas. The plasma potential is free to perturb with the driving RF frequency, and thus results in large fluctuations of the measured ion current in the retardation region of the probe trace[87]. The most common method of obtaining an accurate I-V trace in an RF environment is to use a series of RF chokes to act as a low-pass filter. This results in a measurement of the DC offset of the signal, which in this instance is the average current. An additional consequence of using Langmuir probes in helicon plasmas is that large magnetic fields in the vicinity of the probe can cause the electron Larmor radius to decrease below the probe radius. In this instance, the probe will deplete electrons along that field line and only allow further electron collection if they diffuse across the magnetic field lines. This results in an indistinct “knee” where the space potential is that of the depleted force tube rather than that of the bulk plasma[86]. This can be avoided by selecting a probe radius that will always be less than the Larmor radius.

Given the difficulties associated with the traditional Langmuir probe traces, alternate methods of determining the plasma electron temperature were developed. The simplest of designs is that of the triple Langmuir probe, first developed by Chen and Sekiguchi[88] for instantaneous measurement of the electron temperature. Three probes are connected such that two are biased relative to one another, and the third is left to float such that the net current flow is zero. The bias voltage between the probes is chosen to be a few times the expected electron temperature. The negative probe draws a current equal to the ion saturation current so that the positive probe can draw an equal current of electrons. A typical triple Langmuir probe electrical circuit can be seen in Figure 6.2. The primary assumptions that go into the triple probe are the same as that of the compensated or uncompensated Langmuir probe. The plasma is assumed to be Maxwellian, where the mean-free-path is greater than the plasma sheath size and the probe radius. An additional assumption and design requirement are that the sheath size is smaller than the separation distance of the probes. This is to ensure that the probe sheaths do not overlap one another, causing the floating probe to bias relative to the plasma floating potential due to the collection of a non-zero net current.

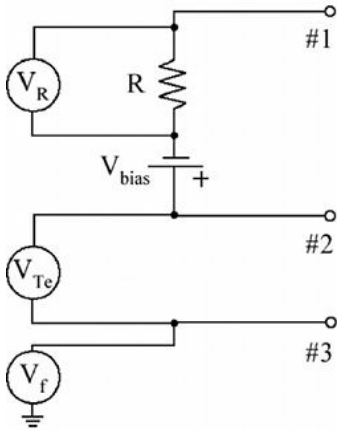

Figure 6.2: Typical triple Langmuir probe circuit[89].

The significance of selecting a bias voltage sufficiently larger than the electron temperature can be seen in the following equation.

$$\frac{I_+ - I_{fl}}{I_+ - I_-} = \frac{1 - e^{-e(V_f - V_+)/k_B T_e}}{1 - e^{-e(V_- - V_+)/k_B T_e}} \tag{6.1}$$

Since the current into the floating probe is zero, and the current into the positive and negative probe tips are equal in magnitude and opposite in sign, the left side of the equation reduces to 1/2. For (V_--V_+) sufficiently larger than T_e, the denominator of the right side approaches unity. Simplifying and solving for the electron temperature yields a straightforward relationship for the electron temperature as a function of the potential difference between the positive and floating probes.

$$T_e = \frac{e}{k_B}\left(\frac{V_+ - V_f}{\ln 2}\right) \tag{6.2}$$

The elegant simplicity of the electron temperature calculations allows for a direct measurement without the need of an I-V trace like the single Langmuir probe. These measurements can be made with excellent time resolution, and, since the potential of the positive and floating probes immersed in an RF plasma will fluctuate in-phase, the probe is immune to oscillations inherent in RF discharges. The only drawback of the triple Langmuir probe in comparison to the single Langmuir probe is its susceptibility to large plasma parameter gradients due to the increased size of the device.

The triple Langmuir probe used to carry out the diagnostic measurements in these experiments was constructed using a 30.5 cm long 4-bore alumina tube with an outer diameter of 1.6 mm and inner diameters equal to 0.35 mm. Three of the bores were used to run 0.325 mm tungsten wire such that 2 mm of the ends were exposed to function as

the triple Langmuir probe tips. An image of the probe can be seen below in Figure 6.3. The probe functioning as the floating probe was connected to an oscilloscope using a high-voltage probe so that the floating potential could be measured with respect to ground. The remaining probes were connected as seen in Figure 6.2 with a bias voltage of 41.33 V and 33 Ω resistor. Oscilloscope high voltage probes were used to measure the potential with respect to ground of the positive and negative probes in the same manner as the floating probe.

Figure 6.3: Triple Langmuir probe used for helicon and superconducting helicon thruster diagnostic measurements.

The triple Langmuir probe is mounted in the vacuum chamber on a set of bi-directional slides in order to perform a two-dimensional map of the plasma electron temperature. The purpose is to analyze the differences between the helicon and superconducting helicon thruster between the plasma source center and the plasma boundary. Any differences in performance could potentially be related to the plasma dynamics at the exit plane, specifically because of the stronger divergence of the magnetic field in the superconducting helicon thruster. If the plasma is capable of more

rapidly detaching in this region, then the local plasma parameters can be used to estimate any potential performance differences. The potential with respect to ground of the positive, negative, and floating probes is measured using an oscilloscope and recorded using a custom LabVIEW VI. The VI performs the calculation of the electron temperature in real time and outputs tabulated data for each potential and the electron temperature.

Using the circuit shown in Figure 6.2, it is possible to determine an estimate of the electron density. If the plasma connects the circuit between probes #1 (negative) and #2 (positive), then Ohm's law can be used to solve for the magnitude of the current flowing into either of these probe tips.

$$I_+ = \frac{V_{bias} - (V_+ - V_f)}{R} \tag{6.3}$$

Using the Bohm flux given in equation (3.6) and the assumption of a Maxwellian plasma, the density as a function of the probe current can be determined.

$$n_p = \frac{I_+}{0.6 A_p e \sqrt{\frac{e\,T_e}{m_i}}} \left(\frac{e^{-e(V_f - V_+)/k_B T_e}}{1 - e^{-e(V_f - V_+)/k_B T_e}} \right) \tag{6.3}$$

Knowing the electron temperature, positive probe potential, and floating probe potential for each location in the two-dimensional sweep of the triple Langmuir probe allows for a two-dimensional profile for the electron density in addition to the electron temperature. This determines if a greater level of ionization has occurred in either of the thruster test cases. Additionally, if the density of neutrals is estimated from the propellant flow rate, an approximation for the propellant utilization can be determined to calculate certain performance metrics for the thruster. This will be discussed in greater detail in the plasma

characterization and thruster performance sections for the respective test cases of the following chapter.

6.1.2 Retarding Potential Analyzer

A retarding potential analyzer (RPA) is a device used to obtain the ion energy distribution function (IEDF) of the emergent particles from an I-V sweep. The RPA consists of a series of four mesh grids and a collector plate housed in an insulated enclosure. As particles enter the RPA, they are first met by the floating grid. The purpose of this grid is to allow the formation of a plasma sheath at the floating potential to minimize plasma perturbations[89]. The next grid is the electron repelling grid and is biased negatively at a magnitude sufficiently greater than the local electron temperature to prevent electrons from further entering the RPA. The third grid is the ion retarding grid which is swept over a range of biases to effectively filter ions out that are not of a high enough energy to overcome the threshold set by the retarding potential. The ions energetic enough to pass through the retarding grid can then be collected by the collector plate, where the current is recorded as a function of the retarding potential. Once a sufficiently high retarding potential is reached, no further ions would be collected. A fourth, or suppression, grid is commonly used to return any secondary electrons liberated from the collector plate. The purpose of this grid is to ensure that the current collected by the collector plate is the true ion current so that electrons removed from the collector plate are not counted as ions. A schematic of the RPA and the relative potential profile can be seen in Figure 6.4.

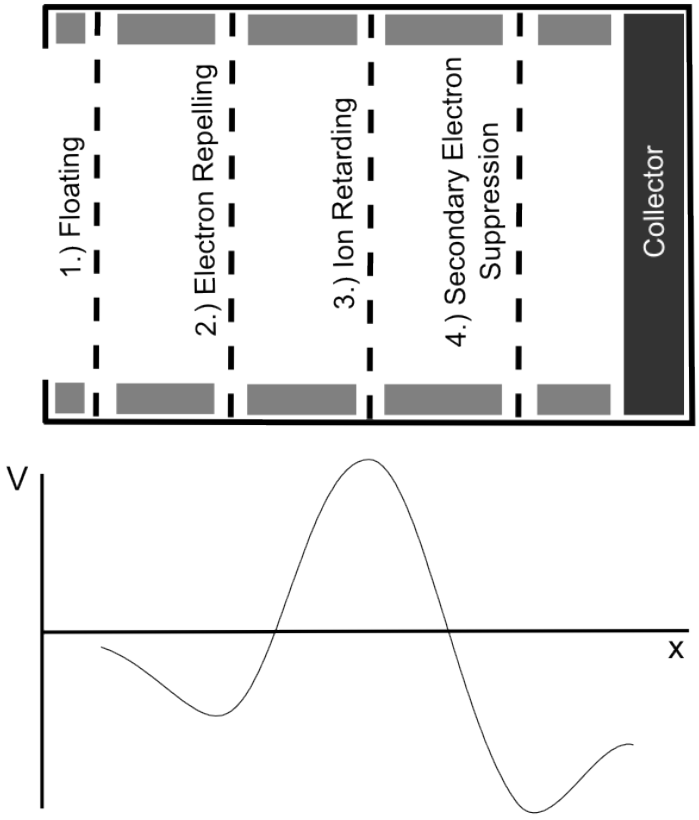

Figure 6.4: RPA schematic with potential profile[72].

The data obtained by the RPA is a current versus voltage trace that initially starts out at the maximum ion current sampled by the RPA but then quickly drops off to zero once the maximum threshold energy of the distribution is reached. The data can then be differentiated with respect to the bias voltage to determine the IEDF, centered at the local plasma potential. An example of the data trace and derivative can be seen in Figure 6.5. In many instances with the helicon thruster, a two peak distribution is obtained. This occurs when a fraction of the initial bulk ion distribution is accelerated to produce a beam. The higher energy distribution is that of the beam, whereas the lower distribution

is the result of beam ion collisions with neutrals. This potential has been found to be equal to that of the upstream plasma potential as measured by an emissive probe[90].

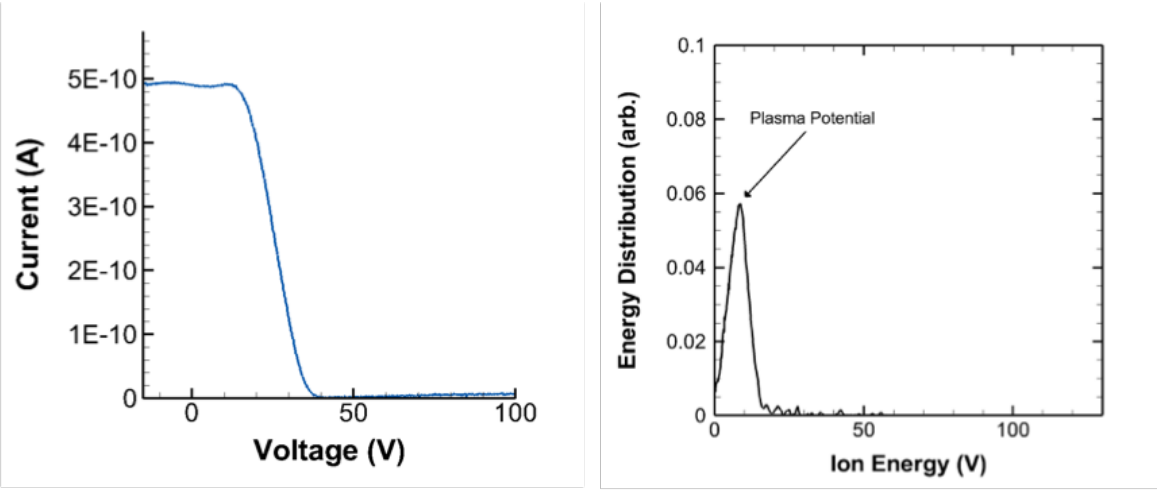

Figure 6.5: RPA schematic with potential profile[72].

Other effects that can be observed with the RPA include the energy dependence of the charge-exchange cross-section by means of ion beam decay over distance[91]. The beam energy was observed to increase as the RPA was moved farther downstream, but always remained within the initial distributions. A sample of the data collected in this study is shown for illustrative purposes in Figure 6.6. Over the charge-exchange length scale, lower energy ions are preferentially lost due to charge-exchange collisions, resulting in a lower density, higher energy ion distribution contained within the high-energy tail of the initial ion beam distribution. As the beam ions are lost and become part of the lower energy distribution, this background plasma potential begins to increase as evidenced by the upward shift of the low energy background distribution. While beam densities decrease as a result of Boltzmann expansion, the upward trend of the beam and plasma potentials could only be explained by the energy dependence of the charge-exchange cross-sections.

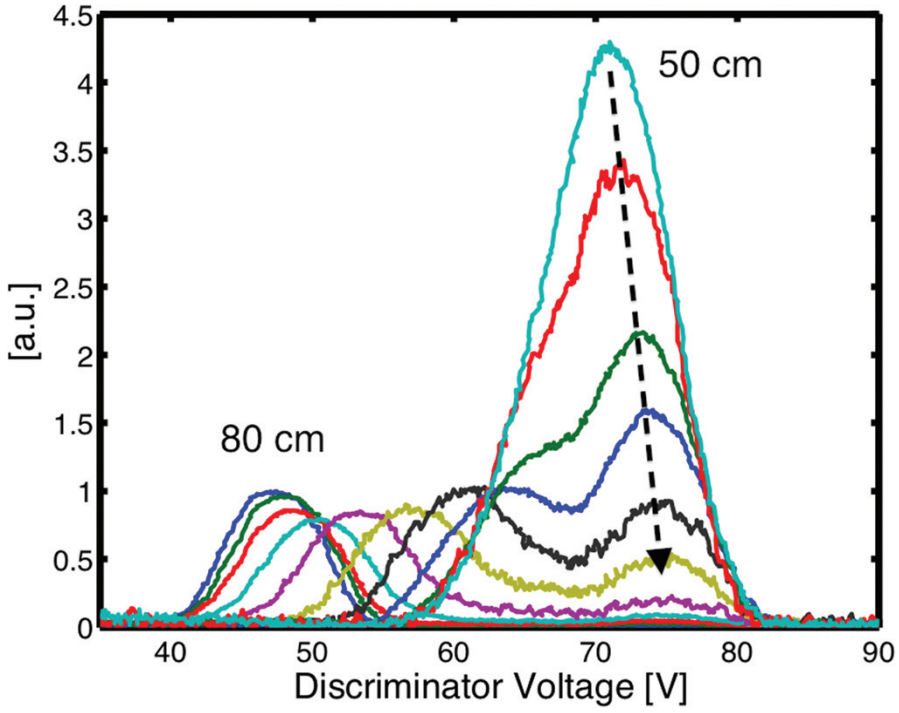

Figure 6.6: RPA data demonstrating ion beam decay as a result of charge-exchange collisions[91].

The RPA used in these experiments is the commercially available Model FC-71A Faraday Cup from Kimball Physics (Figure 6.7). The collector plate is housed in a grounded stainless-steel cylinder and connected to an ammeter via a BNC cable. The total length of the device is 77.54 mm and the diameter of the stainless-steel cylinder is 13.21 mm. Four grids are screwed onto the aperture and separated with alumina spacers to maintain electrical isolation of each grid. Originally, the grids had a square cross-section of 25.4 mm side length but were modified to have a circular cross-section with a 25.4 mm diameter in order to perform measurements within the plasma source tube. The grid aperture size is 5.0 mm in diameter with a grid separation of 2.64 mm. The first grid was left floating, the electron repelling grid was set to -30 V, the ion retarding grid was swept from 0 V up to 800 V, and the electron suppression grid was set to -80 V.

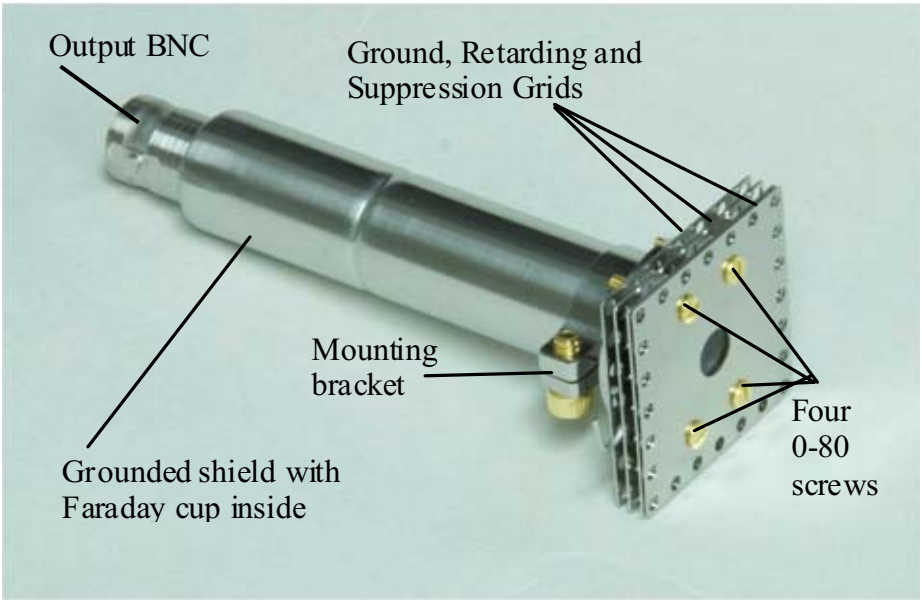

Figure 6.7: Model FC-71A Faraday Cup from Kimball Physics[92].

A bi-directional, motorized translation stage was used to change the position of the RPA while under vacuum. The RPA was placed inside of a brass tube to act as a boom so that measurements inside of the plasma source would be possible. An image of the mounted RPA can be seen in Figure 6.8. To prevent interaction of the RPA or boom with the plasma, both were coated with a layer of Kapton tape, then mounted to the translation stage with a clamp. The RPA housing was grounded through the output BNC shielding. A custom LabVIEW VI was used sweep and record the retarding grid voltage in 1 V increments set by a sourcemeter, then measure the corresponding current from the ammeter. The output file is the I-V trace over the designated retarding grid voltage range. The raw data was then differentiated in Matlab using a fourth order central differencing scheme in order to obtain the ion energy distribution function.

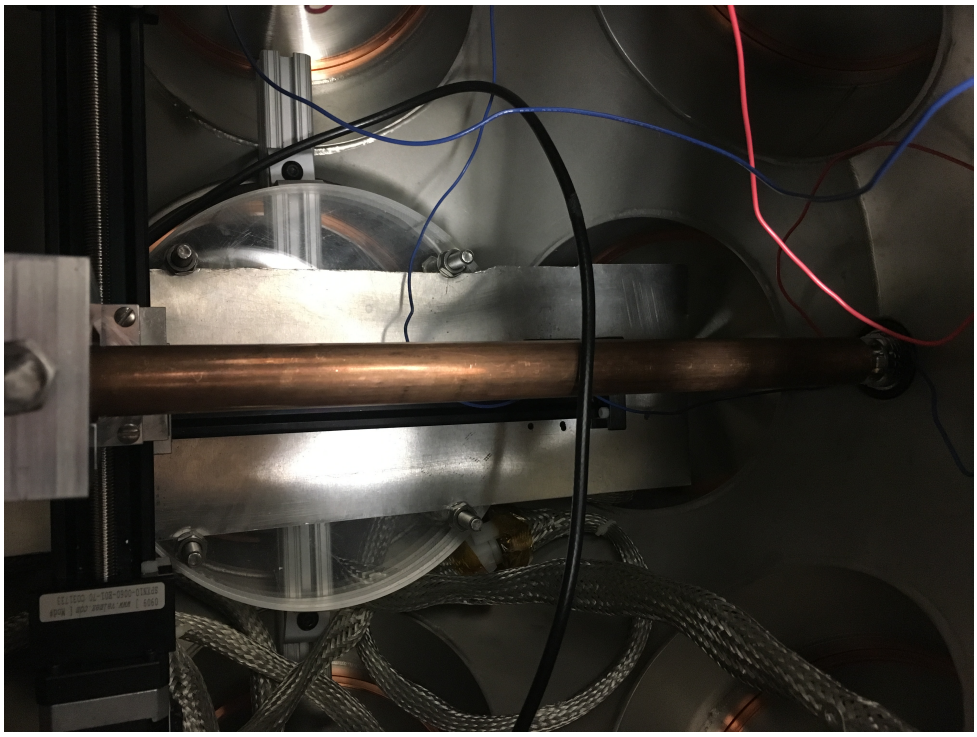

Figure 6.8: RPA within brass boom and mounted to bi-directional slides within vacuum chamber. Image taken from above.

6.2 Experimental Setup and Operation

To avoid the added challenges of enclosing the entirety of the thruster in a vacuum chamber, requiring a custom RF power feedthrough, all of the components were placed outside of the chamber and the exhaust vents into a 66-liter spherical vacuum chamber. Connected to the chamber is an Adixen turbo pump and Leybold EcoDry M roughing pump, capable of achieving a base pressure of approximately $2(10^{-8})$ Torr. In order to regulate the turbopump temperature, a chiller running antifreeze was connected to the turbo using the manufacturer constructed coolant lines. An InstruTech Hornet ion gauge and Worker Bee convection gauge were used to measure the pressure within the vacuum chamber. The set of motorized, bi-directional slides described in the previous

section were placed inside the vacuum chamber to hold the plasma diagnostic tools. Two feedthroughs were allocated for the diagnostic harnesses in order to set the necessary biases. The plasma source tube is connected to the chamber through a 2-3/4" ConFlat (CF) flange with a 3.5 cm outer diameter and 30.5 cm long Pyrex tube fused to the stainless-steel flange. The chamber feedthrough is offset from the inner wall by 3.5 cm. Between the vacuum feedthrough and the plasma source tube is a 10.5 cm stainless-steel extension that increases the length of the plasma source and further offsets the helicon thruster from the vacuum chamber wall. The end of the glass tube reduces to a valve stem for ¼" tubing in order to introduce the propellant to the system. The propellant used throughout this study is argon, where the flowrate is controlled using a 10-micron orifice. At the choked flow condition, this sets the volumetric flow rate at 3.1 sccm, equivalent to a mass flow rate of $9.3(10^{-8})$ kg/s. A diagram of the source tube length scales can be seen in Figure 6.9.

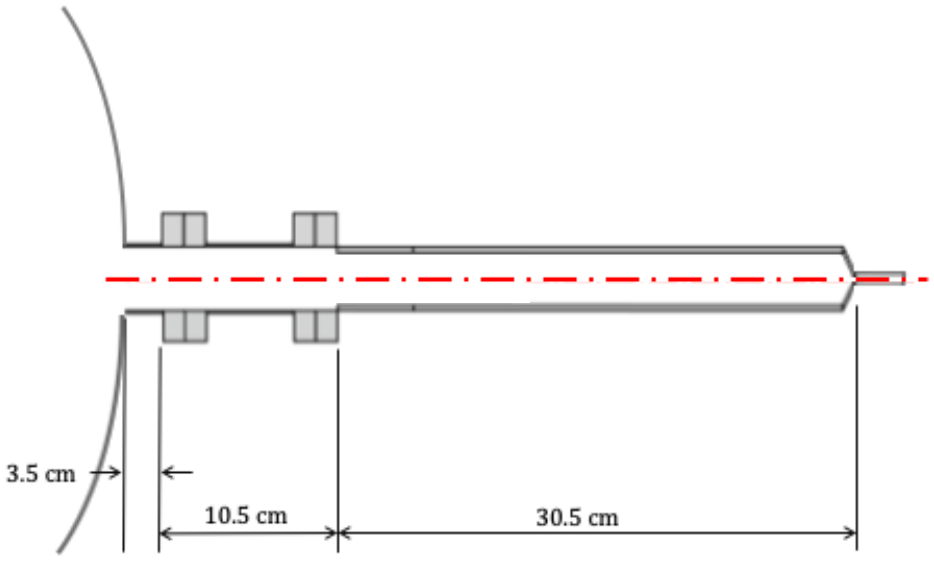

Figure 6.9: Vacuum chamber feedthrough and plasma source tube length scales.

Surrounding the plasma source tube is the same aluminum housing described in detail in Sections 4.1.2 and 4.1.3. The Swagelok® fittings were oriented so that the inlet is placed vertically below the outlet. The inlet connects to a liquid nitrogen reservoir and the outlet connects to a copper tube for excess liquid nitrogen to collect once the aluminum annulus is filled. To ensure cryogenic temperatures around the superconductors, a thermocouple was placed through the outlet tubing to measure the temperature at the outlet. These components are kept in place during operation and test of the standard helicon thruster and superconducting mode to directly compare the two system performances with identical setups and conditions. Between the plasma source tube and inner diameter of the aluminum housing lies the RF antenna. To maintain electrical isolation, a layer of Kapton was placed between the antenna and aluminum housing.

The selected antenna is a double-saddle, quarter-turn antenna where the scaling was determined using an analysis by Chen[31], and discussed in greater detail in Section 2.3.1. The radius of the antenna is fixed according to the system dimensions already set in place. With a known radius, the antenna length is determined using the antenna aspect ratio, also known as the gain factor. This ensures that the antenna wave is properly matched to the resonant ionization energy for the propellant. In the case of argon, the peak in the ionization cross-section occurs at 50 eV. Using this ionization energy and an antenna radius of 3.5 cm, equation (2.13) gives an antenna length of 15.5 cm. Since the antenna resides coaxially between the plasma source tube and the superconductor housing, the antenna power leads must be introduced axially. In order to prevent stray

magnetic fields from retarding current flow through the antenna, the leads must run parallel in close proximity. If two 12.5 mm wide, 125 mm long copper straps are used for the antenna leads, this effectively creates a parallel capacitor that introduces additional impedance to the circuit. To electrically isolate the two leads, a 1.25 mm Kapton layer was placed between them. The capacitance and inductance of the antenna leads can then be calculated using the following equations, respectively.

$$C_f = \varepsilon \frac{W_{pp}}{d_{pp}} L_{pp} \tag{6.4}$$

$$L_f = \mu_0 \frac{d_{pp}}{W_{pp}} L_{pp} \tag{6.5}$$

An image of the antenna and power feed lines can be seen in Figure 6.10. Since the antenna will be emitting an RF field, and is located outside of the grounded vacuum chamber, the entire thruster must be placed within a Faraday cage for safety precautions and to prevent interference with other thruster components and instrumentation.

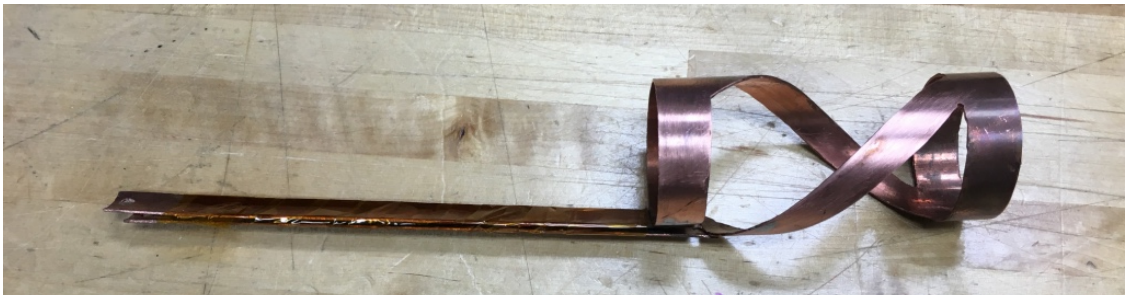

Figure 6.10: Helicon double-saddle antenna with power feed lines.

The antenna operates at a frequency of 13.56 MHz, where the initial waveform is provided by a Keithley 3390 Waveform Generator. This waveform then passes through an Amplifier Research 250 W amplifier to increase the input power. The operating powers for this study are 20 W – 100W in 10 W increments. Before the power is introduced to the antenna, the signal is passed through an L-type matching network

consisting of two variable capacitors. This custom matching network was constructed by researchers at NASA Glenn Research Center and is described in detail in Ref. 93. The purpose of the matching network is to match the impedance of the antenna, power feed lines, and plasma to the 50 Ohm impedance of the amplifier. If the impedances are not matched correctly, a portion of the power is reflected back into the amplifier, while only a fractional amount of transmitted power reaches the antenna and is then used for ionization. The variable capacitors have the capability of being tuned as the impedance of the load changes due to Ohmic heating. The reflected power is tracked with the built-in feature of the amplifier, which actively displays the transmitted and reflected power. In order to support the propagation of the helicon plasma wave, a solenoid powered using a Mastech 3050E DC Power Supply provides an axial magnetic field of approximately 190 G. The magnetic field topology is identical to the system discussed in Chapter 4, where an upstream permanent magnet is used to confine the plasma axially. A diagram and image of the complete superconducting helicon thruster can be seen in Figure 6.11.

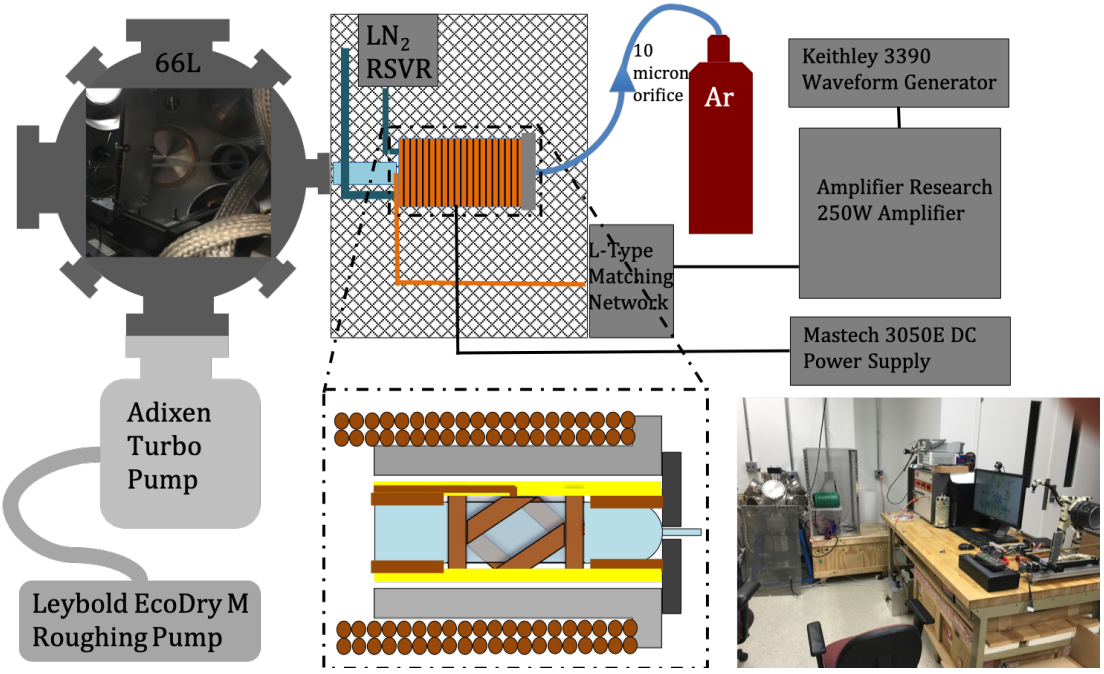

Figure 6.11: Superconducting helicon thruster experimental setup.

The experimental procedure begins with pumping the chamber down to a base pressure of $2(10^{-5})$ Torr using the roughing pump to initially pump down to 0.1 Torr, then allowing the turbo pump to reach the base. The propellant feedline valves are opened in order to clear out the lines back to the propellant tank. The waveform generator is then set to provide a sinusoidal wave with a frequency of 13.56 MHz and peak-to-peak voltage of 3 mV and the amplifier is set to standby. Next, power is provided to the solenoid, producing the 190 G axial magnetic field. The propellant tank is then opened allowing argon to flow into the system. The chamber pressure reaches steady state at approximately $5(10^{-5})$ Torr, at which point the amplifier is turned on and the power is steadily increased to the desired operating power. As the reflected power increases, the matching network is adjusted to reduce the reflected power to zero. The plasma will typically ignite around power levels of 7 W and further ionizes until the power is fixed.

Once the thruster is ignited and operating at the desired power level, the diagnostic (either the triple Langmuir probe or the RPA) biasing is set using the appropriate power supplies. The custom LabVIEW VI then performs the desired measurements and records the data in a Microsoft Excel document. Upon completing one measurement trial, the plasma is extinguished by reducing the amplifier power to zero, setting it to standby, turning off the magnetic field, and closing off the propellant feedline valves. The system then idles for approximately 10 minutes before reigniting the thruster and performing the next trial. This was repeated for 10 trials at power levels of 20 W, 30 W, 40 W, 50W, 60 W, and 100 W for both the triple Langmuir probe and the RPA individually. Given the limited space within the vacuum chamber, only one diagnostic can be placed inside and used at a time, where orientation calibrations must be performed each time a diagnostic is swapped for the other. The locations of the diagnostic measurements can be seen in Figure 6.12.

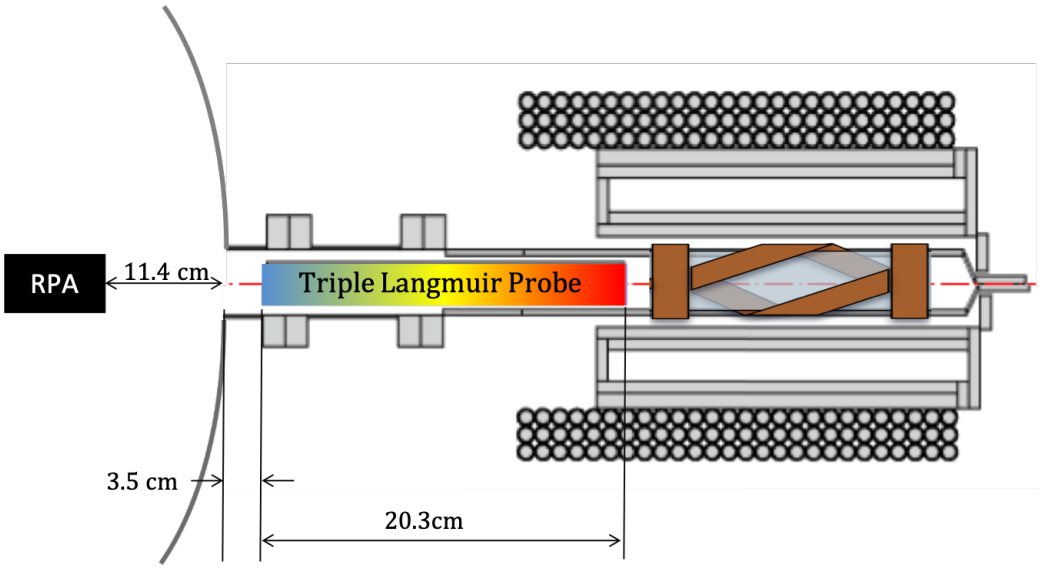

Figure 6.12: Diagnostic measurement locations.

In the superconducting helicon thruster case, the same operating procedure is followed with the exception of the solenoid operation. While the solenoid is operating, a steady source of liquid nitrogen is provided to the liquid nitrogen reservoir that feeds into the annulus of the superconductor housing. This lowers the temperature of the superconductors to approximately 77 K, at which point the solenoid power supply is turned off by opening a circuit breaker. To prevent kickback current from flowing into the power supply, a snubber diode was placed along the power lines, along with several RF chokes to prevent any stray induced current from the antenna. A Gauss meter is then used to verify that the magnetic field is maintained by the superconductors before continuing with the thruster operation as described above. To keep the superconductors below their critical temperature, a steady supply of liquid nitrogen must be maintained in the reservoir. To prevent heat conduction to the superconductors and rapid liquid nitrogen evaporation, the entire aluminum superconductor housing is wrapped in thermal insulation. Additionally, the antenna power lines are wrapped in Kapton to avoid short circuiting due to condensation around the liquid nitrogen inlet and outlet. An image of the superconducting helicon thruster in operation can be seen in Figure 6.13.

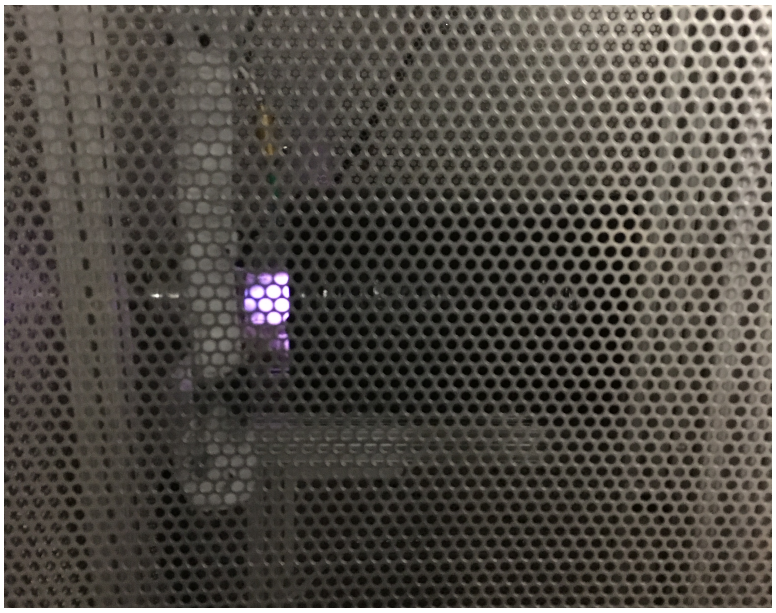

Figure 6.13: Superconducting helicon thruster in operation.

6.3 Plasma Characterization and Thruster Performance

The first diagnostic used to characterize the plasma was the triple Langmuir probe described above. A two-dimensional sweep of the thruster was performed in the region downstream of the antenna, prior to expansion into the vacuum chamber. A sample electron temperature sweep can be seen in Figure 6.14, and the full data collection for the electron temperature measurements are located in Appendix A. The color plot is the average electron temperature of ten independent measurement sets. As the probe performs measurements closer to the bulk plasma, the electron temperature becomes more uniform. The region used to average the bulk electron temperature is boxed in orange. The next two images show an axial and radial cut, respectively. The red line corresponds to the location of the axial cut, and the green line indicates the location of the radial cut. The standard deviation of the data is indicated with the confidence interval markers. As the electron temperature increases farther downstream, it is no longer

considered small with respect to the positive and negative probe bias, meaning the validity of these measurements becomes questionable. The shaded region of the axial cut represents the data subject to the breakdown of the triple Langmuir probe theory. It is important to note that although the large electron temperatures are in doubt, the valid probe measurements do indicate an increase in electron temperature before increasing beyond the bounds of the assumptions in the probe theory. This observation could represent the location of the free-standing plasma sheath or CFDL. Similar trends are observed in the superconducting helicon thruster data found in Appendix B.

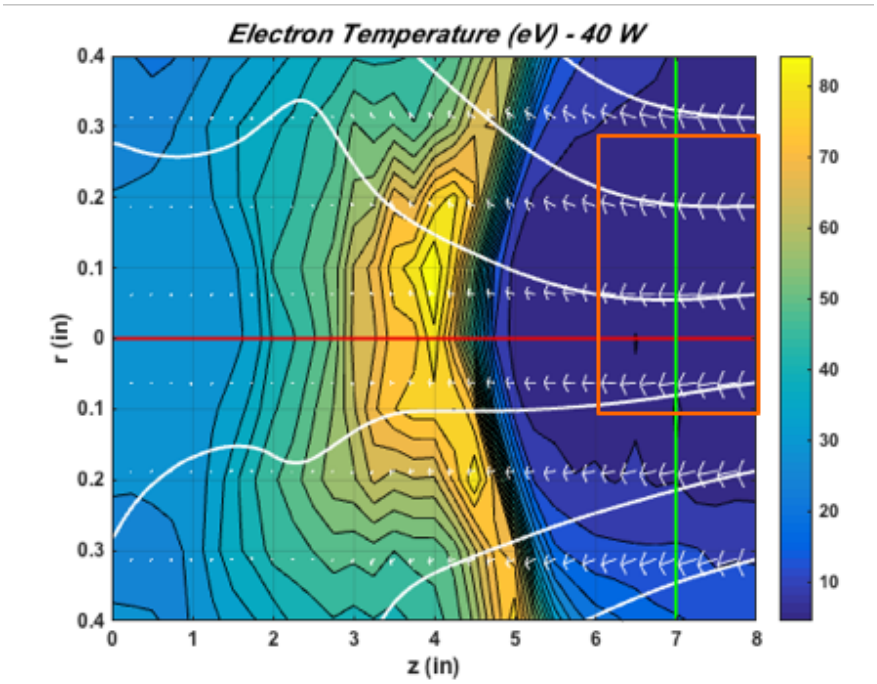

Figure 6.14: Electron temperature profile for the helicon thruster at 40 W of RF input power.

The bulk electron temperature summaries for both the helicon thruster and the superconducting helicon thruster are shown in Figure 6.15. For each data point, the electron temperature was averaged over all ten trials at each power input for the uniform

bulk regions indicated in Appendices A and B. The plot also shows the confidence interval to two standard deviations and demonstrates a high level of uniformity for the bulk electron temperature. At each power input, the electron temperature is larger in the superconducting helicon thruster, indicated a higher level of electron heating. Additionally, the electron temperature increases with respect to input power before dropping off steadily. This is indicative of a power coupling mode shift as power is initially consumed in electron heating but drops off as more power contributes to ionization rather than into the electrons. This is readily verified by the electron density calculation in equation (6.3). The electron density is calculated and plotted for each data point in the two-dimensional sweep. The density profiles for the helicon and superconducting helicon thrusters are provided in Appendices C and D, respectively. As was done with the electron temperature in the bulk of the plasma, the average electron density versus input power is shown in Figure 6.16.

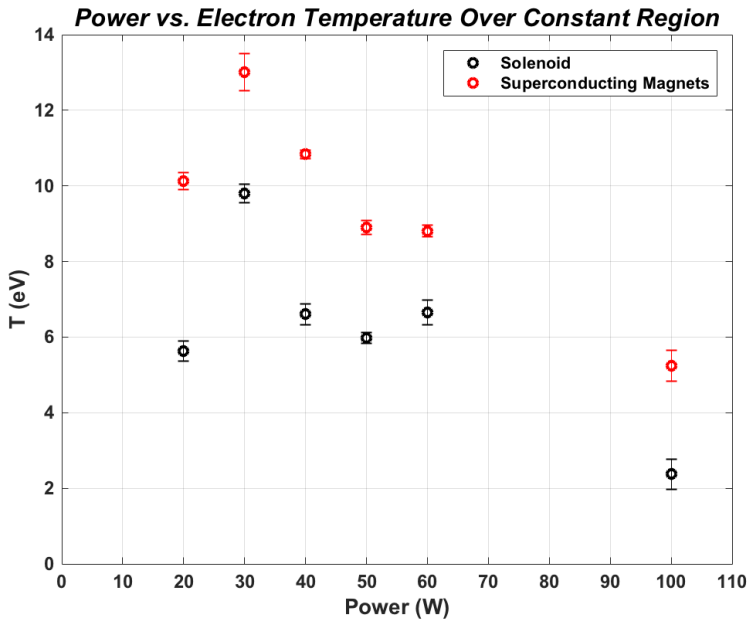

Figure 6.15: Electron temperature measurements in the bulk plasma for the helicon and superconducting helicon thrusters with 2σ confidence intervals.

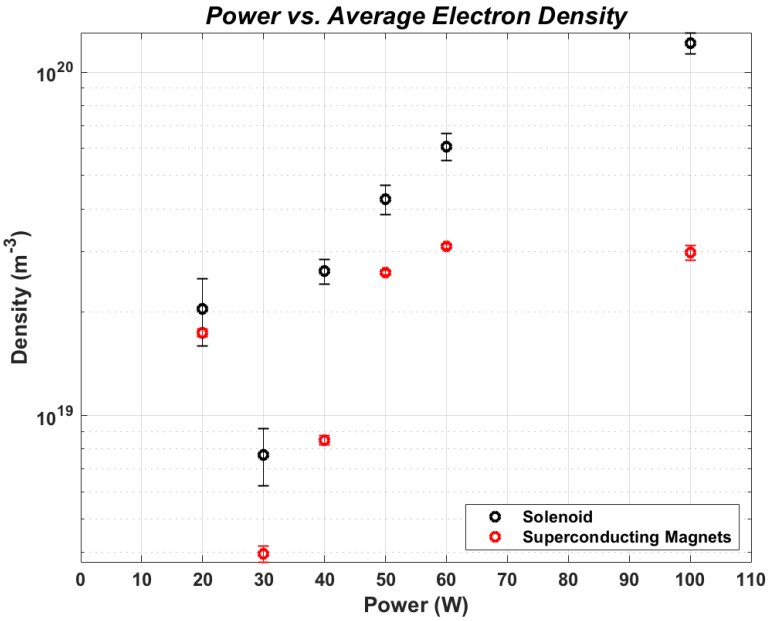

Figure 6.16: Electron density measurements in the bulk plasma for the helicon and superconducting helicon thrusters with 2σ confidence intervals.

The electron temperature observations are also present in the electron density data. The larger electron temperatures in the superconducting helicon thruster correspond

to lower electron densities due to a larger fraction of the input power applied towards electron heating rather than ionization. If the initial increase in electron temperature with respect to input power is indicative of the E-H mode shift, then the electron density data supports this observation since the density drops off initially with larger electron heating. Since another larger electron density increase is not observed, it is likely that the thrusters never transition into helicon-wave coupling. This could be due to the large surface area to volume ratio, meaning larger wall losses, or that the input power levels in this study are not sufficient to achieve this mode transition. Since the subject of this analysis is the comparison of the helicon and superconducting helicon thrusters for low input power station-keeping applications, further exploration of larger input powers could be the focus of a future study.

The triple Langmuir probe provides a means of characterizing the bulk plasma but is not adequate for measurements downstream of the plasma boundary since the electron temperature and density rapidly drop off. Additionally, it would not provide means of characterizing the ion beam, which is the primary interest in determining the potential structure and ion acceleration profile. The RPA was then used to measure the downstream ion energy of the beam and background plasma. In determining the continuity of the potential structure, the triple Langmuir probe records the bulk floating potential with respect to ground, which is also used in the calculation of the electron temperature. A sample of the floating potential profile can be seen in Figure 6.17. The raw measurements of the floating potentials in the helicon and superconducting helicon thrusters can be seen in Appendixes E and F, respectively. By assuming steady-state conditions and that the ion flux into the floating probe is equal to the electron flux, then

the plasma potential can be calculated from the floating potential and the electron temperature using equation (3.3). The floating, V_f, and plasma, V_s, potentials versus the RF input power for the helicon and superconducting helicon thrusters are shown in Figure 6.18 and Figure 6.19, respectively. This provides the potentials present in the bulk plasma and will become relevant after the RPA measurement discussion.

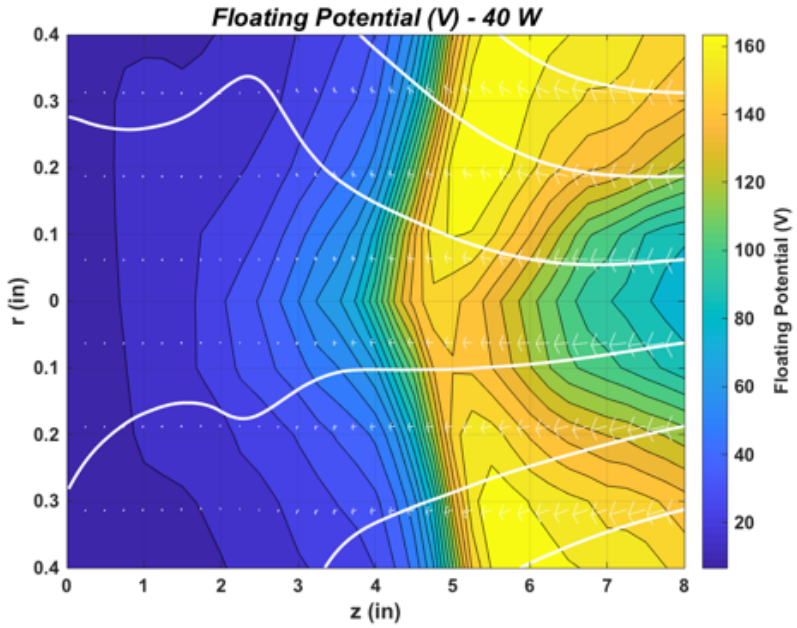

Figure 6.17: Floating potential profile for the helicon thruster at 40 W of RF input power.

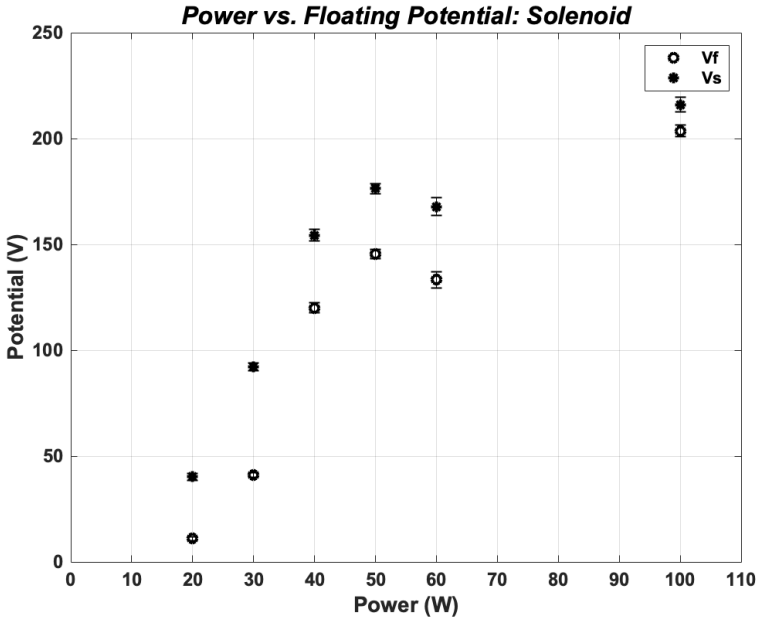

Figure 6.18: Floating and plasma potentials in the bulk plasma for the helicon thruster with 2σ confidence intervals.

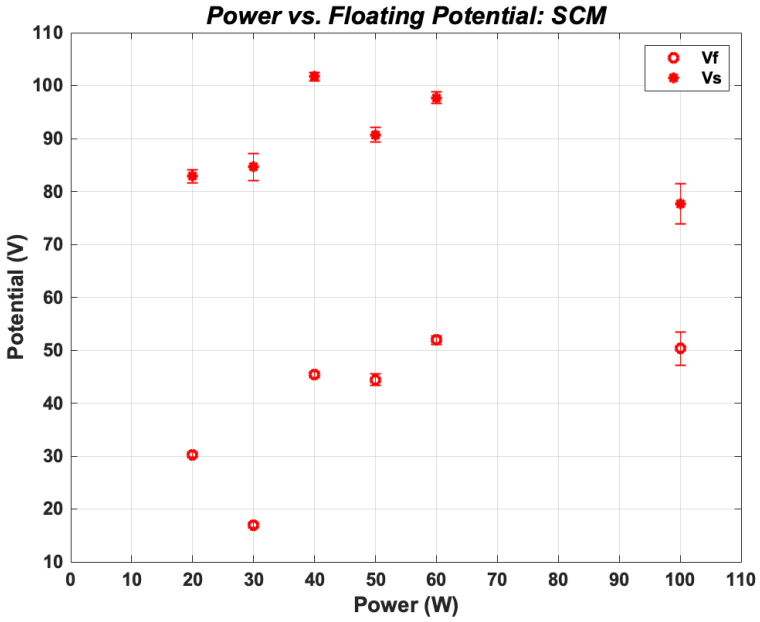

Figure 6.19: Floating and plasma potentials in the bulk plasma for the superconducting helicon thruster with 2σ confidence intervals.

In order to determine an approximation for the thruster performance, the RPA was used to measure the ion energies present in the expansion region where the source tube connects to the inner vacuum chamber walls. The RPA current versus voltage traces for all measurement trials, the corresponding average with standard deviation confidence intervals, and the first derivative of each with respect to the voltage can be seen in Appendix G for the helicon thruster and Appendix H for the superconducting helicon thruster. As stated previously, the first derivative with respect to the voltage represents the IEDF. In the helicon and superconducting helicon thruster, there are two distributions present for each power level. Figure 6.20 is a sample IEDF for the helicon thruster showing the presence of the two distributions. Similar results are seen in comparable devices[90], and are attributed to the beam potential (higher energy distribution) and the bulk plasma potential (lower energy distribution). The lower energy downstream population is formed as a result of beam ion collisions with neutrals. In previous experiments, this was verified by comparing the measured lower RPA energy with the bulk plasma potential as measured by an emissive probe. A summary of the energies measured by the RPA can be seen in Figure 6.21. An additional metric obtained from the RPA current versus voltage traces is the maximum ion current measured on-axis and can be seen in Figure 6.22. In the 50 W and 60 W cases for the superconducting helicon thruster, the raw I-V traces seen in Appendix H show two distinctly different, but repeatable ion current profiles. This could indicate a mode transition region and are averaged based on like profiles as indicated by the two different points in Figure 6.22.

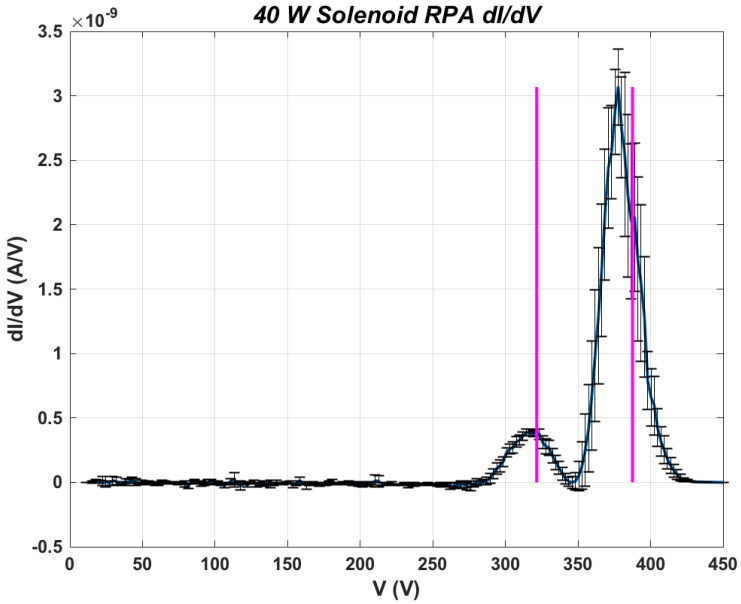

Figure 6.20: Averaged first derivative of the RPA current with respect to the bias voltage for the helicon thruster at 40 W of RF input power.

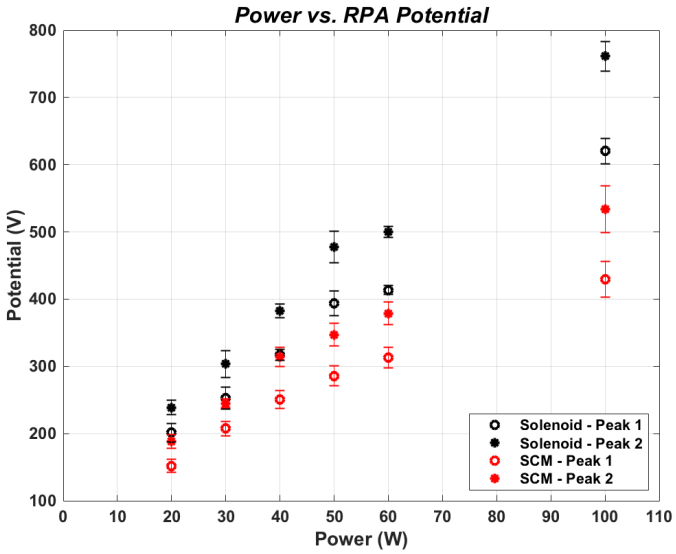

Figure 6.21: Ion energies measured by the RPA for both distributions observed in the IEDFs for the helicon and superconducting helicon thrusters with 2σ confidence intervals.

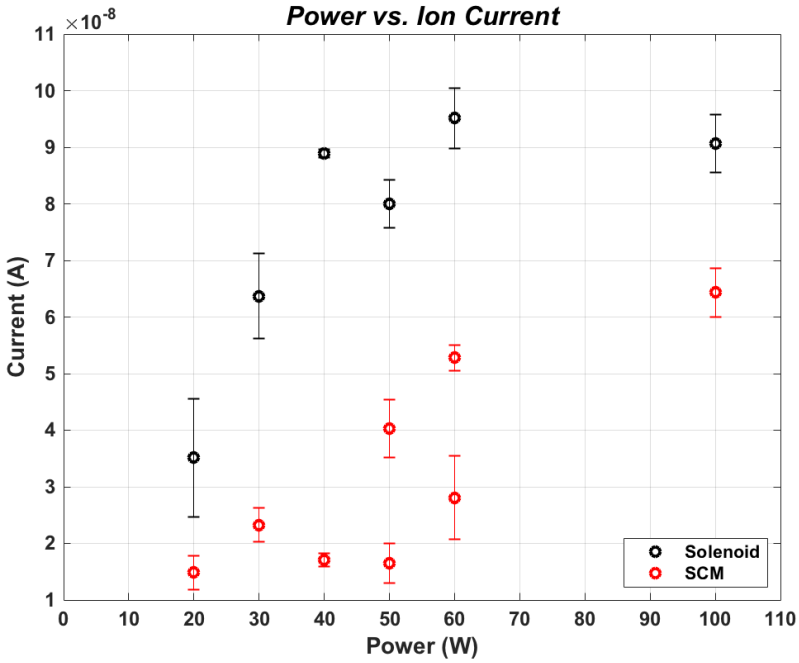

Figure 6.22: Ion currents measured by the RPA for the helicon and superconducting helicon thrusters with 2σ confidence intervals.

Given that the RPA measurements are taken downstream of where the plasma expands into the vacuum chamber, it is possible that the current expands beyond the acceptance area of the RPA aperture. To ensure that the full ion current is collected, or corrected for, in the current versus power plots, a radial sweep of the ion current was performed with the RPA. The current was measured incrementally across a three-inch length centered with the thruster centerline. The current versus voltage plots and first derivative with respect to voltage at 50 W of RF input power for the helicon and superconducting helicon thrusters can be seen in Appendixes I and J, respectively. Using the measured ion currents, the radial profile of the beam was then plotted in Figure 6.23. Since the bulk of the current is contained within a one-inch diameter aperture, the plasma does not expand beyond the source tube diameter. To correct for the spread in the ion current measurements, the total current was obtained by integrating over the radial ion

current profile. This results in a total current of $1.18(10^{-6})$ A in the helicon thruster and $7.24(10^{-7})$ A in the superconducting helicon thruster. Taking the ratio of the total current and the maximum on-axis current from Figure 6.22, yields an expansion factor of 13.3 for the helicon thruster and 10.3 for the superconducting helicon thruster. This expansion factor is assumed to be constant across the various RF input power levels for each device. The corrected ion current versus input power can be seen in Figure 6.24. These ion currents are then used for any further calculations requiring the ion current.

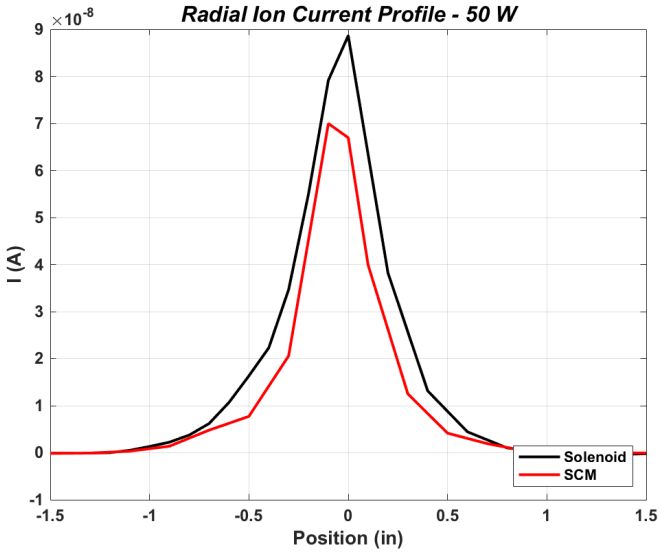

Figure 6.23: Ion current radial profile for the helicon and superconducting helicon thrusters at 50 W RF input power.

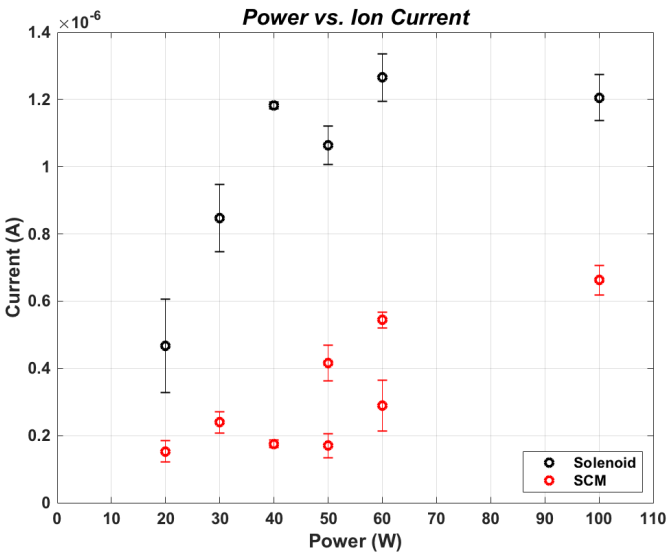

Figure 6.24: Expansion corrected ion currents measured by the RPA for the helicon and superconducting helicon thrusters with 2σ confidence intervals.

6.4 Discussion and System Comparisons

The first major discussion point is the large ion energies measured downstream by the RPA as seen in Figure 6.21. In every case, the ion energies are in excess of 100 eV up to nearly 800 eV. Other studies report beam energies under 100 eV[90,94,95,96,97,98,99], with a few exceptions above 100 eV[91,100]. In the studies with large measured beam energies, the measured potential is compared to that calculated using Boltzmann, or ambipolar, expansion. The density and plasma potential relations for Boltzmann expansion are as follows.

$$n_e(z) = n_{s,0} e^{\frac{e(V_s(z) - V_{s,0})}{kT_e}} \tag{6.6}$$

$$V_s(z) = V_{s,0} + \frac{kT_e}{e} \ln\left(\frac{n_e(z)}{n_{s,0}}\right) \tag{6.7}$$

Here, the subscript naught refers to the respective parameter in the bulk plasma. If the calculated electron temperature using plasma potential and density measurements

exceeds the electron temperature measured using a Langmuir probe, then Boltzmann expansion is not sufficient to account for the acceleration of the ion beam. Initially, the discrepancy in the measured beam potential was attributed to ion-neutral charge-exchange collisions[91]. As the RPA is moved farther from the plasma expansion region of the diverging magnetic field, the ratio of distance to mean free path for charge-exchange increases. Since the charge-exchange collision cross-sections have a dependency on energy, ions in the lower tail of the IEDF are preferentially lost due to the charge-exchange collisions and become part of the low energy background distribution. This effect can be seen in Figure 6.6.

In a follow-up study, further measurements of anomalous acceleration were attributed to the self-bias effect. Since the ratio of the electron plasma frequency to the RF frequency is much larger than the ratio of the ion plasma frequency to the RF frequency, electrons are able to transit the acceleration region and system length within an RF period, whereas the ions are unable to respond to the changes in the plasma potential[100]. This results in an imbalance of particle flux that yields a self-biased potential difference over the acceleration region that inhibits electron flow and simultaneously increases ion flow. This is more prevalent in the E-mode coupling of the RF power to the plasma since lower densities correspond to a larger skin depth, thus less ion shielding from the RF fluctuations of the antenna. As the density increases, and the coupling mode transitions, the skin depth decreases, shielding the ions and reducing the self-bias effect. Furthermore, the sheath drop at the exit plane is set by the grounded wall boundary condition. In situations where the boundary condition is that of an insulating glass wall, like the focus of this dissertation, larger self-bias potential differences can be supported.

To quantify the impact of charge-exchange collisions on the downstream measured ion energies, the model by Rapp and Francis[101] for the charge-exchange cross-sections of argon as a function of energy is used to determine the charge-exchange mean free path as shown in Figure 6.26. The mean free path for charge-exchange collisions is calculated as follows:

$$\lambda_{CX}(z) = \frac{1}{n_n \sigma_{CX}} \tag{6.8}$$

where the beam energy, or difference in the potential of the two distributions measured by the RPA, is used to determine the charge-exchange collision cross-section, σ_{CX}. A plot of the beam energy versus input RF power can be seen in Figure 6.31. Here, the neutral density in the vacuum chamber is calculated using the background chamber pressure, $5.5(10^{-5})$ Torr, the pumping speed of the turbo pump, 2100 L/s, and the volumetric flow rate of the propellant, 3.1 sccm. The results in a neutral density of about $2.5(10^{18})$ m^{-3}. The calculated mean free paths for each input power level can be seen in Figure 6.27. Given that the mean free path for charge-exchange collisions is large compared to the measurement length scale, it is unlikely that this significantly impacts the measured downstream IEDF due to the low neutral density in this region.

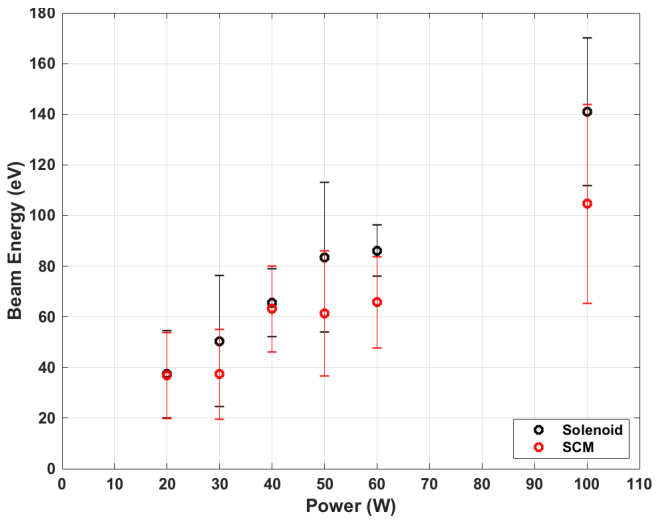

Figure 6.25: Beam energies given as the difference in energy between the two distributions measured by the RPA.

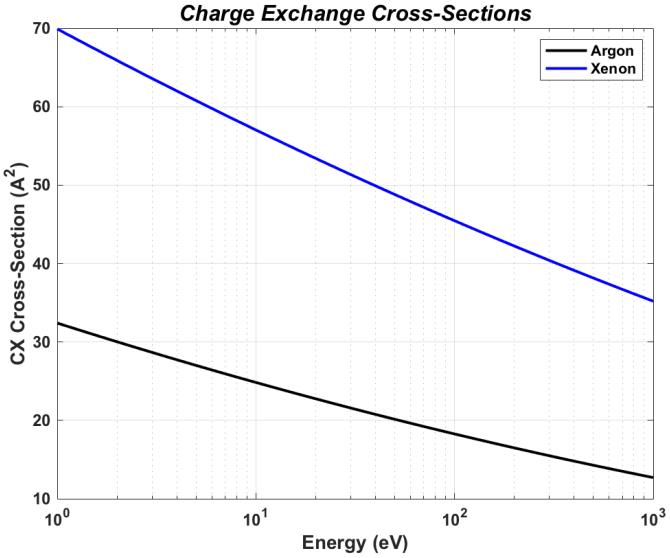

Figure 6.26: Argon and xenon collision cross-sections as a function of energy from the model by Rapp and Francis[101].

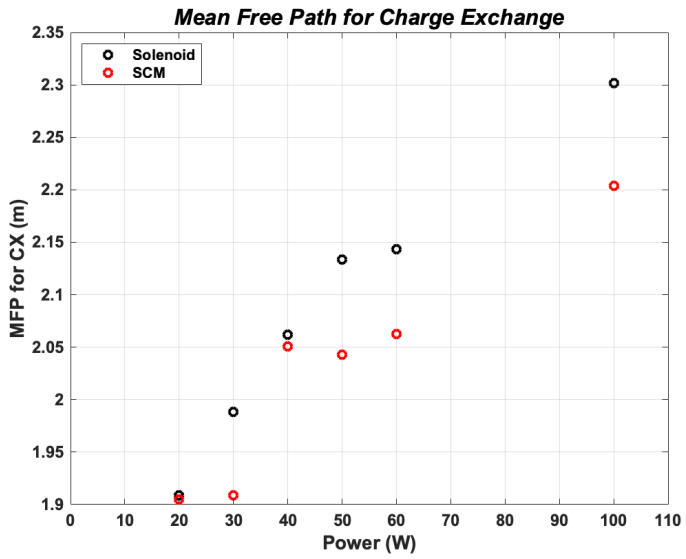

Figure 6.27: Mean free path for charge-exchange collisions.

To see the impact of Boltzmann expansion, equation (6.7) is used to calculate the electron temperature required to provide enough of a potential difference to accelerate the beam to the measured potentials. The beam ions are assumed to be accelerated over the potential difference between the beam population and the background population measured by the RPA. The upstream plasma density used is that calculated using the triple Langmuir probe data provided in Figure 6.16 and can be seen in Figure 6.28. The downstream plasma density is calculated using the ion current measured by the RPA provided in Figure 6.24 and is given by equation (6.9), derived from the particle flux entering the RPA.

$$n_{RPA} = \frac{I_{RPA}}{A_{RPA}\eta_{tr}e\sqrt{\frac{2e(V_{beam} - V_s)}{m_i}}} \tag{6.9}$$

The electron temperature required to accelerate the ions strictly from Boltzmann expansion compared to the upstream electron temperature measured by the triple Langmuir probe can be seen in Figure 6.29 and Figure 6.30. In each instance, with the

exception of the 100 W power levels, the measured electron temperature is sufficiently large enough to account for the separation of the beam ions from the background population measured by the RPA. Since the measured bulk electron temperature is larger than the electron temperature from Boltzmann expansion, it is likely that additional power is consumed to further heat the electrons.

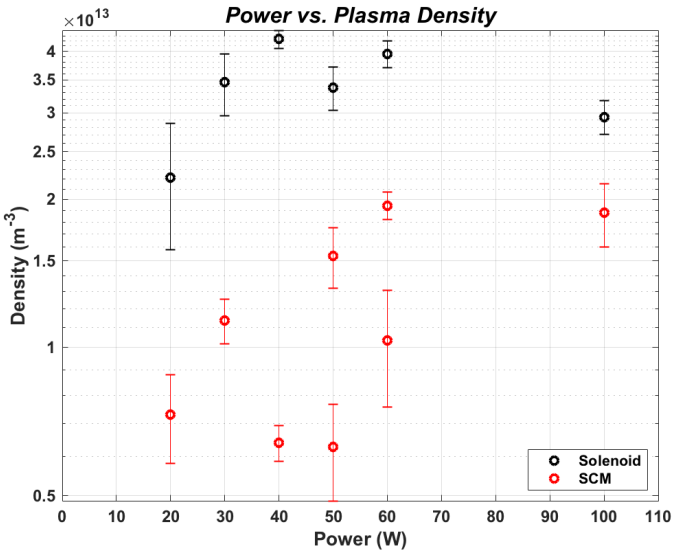

Figure 6.28: Downstream plasma density calculated using the RPA measured ion current.

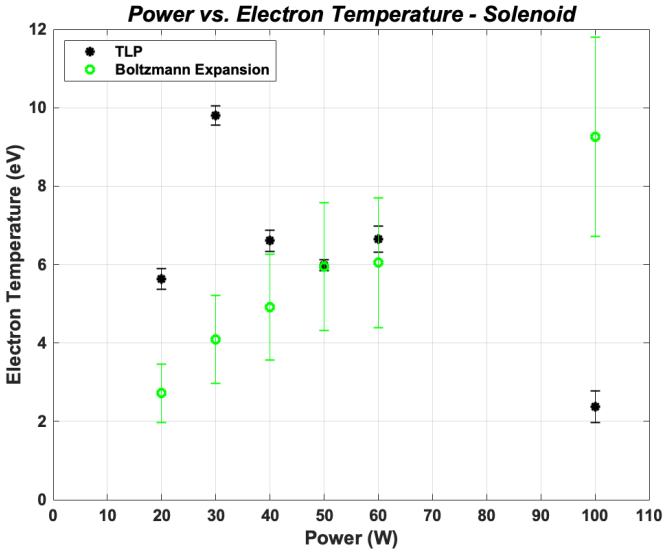

Figure 6.29: Bulk electron temperature compared to the electron temperature required to accelerate the ions to the beam potential measured by the RPA in the helicon thruster.

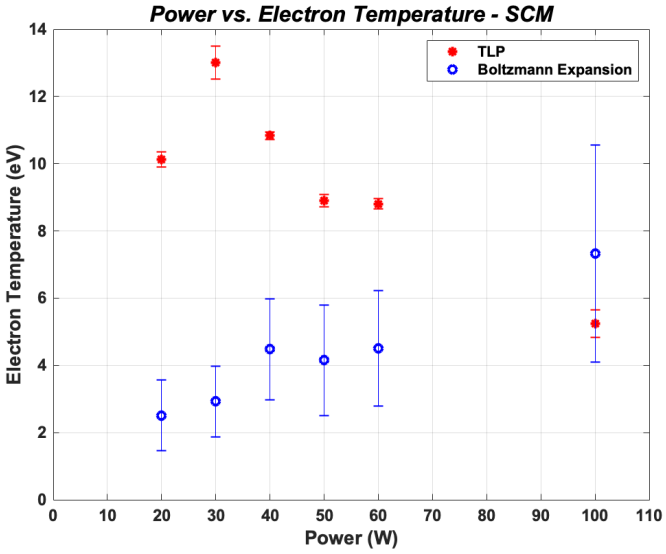

Figure 6.30: Bulk electron temperature compared to the electron temperature required to accelerate the ions to the beam potential measured by the RPA in the superconducting helicon thruster.

The large potentials measured by the RPA are the primary focus of the anomalous acceleration. While Boltzmann expansion is sufficient to account for the accelerated beam ions from the background potential measured by the RPA, the primary discrepancy

is that the background population is still of a significantly higher potential than the bulk plasma potential calculated using floating potentials measured by the triple Langmuir probe (as shown in Figure 6.18 and Figure 6.19 compared to Figure 6.21). It is likely that both the beam and background populations were accelerated collectively from the plasma boundary to the expansion region where the source tube opens into the vacuum chamber, given that the region downstream of the plasma boundary is likely to be collisionless due to the low densities measured by the RPA. This indicates that the particles contributing to thrust might not just include the beam but also the lower energy, background population. This leaves the region along the source tube between the plasma boundary and the vacuum chamber expansion region as the region where the acceleration likely occurs.

Figure 6.31 illustrates the acceleration region in question along with the magnetic field strength and streamlines. Since the boundary walls leading up to the vacuum chamber are insulating, and the magnetic field lines terminate on this boundary, it is possible that electrons collect on this boundary leading to a charged wall condition where the potential is a function of the axial location. In order for this to be possible, the electrons must be magnetized, meaning the electron Larmor radius is small compared to the device radius. Given the conditions measured by the triple Langmuir probe, the electrons can be considered magnetized as seen in the scaling plots of Appendices K and L. Additionally, since the skin depth is not negligibly small, also seen in Appendices K and L, it extends into the bulk plasma such that the magnetized boundary electrons are subject to further heating from the RF antenna. The final set of scaling plots shown in Appendices K and L indicate that the ratio of the ion plasma frequency to the RF frequency is small compared to the ratio of the electron plasma frequency to the RF

frequency. From the study discussed above, this means that the ions within the skin depth are less capable of responding to the RF fluctuations from the antenna and can form a self-bias potential contributing to the acceleration of the ions.

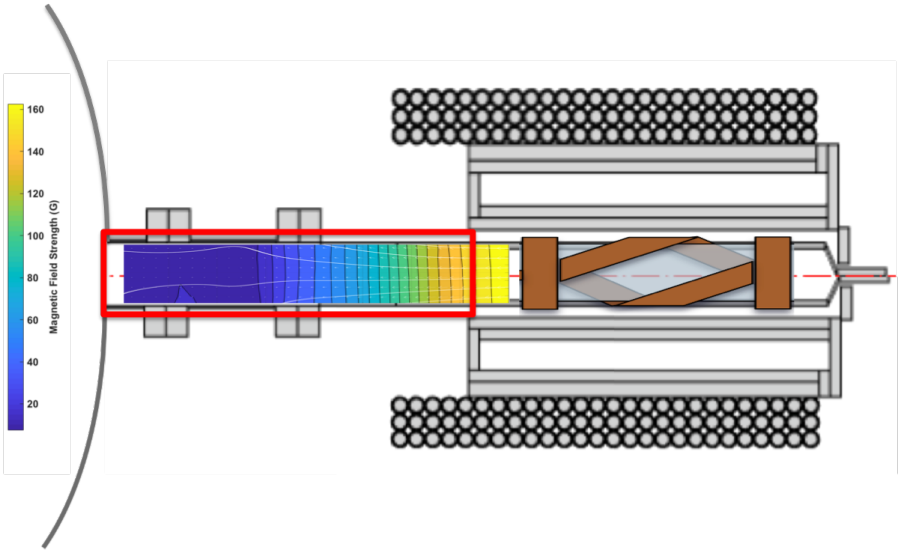

Figure 6.31: Thruster diagram with acceleration region, shown in red box, and magnetic field measurements.

One of the consequences of the magnetized electrons within the skin depth is further power deposition to heat these electrons. This is supported with the electron temperature measurements in Appendices A and B, as well as reports found in the literature [102]. The radial cuts of the electron temperature profiles indicate that the boundary electrons are of a higher temperature than those residing in the bulk. The magnetized electrons closer to the boundary wall will intersect the boundary farther upstream than the cooler electrons closer to the thruster centerline. This leads to more larger wall potentials upstream that decrease along the wall in the downstream direction. Since the boundary wall is an insulator and not grounded, the potential conditions are not fixed and likely set by the upstream boundary conditions within the plasma. This

effectively forms a hemispherical potential structure as seen in the floating potential profile shown in Appendices E and F. An example of the hemispherical potential structure can be seen in Figure 6.17. This has also been observed and is supported by studies found in the literature[95]. Furthermore, larger potentials along the boundary magnetic field lines have been shown to result in high density conical regions in the expansion region of the plasma[96]. The ions diverge more rapidly due to potential difference resulting from the separation of charge as the hot boundary electrons diverge with the magnetic field. The large ion energies measured by the RPA are thus likely due to the fact that the majority of the low energy ions are lost to the boundary wall in the acceleration region, where the high energy, axial ions capable of traversing the plasma boundary without RF influence are further accelerated by the resulting axial potential difference. These high energy, accelerated ions are then collected downstream by the RPA.

Similar conditions have been investigated with comparable results[99]. In this study, an insulating glass tube was placed at the expansion region of an RF plasma. This caused the geometric expansion region to shift farther downstream from the magnetic expansion region, not unlike the conditions presented herein. Higher ion population energies were reported in instances with the insulating glass tube. The authors maintain that the larger potentials could imply that the extension piece anisotropically charges where the magnetic field terminates, much like what is discussed above, however, this is the subject of ongoing research. While the measured ion energies are substantially less in the Bennet study[99], the scale of their device is much larger than the one in this study. It is likely that the effects of the anomalous acceleration scale inversely with the device size. While a

qualitative model has been presented to explain the large ion populations measured by the RPA, the comparatively large energies warrant investigations outside the scope of this analysis. This will be further detailed in the Future Work section of Chapter 7.

A direct comparison of the superconducting helicon thruster and baseline helicon thruster show comparable plasma characteristics. Beginning with the triple Langmuir probe measurements for the electron temperature and plasma density, larger electron temperatures, and subsequently smaller densities, are seen in the superconducting helicon thruster case. As mentioned in the previous section, this indicates that a larger fraction of the input RF power is consumed to heat the electrons further than the baseline helicon thruster. As such, less power is directed towards ionization, resulting in lower plasma densities. The equation for thrust is given as follows:

$$F = \dot{m} f_{ion} u_e \tag{6.10}$$

In this equation, the ionization fraction, f_{ion}, scales proportionately with the density and the exit velocity, u_e, in the case of a plasma sheath, scales with the square root of the electron temperature. Consequently, thrust scales more favorably with the electron density, meaning that the baseline helicon thruster will slightly outperform the superconducting helicon thruster. This is further seen in the RPA data.

Given that the beam energies shown in Figure 6.25, also indicate more energetic beams for the baseline helicon thruster at larger input powers further suggests a slight improvement over the superconducting helicon thruster. Additionally, the anomalous acceleration seen in the RPA data is less pronounced for the superconducting helicon thruster. Given the explanation provided for the anomalous acceleration, it is very likely that the decrease in performance is linked to the magnetic field geometry. Since the

superconducting helicon thruster demonstrates a more rapid divergence in the magnetic field, the axial potential profile that forms the acceleration region could scale to a shorter length. Furthermore, a more divergent magnetic field could result in more rapid plasma detachment such that the electrons no longer remain magnetized and do not form as large of an ambipolar electric field. While a more collimated beam is ideal to inhibit divergence of the plume, if the particles are not accelerated as a result of the intersection of the magnetic field lines with the source walls, then performance would drop off further. The floating downstream conditions on the equipotential magnetic field lines terminating on the boundary wall would also impact the plasma characteristics upstream. This could also explain the differences in electron temperature and density seen in the triple Langmuir probe data.

To compare the performance of the two systems, the thrust and specific impulse were calculated using equations (6.10) and (1.2), respectively. To calculate the ionization fraction, the maximum measured density (single data point) of all triple probe density data was used to approximate the upstream neutral density. The plasma densities shown in Figure 6.16 were then divided by this approximate neutral density, or $3.66(10^{20})$ m^{-3}. The resulting ionization fractions can be seen in Figure 6.32. The volumetric propellant flow rate was 3.1 sccm, corresponding to a mass flow rate of $9.25(10^{-8})$ kg/s. The exit velocity was then calculated using the RPA measured beam energies seen in Figure 6.25 using the following equation.

$$u_e = \sqrt{\frac{2e(V_{beam} - V_s)}{m_i}} \tag{6.10}$$

Figure 6.33 shows the performance metric comparisons for the two devices. As was evident with the qualitative analysis of the diagnostic measurements, the superconducting helicon thruster is slightly outperformed by the baseline helicon thruster for higher RF input powers. Given the scale of the metrics, the systems are still relatively comparable, and, in many instances, the superconducting helicon thruster is still advantageous given the motivation for the entirety of this analysis.

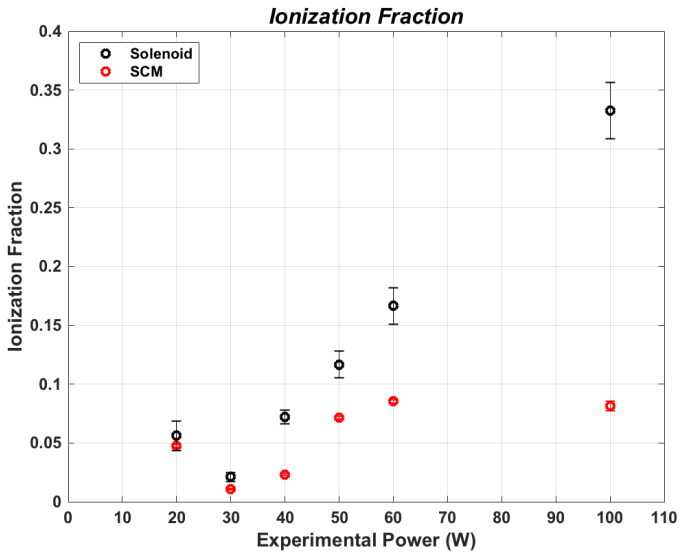

Figure 6.32: Ionization fraction as a function of the plasma density measured by the triple Langmuir probe and approximate upstream neutral density.

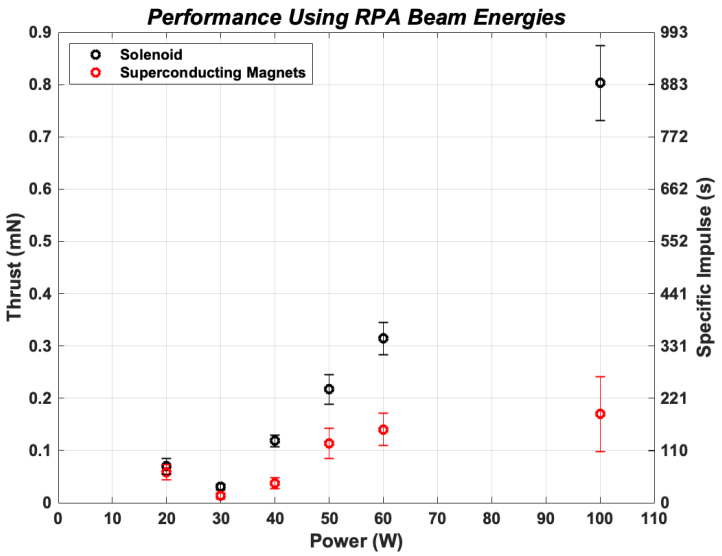

Figure 6.33: Helicon thruster and superconducting helicon thruster performance metrics.

The goal of this study was to investigate the efficiency benefits of using a superconducting magnet system for a helicon thruster. While the performance metrics slightly favor the baseline helicon thruster, comparable performance with power mitigation benefits would provide instances where the superconducting helicon thruster is more beneficial. Using the efficiency analysis from Chapter 3 and the electron temperature measurements from the triple Langmuir probe, the expected efficiency of the two systems can be calculated and is seen in Figure 6.34. It is important to note that the baseline helicon thruster does account for the continuous power that must be supplied to the electromagnet. From an efficiency point, the superconducting helicon thruster is more advantageous than the baseline helicon thruster. Provided the thermal management subsystem is properly developed, the on-board power requirements can be mitigated using the superconducting helicon thruster since continuous power to the electromagnet is no longer necessary. While the efficiencies are still largely less than current state-of-the-art thrusters, the helicon thruster advantages outlined previously make it attractive for

further development. Further investigation into the anomalous acceleration of the ions could provide means of improving the performance of both helicon and superconducting helicon thrusters.

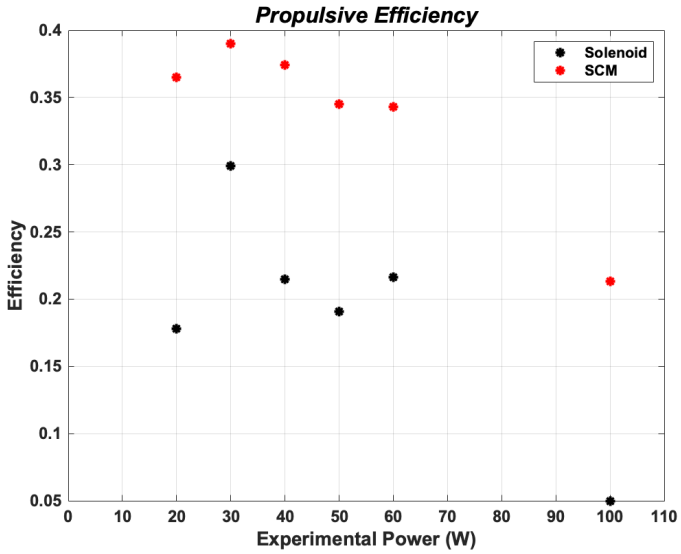

Figure 6.34: Helicon thruster and superconducting helicon propulsive efficiency.

7. Chapter 7: Conclusion and Future Work

7.1 Summary of Results and Contributions

A complete superconducting helicon thruster system has been presented and characterized in comparison to the traditional, baseline helicon thruster. The primary objective of the study was to identify how the efficiency of the helicon thruster would be improved if a superconducting magnet system was used in place of the electromagnet. To begin, an efficiency analysis was performed to identify the impact of mitigating the power requirement on the electromagnet using helicon thruster compared to the superconducting helicon thruster. This analysis identified that the primary driving term in the efficiency determination is the power draw to the sheath. For typical electron temperatures of 10 eV, the power draw to the electromagnet accounts for 3% of the total power. Using electron temperature and ion beam energy measurements, this was shown to be more substantial due to the differences in the magnetic field geometry that results in larger electron temperatures. In the case of the sheath acceleration model, the acceleration profile is highly dependent upon the electron temperature, thus resulting in further efficiency improvements. This serves as the first major contribution to the state-of-the-art.

Following the analytic efficiency analysis, a design for the superconducting helicon thruster was proposed with in-space platform considerations for the superconducting magnet subsystem and the thermal management subsystem. The purpose of the superconducting magnet subsystem was to provide a magnetic field geometry, optimized with confinement considerations from the efficiency analysis. It was then

shown experimentally that the magnetic field from a solenoid can be maintained by a superconducting tube below its critical temperature without the necessity of constant input power. The magnetic field geometry was nearly consistent between the two magnets with the exception of a more rapidly diverging magnetic field in the superconducting magnet case due to a shorter source length. With the superconducting magnet subsystem, a COMSOL Multiphysics model is presented that accurately predicts the magnetic field topology of a tube shaped superconductor at steady state. In order to accommodate the thermal requirements of the superconductors, a thermal management subsystem was also proposed in order to maintain cryogenic temperatures for in-space applications in a closed-loop manor. This design served the purpose of guiding the test of a laboratory model for the superconducting helicon thruster. In practice, an open-loop cooling system was used in order to maintain cryogenic temperatures through the testing. This is a novel approach to power loss mitigation for helicon thrusters that also has potential scientific ramifications in that magnetic fields can be achieved at no Ohmic power dissipation, where the topology of the field is only limited to the manufacturing limitations of solid superconducting material. This design and analysis serve as the second major contribution to the state-of-the-art.

Experimentally, a triple Langmuir probe and retarding potential analyzer (RPA) were used to characterize the plasma. The triple Langmuir probe data demonstrated that a larger fraction of the input RF power was used to heat the electrons in the superconducting helicon thruster case. Consequentially, this yielded a lower plasma density within the bulk plasma. The downstream ion energies were measured with the RPA and showed slightly lower energies in the superconducting helicon thruster than in

the baseline helicon thruster. The ion energies measured were still substantially larger than any reported in the literature. A model to explain this anomalous ion acceleration was proposed and will be the subject of future work. Using the measured electron temperature and ion energies, it was shown that the baseline helicon thruster demonstrates slight better performance metrics, however this comes at the cost of lower propulsive efficiencies. In instances where maximum thrust and maximum specific impulses are desired, the baseline helicon thruster would be more advantageous. If RF input power mitigation is of larger concern, the superconducting helicon thruster outperforms the baseline helicon thruster. This is the first study to detail and characterize the plasma parameters of such a thruster and how it impacts the baseline design of conventional helicon thrusters, and serves as the third major contribution to the state-of-the-art. This could also be linked to the anomalous ion acceleration and will warrant further investigation to verify the mechanism behind the large ion energies measured using the RPA. While large beam ion energies have been observed, the energies measured in this study far exceed those reported in the literature. As such, the discovery of this anomalous acceleration mechanism provides yet another contribution to the state-of-the-art due to the potential ground-breaking application this would have on the performance of the helicon thruster. Lastly, this research provides a test-bed for future in-situ resource utilization applications, particularly, for water vapor propellant usage.

7.2 Future Work

The primary focus of future work would focus on the anomalous acceleration mechanism discussed in Chapter 6. The large emergent ion energies measured by the

RPA are substantially larger than any reported in literature. Understanding the true mechanism and verifying the proposed model would improve the understanding of the downstream plasma characteristics of a helicon plasma. Additionally, if the mechanism can be reproduced for an on-orbit helicon thruster platform, then the helicon thruster could potentially emerge as a competitor with the ion engine and Hall effect thruster. While the triple Langmuir probe serves as a good diagnostic for the bulk plasma, and the RPA can be used to characterize the ion beam, a different diagnostic should be used to characterize the acceleration region between the bulk and expanded plasma. Two such diagnostics that could be utilized are the emissive probe and flush mounted Langmuir probe.

The emissive probe is a diagnostic tool that is used to measure the local plasma potential. Knowing the evolution of the plasma potential from the bulk plasma to the downstream expansion measured by the RPA would provide a vital understanding as to where the actual ion acceleration takes place. Having a two-dimensional contour of the plasma potential, much like what was done in this study with the electron temperature, would allow for verification of the proposed acceleration model. If the potential contours correspond to the divergence of the magnetic field, then we can gain an understanding of how the magnetic field contributes to ion acceleration. Additionally, a flush mounted Langmuir probe system would help provide an understanding about the charging of the insulating boundary walls. By using a ceramic insert with a flush, metal probe, wall potential measurements can be made at several points along the axis of the source tube. This may provide a clearer understanding of the axial dependence of the plasma parameters that may contribute to ion acceleration. If the proposed acceleration

mechanism is verified, then a design can be produced that would take advantage of the ion acceleration to improve the state-of-the-art helicon thruster.

Further research with the superconducting helicon thruster would be investigation of the plasma characteristics with water vapor propellant. Since the helicon thruster is very amenable to water vapor, understanding the performance metrics using water vapor would provide an excellent test bed for future in-situ resource utilization technologies. Additionally, if the anomalous ion acceleration is characterized and well understood, then knowing its impact with water vapor propellant would help contribute to the further development of the technology.

Appendix A: Helicon Thruster Triple Langmuir Probe Data – Electron Temperature

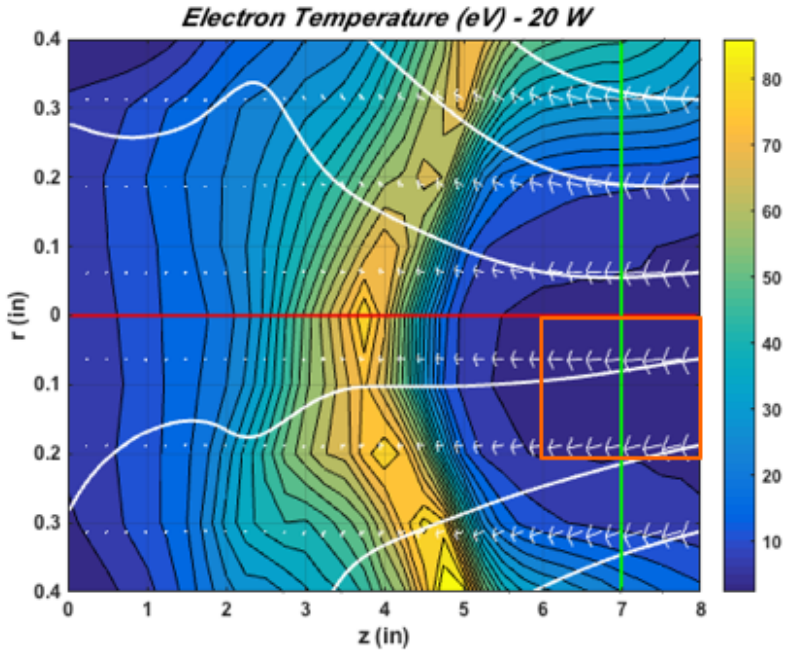

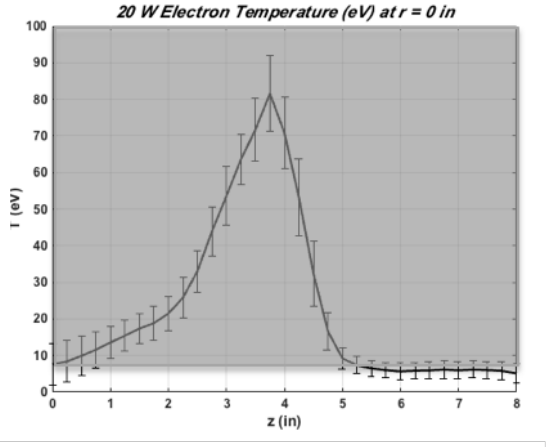

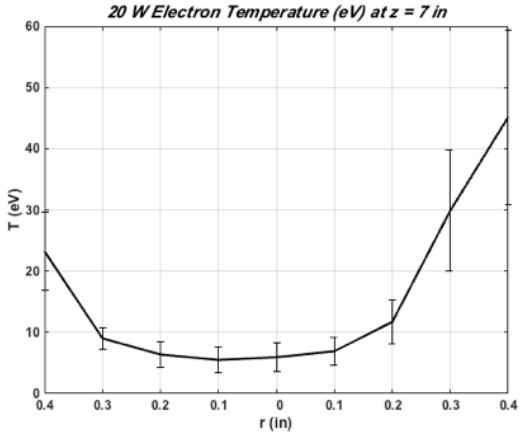

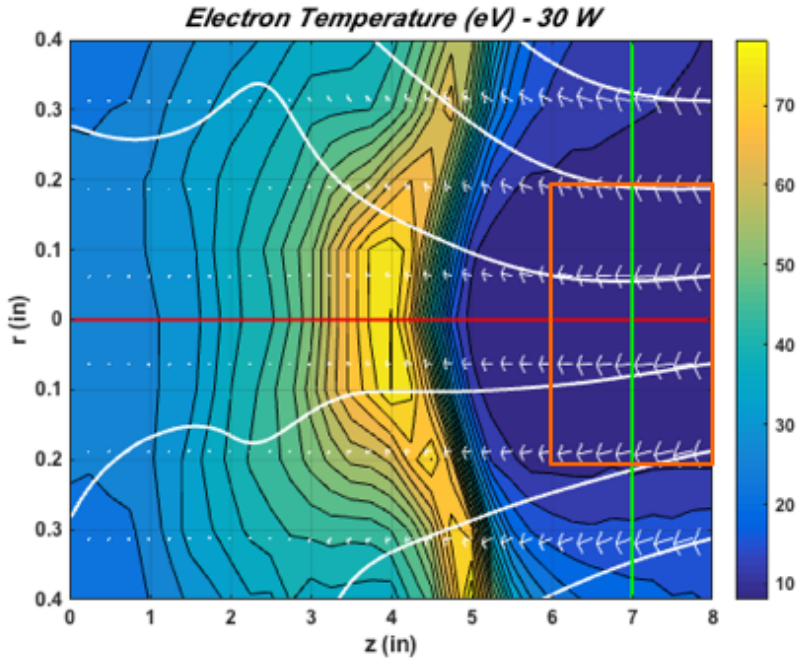
Electron Temperature (eV) - 30 W
r (in)
z (in)

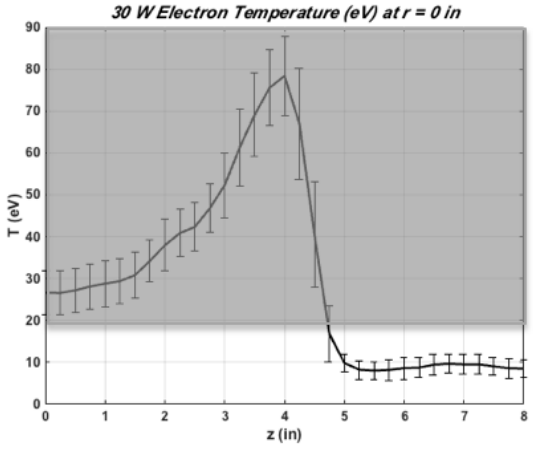
30 W Electron Temperature (eV) at r = 0 in
T (eV)
z (in)

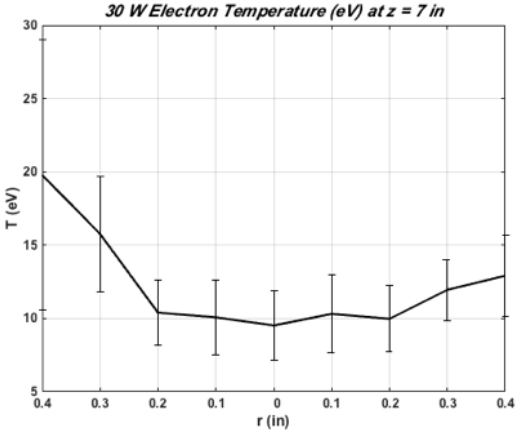
30 W Electron Temperature (eV) at z = 7 in
T (eV)
r (in)

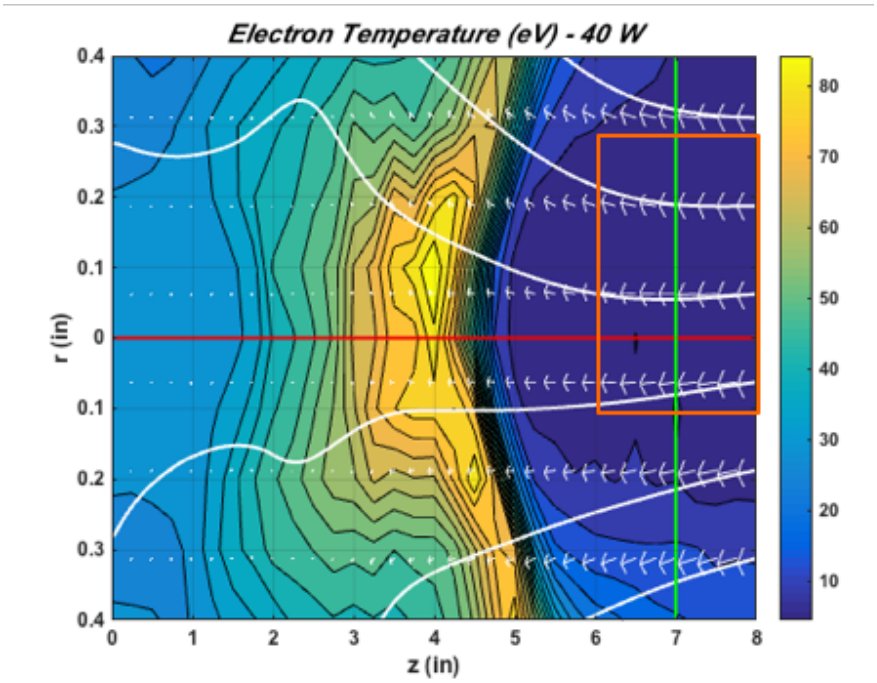
Electron Temperature (eV) - 40 W
r (in)
z (in)

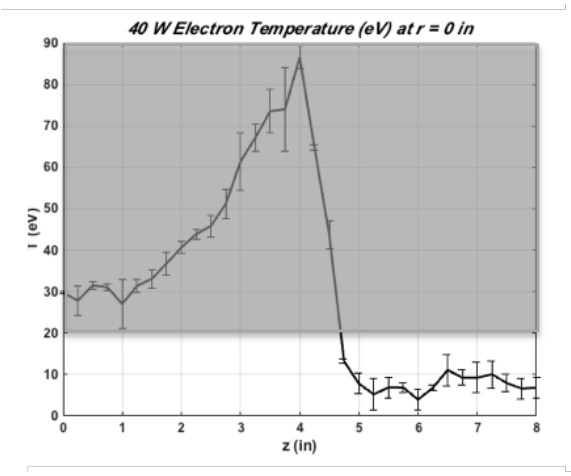
40 W Electron Temperature (eV) at r = 0 in
T (eV)
z (in)

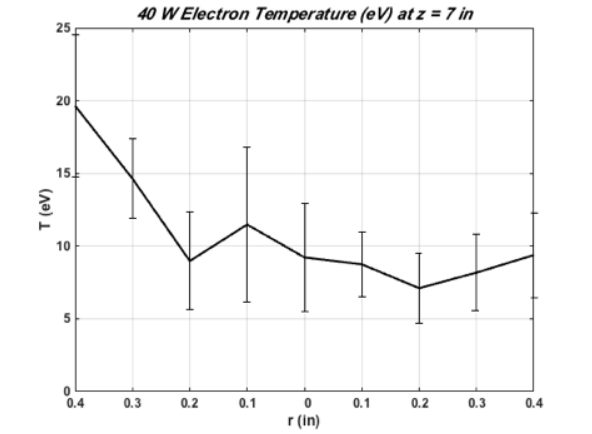
40 W Electron Temperature (eV) at z = 7 in
T (eV)
r (in)

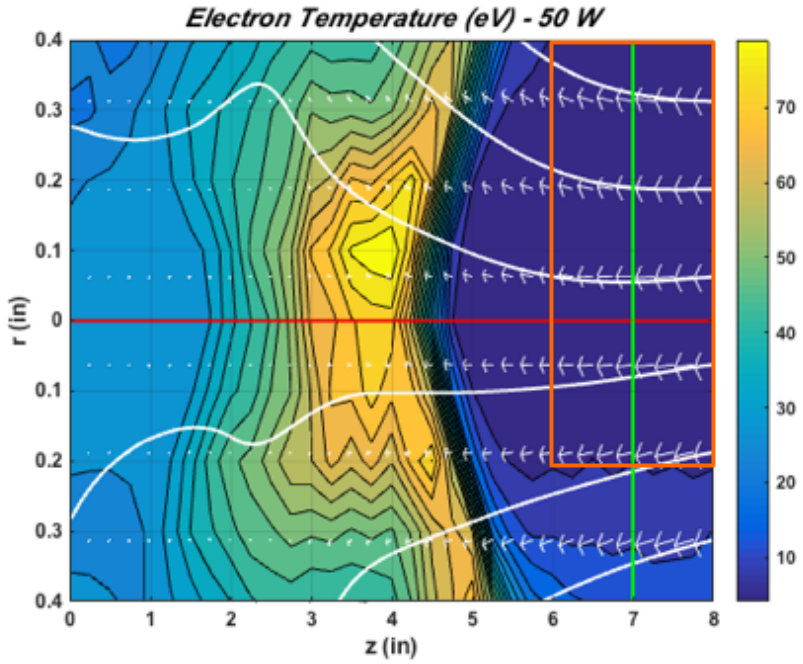
Electron Temperature (eV) - 50 W
r (in)
z (in)

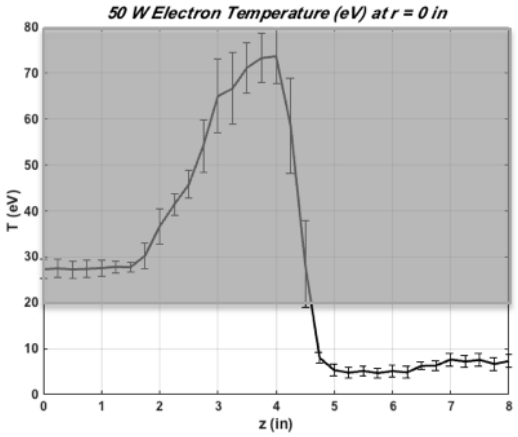
50 W Electron Temperature (eV) at r = 0 in
T (eV)
z (in)

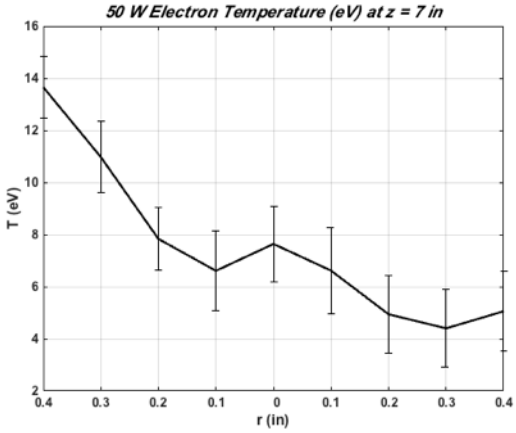
50 W Electron Temperature (eV) at z = 7 in
T (eV)
r (in)

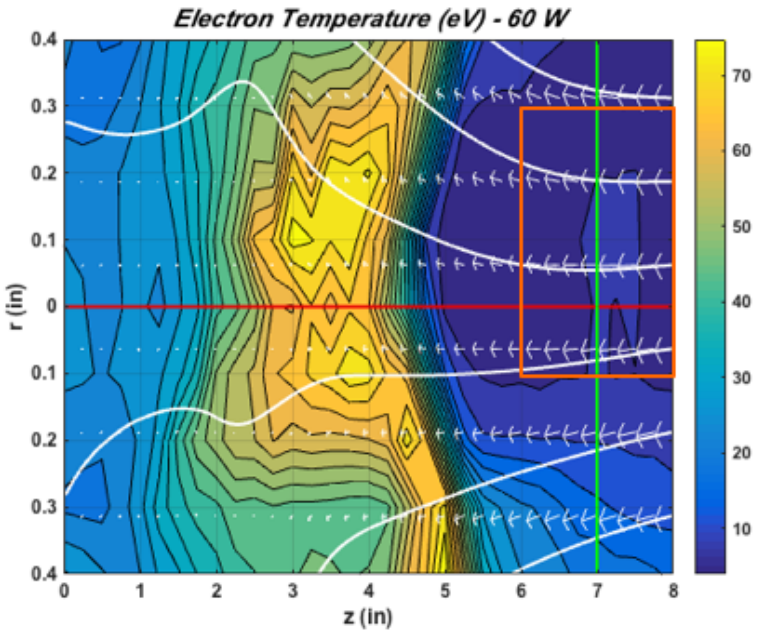
Electron Temperature (eV) - 60 W
r (in)
z (in)

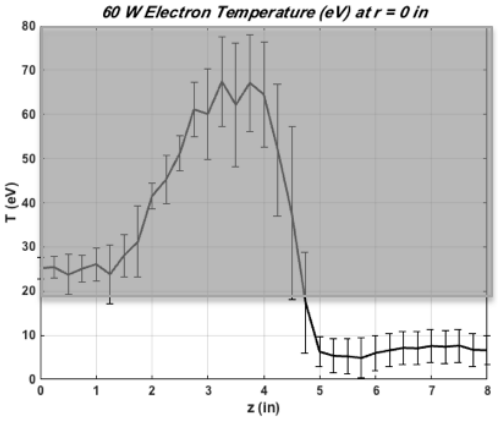
60 W Electron Temperature (eV) at r = 0 in
T (eV)
z (in)

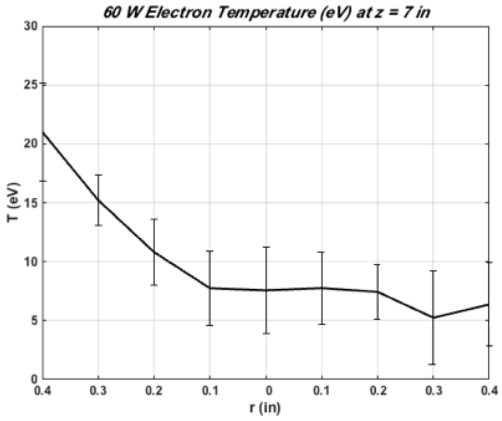
60 W Electron Temperature (eV) at z = 7 in
T (eV)
r (in)

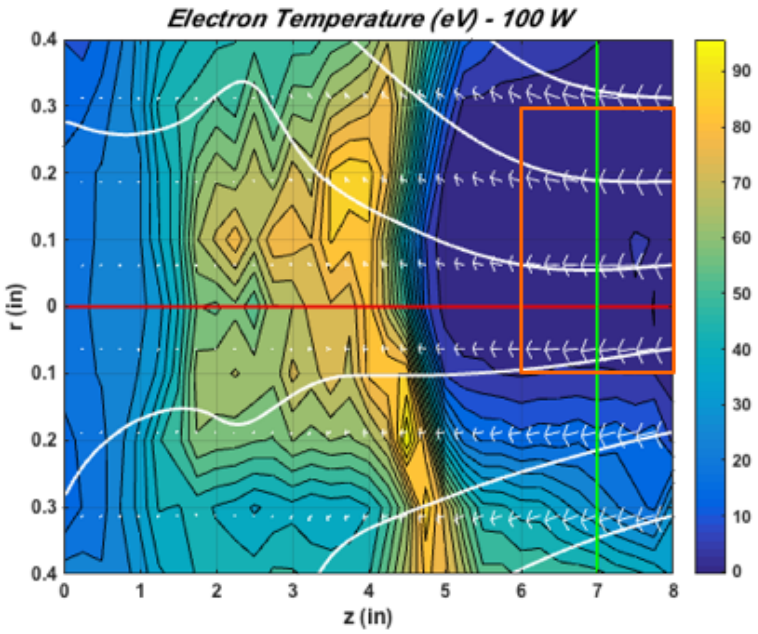
Electron Temperature (eV) - 100 W
r (in)
z (in)

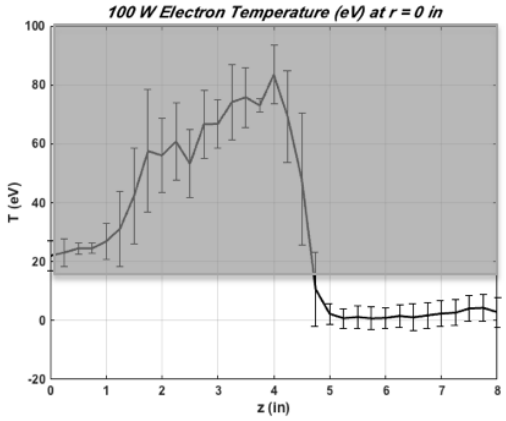
100 W Electron Temperature (eV) at r = 0 in
T (eV)
z (in)

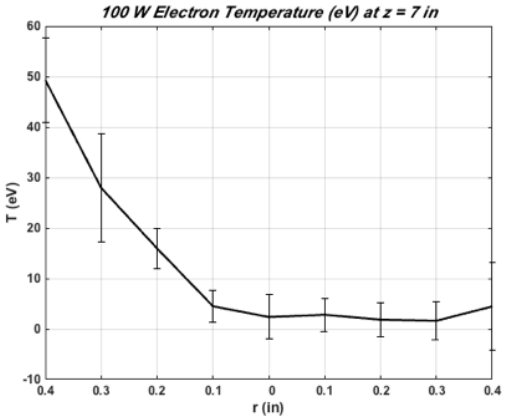
100 W Electron Temperature (eV) at z = 7 in
T (eV)
r (in)

Appendix B: Superconducting Helicon Thruster Triple Langmuir Probe Data – Electron Temperature

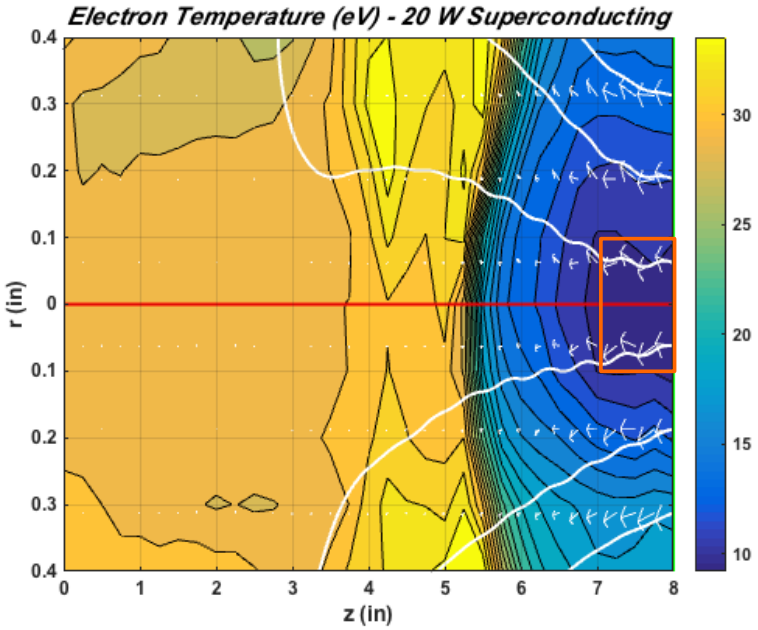

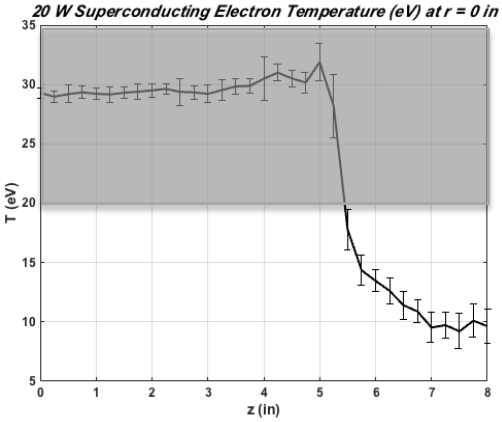

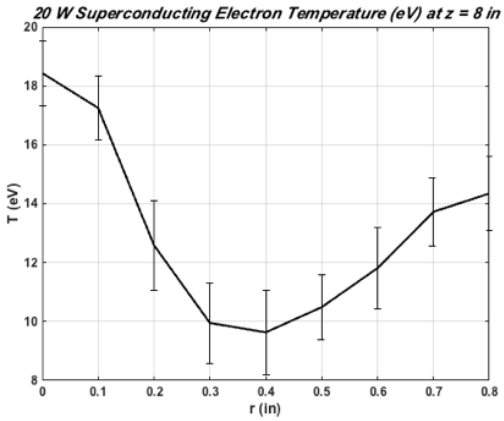

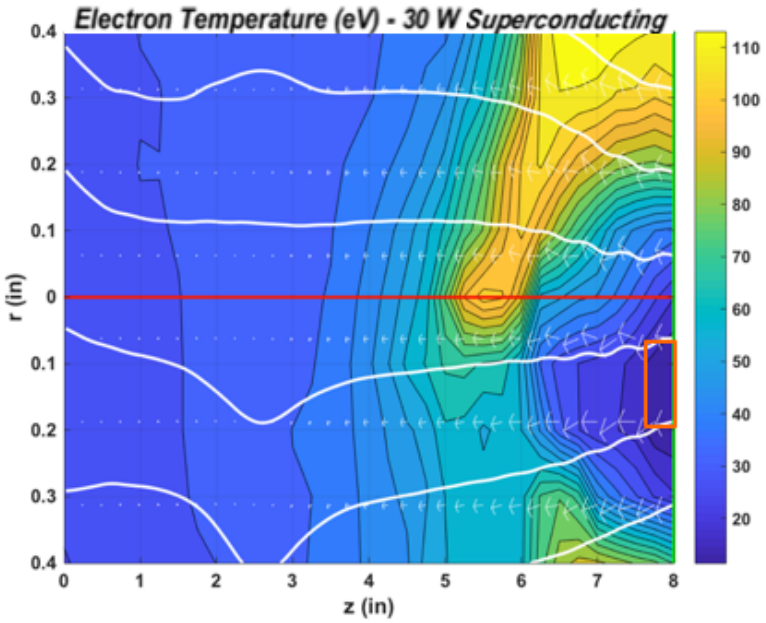
Electron Temperature (eV) - 30 W Superconducting
r (in)
z (in)

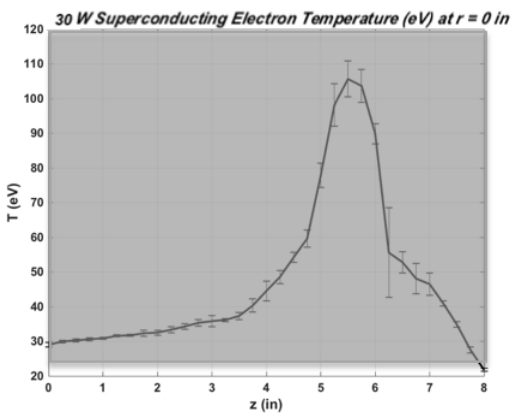
30 W Superconducting Electron Temperature (eV) at r = 0 in
T (eV)
z (in)

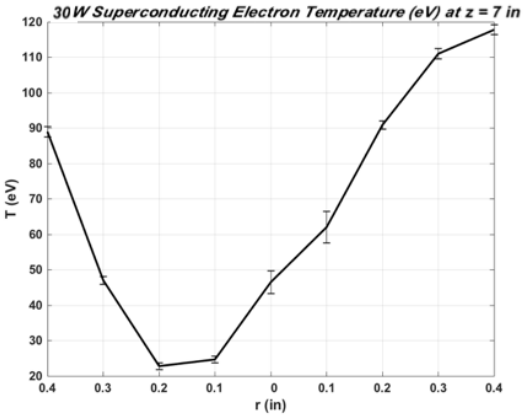
30 W Superconducting Electron Temperature (eV) at z = 7 in
T (eV)
r (in)

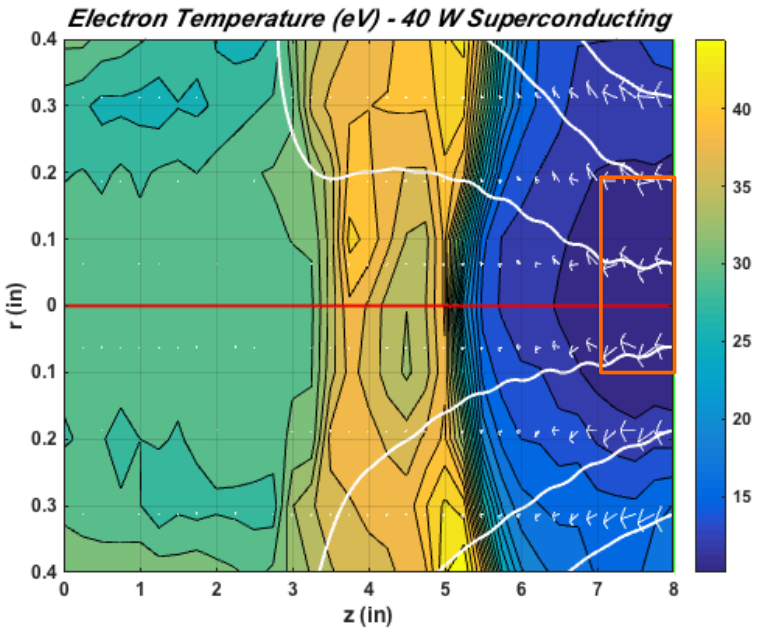
Electron Temperature (eV) - 40 W Superconducting
r (in)
z (in)

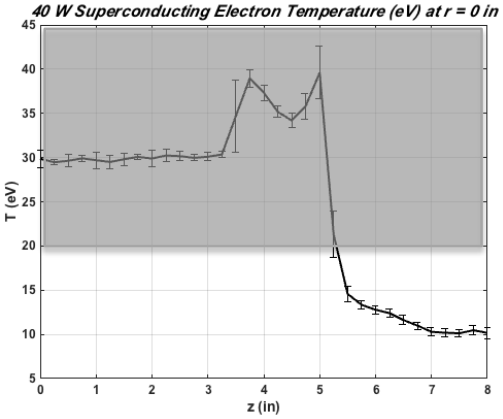
40 W Superconducting Electron Temperature (eV) at r = 0 in
T (eV)
z (in)

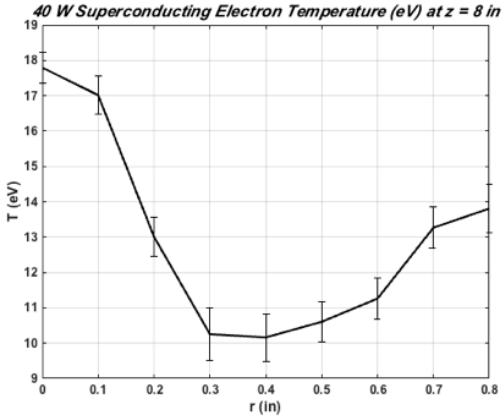
40 W Superconducting Electron Temperature (eV) at z = 8 in
T (eV)
r (in)

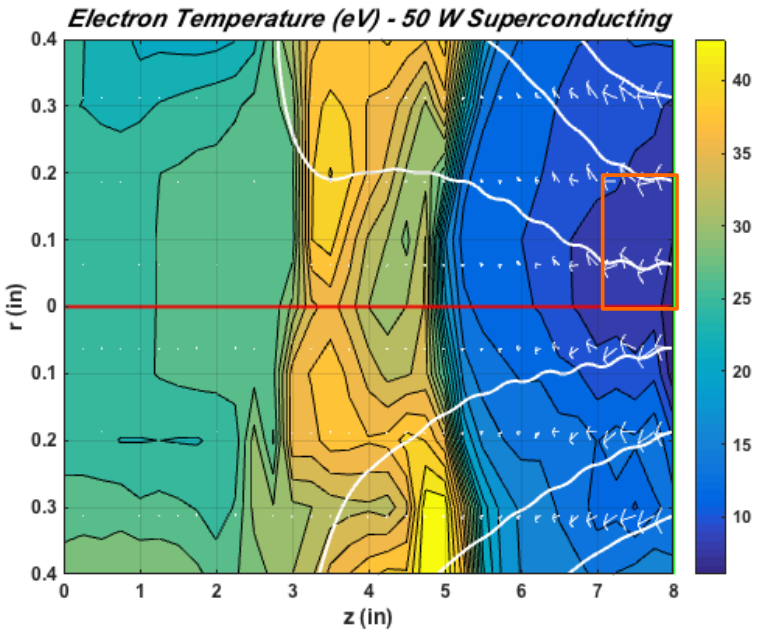
Electron Temperature (eV) - 50 W Superconducting
r (in)
z (in)

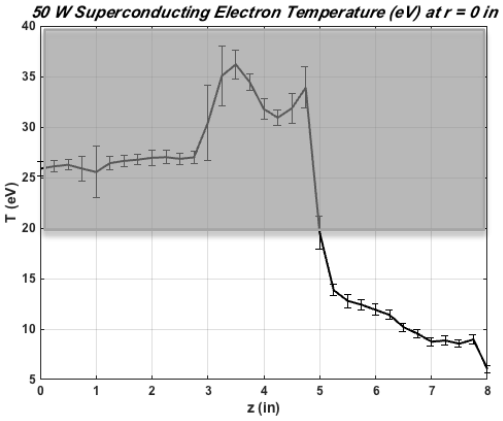
50 W Superconducting Electron Temperature (eV) at r = 0 in
T (eV)
z (in)

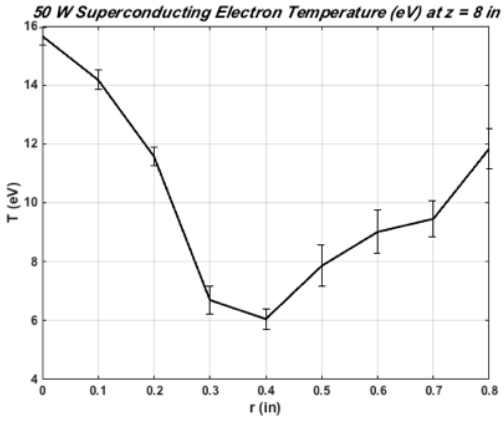
50 W Superconducting Electron Temperature (eV) at z = 8 in
T (eV)
r (in)

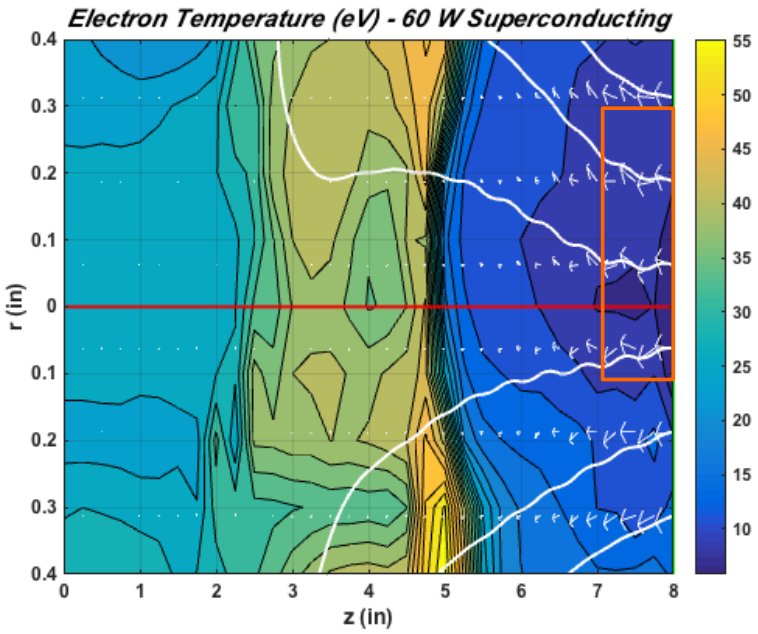
Electron Temperature (eV) - 60 W Superconducting
r (in)
z (in)

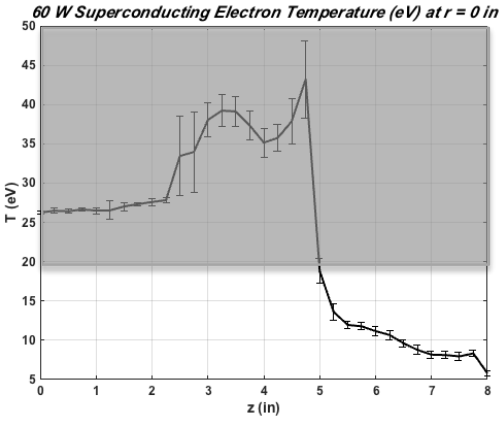
60 W Superconducting Electron Temperature (eV) at r = 0 in
T (eV)
z (in)

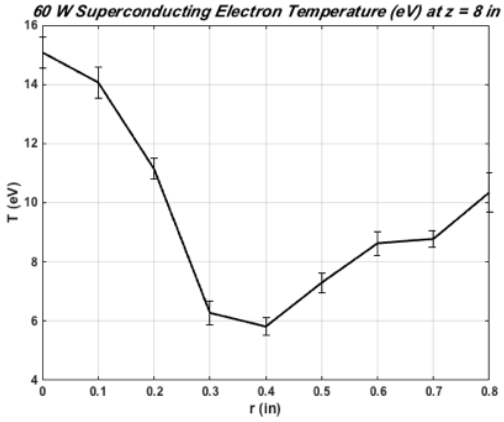
60 W Superconducting Electron Temperature (eV) at z = 8 in
T (eV)
r (in)

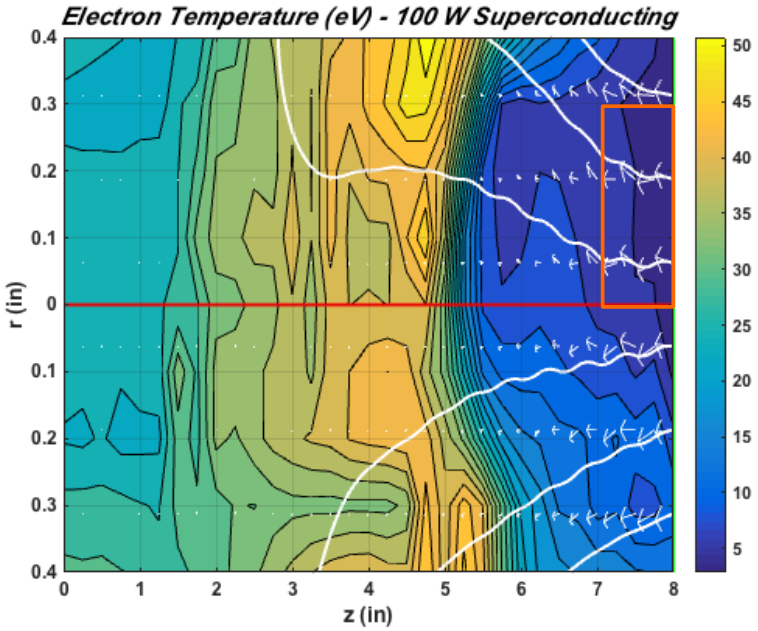
Electron Temperature (eV) - 100 W Superconducting
r (in)
z (in)

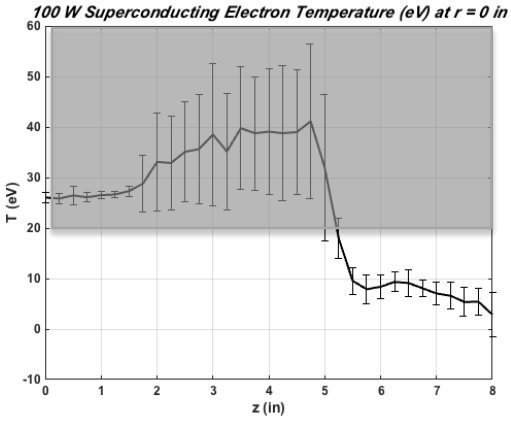
100 W Superconducting Electron Temperature (eV) at r = 0 in
T (eV)
z (in)

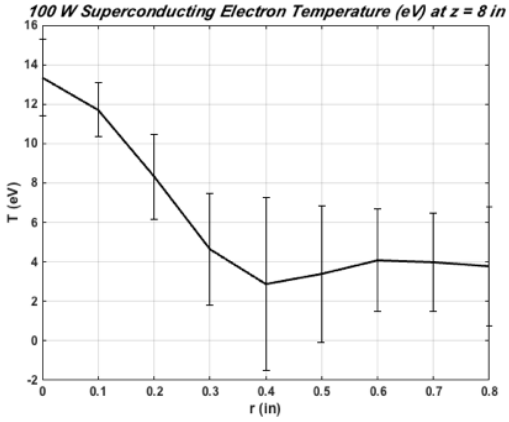
100 W Superconducting Electron Temperature (eV) at z = 8 in
T (eV)
r (in)

Appendix C: Helicon Thruster Triple Langmuir Probe Data – Electron Density

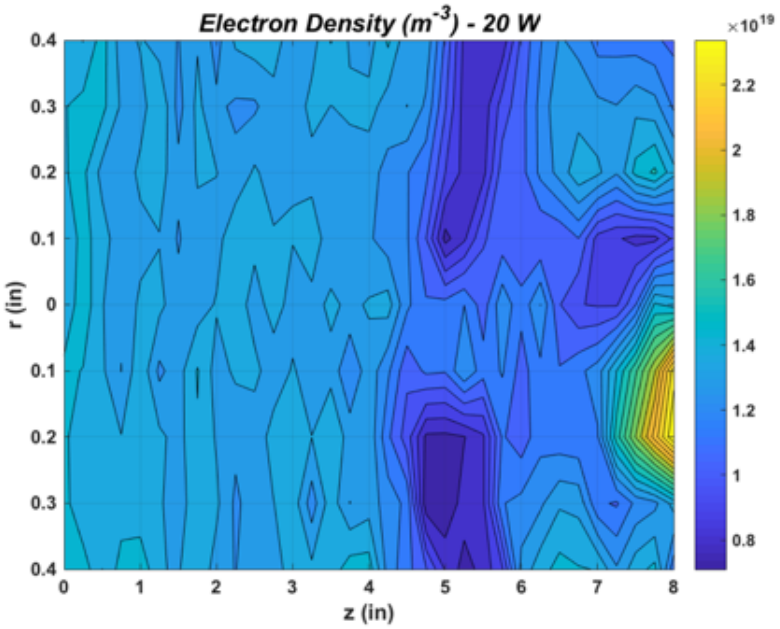

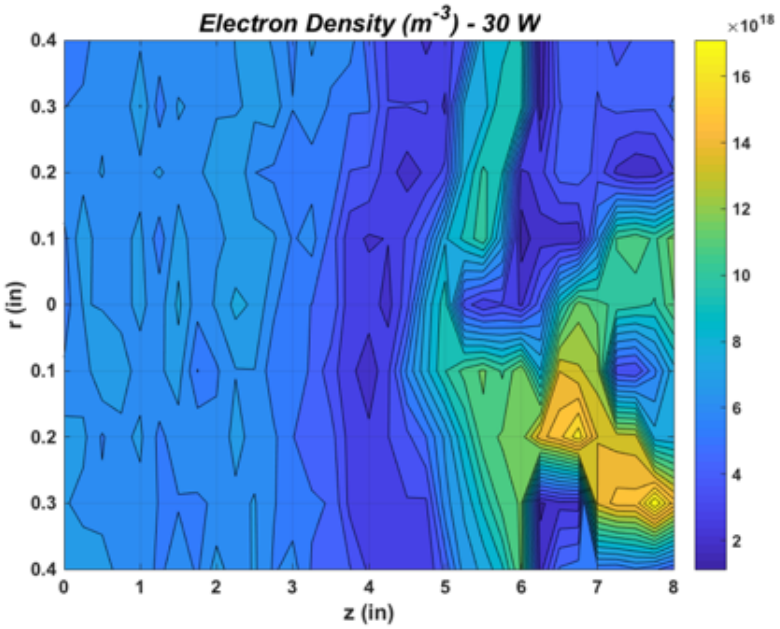

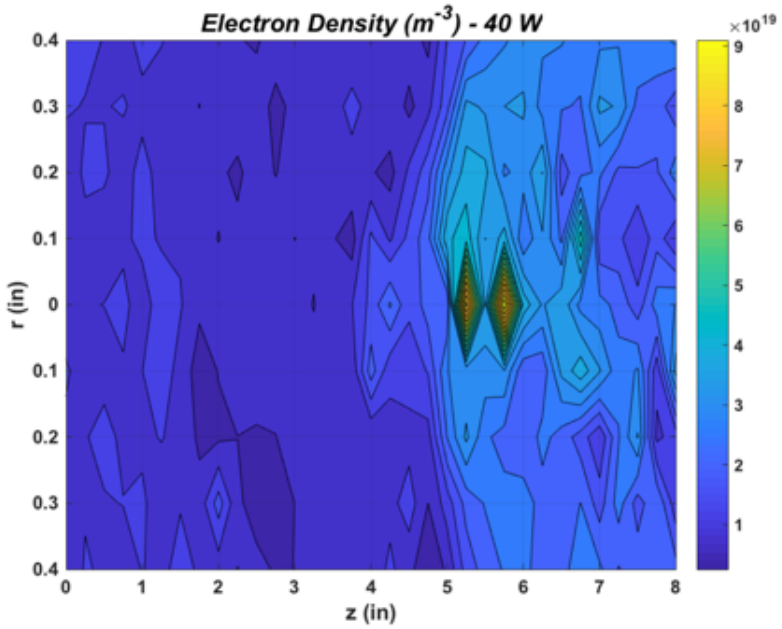
Electron Density (m^{-3}) - 40 W
×10^19
9
8
7
6
5
4
3
2
1
0.4
0.3
0.2
0.1
0
0.1
0.2
0.3
0.4
r (in)
0
1
2
3
4
5
6
7
8
z (in)

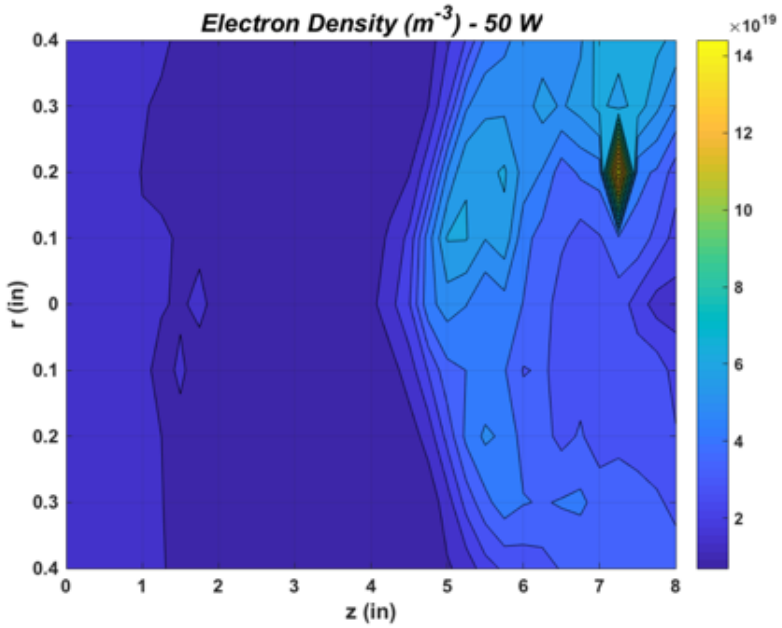
Electron Density (m^{-3}) - 50 W
×10^19
14
12
10
8
6
4
2
0.4
0.3
0.2
0.1
0
0.1
0.2
0.3
0.4
r (in)
0
1
2
3
4
5
6
7
8
z (in)

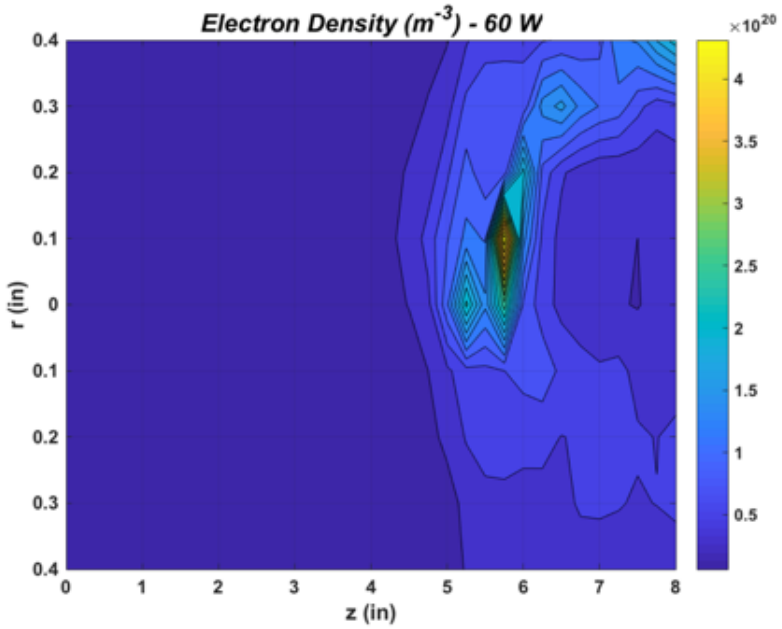
Electron Density (m^{-3}) - 60 W
×10^20
4
3.5
3
2.5
2
1.5
1
0.5
0.4
0.3
0.2
0.1
0
0.1
0.2
0.3
0.4
r (in)
0
1
2
3
4
5
6
7
8
z (in)

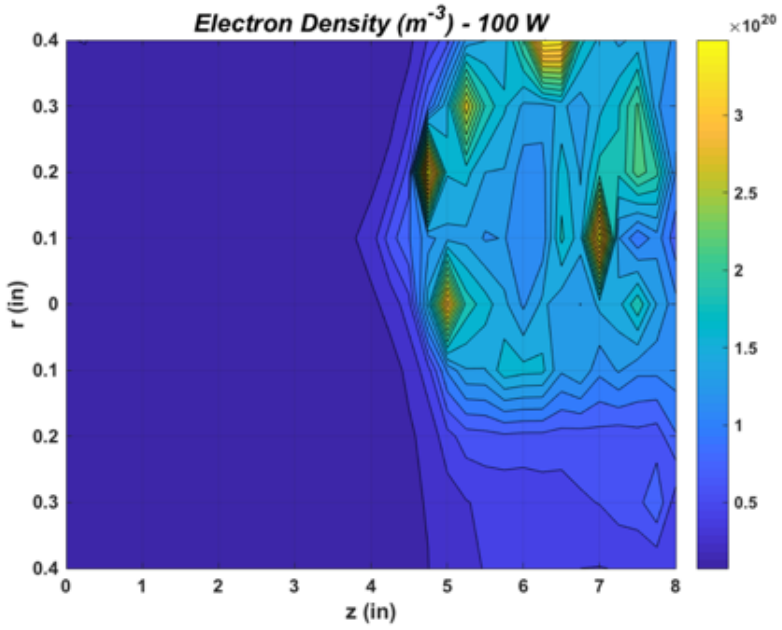
Electron Density (m^{-3}) - 100 W
×10^20
3
2.5
2
1.5
1
0.5
0.4
0.3
0.2
0.1
0
0.1
0.2
0.3
0.4
r (in)
0
1
2
3
4
5
6
7
8
z (in)

Appendix D: Superconducting Helicon Thruster Triple Langmuir Probe Data – Electron Density

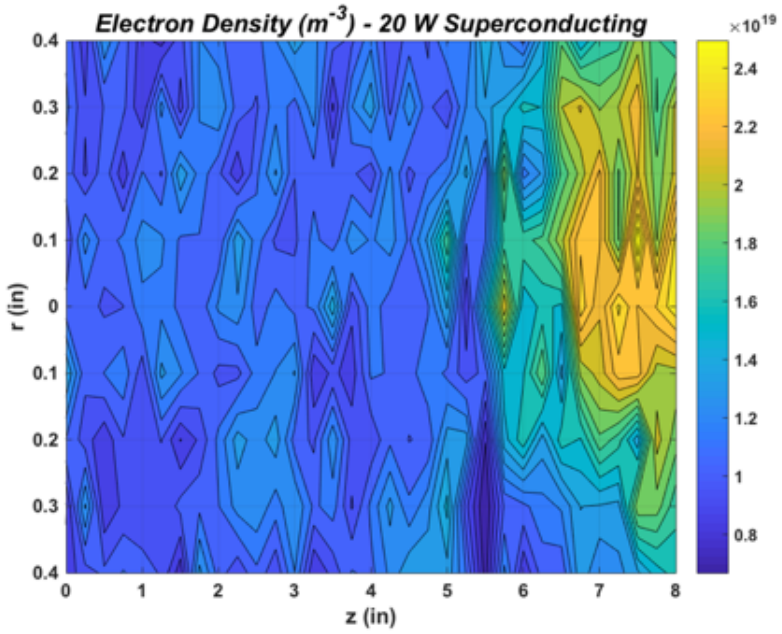

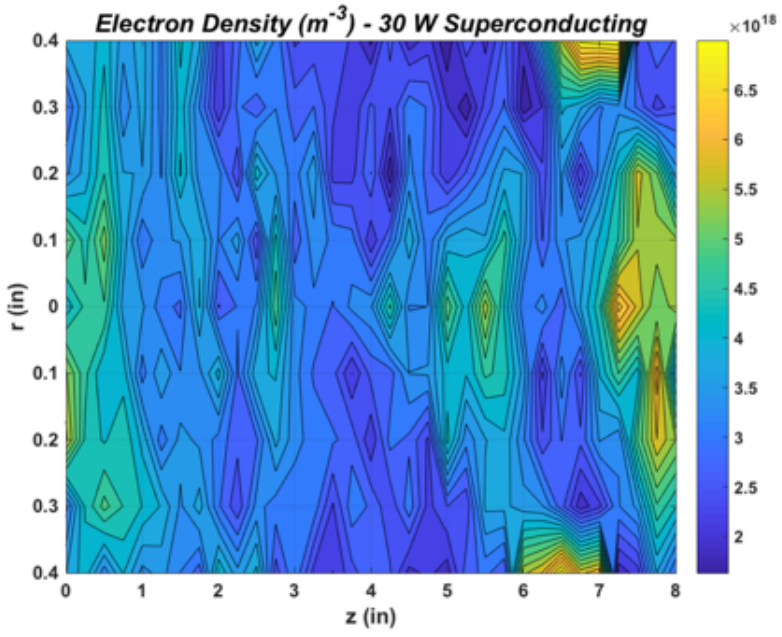

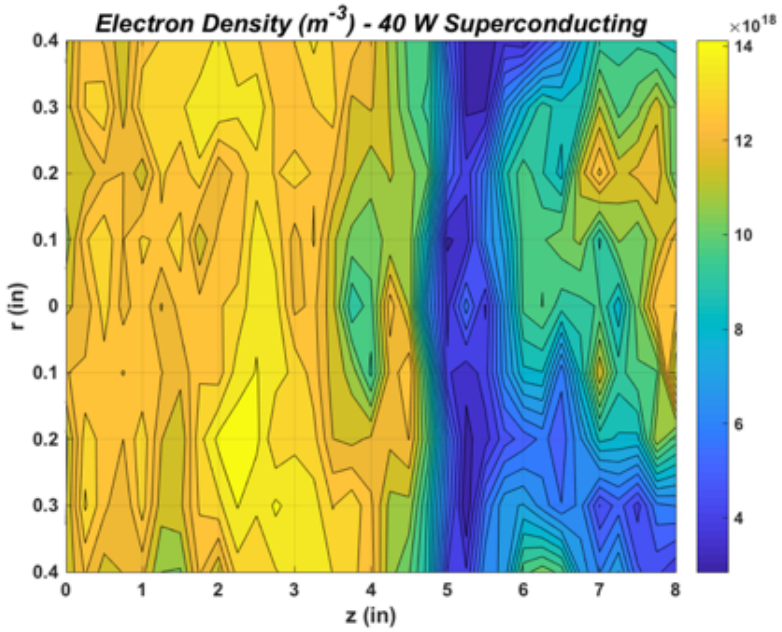
Electron Density (m^{-3}) - 40 W Superconducting
×10^18
14
12
10
8
6
4
r (in)
0.4
0.3
0.2
0.1
0
0.1
0.2
0.3
0.4
0
1
2
3
4
5
6
7
8
z (in)

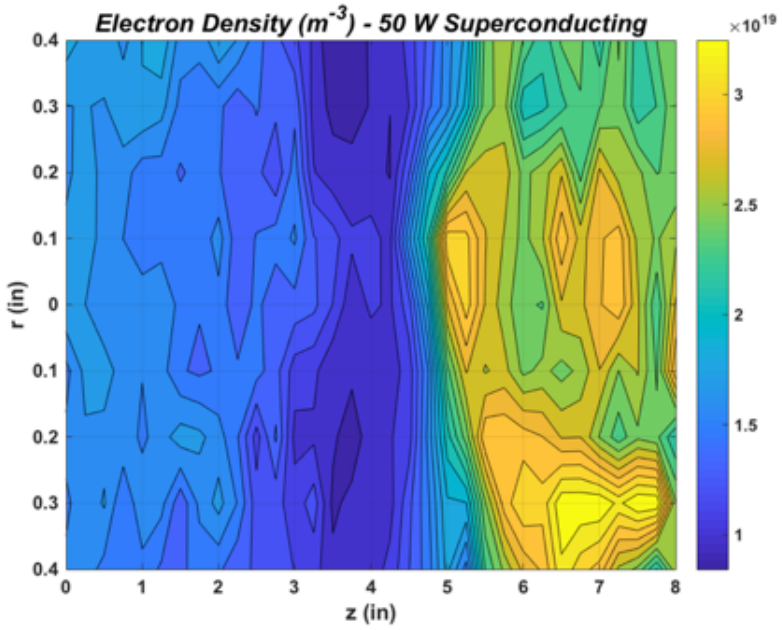
Electron Density (m^{-3}) - 50 W Superconducting
×10^19
3
2.5
2
1.5
1
r (in)
0.4
0.3
0.2
0.1
0
0.1
0.2
0.3
0.4
0
1
2
3
4
5
6
7
8
z (in)

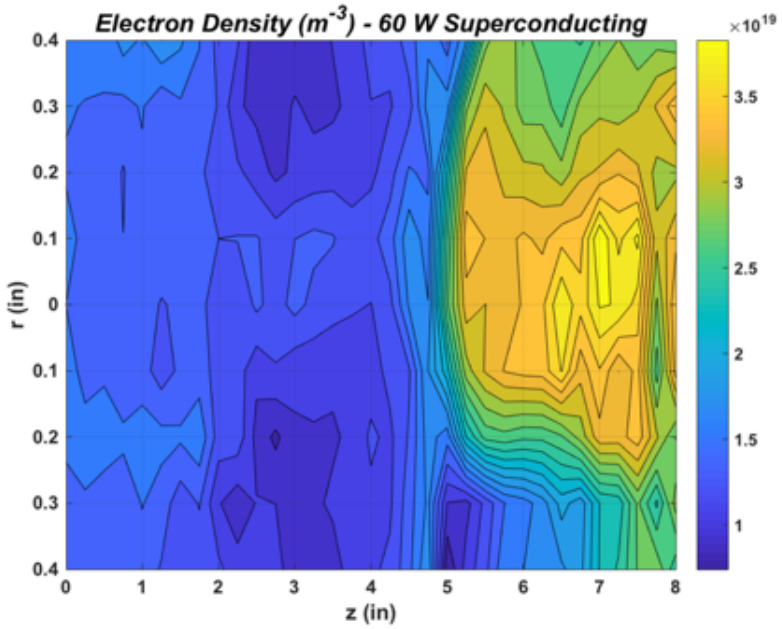
Electron Density (m^{-3}) - 60 W Superconducting
×10^19
3.5
3
2.5
2
1.5
1
r (in)
0.4
0.3
0.2
0.1
0
0.1
0.2
0.3
0.4
0
1
2
3
4
5
6
7
8
z (in)

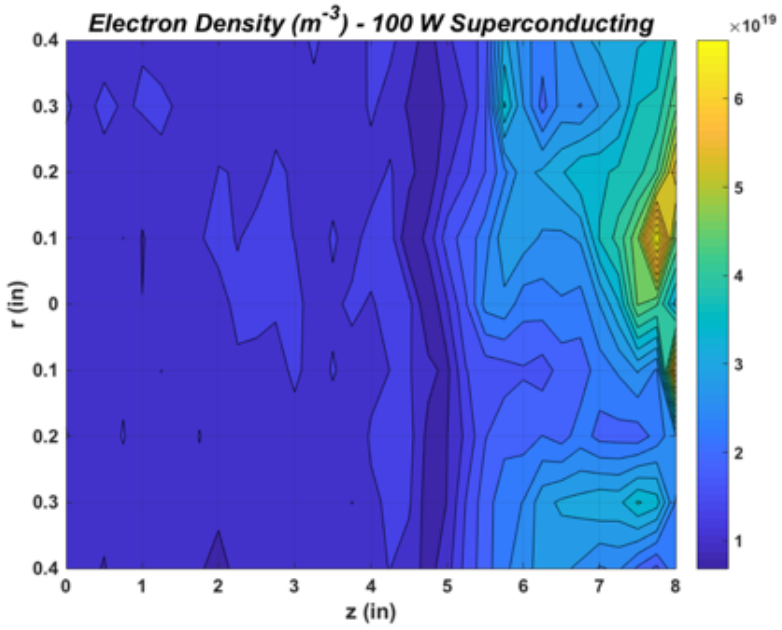
Electron Density (m^{-3}) - 100 W Superconducting
×10^19
6
5
4
3
2
1
r (in)
0.4
0.3
0.2
0.1
0
0.1
0.2
0.3
0.4
0
1
2
3
4
5
6
7
8
z (in)

Appendix E: Helicon Thruster Triple Langmuir Probe Data – Floating Potential

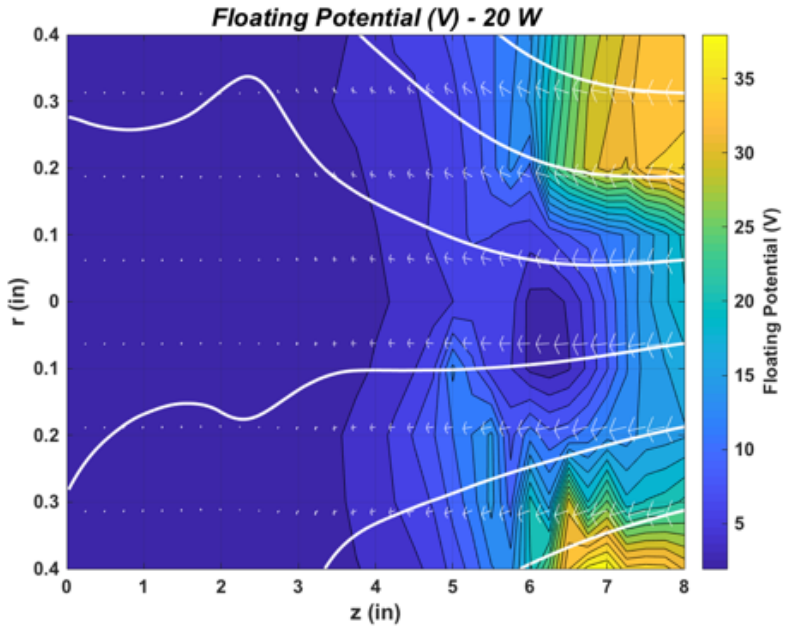

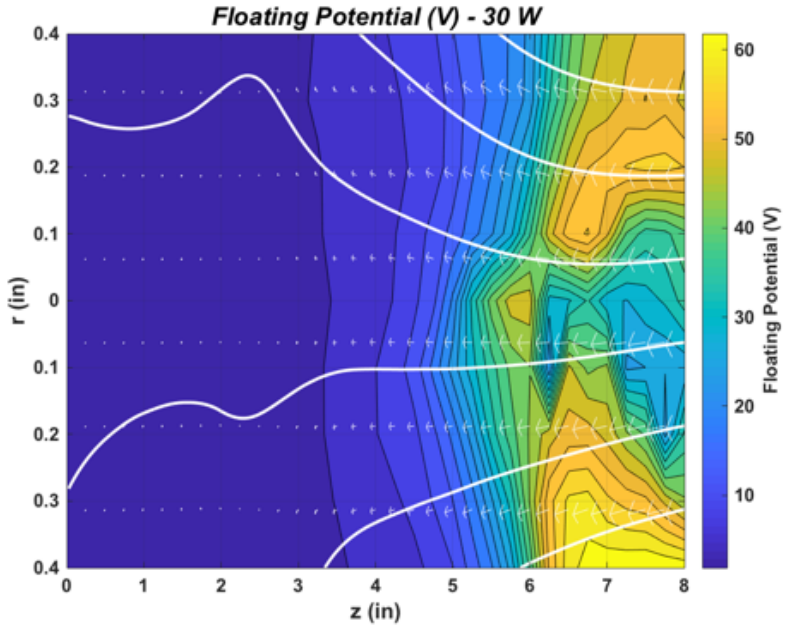

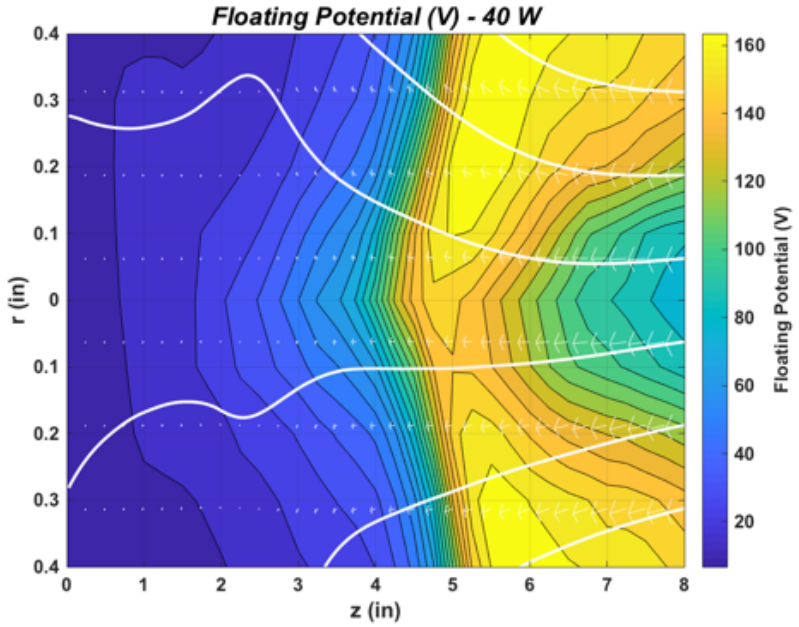
Floating Potential (V) - 40 W
r (in)
z (in)
Floating Potential (V)
0.4
0.3
0.2
0.1
0
0.1
0.2
0.3
0.4
0
1
2
3
4
5
6
7
8
160
140
120
100
80
60
40
20

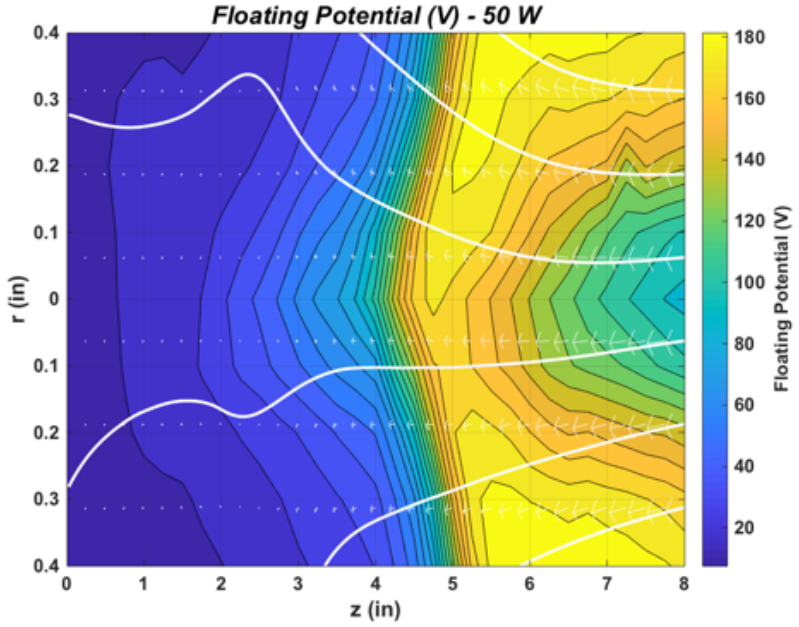
Floating Potential (V) - 50 W
r (in)
z (in)
Floating Potential (V)
0.4
0.3
0.2
0.1
0
0.1
0.2
0.3
0.4
0
1
2
3
4
5
6
7
8
180
160
140
120
100
80
60
40
20

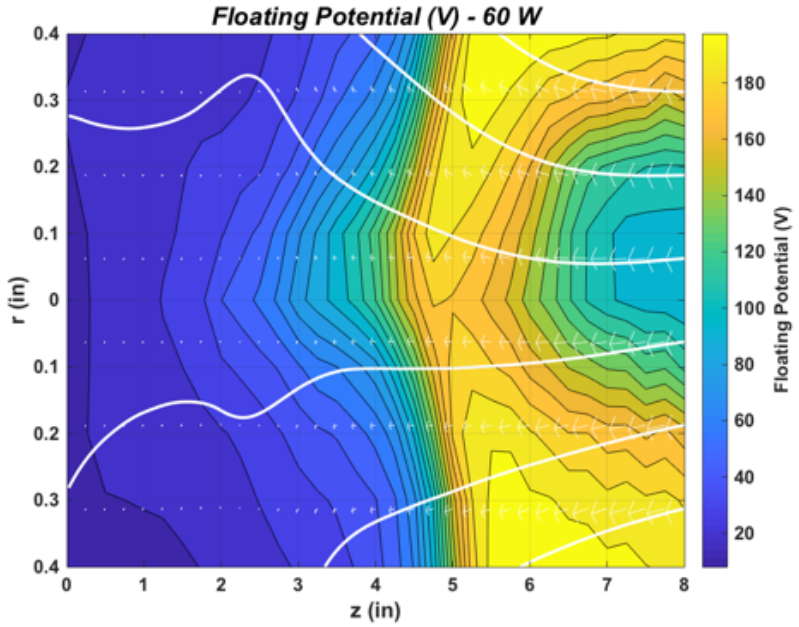
Floating Potential (V) - 60 W
r (in)
z (in)
Floating Potential (V)
0.4
0.3
0.2
0.1
0
0.1
0.2
0.3
0.4
0
1
2
3
4
5
6
7
8
180
160
140
120
100
80
60
40
20

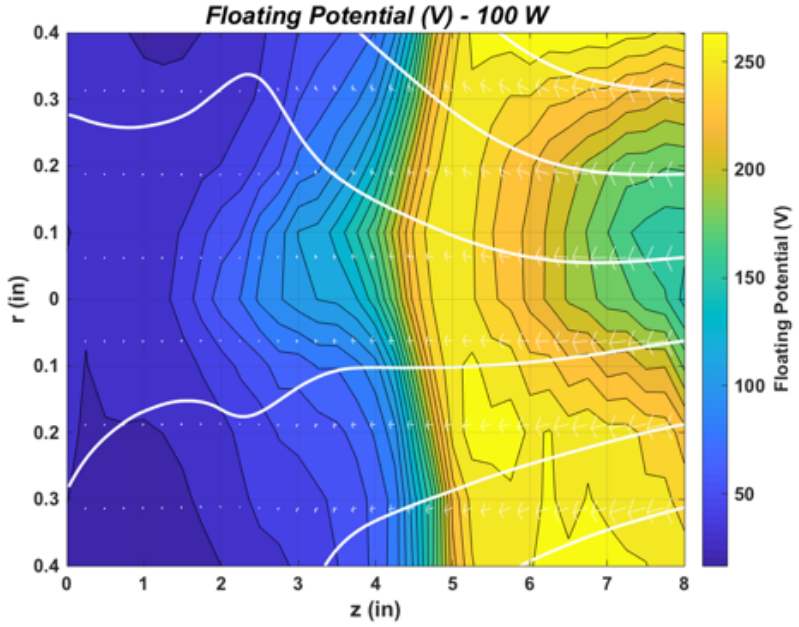
Floating Potential (V) - 100 W
r (in)
z (in)
Floating Potential (V)
0.4
0.3
0.2
0.1
0
0.1
0.2
0.3
0.4
0
1
2
3
4
5
6
7
8
250
200
150
100
50

Appendix F: Superconducting Helicon Thruster Triple Langmuir Probe Data – Floating Potential

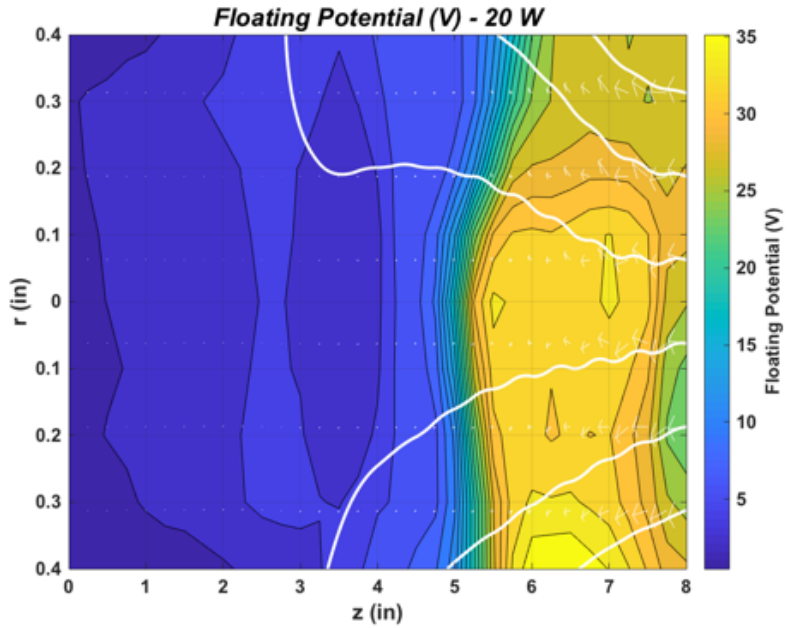

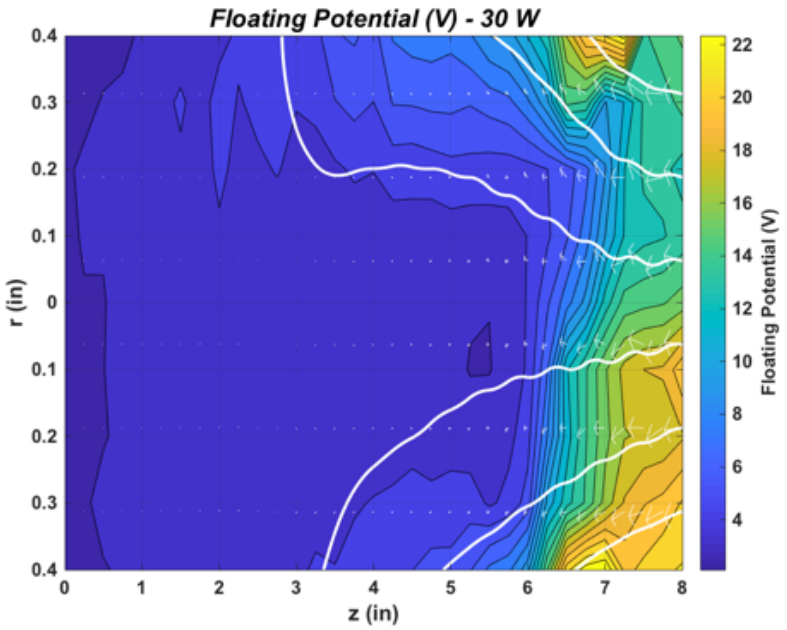

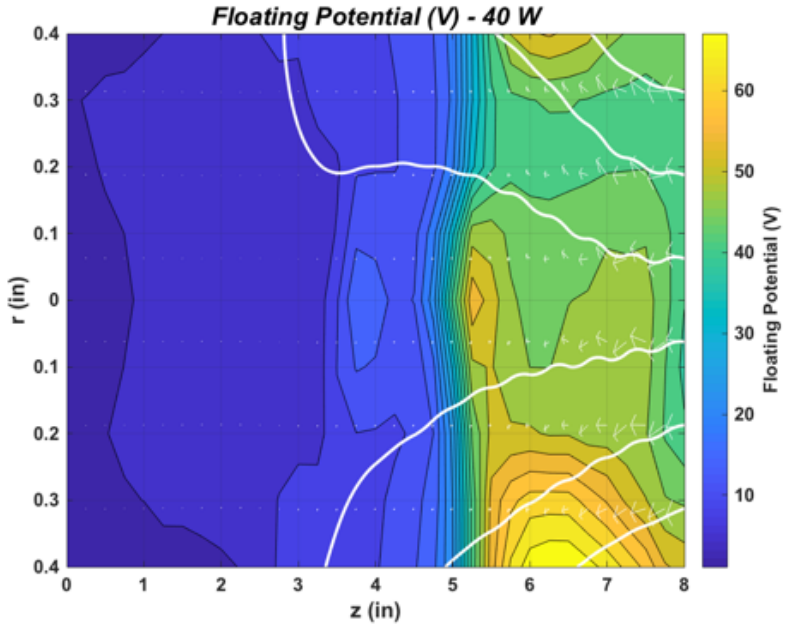
Floating Potential (V) - 40 W
r (in)
z (in)
Floating Potential (V)
0.4
0.3
0.2
0.1
0
0.1
0.2
0.3
0.4
0
1
2
3
4
5
6
7
8
10
20
30
40
50
60

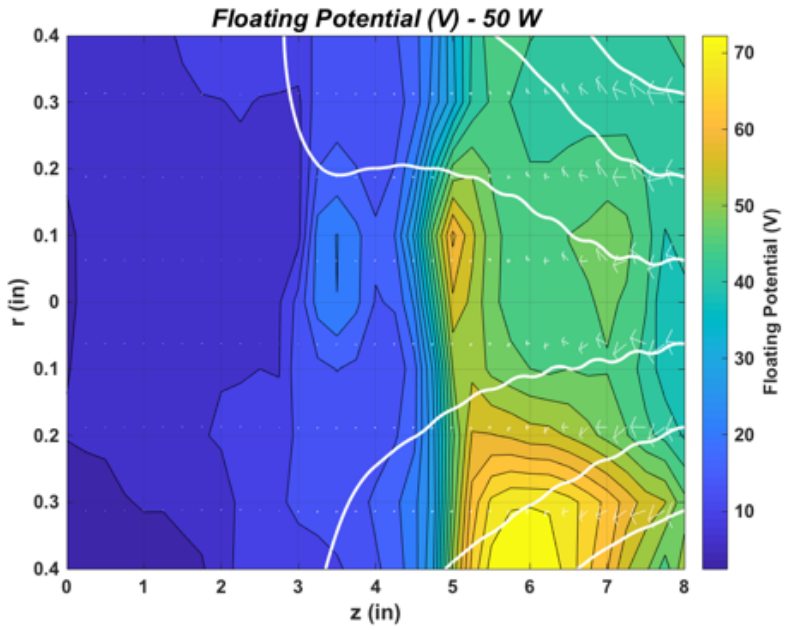
Floating Potential (V) - 50 W
r (in)
z (in)
Floating Potential (V)
0.4
0.3
0.2
0.1
0
0.1
0.2
0.3
0.4
0
1
2
3
4
5
6
7
8
10
20
30
40
50
60
70

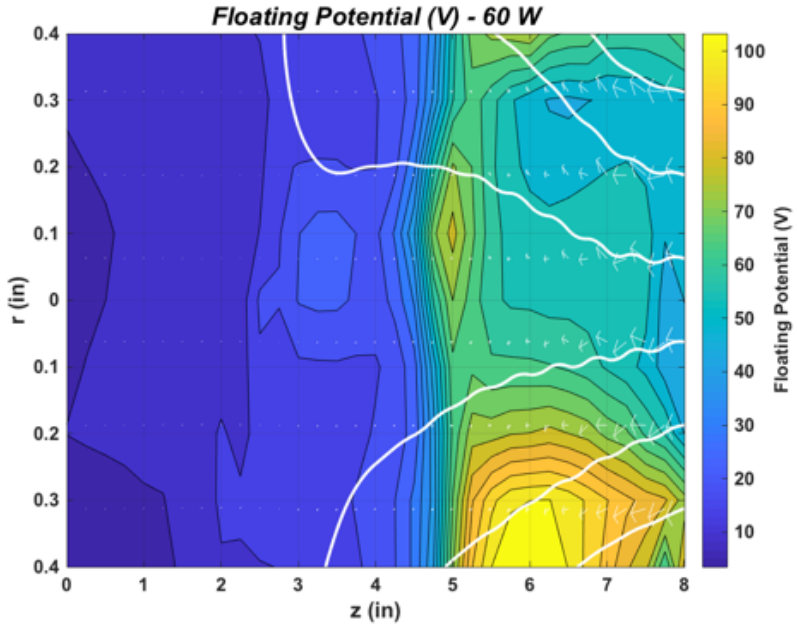
Floating Potential (V) - 60 W
r (in)
z (in)
Floating Potential (V)

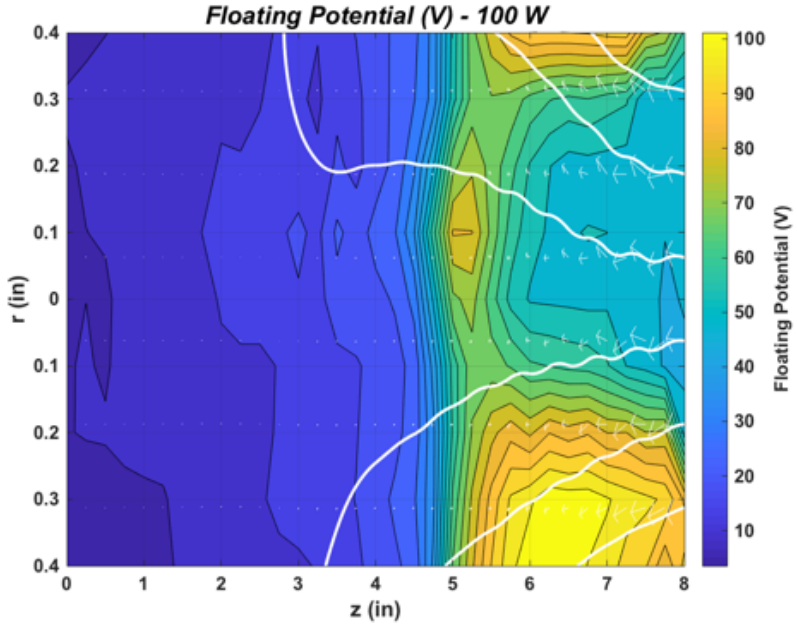
Floating Potential (V) - 100 W
r (in)
z (in)
Floating Potential (V)

Appendix G: Helicon Thruster RPA Data

20 W

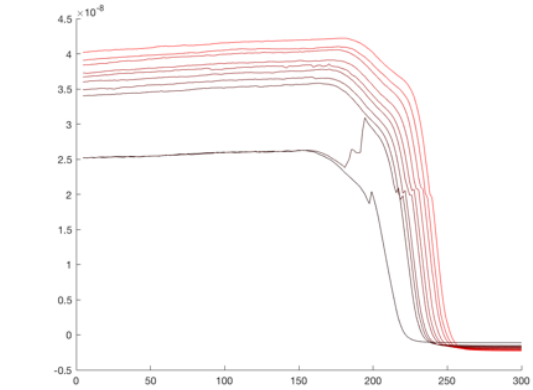

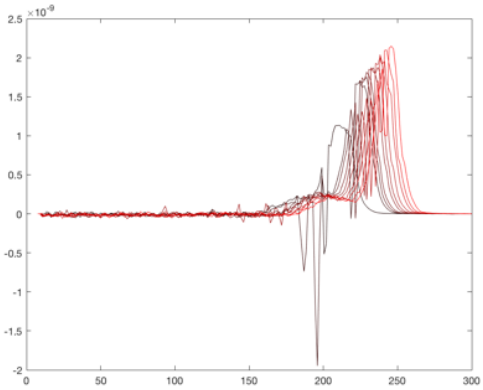

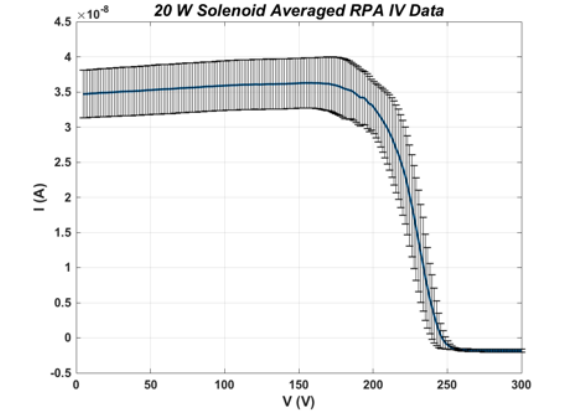

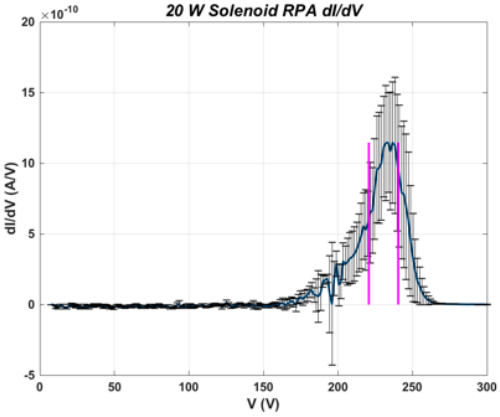

30 W

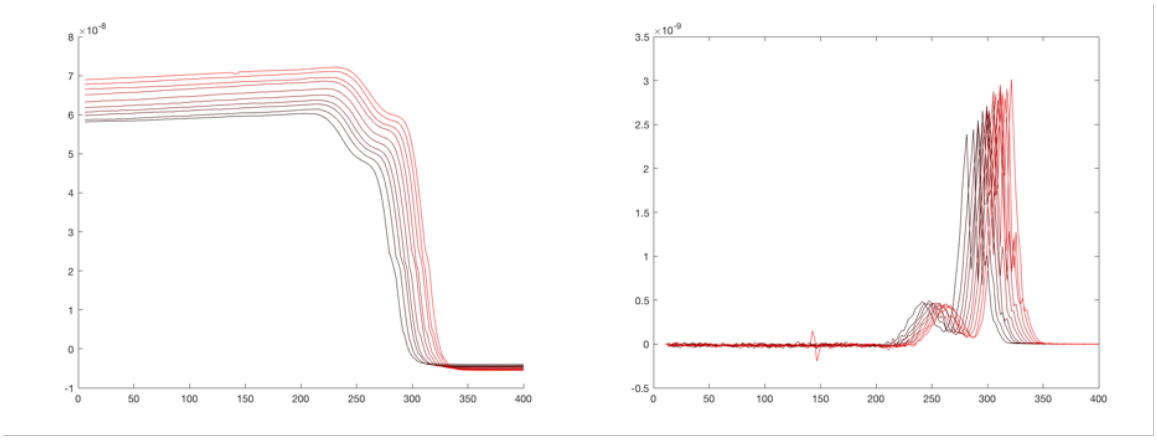
×10^-8
×10^-9

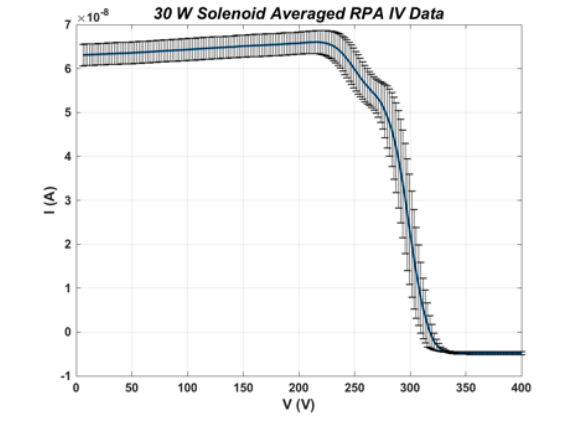
30 W Solenoid Averaged RPA IV Data
×10^-8
I (A)
V (V)

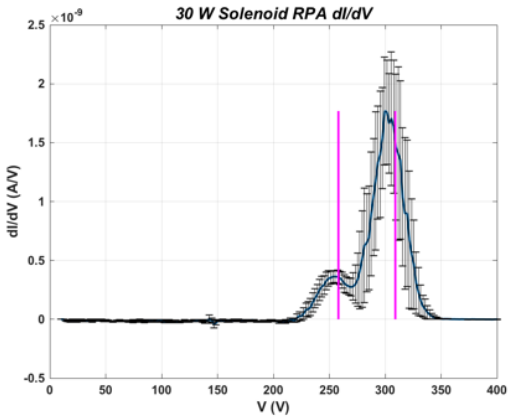
30 W Solenoid RPA dI/dV
×10^-9
dI/dV (A/V)
V (V)

40 W

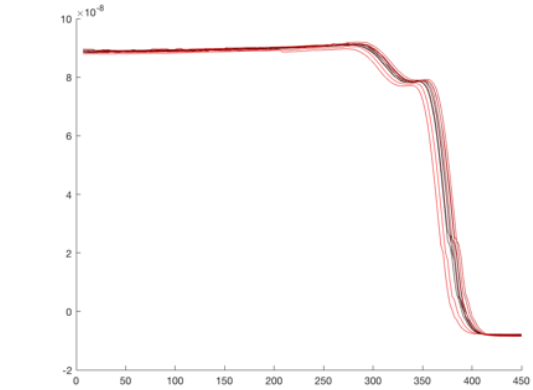
×10^-8
10
8
6
4
2
0
-2
0 50 100 150 200 250 300 350 400 450

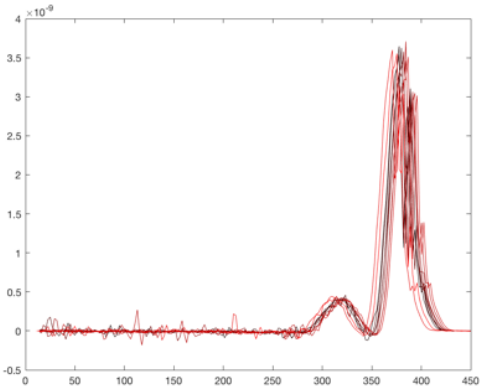
×10^-9
4
3.5
3
2.5
2
1.5
1
0.5
0
-0.5
0 50 100 150 200 250 300 350 400 450

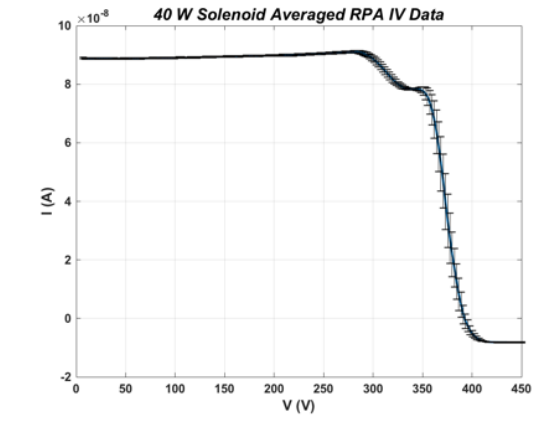
40 W Solenoid Averaged RPA IV Data
×10^-8
I (A)
V (V)
10
8
6
4
2
0
-2
0 50 100 150 200 250 300 350 400 450

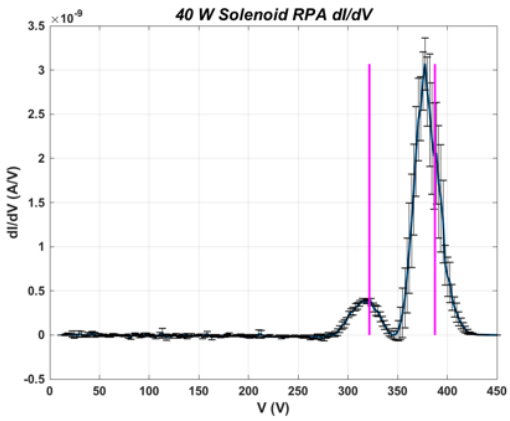
40 W Solenoid RPA dI/dV
×10^-9
dI/dV (A/V)
V (V)
3.5
3
2.5
2
1.5
1
0.5
0
-0.5
0 50 100 150 200 250 300 350 400 450

50 W

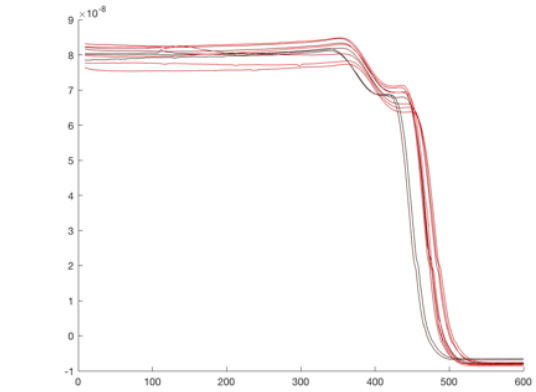
×10^-8
9
8
7
6
5
4
3
2
1
0
-1
0
100
200
300
400
500
600

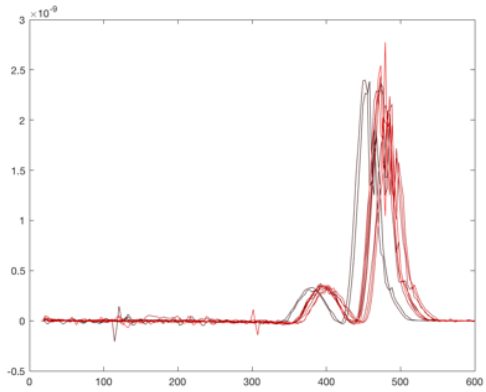
×10^-9
3
2.5
2
1.5
1
0.5
0
-0.5
0
100
200
300
400
500
600

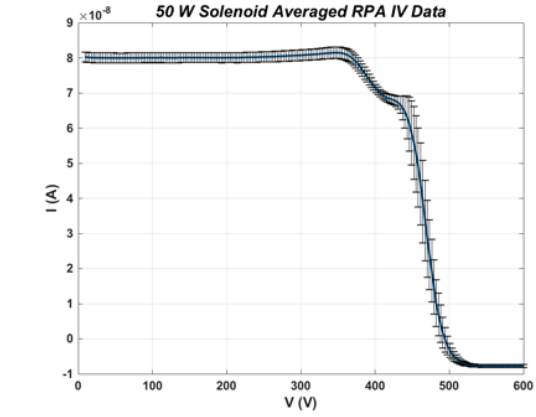
50 W Solenoid Averaged RPA IV Data
×10^-8
I (A)
V (V)
9
8
7
6
5
4
3
2
1
0
-1
0
100
200
300
400
500
600

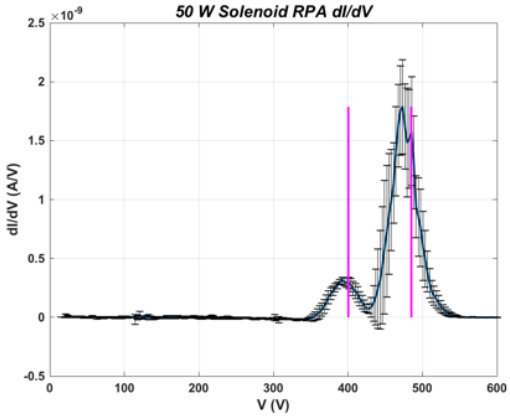
50 W Solenoid RPA dI/dV
×10^-9
dI/dV (A/V)
V (V)
2.5
2
1.5
1
0.5
0
-0.5
0
100
200
300
400
500
600

60 W

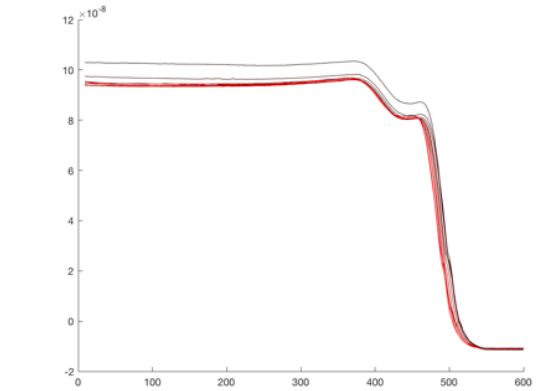
×10^-8
12
10
8
6
4
2
0
-2
0
100
200
300
400
500
600

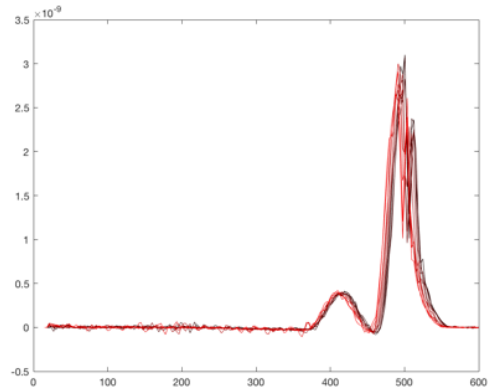
×10^-9
3.5
3
2.5
2
1.5
1
0.5
0
-0.5
0
100
200
300
400
500
600

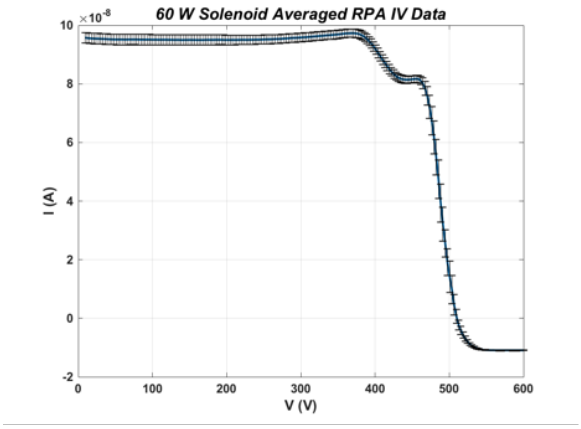
60 W Solenoid Averaged RPA IV Data
×10^-8
I (A)
V (V)
10
8
6
4
2
0
-2
0
100
200
300
400
500
600

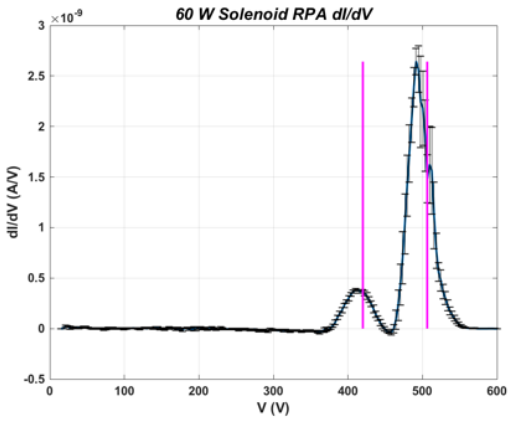
60 W Solenoid RPA dI/dV
×10^-9
dI/dV (A/V)
V (V)
3
2.5
2
1.5
1
0.5
0
-0.5
0
100
200
300
400
500
600

100 W

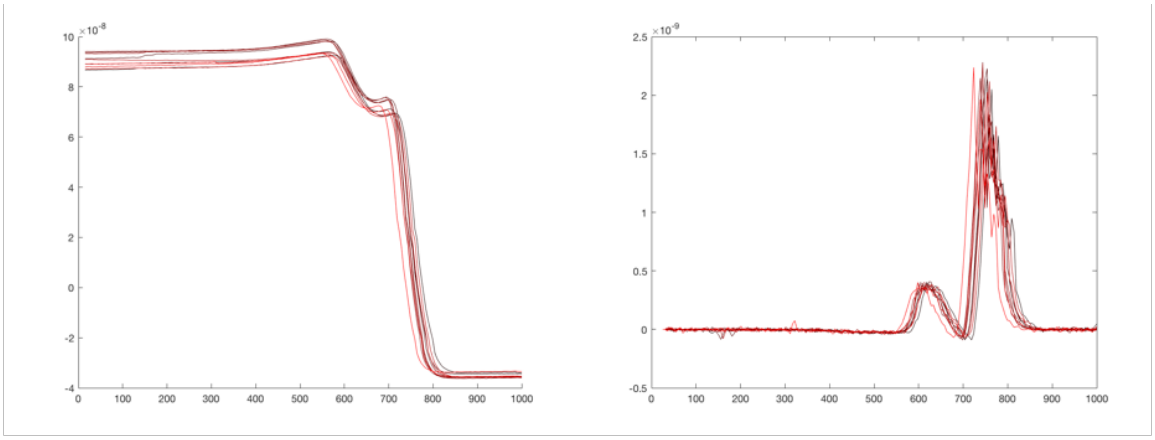
×10^-8
×10^-9

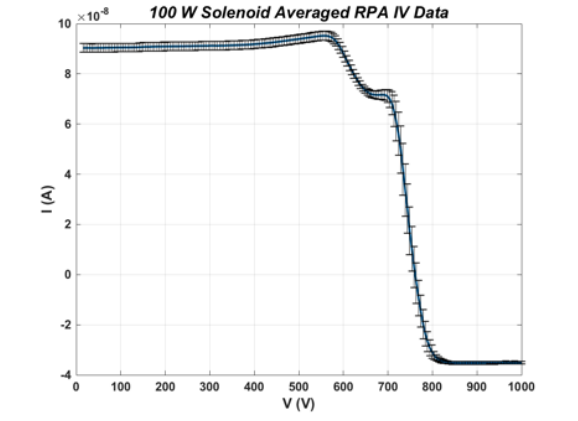
100 W Solenoid Averaged RPA IV Data
×10^-8
I (A)
V (V)

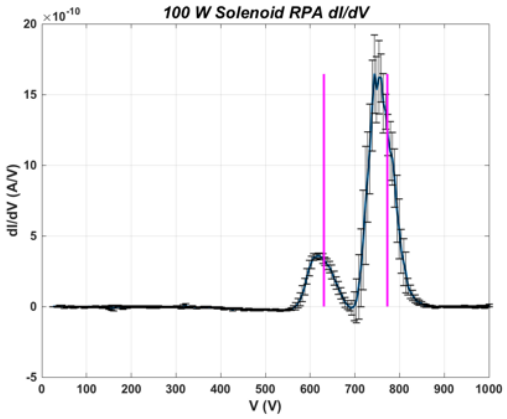
100 W Solenoid RPA dI/dV
×10^-10
dI/dV (A/V)
V (V)

Appendix H: Superconducting Helicon Thruster RPA Data

20 W

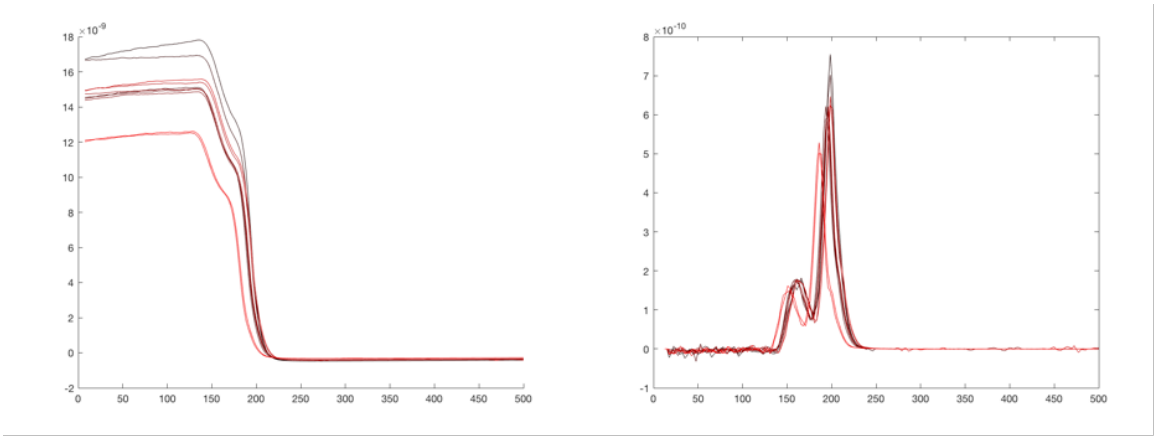

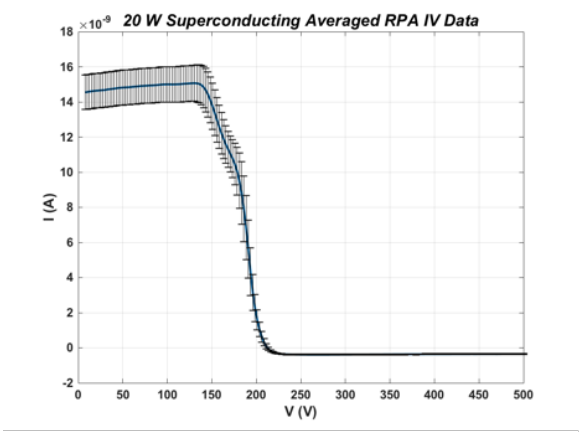

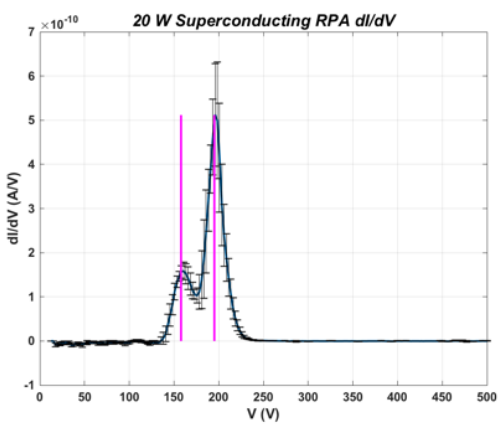

30 W

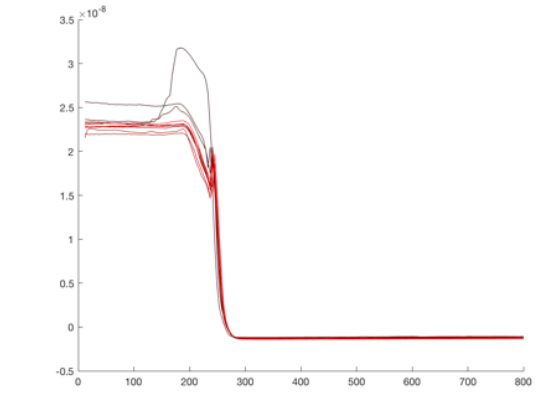
×10^-8
3.5
3
2.5
2
1.5
1
0.5
0
-0.5
0
100
200
300
400
500
600
700
800

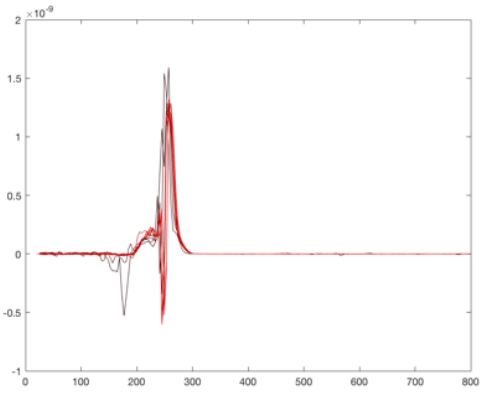
×10^-9
2
1.5
1
0.5
0
-0.5
-1
0
100
200
300
400
500
600
700
800

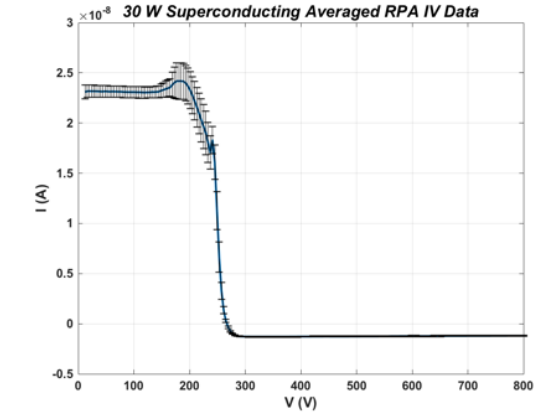
30 W Superconducting Averaged RPA IV Data
×10^-8
I (A)
V (V)
3
2.5
2
1.5
1
0.5
0
-0.5
0
100
200
300
400
500
600
700
800

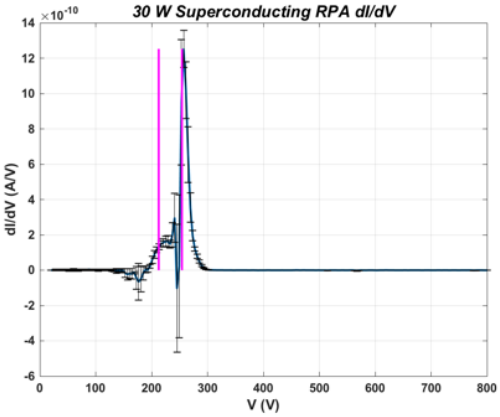
30 W Superconducting RPA dI/dV
×10^-10
dI/dV (A/V)
V (V)
14
12
10
8
6
4
2
0
-2
-4
-6
0
100
200
300
400
500
600
700
800

40 W

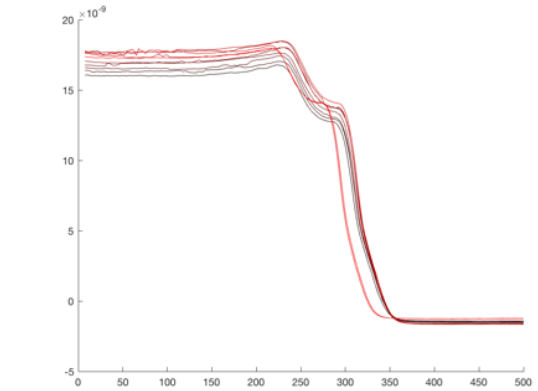
×10^-9
20
15
10
5
0
-5
0 50 100 150 200 250 300 350 400 450 500

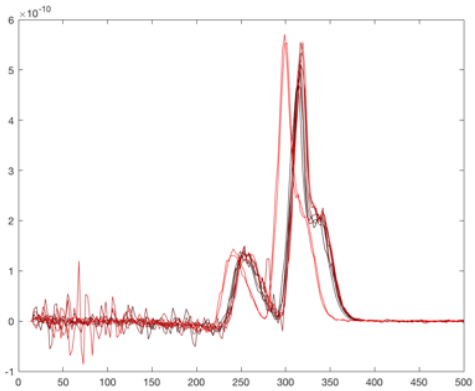
×10^-10
6
5
4
3
2
1
0
-1
0 50 100 150 200 250 300 350 400 450 500

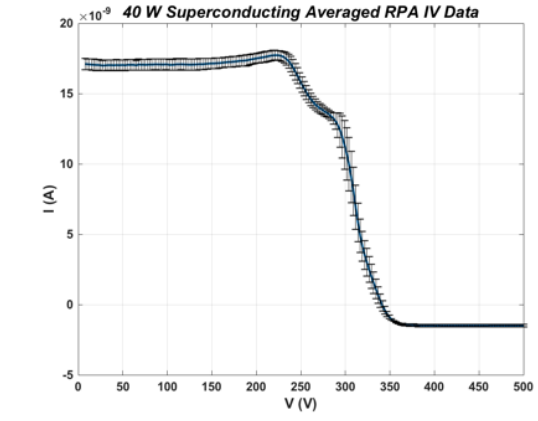
×10^-9
40 W Superconducting Averaged RPA IV Data
I (A)
V (V)
20
15
10
5
0
-5
0 50 100 150 200 250 300 350 400 450 500

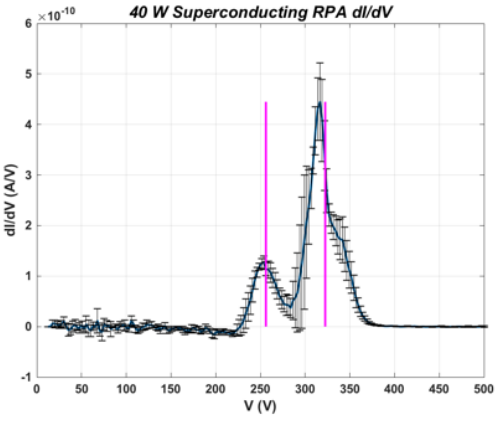
×10^-10
40 W Superconducting RPA dI/dV
dI/dV (A/V)
V (V)
6
5
4
3
2
1
0
-1
0 50 100 150 200 250 300 350 400 450 500

50 W

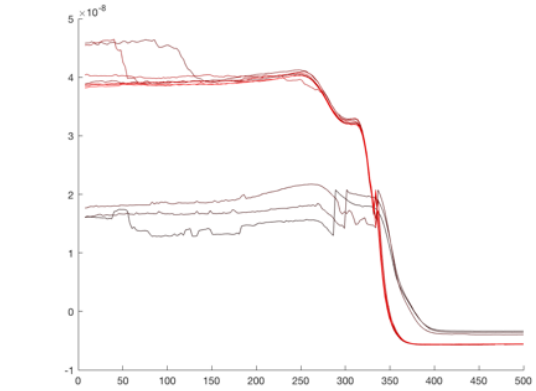
×10^-8
5
4
3
2
1
0
-1
0 50 100 150 200 250 300 350 400 450 500

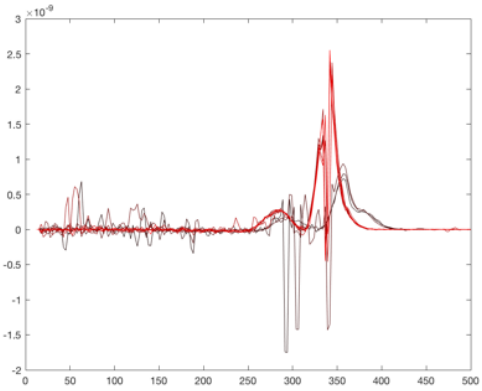
×10^-9
3
2.5
2
1.5
1
0.5
0
-0.5
-1
-1.5
-2
0 50 100 150 200 250 300 350 400 450 500

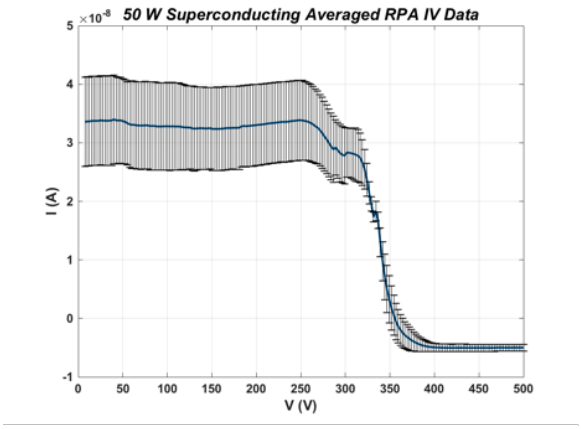
×10^-8 50 W Superconducting Averaged RPA IV Data
I (A)
V (V)
5
4
3
2
1
0
-1
0 50 100 150 200 250 300 350 400 450 500

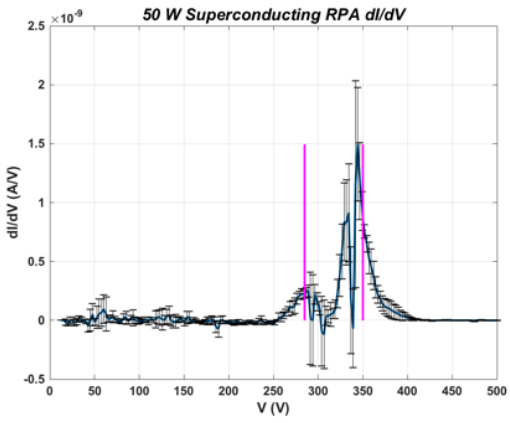
×10^-9 50 W Superconducting RPA dI/dV
dI/dV (A/V)
V (V)
2.5
2
1.5
1
0.5
0
-0.5
0 50 100 150 200 250 300 350 400 450 500

60 W

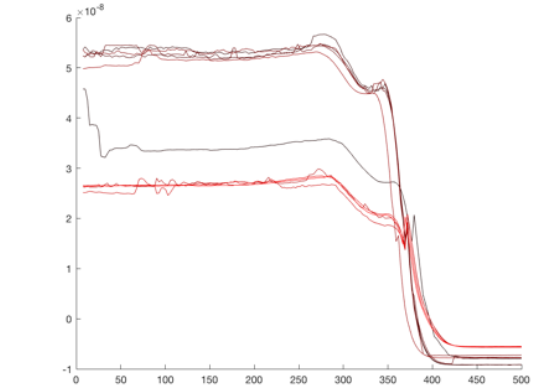
×10^-8
6
5
4
3
2
1
0
-1
0 50 100 150 200 250 300 350 400 450 500

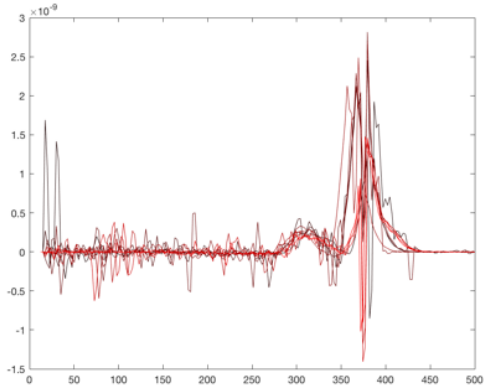
×10^-9
3
2.5
2
1.5
1
0.5
0
-0.5
-1
-1.5
0 50 100 150 200 250 300 350 400 450 500

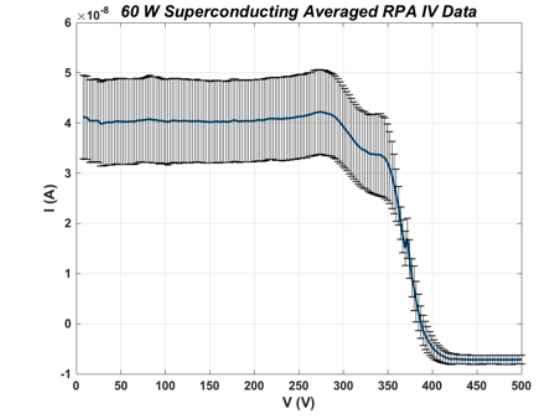
60 W Superconducting Averaged RPA IV Data
×10^-8
I (A)
V (V)
6
5
4
3
2
1
0
-1
0 50 100 150 200 250 300 350 400 450 500

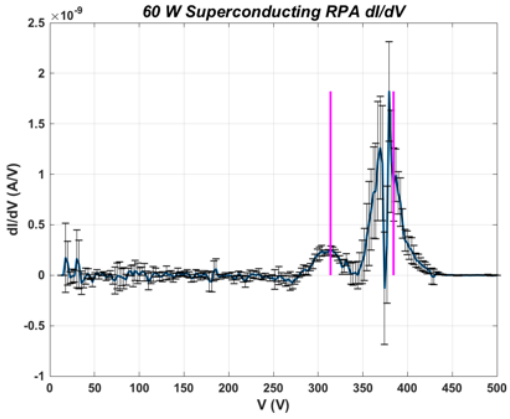
60 W Superconducting RPA dI/dV
×10^-9
dI/dV (A/V)
V (V)
2.5
2
1.5
1
0.5
0
-0.5
-1
0 50 100 150 200 250 300 350 400 450 500

100 W

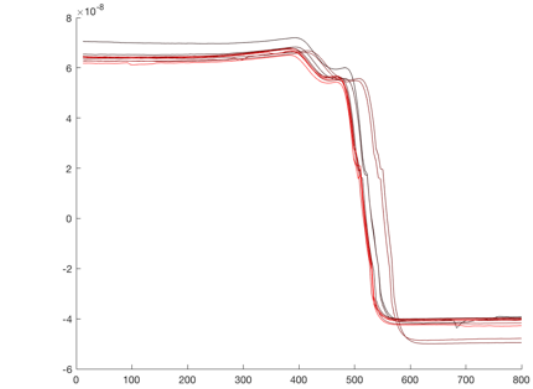

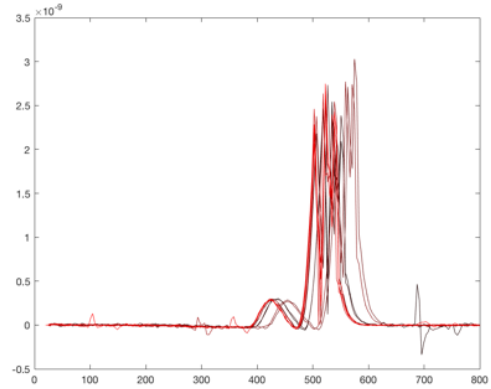

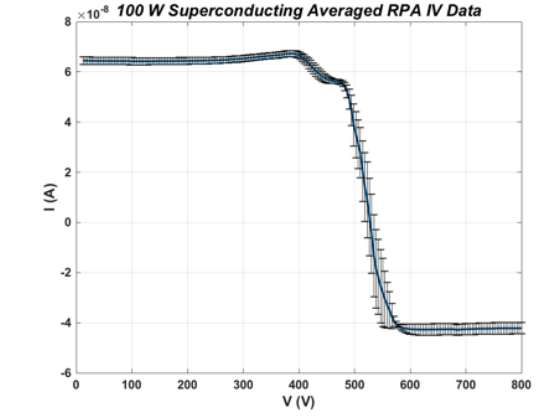
100 W Superconducting Averaged RPA IV Data
I (A)
V (V)

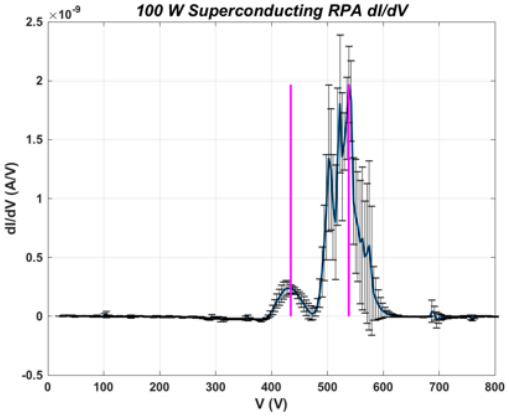
100 W Superconducting RPA dI/dV
dI/dV (A/V)
V (V)

Appendix I: Helicon Thruster RPA Data – 50 W Radial Profile

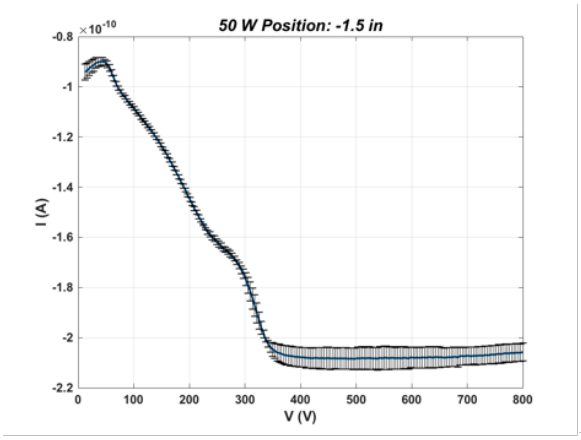

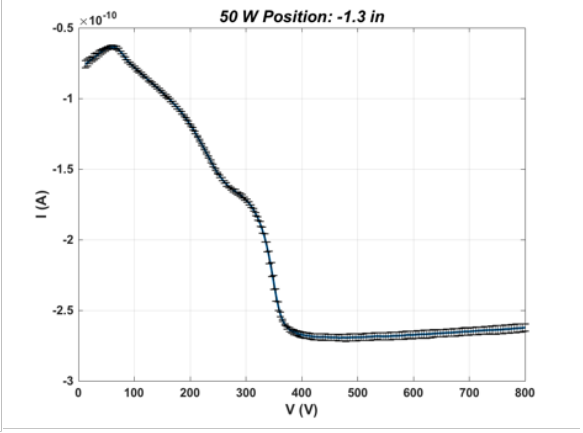

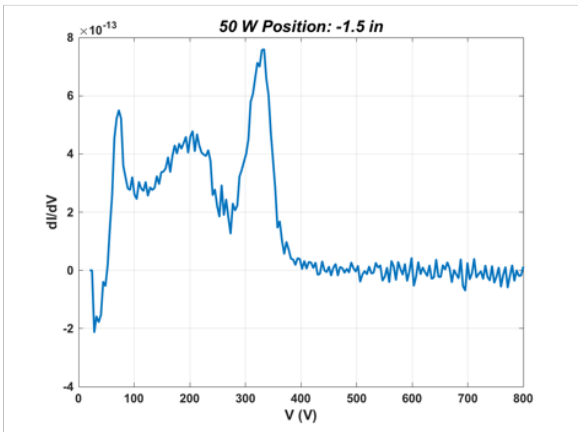

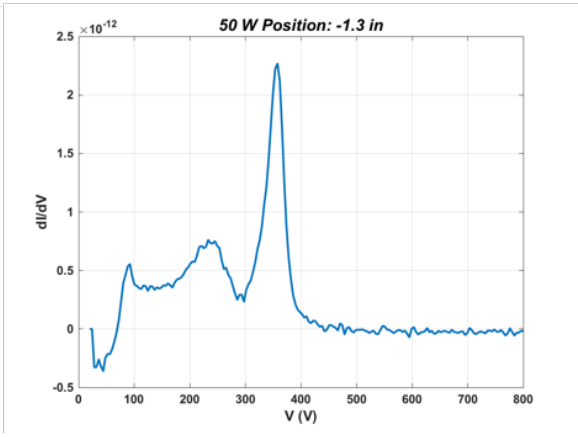

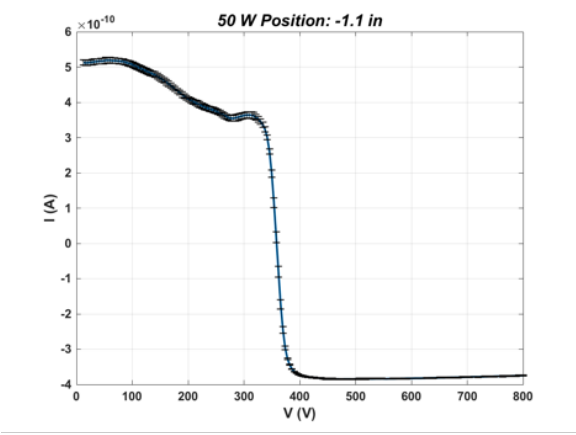
50 W Position: -1.1 in
×10^-10
I (A)
V (V)

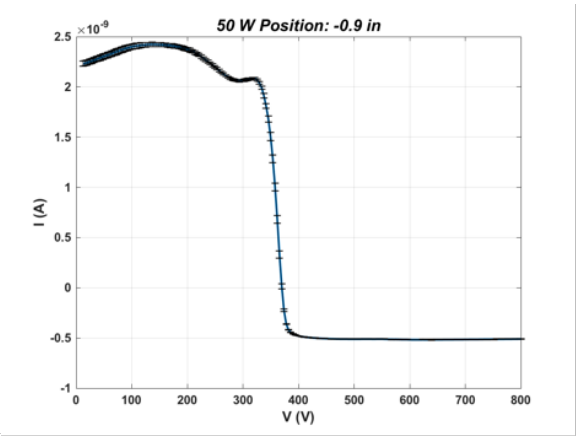
50 W Position: -0.9 in
×10^-9
I (A)
V (V)

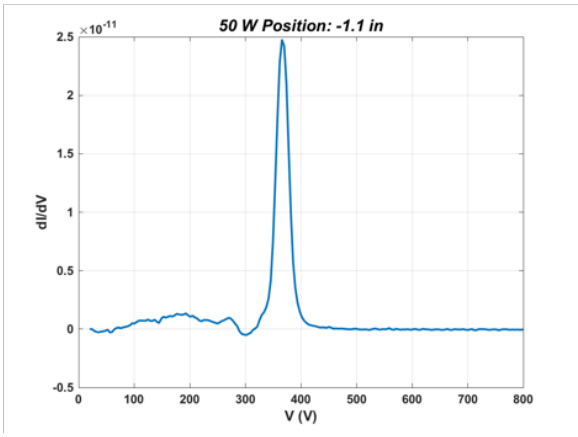
50 W Position: -1.1 in
×10^-11
dI/dV
V (V)

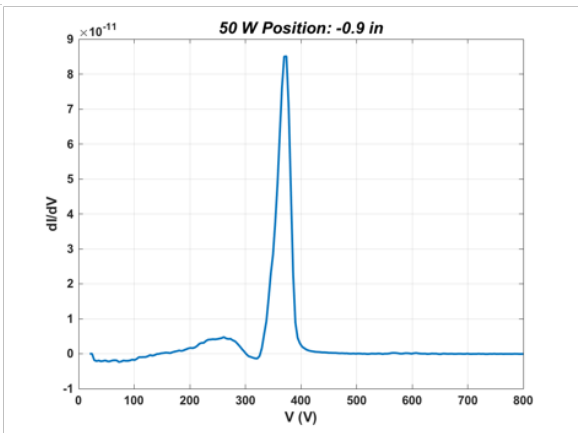
50 W Position: -0.9 in
×10^-11
dI/dV
V (V)

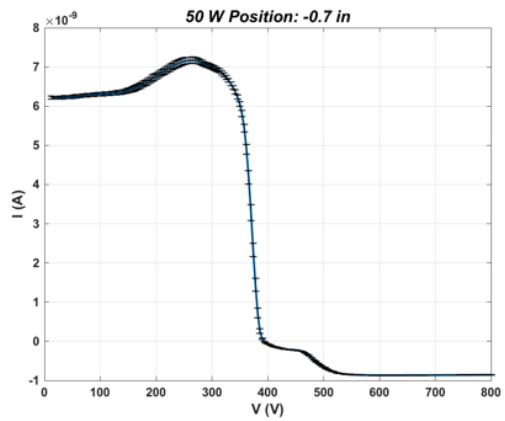
50 W Position: -0.7 in
×10^-9
I (A)
V (V)

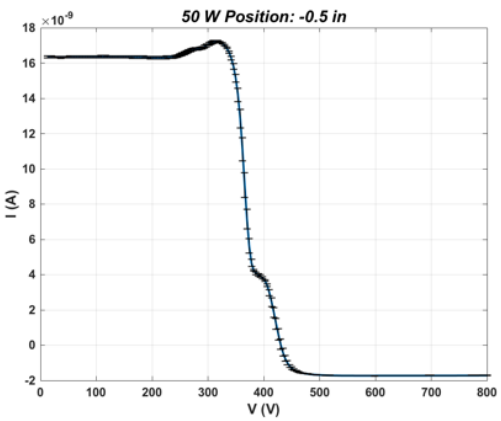
50 W Position: -0.5 in
×10^-9
I (A)
V (V)

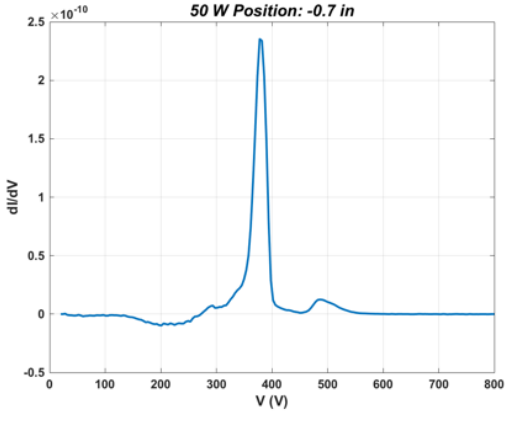
50 W Position: -0.7 in
×10^-10
dI/dV
V (V)

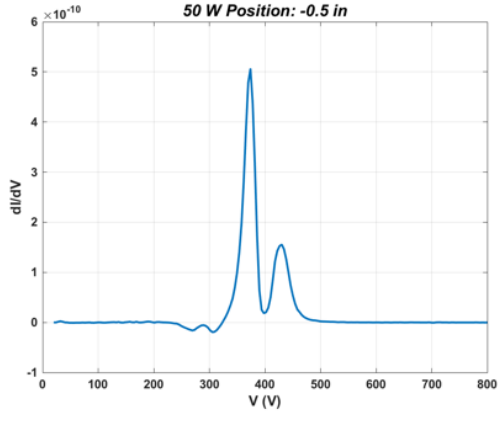
50 W Position: -0.5 in
×10^-10
dI/dV
V (V)

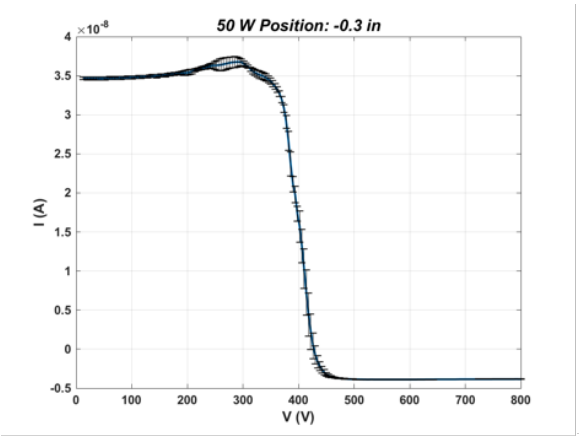
50 W Position: -0.3 in
×10^-8
I (A)
V (V)

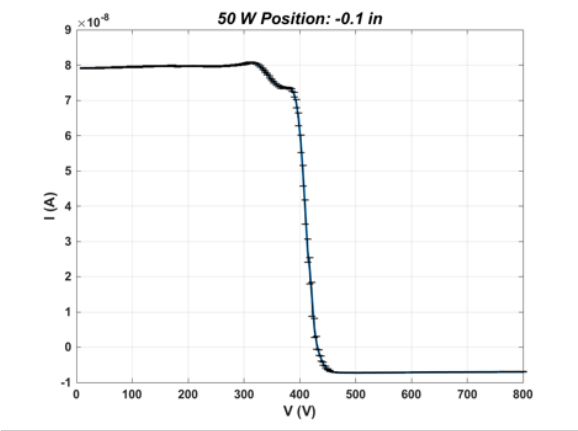
50 W Position: -0.1 in
×10^-8
I (A)
V (V)

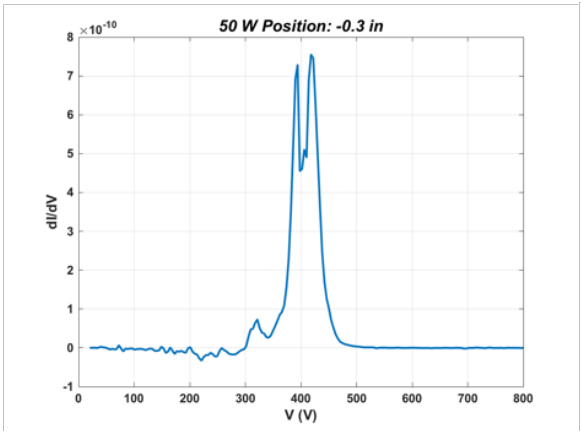
50 W Position: -0.3 in
×10^-10
dI/dV
V (V)

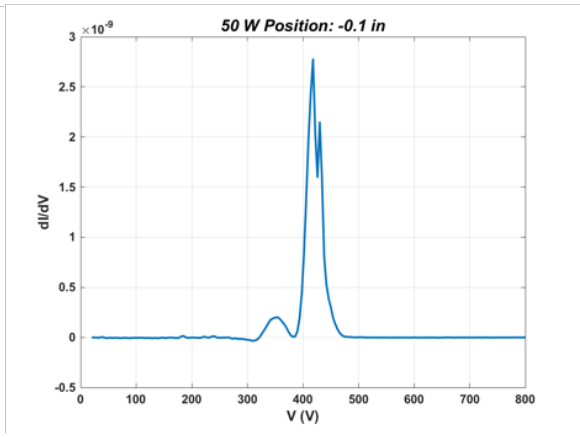
50 W Position: -0.1 in
×10^-9
dI/dV
V (V)

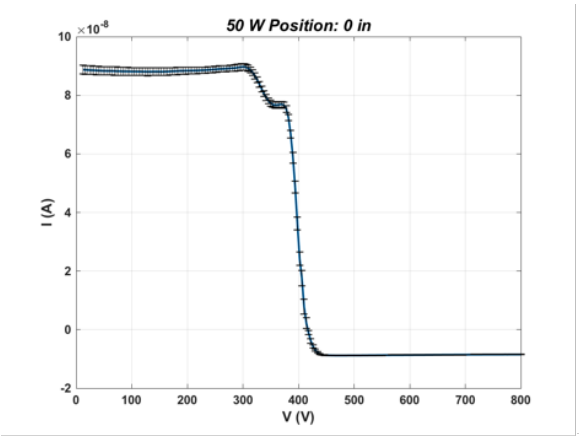
50 W Position: 0 in
×10^-8
I (A)
V (V)

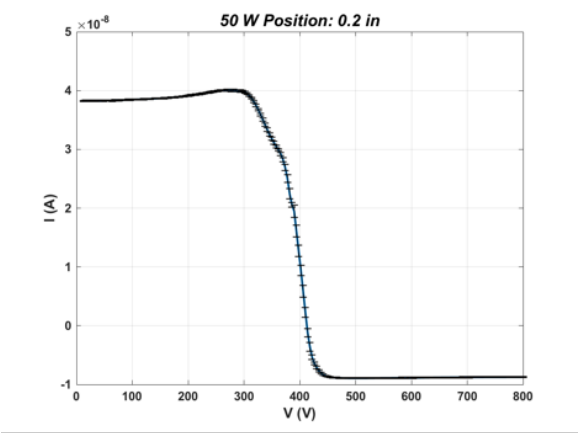
50 W Position: 0.2 in
×10^-8
I (A)
V (V)

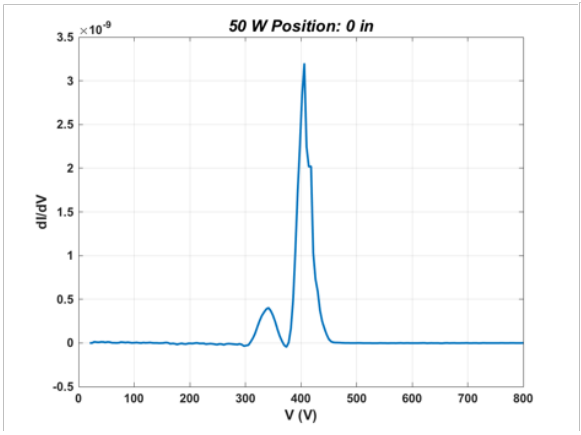
50 W Position: 0 in
×10^-9
dI/dV
V (V)

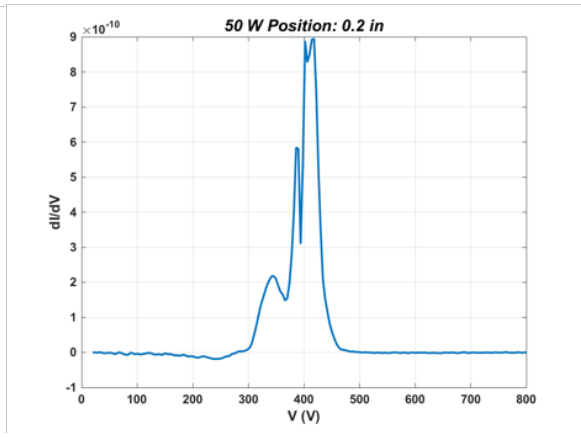
50 W Position: 0.2 in
×10^-10
dI/dV
V (V)

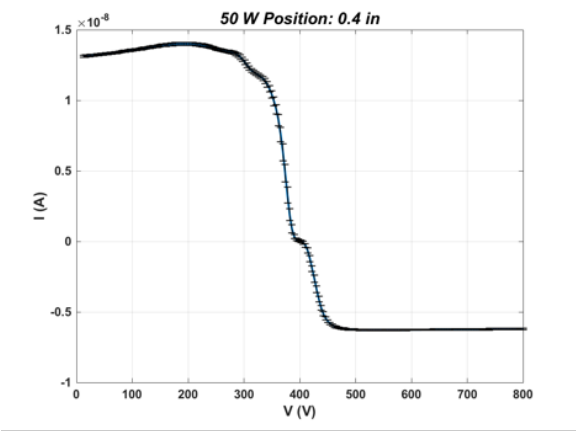
50 W Position: 0.4 in
×10^-8
I (A)
V (V)

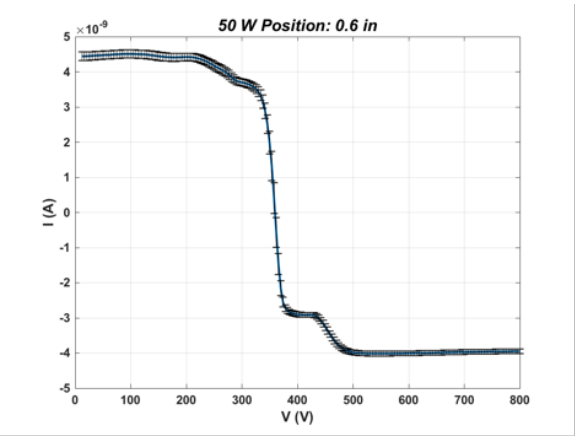
50 W Position: 0.6 in
×10^-9
I (A)
V (V)

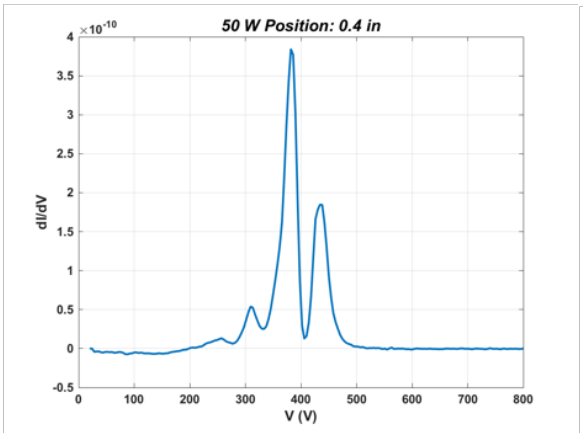
50 W Position: 0.4 in
×10^-10
dI/dV
V (V)

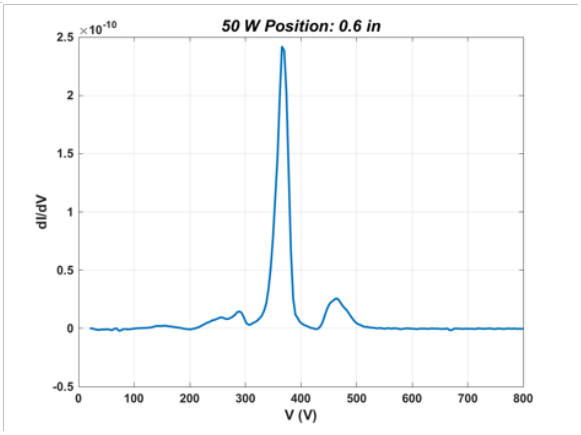
50 W Position: 0.6 in
×10^-10
dI/dV
V (V)

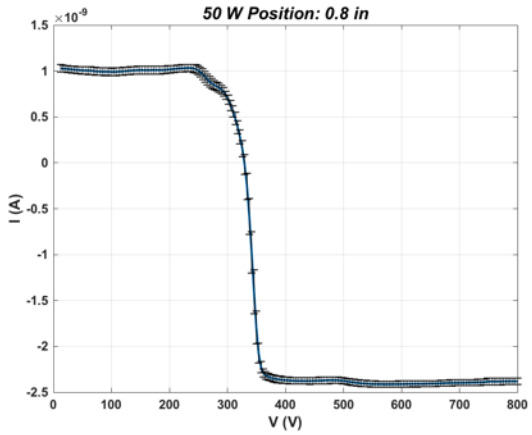
50 W Position: 0.8 in
×10^-9
I (A)
V (V)

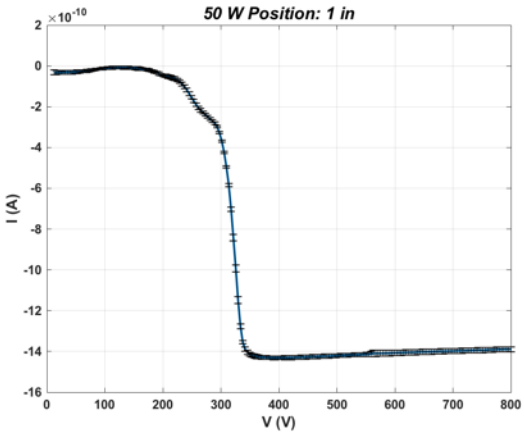
50 W Position: 1 in
×10^-10
I (A)
V (V)

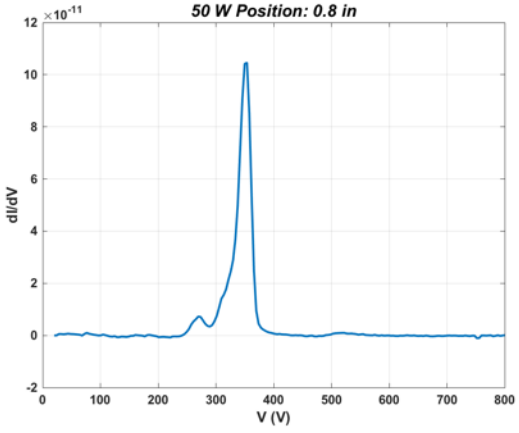
50 W Position: 0.8 in
×10^-11
dI/dV
V (V)

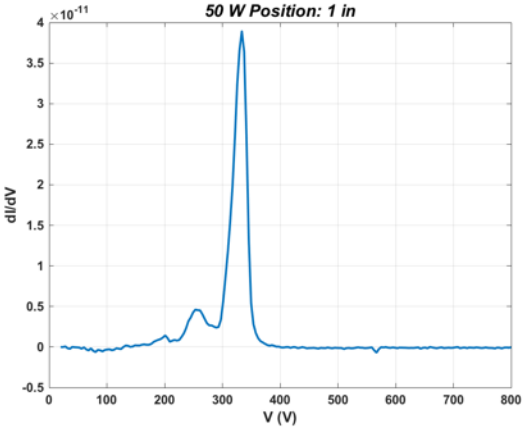
50 W Position: 1 in
×10^-11
dI/dV
V (V)

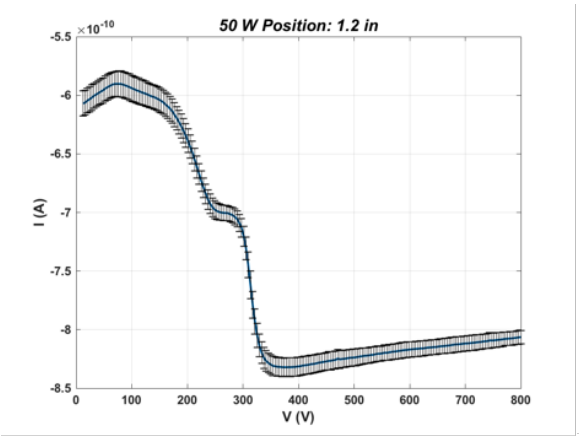
50 W Position: 1.2 in
×10^-10
I (A)
V (V)

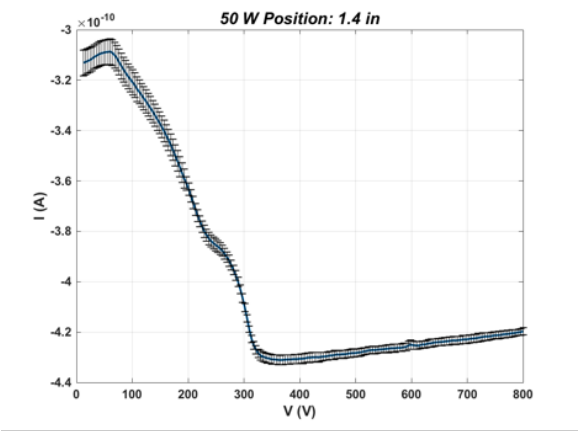
50 W Position: 1.4 in
×10^-10
I (A)
V (V)

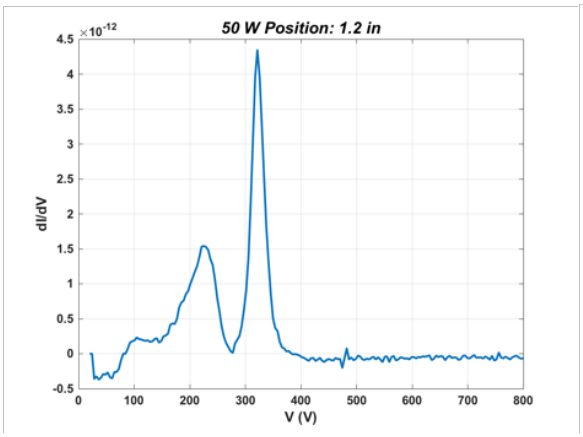
50 W Position: 1.2 in
×10^-12
dI/dV
V (V)

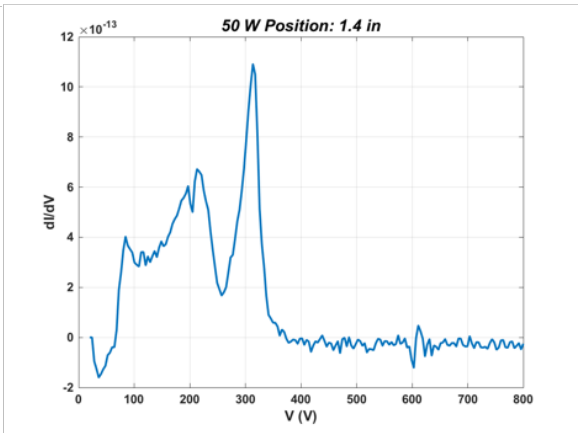
50 W Position: 1.4 in
×10^-13
dI/dV
V (V)

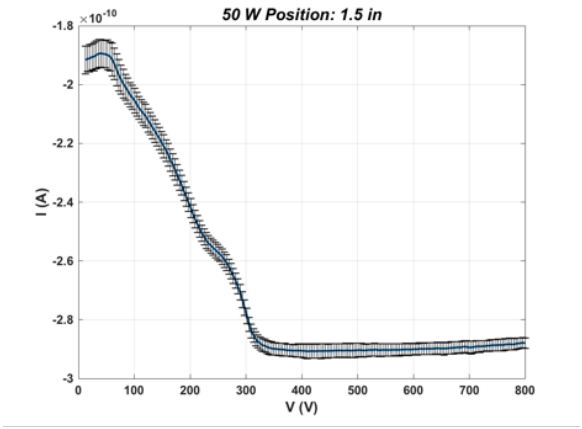
50 W Position: 1.5 in
×10^-10
-1.8
-2
-2.2
-2.4
-2.6
-2.8
-3
I (A)
0
100
200
300
400
500
600
700
800
V (V)

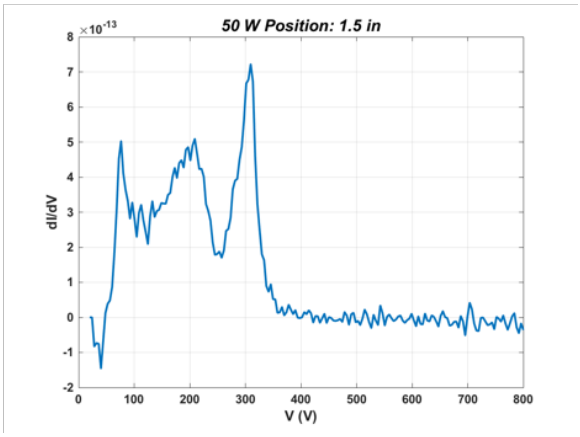
50 W Position: 1.5 in
×10^-13
8
7
6
5
4
3
2
1
0
-1
-2
dI/dV
0
100
200
300
400
500
600
700
800
V (V)

Appendix J: Superconducting Helicon Thruster RPA Data – 50 W Radial Profile

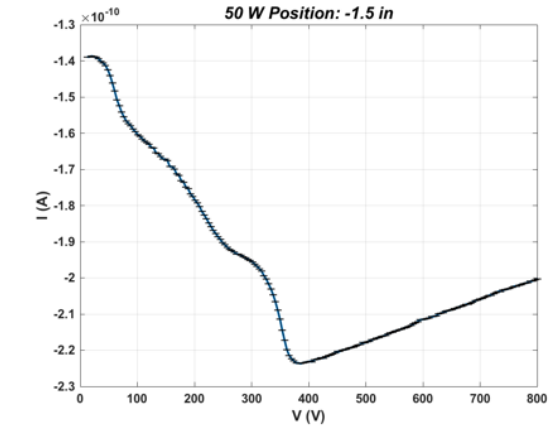

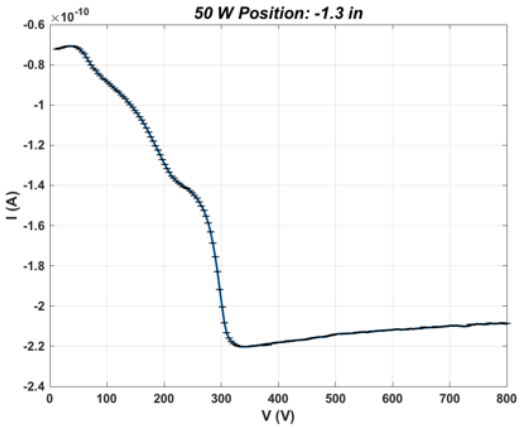

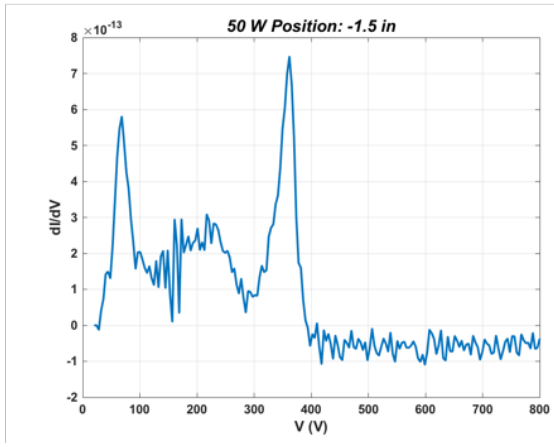

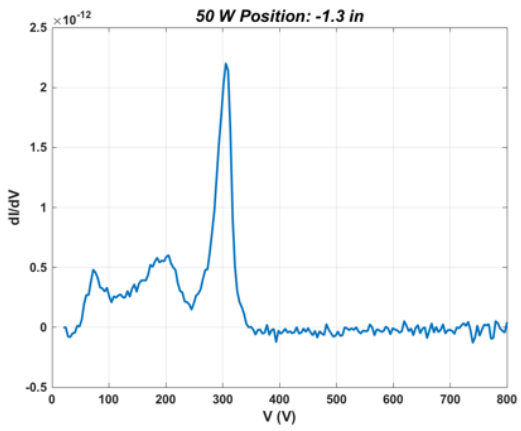

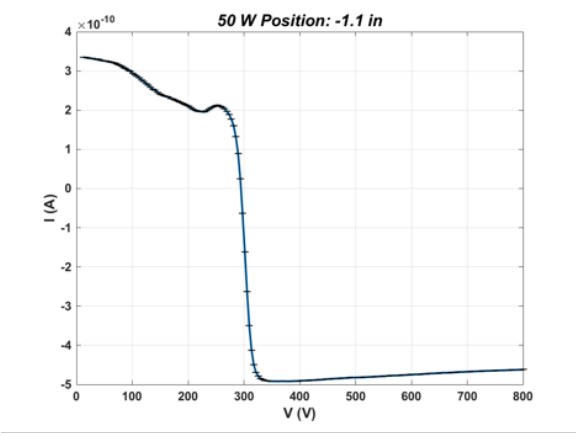
50 W Position: -1.1 in
×10^-10
I (A)
V (V)

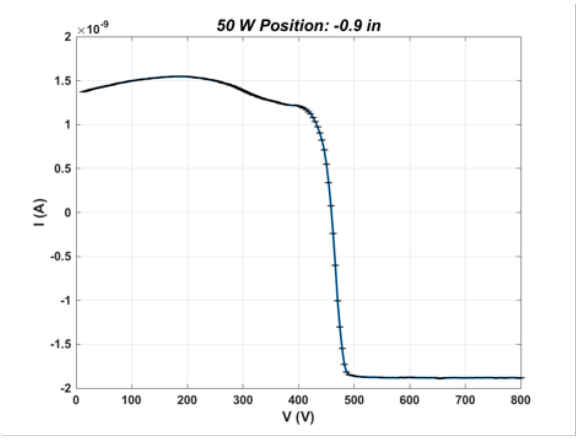
50 W Position: -0.9 in
×10^-9
I (A)
V (V)

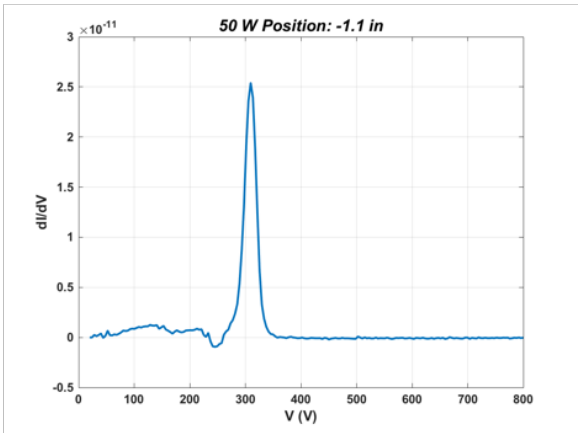
50 W Position: -1.1 in
×10^-11
dI/dV
V (V)

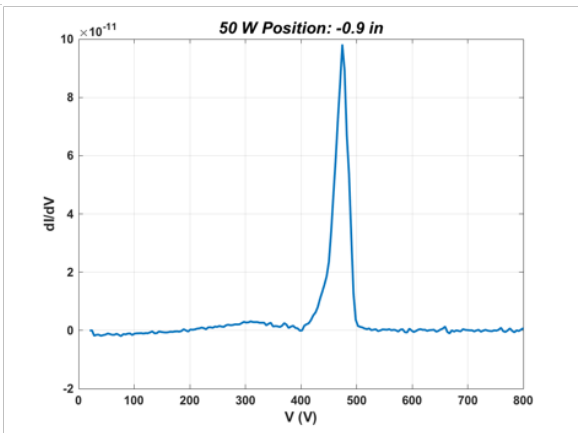
50 W Position: -0.9 in
×10^-11
dI/dV
V (V)

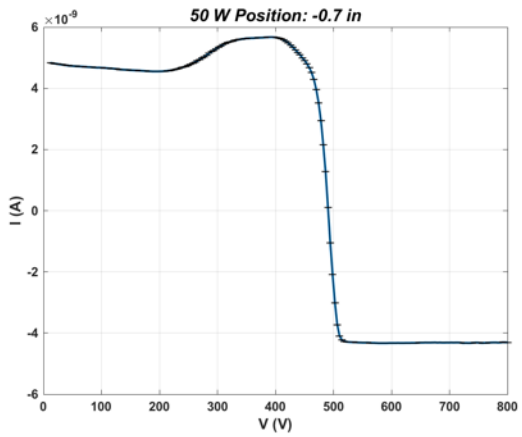
50 W Position: -0.7 in
×10^-9
I (A)
V (V)

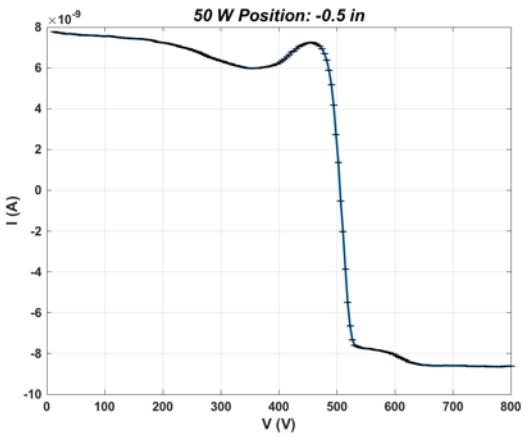
50 W Position: -0.5 in
×10^-9
I (A)
V (V)

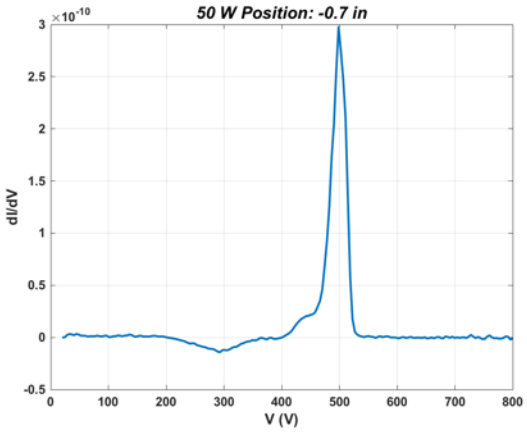
50 W Position: -0.7 in
×10^-10
dI/dV
V (V)

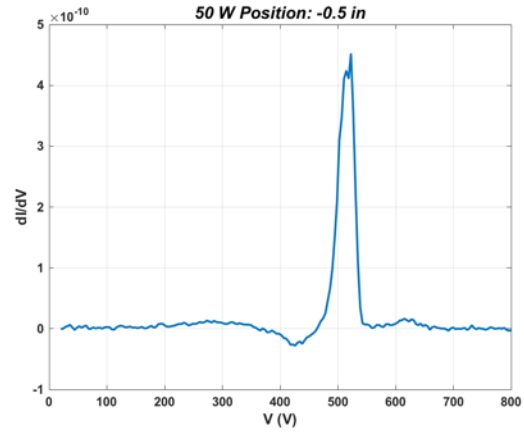
50 W Position: -0.5 in
×10^-10
dI/dV
V (V)

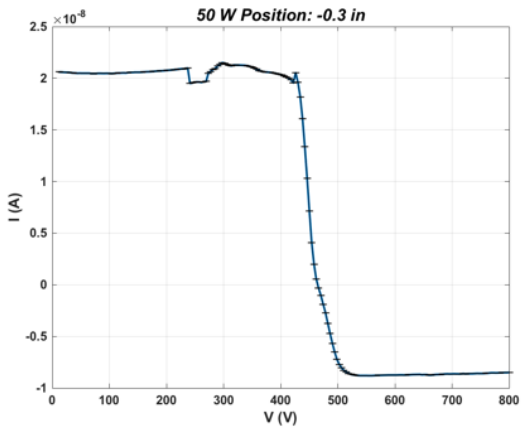
50 W Position: -0.3 in
×10^-8
I (A)
V (V)

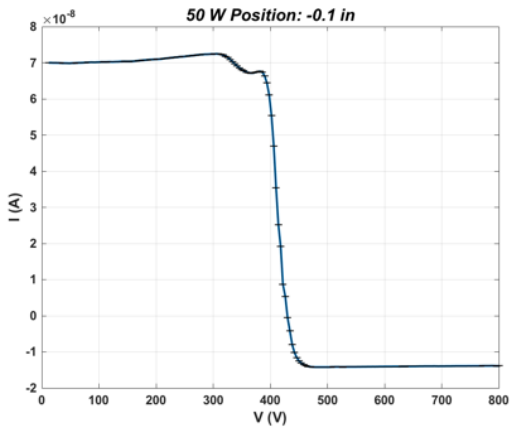
50 W Position: -0.1 in
×10^-8
I (A)
V (V)

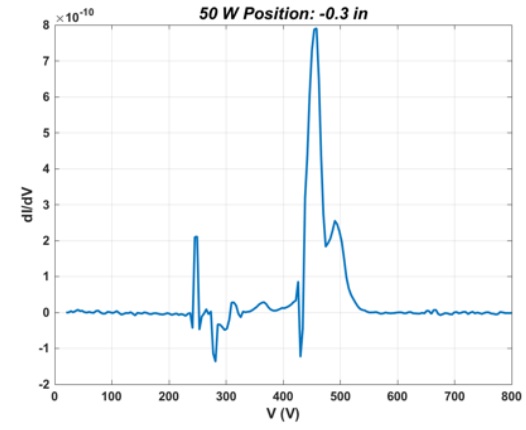
50 W Position: -0.3 in
×10^-10
dI/dV
V (V)

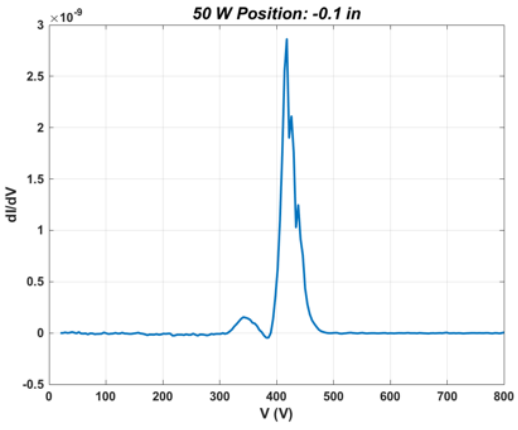
50 W Position: -0.1 in
×10^-9
dI/dV
V (V)

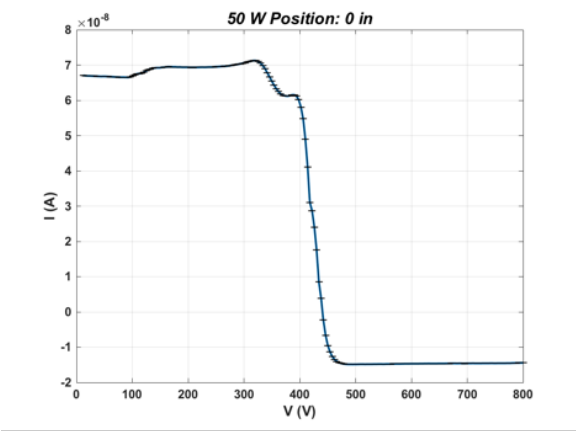
50 W Position: 0 in
×10^-8
I (A)
V (V)

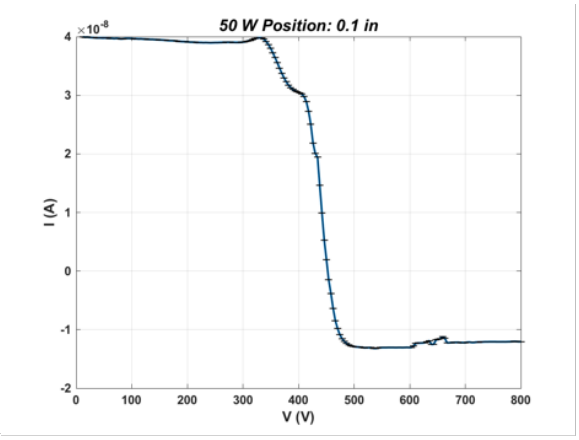
50 W Position: 0.1 in
×10^-8
I (A)
V (V)

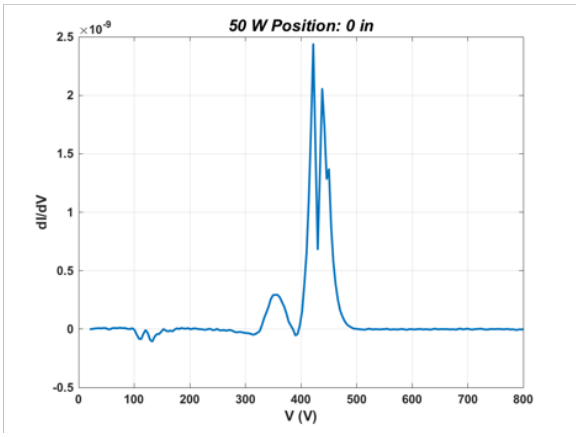
50 W Position: 0 in
×10^-9
dI/dV
V (V)

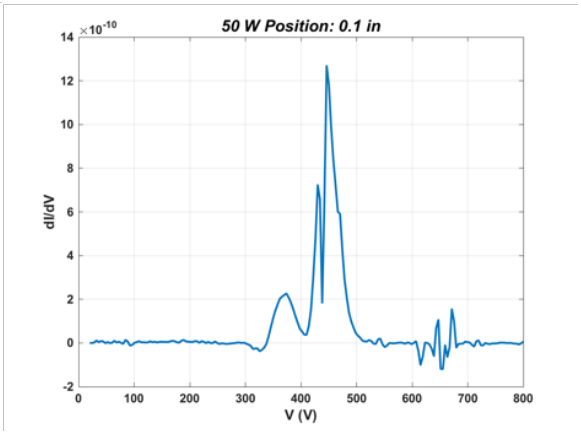
50 W Position: 0.1 in
×10^-10
dI/dV
V (V)

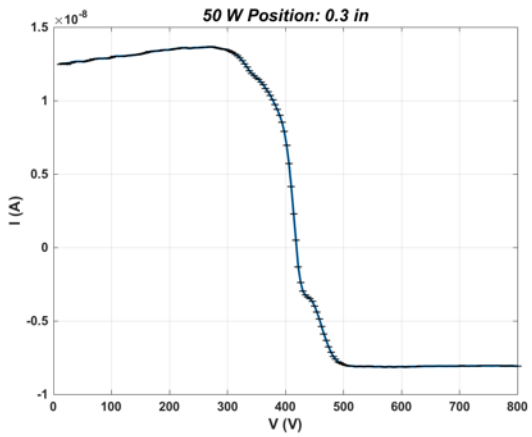
50 W Position: 0.3 in
×10^-8
I (A)
V (V)

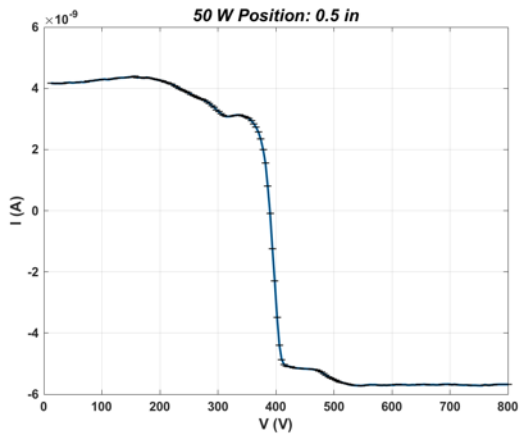
50 W Position: 0.5 in
×10^-9
I (A)
V (V)

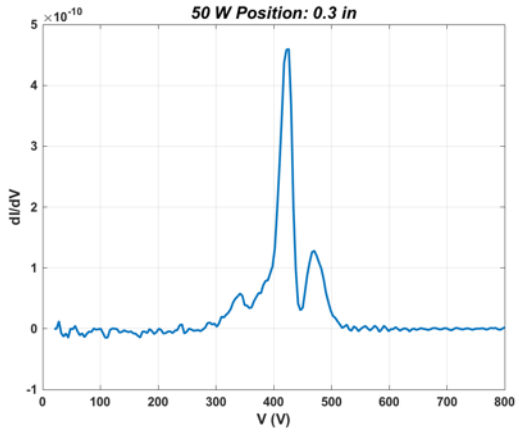
50 W Position: 0.3 in
×10^-10
dI/dV
V (V)

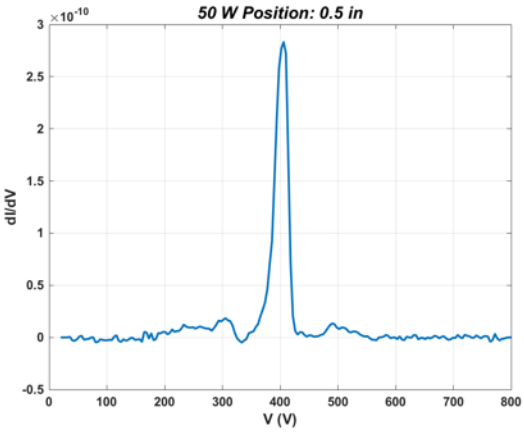
50 W Position: 0.5 in
×10^-10
dI/dV
V (V)

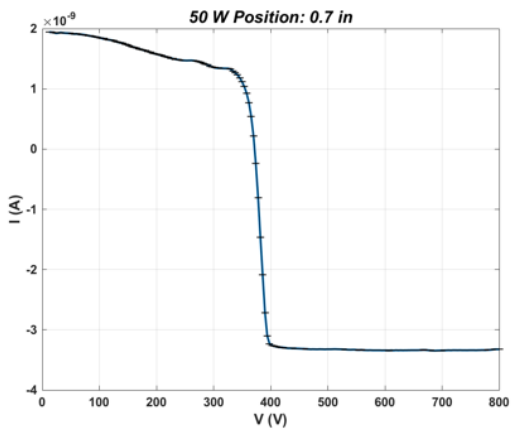
50 W Position: 0.7 in
×10^-9
I (A)
V (V)

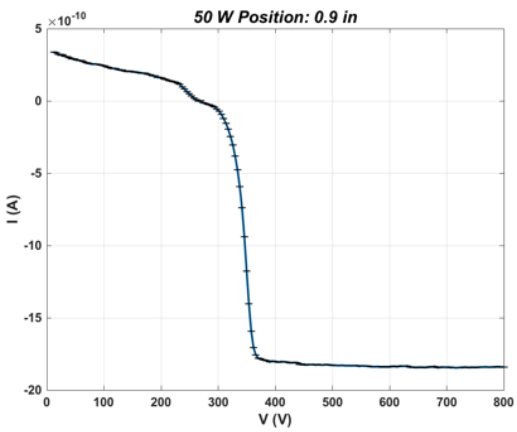
50 W Position: 0.9 in
×10^-10
I (A)
V (V)

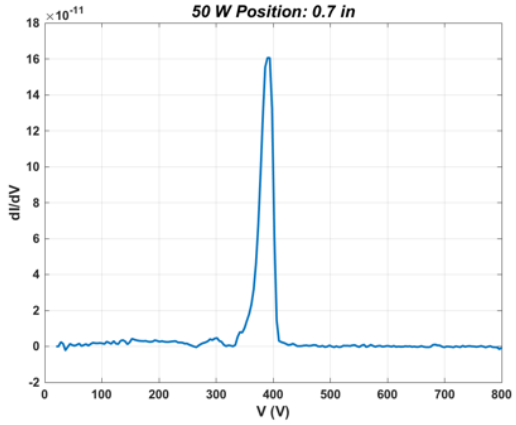
50 W Position: 0.7 in
×10^-11
dI/dV
V (V)

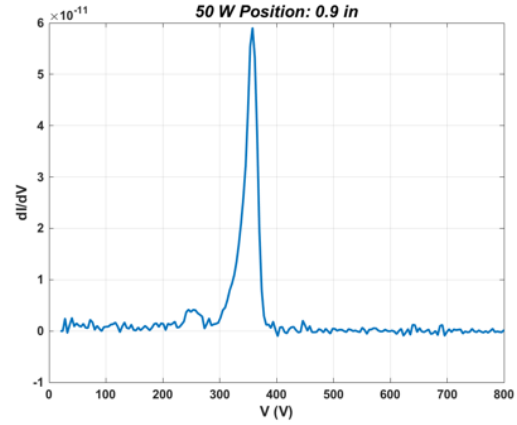
50 W Position: 0.9 in
×10^-11
dI/dV
V (V)

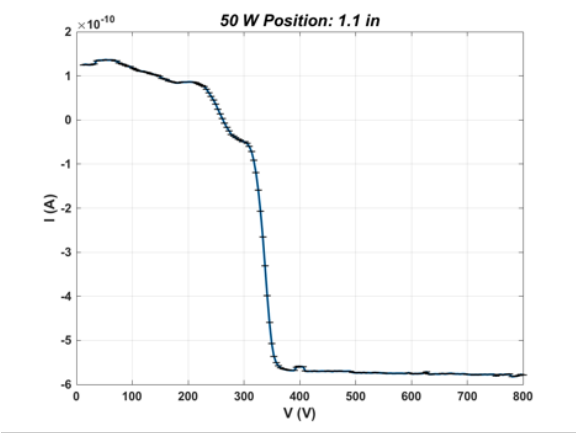
50 W Position: 1.1 in
×10^-10
I (A)
V (V)

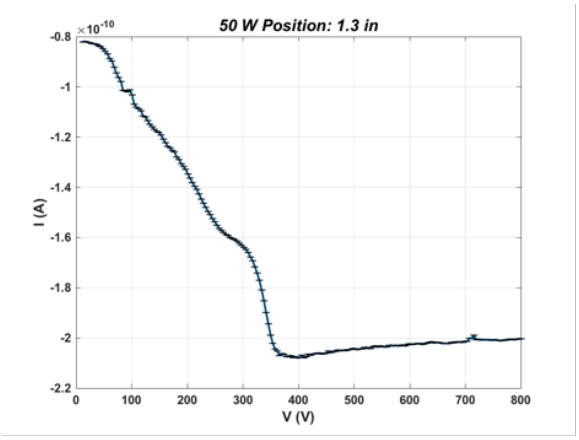
50 W Position: 1.3 in
×10^-10
I (A)
V (V)

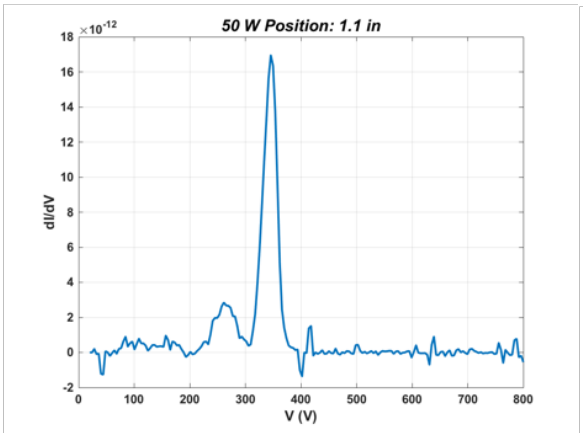
50 W Position: 1.1 in
×10^-12
dI/dV
V (V)

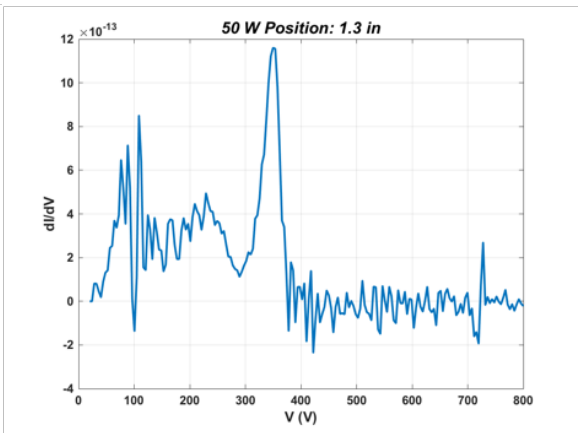
50 W Position: 1.3 in
×10^-13
dI/dV
V (V)

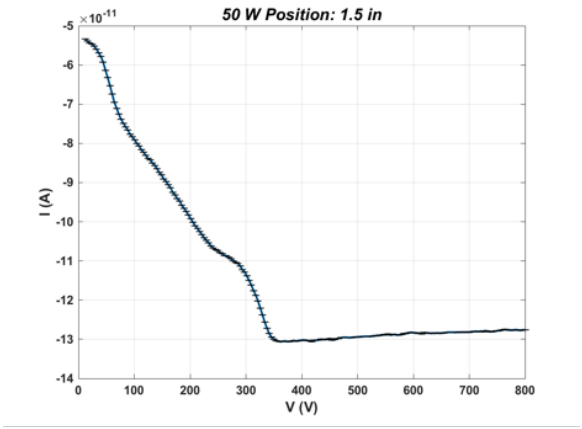
50 W Position: 1.5 in
×10^-11
I (A)
V (V)

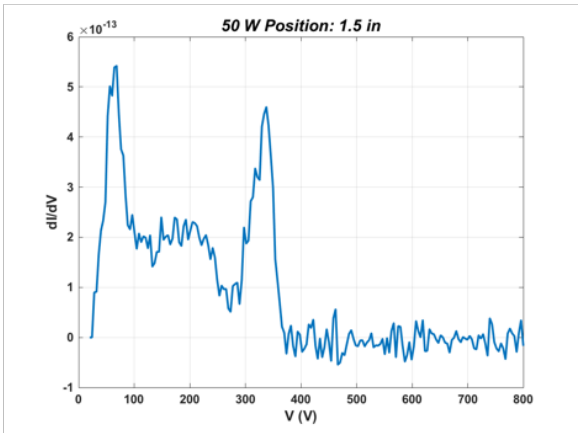
50 W Position: 1.5 in
×10^-13
dI/dV
V (V)

Appendix K: Helicon Thruster Length and Time Scales

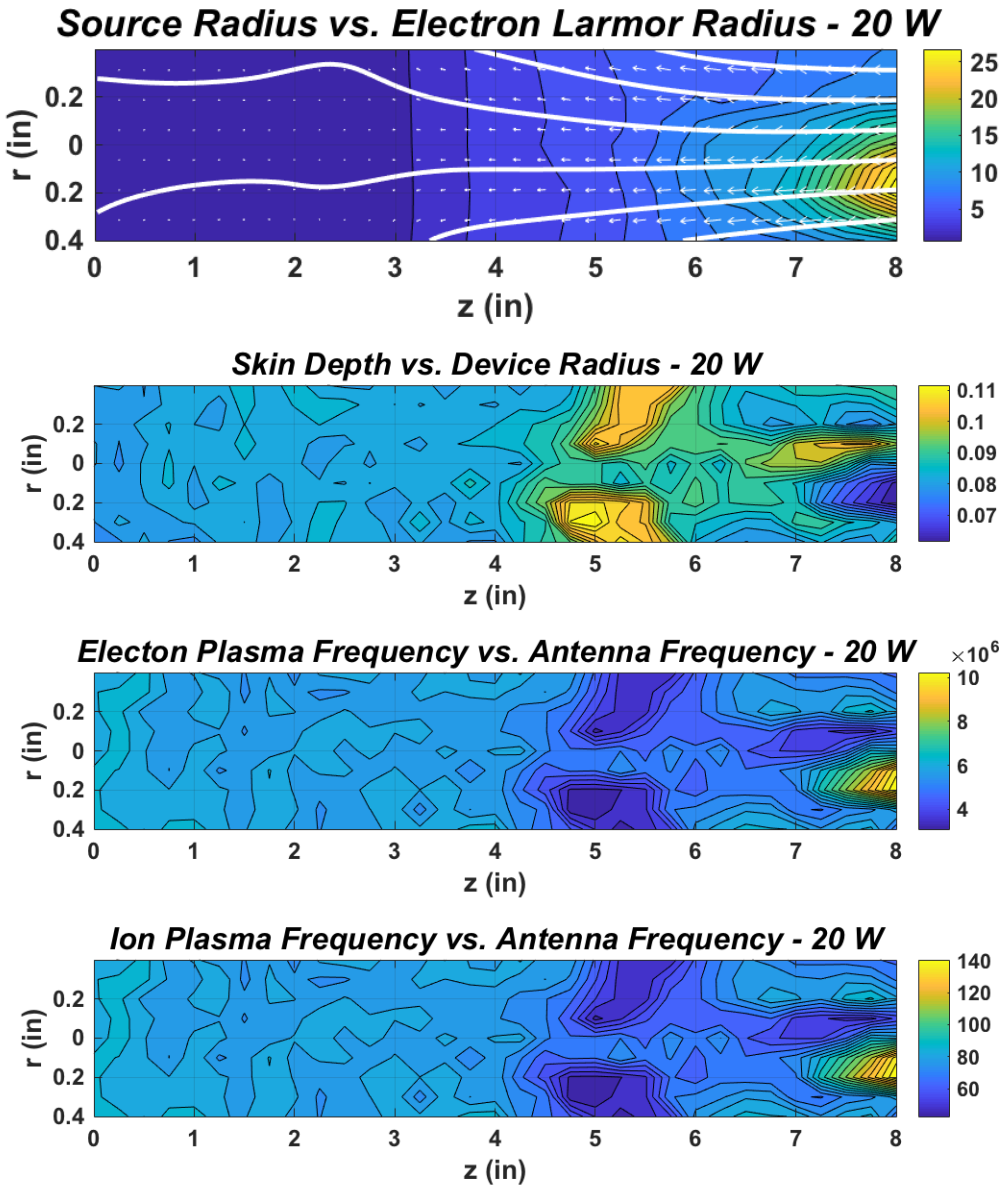

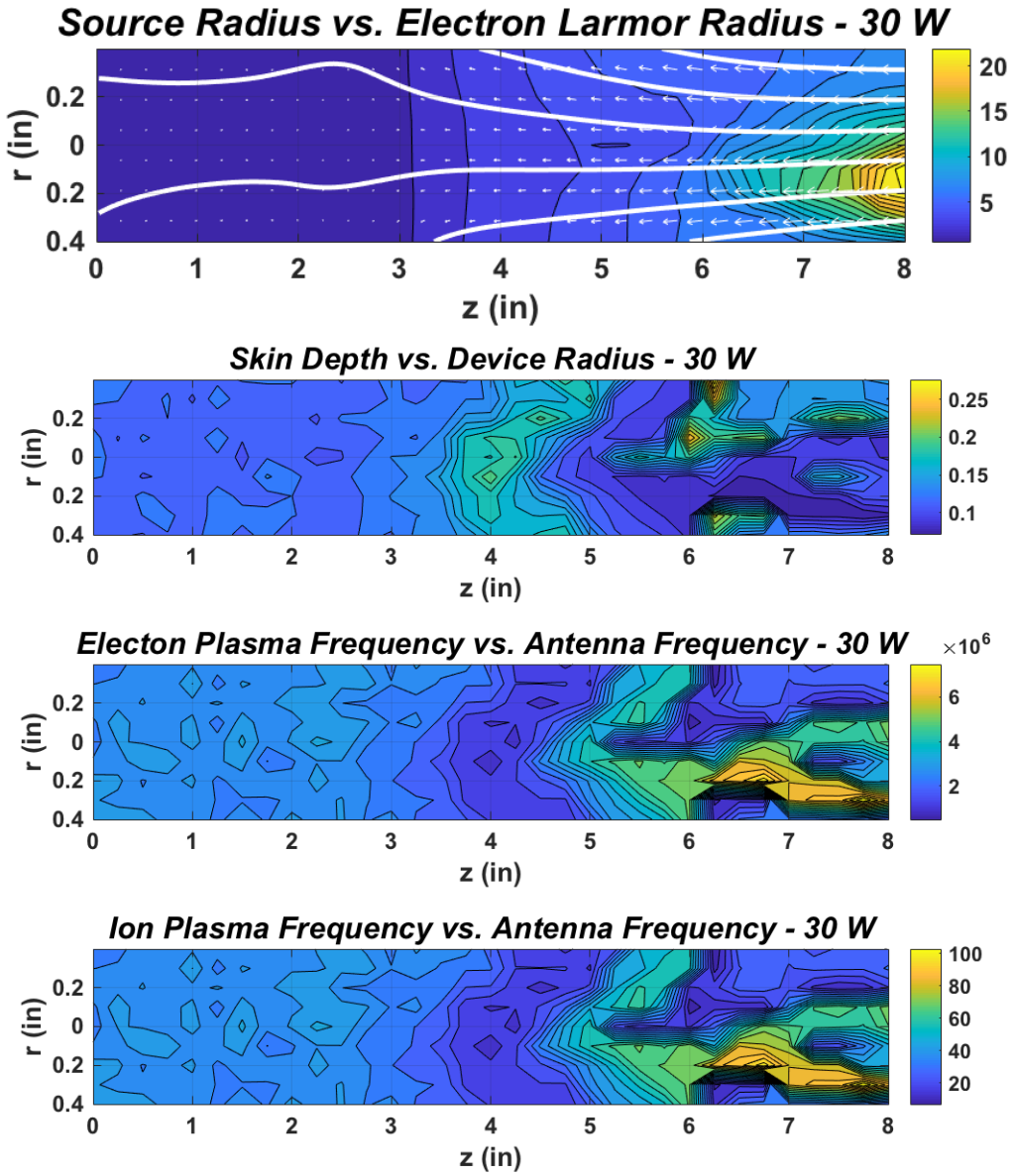
Source Radius vs. Electron Larmor Radius - 30 W
r (in)
z (in)
Skin Depth vs. Device Radius - 30 W
r (in)
z (in)
Electon Plasma Frequency vs. Antenna Frequency - 30 W
×10^6
r (in)
z (in)
Ion Plasma Frequency vs. Antenna Frequency - 30 W
r (in)
z (in)

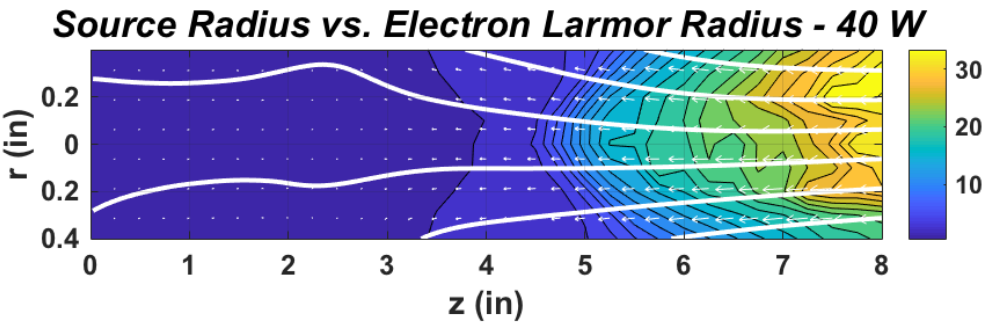
Source Radius vs. Electron Larmor Radius - 40 W
r (in)
z (in)
0.4
0.2
0
0.2
0.4
0
1
2
3
4
5
6
7
8
30
20
10

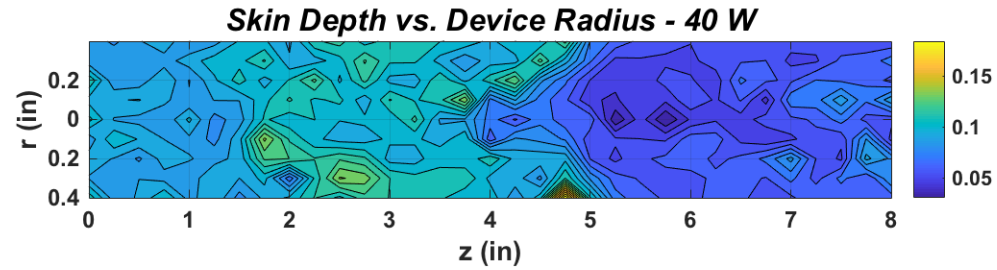
Skin Depth vs. Device Radius - 40 W
r (in)
z (in)
0.2
0
0.2
0.4
0
1
2
3
4
5
6
7
8
0.15
0.1
0.05

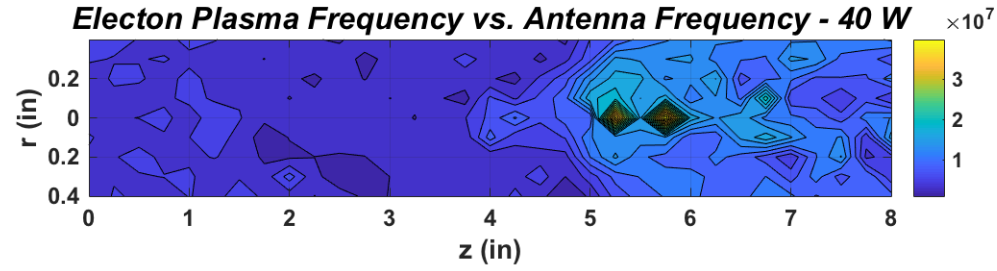
Electon Plasma Frequency vs. Antenna Frequency - 40 W
×10^7
r (in)
z (in)
0.2
0
0.2
0.4
0
1
2
3
4
5
6
7
8
3
2
1

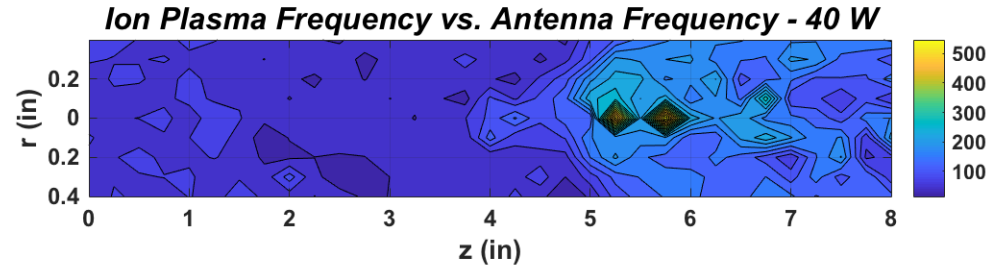
Ion Plasma Frequency vs. Antenna Frequency - 40 W
r (in)
z (in)
0.2
0
0.2
0.4
0
1
2
3
4
5
6
7
8
500
400
300
200
100

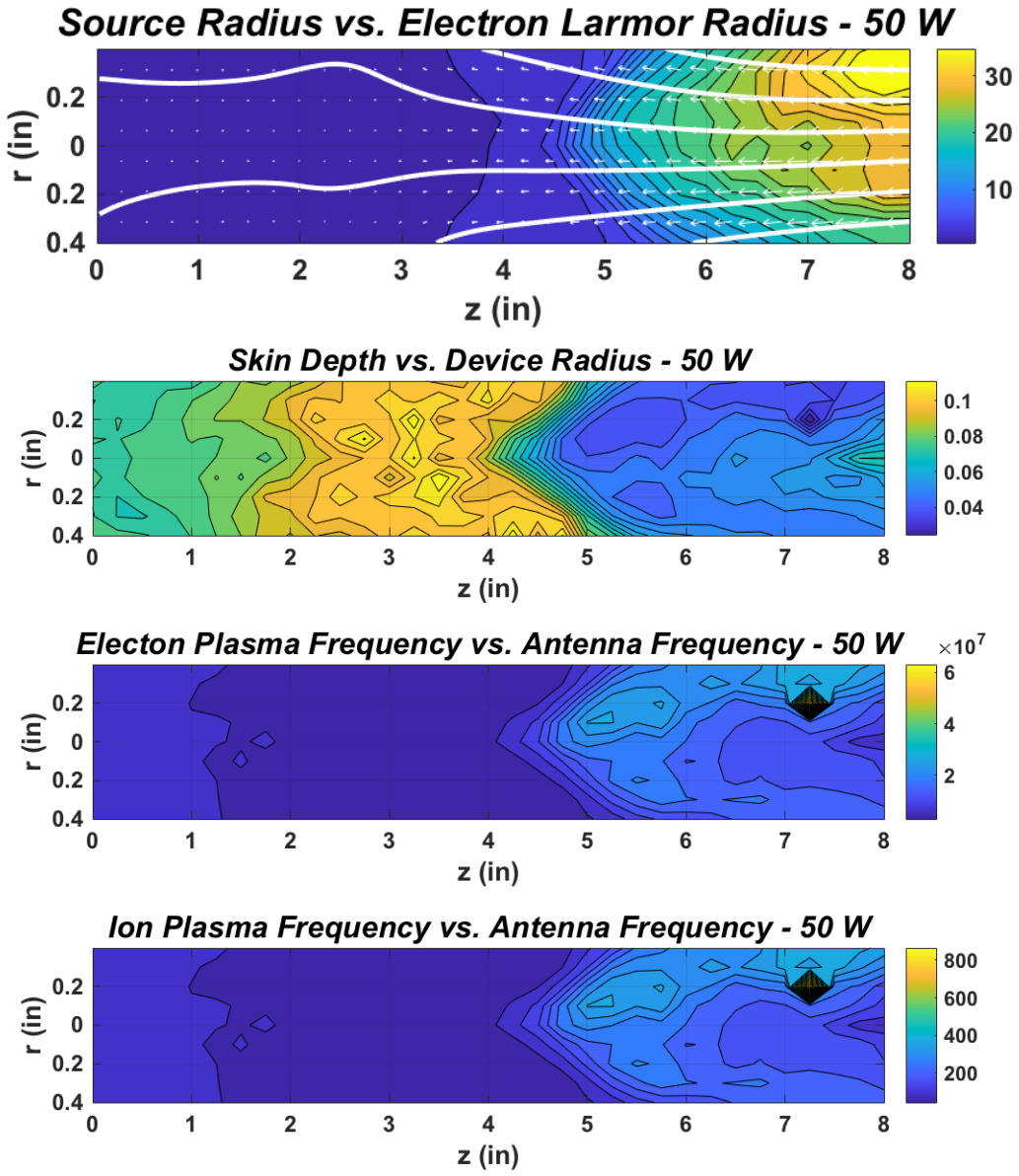
Source Radius vs. Electron Larmor Radius - 50 W
r (in)
z (in)
Skin Depth vs. Device Radius - 50 W
r (in)
z (in)
Electon Plasma Frequency vs. Antenna Frequency - 50 W
×10^7
r (in)
z (in)
Ion Plasma Frequency vs. Antenna Frequency - 50 W
r (in)
z (in)

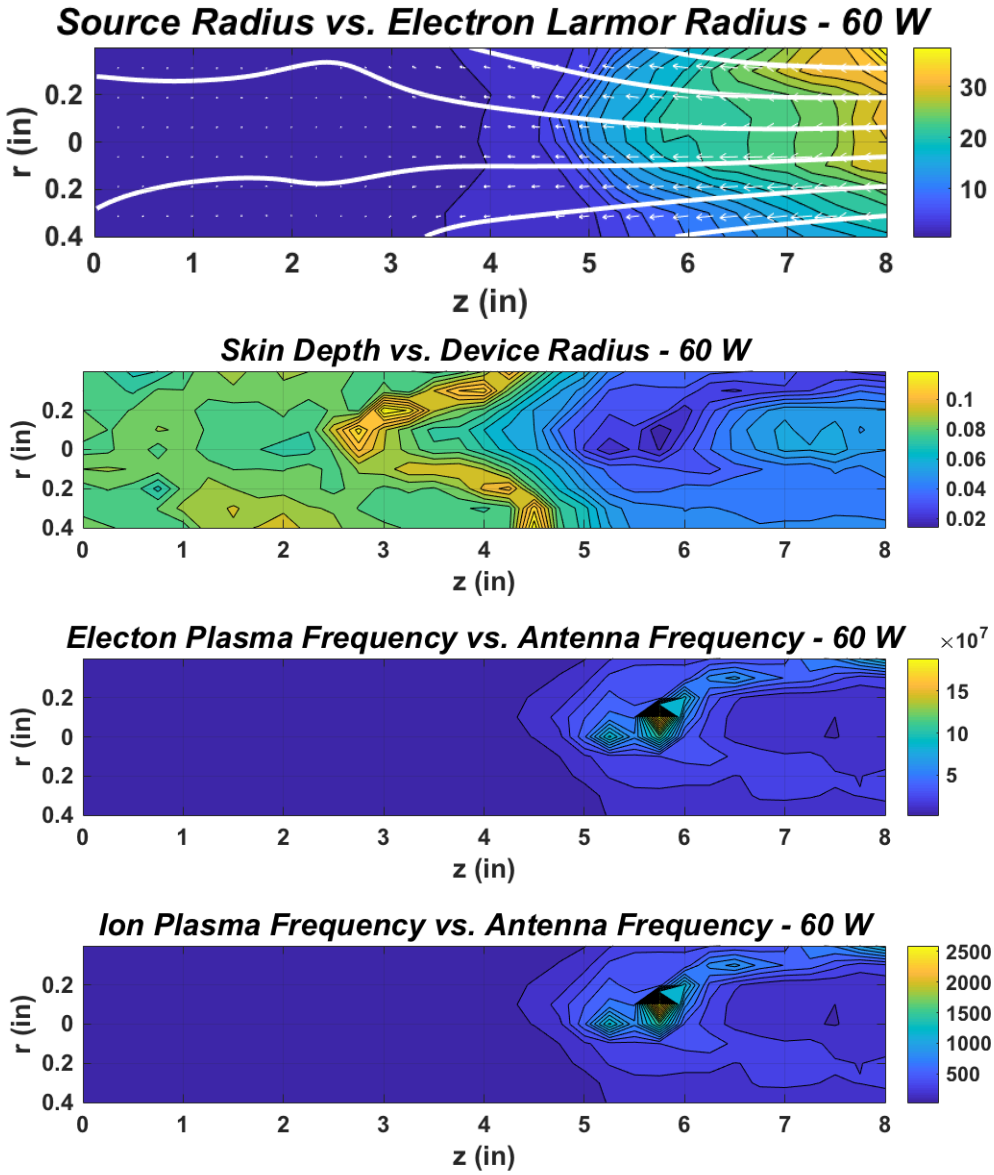
Source Radius vs. Electron Larmor Radius - 60 W
r (in)
z (in)
Skin Depth vs. Device Radius - 60 W
r (in)
z (in)
Electon Plasma Frequency vs. Antenna Frequency - 60 W
×10^7
r (in)
z (in)
Ion Plasma Frequency vs. Antenna Frequency - 60 W
r (in)
z (in)

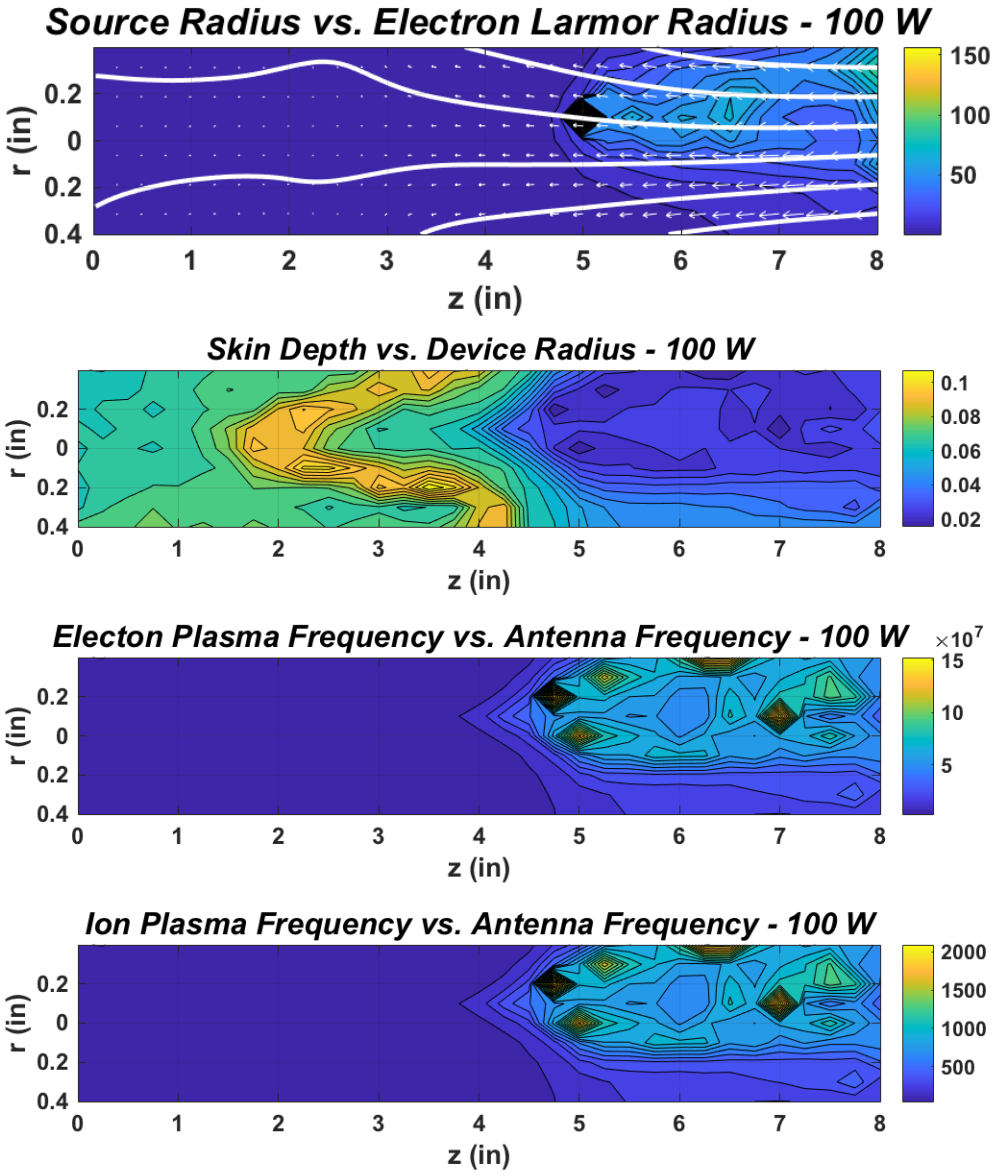
Source Radius vs. Electron Larmor Radius - 100 W
r (in)
z (in)
150
100
50
Skin Depth vs. Device Radius - 100 W
0.1
0.08
0.06
0.04
0.02
Electon Plasma Frequency vs. Antenna Frequency - 100 W
×10^7
15
10
5
Ion Plasma Frequency vs. Antenna Frequency - 100 W
2000
1500
1000
500

Appendix L: Superconducting Helicon Thruster Length and Time Scales

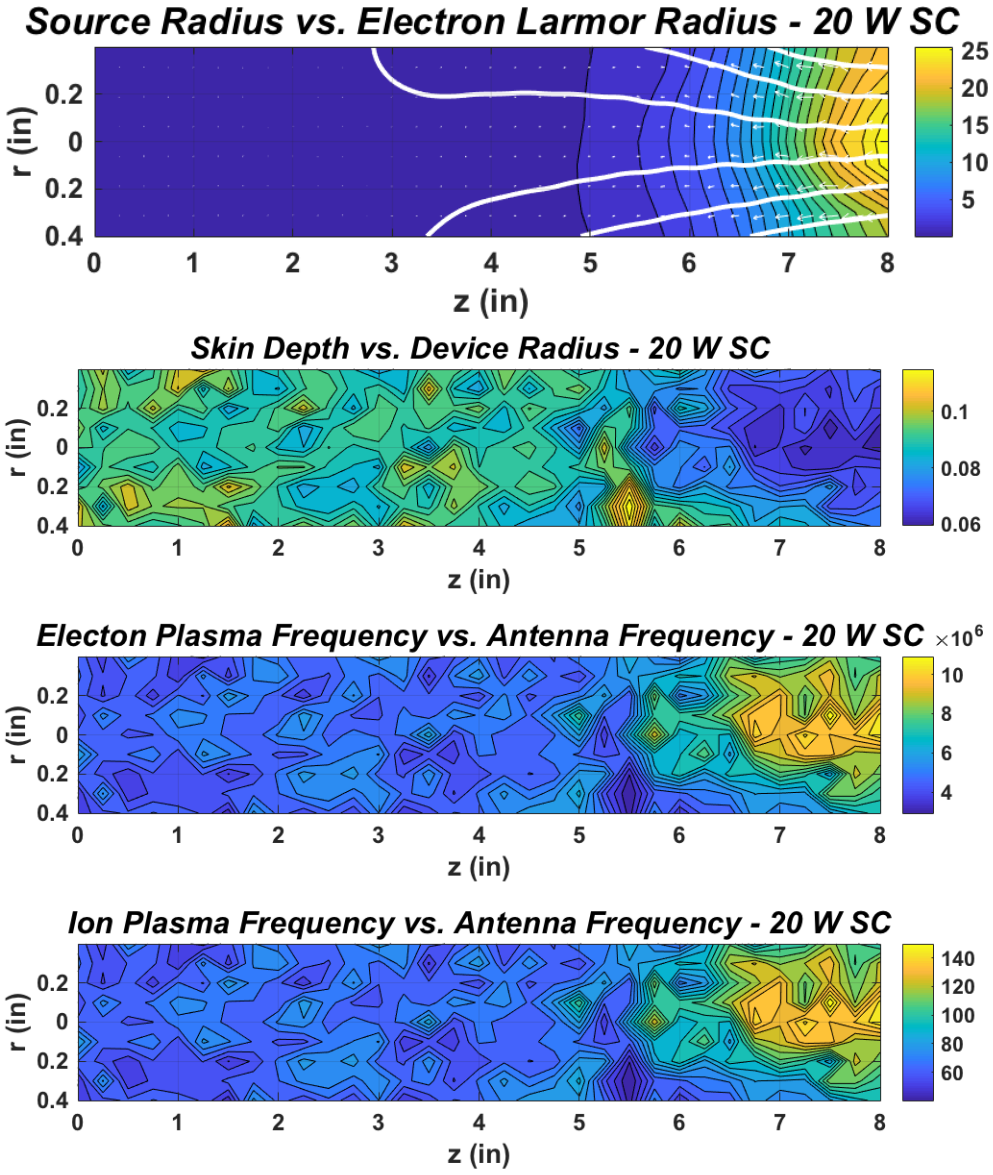

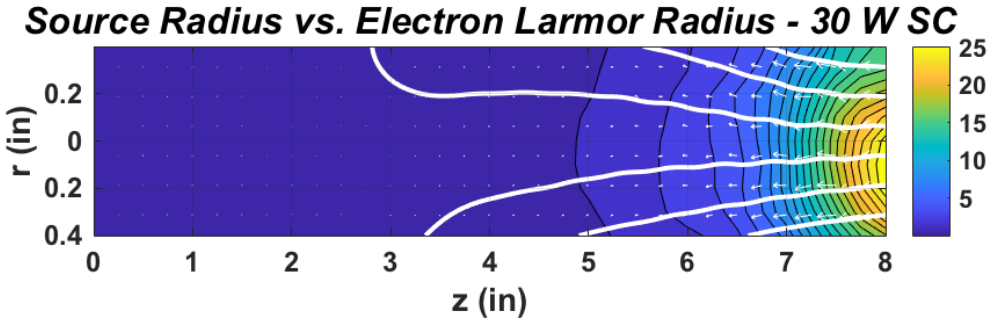
Source Radius vs. Electron Larmor Radius - 30 W SC
r (in)
z (in)
0.2
0
0.2
0.4
0
1
2
3
4
5
6
7
8
25
20
15
10
5

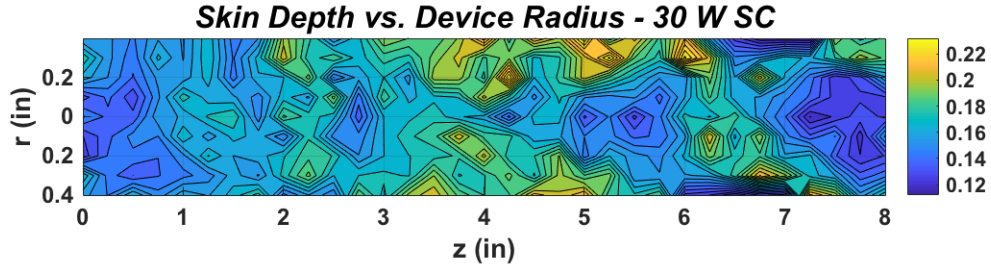
Skin Depth vs. Device Radius - 30 W SC
r (in)
z (in)
0.2
0
0.2
0.4
0
1
2
3
4
5
6
7
8
0.22
0.2
0.18
0.16
0.14
0.12

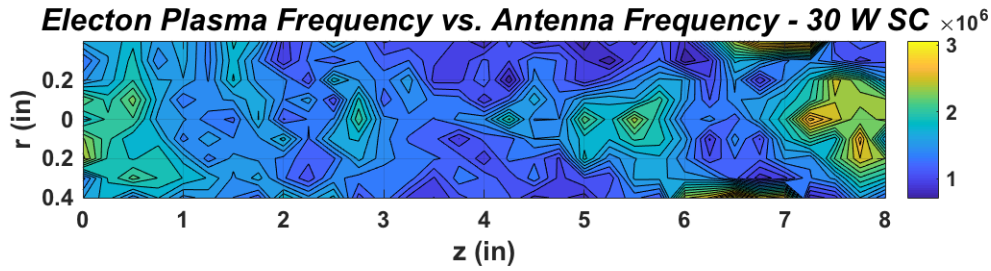
Electon Plasma Frequency vs. Antenna Frequency - 30 W SC
×10^6
r (in)
z (in)
0.2
0
0.2
0.4
0
1
2
3
4
5
6
7
8
3
2
1

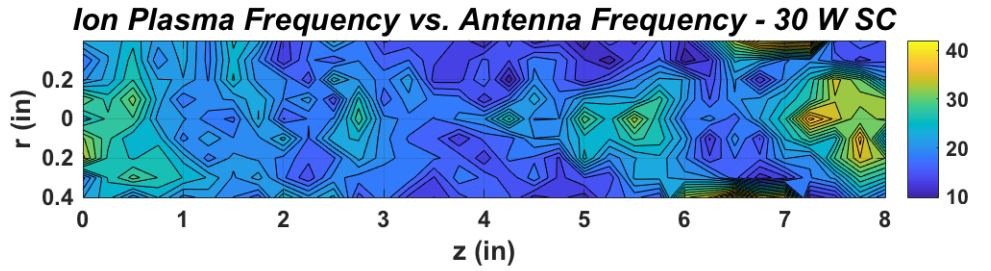
Ion Plasma Frequency vs. Antenna Frequency - 30 W SC
r (in)
z (in)
0.2
0
0.2
0.4
0
1
2
3
4
5
6
7
8
40
30
20
10

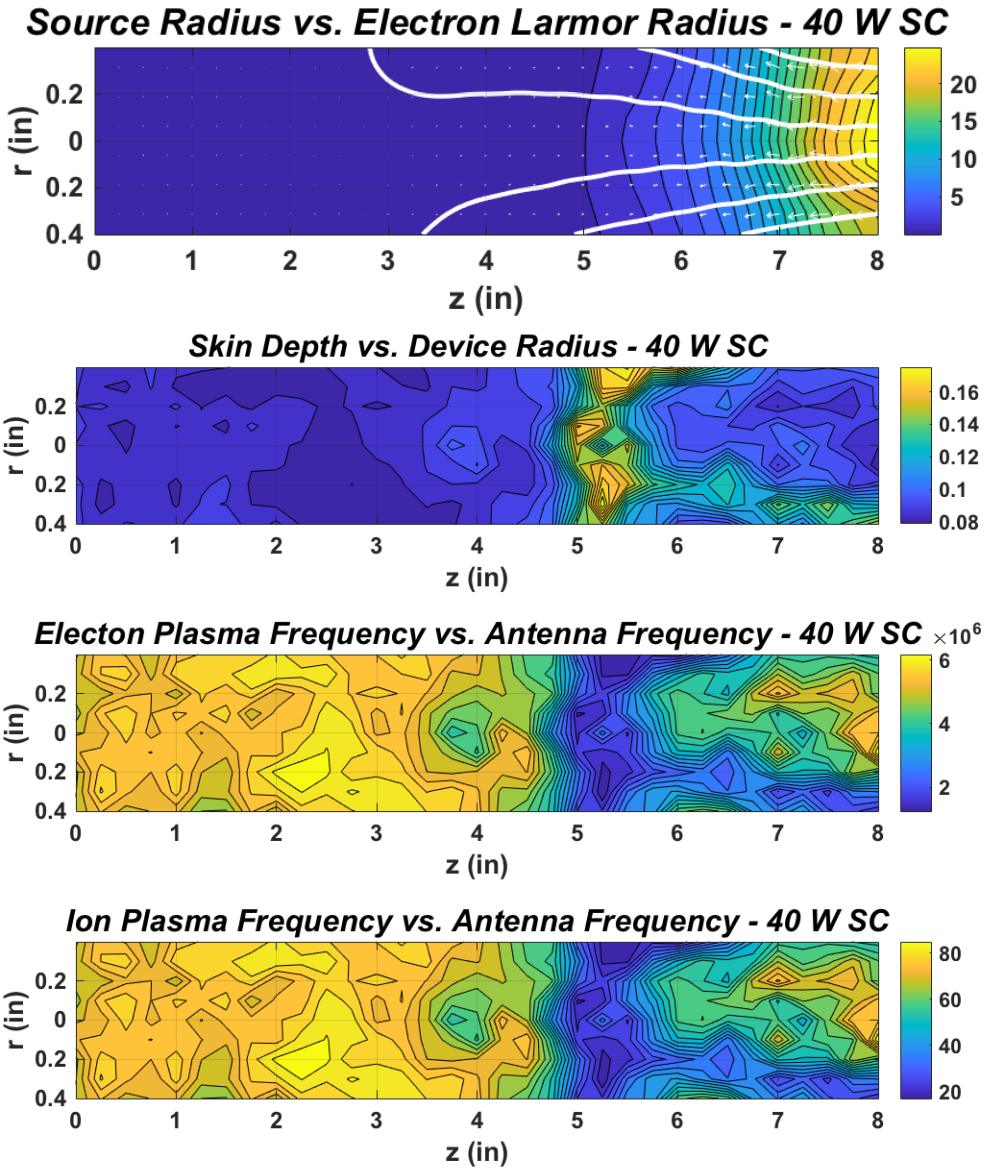
Source Radius vs. Electron Larmor Radius - 40 W SC
r (in)
z (in)
Skin Depth vs. Device Radius - 40 W SC
Electon Plasma Frequency vs. Antenna Frequency - 40 W SC
×10^6
Ion Plasma Frequency vs. Antenna Frequency - 40 W SC

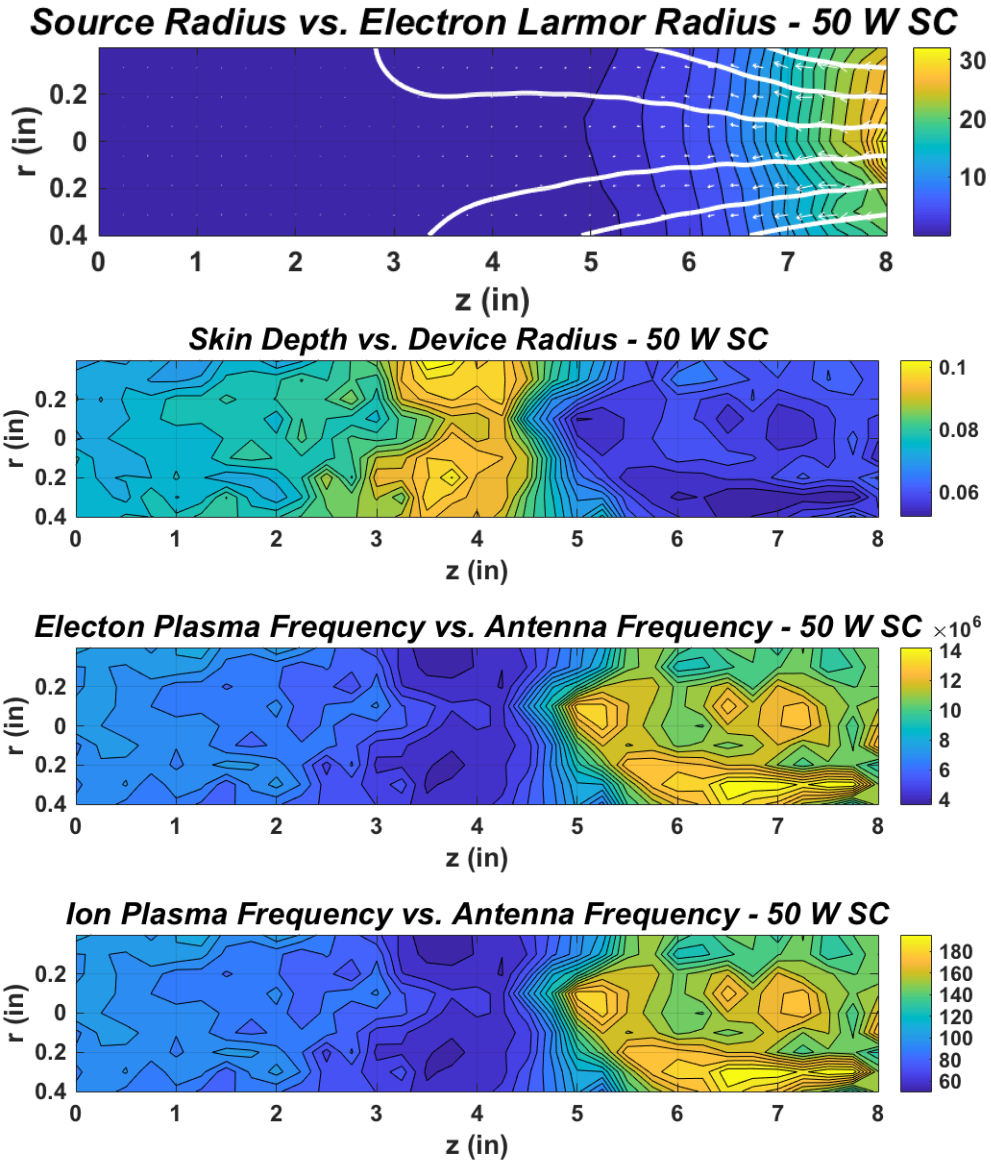
Source Radius vs. Electron Larmor Radius - 50 W SC
r (in)
z (in)
Skin Depth vs. Device Radius - 50 W SC
r (in)
z (in)
Electon Plasma Frequency vs. Antenna Frequency - 50 W SC
×10^6
r (in)
z (in)
Ion Plasma Frequency vs. Antenna Frequency - 50 W SC
r (in)
z (in)

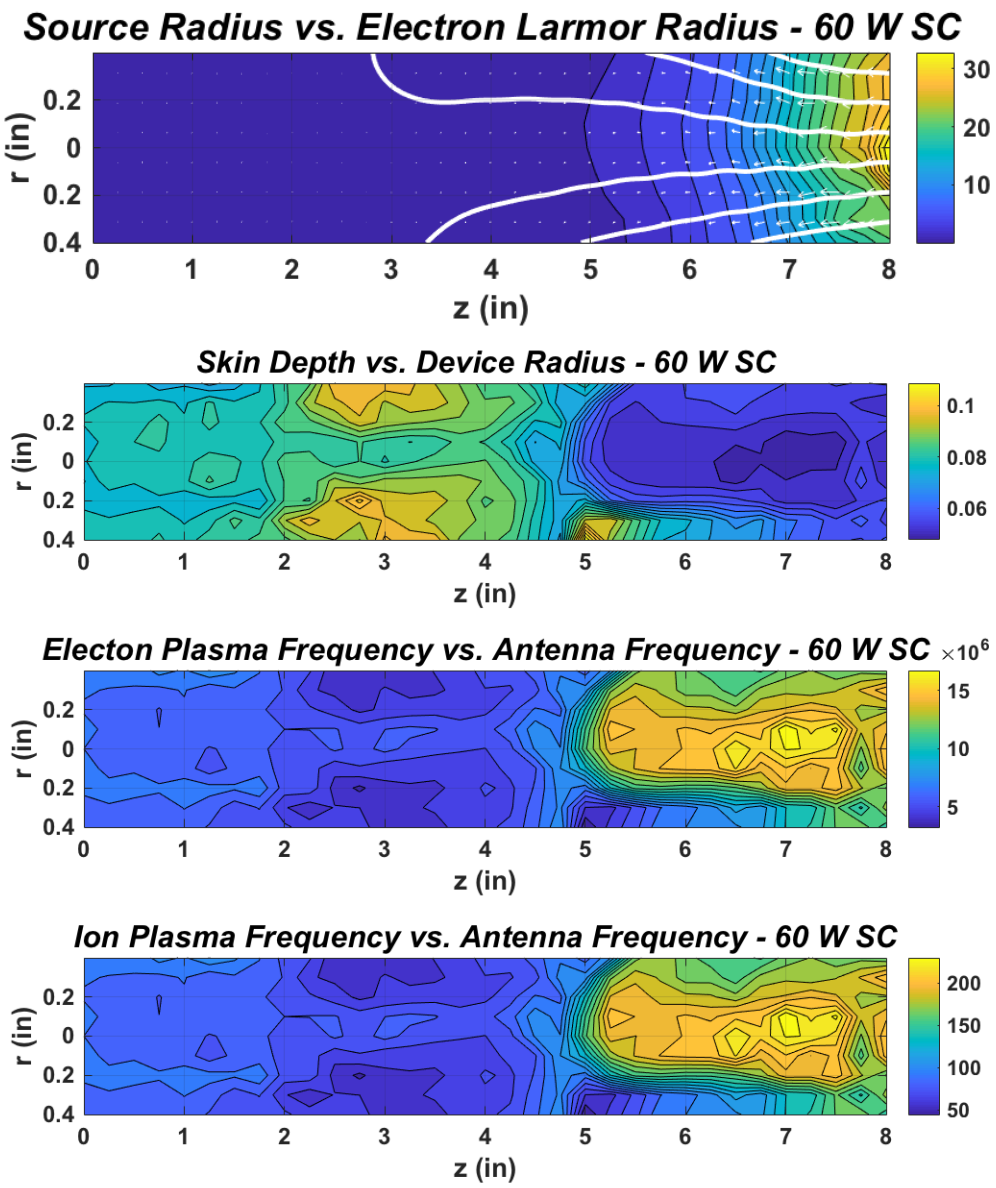
Source Radius vs. Electron Larmor Radius - 60 W SC
r (in)
z (in)
Skin Depth vs. Device Radius - 60 W SC
Electon Plasma Frequency vs. Antenna Frequency - 60 W SC
×10^6
Ion Plasma Frequency vs. Antenna Frequency - 60 W SC

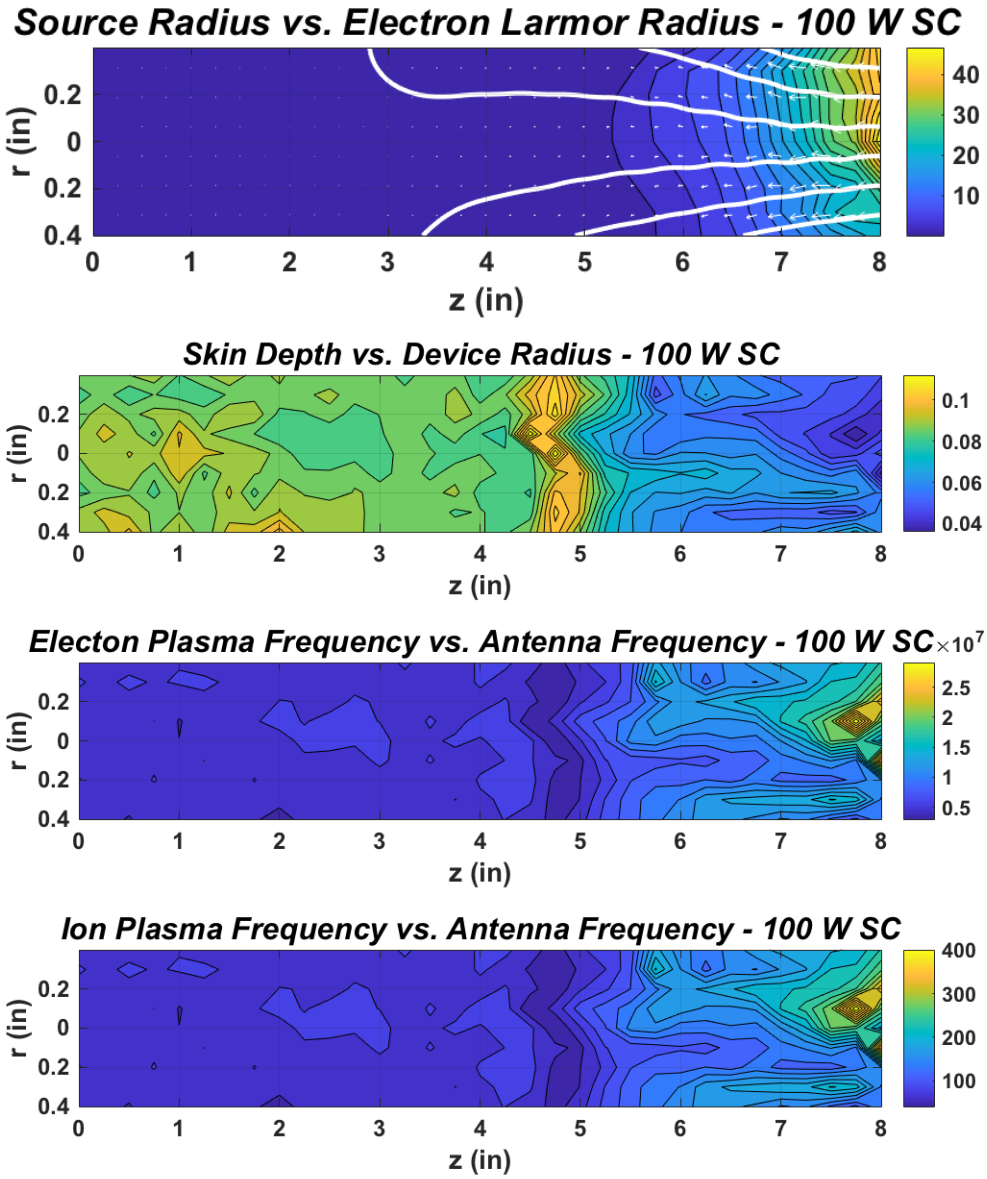
Source Radius vs. Electron Larmor Radius - 100 W SC
r (in)
z (in)
Skin Depth vs. Device Radius - 100 W SC
r (in)
z (in)
Electon Plasma Frequency vs. Antenna Frequency - 100 W SC
×10^7
r (in)
z (in)
Ion Plasma Frequency vs. Antenna Frequency - 100 W SC
r (in)
z (in)

Bibliography

[1] Choueiri, E. Y., "A Critical History of Electric Propulsion: The First 50 Years (1906-1956)," *Journal of Propulsion and Power*, Vol. 20, No. 2, 2004, pp. 193-203.

[2] Sutton, G. P. and Biblarz, O., *Rocket Propulsion Elements,* 7th ed., Wiley-Interscience, New York, 2001, Chap. 19.

[3] Hoskins, W. A. et al, "30 Years of Electric Propulsion Flight Experience at Aerojet Rocketdyne," Paper IEPC-2013-439, *33rd International Electric Propulsion Conference*, Washington D.C., October 2013.

[4] Herman, D. A. et al, "NASA's Evolutionary Xenon Thruster Long-Duration Test Results," *Journal of Propulsion and Power*, Vol. 28, No. 3, 2012, pp. 625-635.

[5] Boswell, R. W., "Very Efficient Plasma Generation by Whistler Waves Near the Lower Hybrid Frequency," *Plasma Phys. And Controlled Fusion*, Vol. 26, No. 10, 1984, pp. 1147-1162.

[6] DeMaio, M., "Development and Test of a Permanent Magnet Helicon Thruster," Masters Thesis, University of Maryland, College Park, 2010.

[7] Charles, C., "Helicon Double-Layer Thrusters," *Proc. 27th Int. Conf. on Plasmas and Ionized Gases*, Eindhoven, July 2005, Topical 5.

[8] Chen, F. F., "Plasma Ionization by Helicon Waves," *Plasma Phys. and Controlled Fusion,* Vol. 33, No. 4, 1991, pp. 339-364.

[9] Sinenian, N., "Propulsion Mechanisms in a Helicon Plasma Thruster," Master's Thesis, Department of Nuclear Science and Engineering and Department of Electrical Engineering and Computer Science, Massachusetts Institute of Technology, Cambridge, MA, 2008.

[10] Faust, A. J. and Sedwick, R. J., "Comparison of Plasma Diagnostics for an Argon and Helium Gas Helicon Thruster," Paper AIAA 2013-3828, *49th AIAA/ASME/SAE/ASEE Joint Propulsion Conference and Exhibit,* San Jose, CA, 2013.

[11] Williams, L. and Walker, M., "Thrust Measurements of a Helicon Plasma Source," Paper AIAA-2011-5893, *47th AIAA/ASME/SAE/ASEE Joint Propulsion Conference & Exhibit,* San Diego, CA, 2011.

[12] Pottinger, S., Lappas, V., Charles, C., and Boswell, R.W., "Performance Characterization of Helicon Double Layer Thruster Using Direct Thrust Measurements," *J. Phys. D: Appl. Phys.*, Vol. 44, 2011, p. 235201.

[13] Takahashi, K., et al., "Direct Thrust Measurements of a Permanent Magnet Helicon Double Layer Thruster," *Appl. Phys Lett.*, Vol. 98, 2011, p. 141503.

[14] Ziemba, T. et al, "High Power Helicon Thruster," Paper AIAA 2005-4119, *41st AIAA/ASME/SAE/ASEE Joint Propulsion Conference & Exhibit*, Tuscon, AZ, 2005.

[15] Manente, M. et al, "Feasibility Study of a Low Power Helicon Thruster," ESA Report, 2008.

[16] Williams, L. and Walker, M., "Initial Performance Evaluation of a Gridded Radio Frequency Ion Thruster," *AIAA Journal of Propulsion and Power*, Vol. 30, No. 3, 2014, pp. 645-655.

[17] Peterson, P., et al., "Performance and Plume Characterization of a Helicon Hall Thruster," Paper IEPC-2011-269, *The 32nd International Electric Propulsion Conference*, Wiesbaden, Germany, September 11-15 2011.

[18] Chang-Díaz, F.R., "The VASIMR Rocket," *Sci. Amer.*, Vol. 283, 2000, pp. 90-97.

[19] Chang-Díaz, F.R., "An Overview of the VASIMR Engine: High Power Space Propulsion with RF Plasma Generation and Heating," *Radio Frequency Power in Plasmas*, 14th Topical Conference, Oxnard, CA, AIP Conference Proceedings, Vol. 595, 2001, p. 3.

[20] Cassady, L. D. et al, "VASIMR® Performance Results," Paper AIAA 2010-6772, *40th AIAA/ASME/SAE/ASEE Joint Propulsion Conference and Exhibit*, Nashville, TN, July 2010.

[21] Petro, E. and Sedwick, R., "Survey of Moderate-Power Electric Propulsion Systems," *Journal of Spacecraft and Rockets*, Vol. 54, No. 3, 2017, pp.529-541.

[22] Fruchtman, A., "Neutral Depletion in a Collisionless Plasma", *IEEE Trans. Plasma Sci.,* Vol. 36, No. 2, 2008, pp. 403-413.

[23] Chen, F. F., "Permanent Magnet Helicon Source for Ion Propulsion", *IEEE Trans. Plasma Sci.,* Vol. 36, No. 5, 2008, pp. 2095-2110.

[24] Shamrai, K., et al., "Compact Helicon Plasma Source with Permanent Magnets for Electric Propulsion Application," Paper AIAA-2006-4845, *42nd AIAA/ASME/SAE/ASEE Joint Propulsion Conference & Exhibit,* Sacramento, CA, 2006.

[25] Forrest, A. M., "Meissner and Ochsenfeld revisited", *Eur. J. Phys.*, Vol. 4, 1983, pp. 117-120.

[26] Wilson, A., Vitucci, J. J., and Sedwick, R. J., "Flux Tailoring of a Permanent Magnet Field with a High Temperature Superconducting Tube for a Helicon Plasma Source," *IEEE Trans. Appl. Supercond.*, Vol. 22, No. 5, 2012, pp. 3900705.

[27] Kittel, C., *Introduction to Solid State Physics*, Hoboken, NJ: Wiley, 2005, pp. 259-293.

[28] Chen, F. F., *Introduction to Plasma Physics and Controlled Fusion: Volume 1: Plasma Physics*, New York, NY: Springer, 2006, pp. 30-34.

[29] Boswell, R. W. and Chen, F. F., "Helicons – The Early Years," *IEEE Trans. Plasma Sci.*, Vol. 25, No. 6, 1997, pp. 1229-1244.

[30] Aigrain, P. "Les 'helicons' dans les semiconducteurs," *Proc. Int. Conf. Semiconductor Physics*, Prague, Czechoslovakia, 1960, p. 224.

[31] Chen, F. F., "Plasma Ionization by Helicon Waves," *Plasma Phys. and Controlled Fusion*, Vol. 33, No. 4, 1991, pp.339-364.

[32] Lahane, J. A. and Thonemann, P.C., "Experimental Study of Helicon Wave Propagation in a Gaseous Plasma," *Proc. Phys. Soc.,* Vol. 85, No. 544P, 1965, pp. 301-316.

[33] Chen, F. F. and Popov, O. A. (Ed.), *High Density Plasma Sources*, Woburn, MA: Wiliam Andrew, Inc., 1996, pp.1-75.

[34] Klozenberg, J. P., McNamara, B., and Thonemann, P.C., "Dispersion and Attenuation of Helicon Waves in a Uniform Cylindrical Plasma," *J. Fluid Mech.*, Vol. 21, No. 3, 1965, pp.545-563.

[35] Blevin, H. A. and Christiansen, P. J., "Propagation of Helicon Waves in a Non-Uniform Plasma," *Aust. J. Phys.*, Vol. 19, 1966, pp.501-508.

[36] Boswell, R. W., "Very Efficient Plasma Generation by Whistler Waves Near the Lower Hybrid Frequency," *Plasma Phys. and Controlled Fusion*, Vol. 26, No. 10, 1984, pp. 1147-1162.

[37] Campbell, G. A. et al., "A High Density RF Plasma Source for Etching of Polysilicon and Metal Films on Wafers," *Proceedings of the Society of Photo-Optical Instrumentation Engineers*, Vol. 1803, 1992, pp. 226-234.

[38] Mieno, T., Shoji, J., and Kadota, K., "Control of Hydrocarbon Radicals and Amorphous Carbon Film Deposition by Means of RF Whistler Wave Discharge," *J. Appl. Phys.*, Vol. 31, No. 6A, 1879, pp. 1879-1884.

[39] Chen, F. F., "Experiments on Helicon Plasma Sources," *J. Vac. Sci. Technol.*, Vol. 10, No. 4, 1992, pp. 1389-1401.

[40] Miljak, D. G. and Chen, F. F., "Helicon Wave Excitation with Rotating Antenna Fields," *Plasma Sources Sci. Tech.*, Vol. 7, No. 1, 1998, pp. 61-74.

[41] Porte, L. et al, "Superiority of Half-Wavelength Helicon Antennae," *Plasma Sources Sci. Tech.*, Vol. 12, No. 2, 2003, pp. 287-293.

[42] Degeling, A. W. et al, "Plasma Production from Helicon Waves," *Phys. Plasmas*, Vol. 3, No. 7, 1996, pp. 2788-2796.

[43] Kaeppelin, V., Carrère, M., and Faure, J. B., "Different Operational Regines in a Helicon Plasma Source," *Rev. Sci. Instrum.*, Vol. 72, No. 12, 2001, pp. 4377-4382.

[44] Ellingboe, A. R. and Boswell, R. W., "Capacitive, Inductive, and Helicon-Wave Modes of Operation of a Helicon Plasma Source," *Phys. Plasmas*, Vol. 3, No. 7, 1996, pp. 2797-2804.

[45] Rayner, J. P. and Cheetham, A. D., "Helicon Modes in a Cylindrical Plasma Source," *Plasma Sources Sci. Technol.*, Vol. 8, 1999, pp. 79-87.

[46] Kinder, R. L., Ellingboe, A. R., and Kushner, M. J., "H- to W-mode Transitions and Properties of a Multimode Helicon Plasma Reactor," *Plasma Sources Sci. Technol.*, Vol. 12, 2003, pp. 561-575.

[47] Celik, M., Batishchev, O., and Martinez-Sanchez, M., "Spectral Measurements of mHTX Helicon Discharge Plasma," Paper IEPC-2007-203, *30th International Electric Propulsion Conference*, Florence, Italy, September 2007.

[48] Pucci, J. M. et al, "Preliminary Characterization of a Helicon Plasma Source for Space Propulsion," Paper AIAA 2006-5255, *42nd AIAA/ASME/SAE/ASEE Joint Propulsion Conference and Exhibit*, Sacramento, CA, July 2006.

[49] Keiter, P. A., Scime, E. E., and Balkey, M. M., "Frequency Dependent Effects in Helicon Plasmas," *Phys. Plasmas*, Vol. 4, No. 7, 1997, pp. 2741-2747.

[50] Kim, J. and Chang, H., "A Study on Ion Energy Distribution Functions and Plasma Potentials in Helicon Wave Plasmas," *Phys. Plasmas*, Vol. 3, No. 4, 1996, pp. 1462-1468.

[51] Davies, B. J., "Helicon Wave Propagation. Effect of Electron Inertia," *Journal Plasma Phys.*, Vol. 4, p. 43

[52] Shamrai, K. P. and Taranov, V. B., "Volume and Surface RF Power Absorption in a Helicon Plasma Source," *Plasma Sources Sci. Technol.*, Vol. 5, 1996, pp. 474-491.

[53] Blackwell, D. D. et al, "Evidence for Trivelpiece-Gould Modes in a Helicon Discharge," Paper 145002, *Phys. Rev. Lett.*, Vo1. 88, No. 14, 2002.

[54] Borg, G. G. and Boswell, R. W., "Power Coupling to Helicon and Trivelpiece-Gould Modes in Helicon Sources," *Phys. Plasmas*, Vol. 5, No. 3, 1998, pp. 564-571.

[55] Arnush, D., "The Role of Trivelpiece-Gould Waves in Antenna Coupling to Helicon Waves," *Phys. Plasmas*, Vol. 7, No. 7, 2000, pp. 3042-3050.

[56] Gilland, J., "Application of a Helicon Discharge to Electric Propulsion," Ph.D. Dissertation, University of Wisconsin-Madison, Department of Engineering Physics, 1998.

[57] Charles, C. and Boswell, R. W., "Current-Free Double-Layer Formation in a High-Density Helicon Discharge," *Appl. Rev. Lett.*, Vol. 82, No. 9, 2003, pp. 1356-1358.

[58] Charles, C., "A Review of Recent Laboratory Double Layer Experiments," *Plasma Sources Sci. Technol.*, Vol. 16, 2007, pp. R1-R25.

[59] Williams, L., "Ion Acceleration Mechanisms of Helicon Thrusters," Ph.D. Dissertation, Georgia Institute of Technology, School of Aerospace Engineering, 2013.

[60] Cohen, S. A. et al, "Ion Acceleration in Plasmas Emerging from a Helicon-Heated Magnetic-Mirror Device," *Phys. Plasmas*, Vol. 10, No. 6, 2003, pp. 2593-2596.

[61] Sun, X. et al, "Parallel Velocity and Temperature of Argon Ions in an Expanding, Helicon Source Driven Plasma," *Plasmas Sources Sci. Technol.*, Vol. 13, No. 3, 2004, pp. 359-370.

[62] Sutherland, O., et al., "Experimental Evidence of a Double Layer in a Large Volume Helicon Reactor," *Phys. Rev. Lett.*, Vol. 95, 2005, p. 205002.

[63] Plihon, N., Chabert, P., and Corr, C.S., "Experimental Investigation of Double Layers in Expanding Plasmas," *Physics of Plasmas*, Vol. 14, No. 1, 2007, p. 013506.

[64] Lafleur, T., Charles, C., Boswell, R.W., "Ion Beam Formation in a Very Low Magnetic Field Expanding Helicon Discharge," *Physics of Plasmas*, Vol. 17, No. 4, 2010, p. 043505.

[65] Ling, J., West, M.D., Lafleur, T., Charles, C., and Boswell, R.W., "Thrust Measurements in a Low-Magnetic Field High-Density Mode in the Helicon Double Layer Thruster," *J. Phys. D: Appl. Phys.*, Vol. 43, 2010, p. 305203.

[66] Charles, C., "Helicon Double Layer Thrusters," Topical 5, *XXVIIth ICPIG*, Eindhoven, the Netherlands, July 2005.

[67] Charles, C. and Boswell, R. W., "Laboratory Evidence of a Supersonic Ion Beam Generated by a Current-Free "Helicon" Double-Layer," *Phys. Plasmas*, Vol. 11, No. 4, 2004, pp. 1706-1714.

[68] Gesto, F. N. et al, "Ion Detachment in the Helicon Double-Layer Thruster Exhaust Beam," *Journal of Propulsion and Power*, Vol. 22, No. 1, 2006, pp. 24-30.

[69] Lieberman, M. A., Charles, C., and Boswell, R. W., "A Theory for Formation of a Low Pressure Current-Free Double Layer," *J. Phys. D: Appl. Phys.*, Vol. 39, 2006, pp. 3294-3304.

[70] Chen, F. F., "Physical Mechanism of Current-Free Double Layers," Paper 034502, *Phys. Plasmas*, Vol. 13, 2006.

[71] Siefert, N. S., Stange, S., Boivin, R. F., Scime E. E., Cohen, S. A., and Levinton, F. M., "Ion acceleration in plasmas emerging from a helicon-heated magnetic-mirror device," Paper 2593, *Phys. Plasmas*, Vol. 10, 2003.

[72] Ebersohn, F. H., "Kinetic Method for Quasi-One-Dimensional Simulation of Magnetic Nozzle Plasmadynamics," Ph.D. Dissertation, University of Michigan, Department of Aerospace Engineering, 2016.

[73] Fruchtman, A., "Thrust of a Collisionless Plasma," *IEEE Trans. Plasma Sci.,* Vol. 39, No. 1, 2011, pp. 530-539.

[74] Schmit, P.F. and Fisch, N.J., "Magnetic detachment and plume control in escaping magnetized plasma," *J. Plasma Physics*, Vol. 75, No. 3, 2009, pp. 359-371.

[75] Petro, E.M., and Sedwick, R.J., "Effects of Water-Vapor Propellant on Electrodeless Thruster Performance." *Journal of Propulsion and Power* (2017).

[76] Lehnert, B., "The Quasi-Steady Plasma-Neutral Gas Balance in Magnetic Bottles," *Physica Scripta.,* Vol. 12, 1975, pp. 327-336.

[77] Gilland, J., "Neutral Pumping in a Helicon Discharge," *Plasma Sources Sci. Technol.*, Vol. 7, 1998, pp.416-422.

[78]Abrikosov, A., "Type II Superconductors and the Vortex Lattice", Nobel Lecture, 2003, pp. 59-67.

[79]Sheahen, T., *Introduction to High-Temperature Superconductivity*. New York, NY: Springer, 1994, p. 26.

[80]Kittel, C., *Introduction to Solid State Physics*, Hoboken, NJ: Wiley, 2005, pp. 259-293.

[81] Navarro-Cavallè, et al., "Design of Helicon Plasma Thruster subsystems," Paper AIAA 2014-3699, 50th AIAA/ASME/SAE/ASEE Joint Propulsion Conference and Exhibit, San Jose, CA, July 2014.

[82] Fruchtman, A., "Ambipolar and nonambipolar cross-field diffusions," *Plasma Sources Sci. Tech.*, Vol. 18, 2009, p. 025033.

[83] Porter, A.K., "Space-Deployed, Thin-Walled Enclosure for a Cryogenically-Cooled High Temperature Superconducting Coil," *Ph.D. Dissertation*, Department of Aerospace Engineering, University of Maryland, College Park, MD, 2015.

[84] Flasar, F.M., et al., "Temperatures, Winds, and Composition in the Saturnian System," *Science*, Vol. 307, 2005, pp. 1247-1251.

[85] Mott-Smith, H.M. and Langmuir, I., "The Theory of Collectors in Gaseous Discharges," *Phys. Rev.*, Vol. 28, 1926, pp. 727-763.

[86] Chen, F.F, "Langmuir Probe Diagnostics," Mini-Course on Plasma Diagnostics, IEEE-ICOPS Meeting, Jeju, Korea, June 5, 2003.

[87] Sudit, I.D. and Chen, F.F, "RF Compensated Probes for High-Density Discharges," *Plasma Sources Sci. Technol.*, Vol. 3, 1994, pp. 162-168.

[88] Chen, Sin-Li and Sekiguchi, T., "Instantaneous Direct-Display System of Plasma Parameters by Means of Triple Probe," *J. Appl. Phys.*, Vol. 36, No. 8, 1965, pp. 2363-2375.

[89] Pace, D., "Spontaneous Thermal Waves and Exponential Spectra Associated with a Filamentary Pressure Structure in a Magnetized Plasma," Ph.D. Thesis, University of California, Los Angeles, 2009.

[90] Sheehan, J.P., Collard, T., Ebersohn, F., and Longmier, B.W., "Initial Operation of the CubeSat Ambipolar Thruster," Paper IEPC-2015-243, 34th International Electric Propulsion Conference, Hyogo-kobe, Japan, July 2015.

[91] Wiebold, M., Sung, Y., and Scharer, J.E., "Experimental Observation of Ion Beams in the Madison Helicon eXperiment," Paper 063501, *Phys. Plasmas*, Vol. 18, 2011.

[92] Kimball Physics, *Model FC-71A Faraday Cup: Specifications*, Retrieved from: https://www.kimballphysics.com/fc-71.

[93] Gilland, J.H. and Piefer, G., "Small Helicon Plasma Source Experiments," Paper AIAA 2004-3939, 40th AIAA/ASME/SAE/ASEE Joint Propulsion Conference and Exhibit, Fort Lauderdale, FL, July 2004.

[94] Keesee, A.M. and Scime, E.E, "The Ion Velocity Distribution Function in a Current-Free Double Layer," Paper 093502, *Phys. Plasmas*, Vol. 12, 2005.

[95] Takahashi, K., Igarashi, Y., and Fujiwara, T., "Plane and Hemispherical Potential Structures in Magnetically Expanding Plasmas," Paper 041501, *Appl. Phys. Lett.*, Vol. 97, 2010.

[96] Charles, C., "High Density Conics in a Magnetically Expanding Helicon Plasma," Paper 051502, *Appl. Phys. Lett.*, Vol. 96, 2010.

[97] Sung, Y., Li, Y., and Scharer, J.E., "Observation of Warm, Higher Energy Electrons Transiting a Double Layer in a Helicon Plasma," Paper 034503, *Phys. Plasmas*, Vol. 22, 2015.

[98] Sung, Y., Li., Y., and Scharer, J.E., "Fast, Hot Electron Production and Ion Acceleration in a Helicon Inductive Plasma," Paper 092113, *Phys. Plasmas*, Vol. 23, 2016.

[99] Bennet, A. et al., "Separating the Location of Geometric and Magnetic Expansions in Low-Pressure Expanding Plasmas," Paper 075003, *Plasma Sources Sci. Technol.*, Vol. 27, 2018.

[100] Wiebold, M., Sung, Y., and Scharer, J.E., "Ion Acceleration in a Helicon Source Due to the Self-Bias Effect," Paper 053503, *Phys. Plasmas*, Vol. 19, 2012.

[101] Rapp, D. and Francis, W.E., "Charge Exchange between Gaseous Ions and Atoms," *J. Chem. Phys.*, Vol. 37, 1962, pp. 2631-2645.

[102] Takehashi,. K. et al., "High Temperature Electrons Exhausted from RF Plasma Sources Along a Magnetic Nozzle," Paper 084503, *Phys. Plasmas*, Vol. 24, 2017.